Modelling Flavodiiron Nitric Oxide Reductases: Geometric and Electronic Structure of Key Intermediates and Mechanistic Insights

by

Corey J. White

A dissertation submitted in partial fulfillment
of the requirements for the degree of
Doctor of Philosophy
(Chemistry)
in The University of Michigan
2020

Doctoral Committee:

Professor Nicolai Lehnert, Chair
Professor Steven Ragsdale
Associate Professor Nathaniel Szymczak
Associate Professor Paul Zimmerman

Corey J. White

whitecor@umich.edu

ORCID iD: 0000-0001-6938-7061

Acknowledgements

During my time at the University of Michigan I have significantly grown as a scientist and as a person. I am extremely grateful for Nicolai's mentorship and insight, as well for providing numerous opportunities either via collaboration projects or conference presentations for me to expand on my skillsets. I also would like to thank my committee members Professors Nathaniel Szymczak, Paul Zimmerman, and Stephen Ragsdale for their insight and feedback during our committee meetings. I also greatly appreciate my undergraduate research advisor Professor Jon Fukuto for his mentorship, scientific training, and for inspiring an interest in NO/HNO that has served as a common strand throughout my scientific career.

I also have several collaborators who have been essential in supporting the content within this thesis. I was fortunate to receive the Warner-Linefield Award for International Research, allowing me to work in Prof. Dr. Franc Meyer's lab at the University of Goettingen, Germany between June-August 2016. I thank Prof. Dr. Meyer for inviting me into his lab and thank Dr. Klaudia Kupper for training me. Drs. Klaudia Kupper and Serhiy Demeshko both continued to take Mössbauer and SQUID measurements throughout the entirety of my PhD. I thank Prof. Karsten Krebs and Dr. Debangsu Sil for providing additional Mössbauer characterization and feedback. Lastly, I would like to acknowledge Prof. Amit Majumdar and his students Nabhendu Pal and Manish Jana for synthesizing and providing the mono- and di-nitrosyl complexes discussed in Chapter 3.

I have been very fortunate to work with a wonderful group of friends, scientists, and mentors in the Lehnert laboratory. I thank both Amy Speelman and Ashley McQuarters for their mentorship and patience with me as I entered the lab. Matt – thank you for bringing an aura of levity and camaraderie to the lab through our board game outings. Jill – thank you for being my travelling partner to ICBIC 2019 in Switzerland/Italy. The conference and subsequent travel were one of my highlights during my time in the lab.

Mom and Dad, thank you for your love and support during my time here, for teaching me to be an independent and motivated person, and for always encouraging and supporting my education. Lizzie, thank you for your patience, love, and support. I look forward to what the future holds for us!

Table of Contents

List of Tables

List of Figures

List of Schemes

Abstract

In the face of increasing bacterial resistance to known antibiotics, there is an increasing motivation to study the routes by which bacteria can proliferate. One such route involves the bacterial use of flavodiiron nitric oxide reductases (FNORs), a subclass of flavodiiron proteins (FDPs), to carry out the reduction of nitric oxide (NO) to nitrous oxide (N_2O), thus mitigating the accumulation of toxic levels of NO generated in the human immune response. While enzyme studies on the *Thermatoga maritima* FDP detailed a preliminary route where a high-spin diiron dinitrosyl complex (hs-[{Fe(NO)}^{7}]$_2$ in Enemark-Feltham notation) accumulates before releasing N_2O in the presence or absence of the enzyme's flavin (FMN) cofactor, the structural and electronic prerequisites for non-heme diiron cores to efficiently carry out this reaction had not been systematically studied prior to this work.

Here, several hs-[{Fe(NO)}^{7}]$_2$ and hs-Fe^{II}{Fe(NO)}^{7} model complexes were synthesized and their mechanisms of NO reduction were characterized to identify (1) the electronic prerequisites for N-N coupling with or without the assistance of external reductants, (2) the structural prerequisites for N-N coupling within diiron-dinitrosyl and -mononitrosyl complexes containing the same ligand framework, and (3) the structural prerequisites with respect to the ON-NO bond distance and dihedral angle to carry out N-N coupling.

Our initially reported model system utilized a dinucleating ligand with a N_3O_2 coordination sphere about each iron, where two NO ligands bind in a coplanar geometry. In this complex, the $Fe^{III}Fe^{II}/Fe^{II}Fe^{II}$ redox couple sits more positive than native FNORs, and a stable [hs-{Fe(NO)}^{7}]$_2$ complex was therefore isolated. This complex is the first reported system that undergoes

unimolecular N-N coupling in the presence of one reductive equivalent, affording rapid and quantitative N_2O formation. With more electron donating carboxylate ligand derivatives that enforce a N_2O_3 primary coordination sphere, a diferric $Fe^{III}Fe^{III}$ core can be stabilized. Here, the $[hs\text{-}\{Fe(NO)\}^7]_2$ complex is stable in the solid state, whereas substoichiometric N-N coupling occurs in the absence of external reductants in solution.

Upon the addition of different monodentate N- and O- donor ligands to the above system, the (O)N-Fe-Fe-N(O) dihedral angle and ON-NO distance were perturbed. X-Ray crystallographic data combined with DFT modelling and N_2O yields revealed that dihedral angles above 56.6° and N-N distances above 3.13 Å result in significant inhibition of N_2O yields after 5 minutes. Interestingly, these complexes instead make $Fe^{II}\{Fe(NO)_2\}^{9/10}$ dinitrosyl iron complexes (DNICs) that slowly decompose over 2 hrs.

Lastly, the reactivity of mono- and di-nitrosyl complexes containing the same ligand framework were compared. Here, the $[hs\text{-}\{Fe(NO)\}^7]_2$ complex is the second reported complex that undergoes unimolecular N-N coupling with one equivalent of reductant. The mixed-valent product of the reduction was structurally characterized, providing the first structural data on the product of N-N coupling in diiron complexes. In contrast, the corresponding $hs\text{-}Fe^{II}\{Fe(NO)\}^7$ complex requires two reductive equivalents to facilitate bimolecular N-N coupling, pointing towards a drastically decreased activation barrier for N-N coupling when the substrate NO molecules are held in a *cis* orientation in a diiron complex.

The data discussed in this thesis outline several necessary conditions to achieve N-N coupling: (1) It can occur between *two* $hs\text{-}\{FeNO\}^7$, (2) It more readily occurs from unimolecular coupling in a *cis* $hs\text{-}[\{FeNO\}^7]_2$ dimer, (3) Reduction of one $hs\text{-}\{FeNO\}^7$ unit in the dimer leads to significant activation for N-N coupling, (4) More negative redox potentials activate $hs\text{-}\{FeNO\}^7$

species, and (5) Precise geometric tuning of (O)N-N(O) distances and N-Fe-Fe-N angles are required to facilitate the reaction.

Chapter 1

Introduction[1]

1.1 The Physiological Roles of Nitric Oxide

Nitric oxide (NO) is an endogenously generated molecule that plays an important role in human physiology. It is biosynthesized by three isoforms of nitric oxide synthases (NOS)[2]: neuronal and endothelial nitric oxide synthases, nNOS and eNOS, respectively, generate nanomolar amounts of NO as a signaling agent. Here, NO is detected at nM concentrations by soluble guanylate cyclase (sGC), ultimately inducing the formation of the secondary messenger cyclic GMP, which is then involved in nerve signal transduction and vasodilation.[3] In contrast, inducible NOS (iNOS) can be activated in macrophages to generate acutely toxic, micromolar concentrations of NO at sites of infection as part of the mammalian immune defense.[4] The physiological effects of NO are summarized in Figure 1.1.

In the past 30 years, the one electron reduced and protonated form of NO (nitroxyl, NO^-/HNO), has been recognized as a distinct signaling molecule as well.[5-9] Initial reports placed the pKa of the NO^-/HNO couple at 4.7; however, this was later revised to 11.6 ± 3.4[10, 11], implying that nitroxyl is a largely protonated species at physiologically relevant pH. Additionally, the protonation/deprotonation kinetics are slow, arising from the fact that the ground state of NO^- is a triplet, while that of HNO is a singlet, making protonation of $^3NO^-$ to ^{1}HNO spin forbidden.[6, 11] The recent interest in NO^-/HNO as a signaling molecule arises from new studies showing that HNO

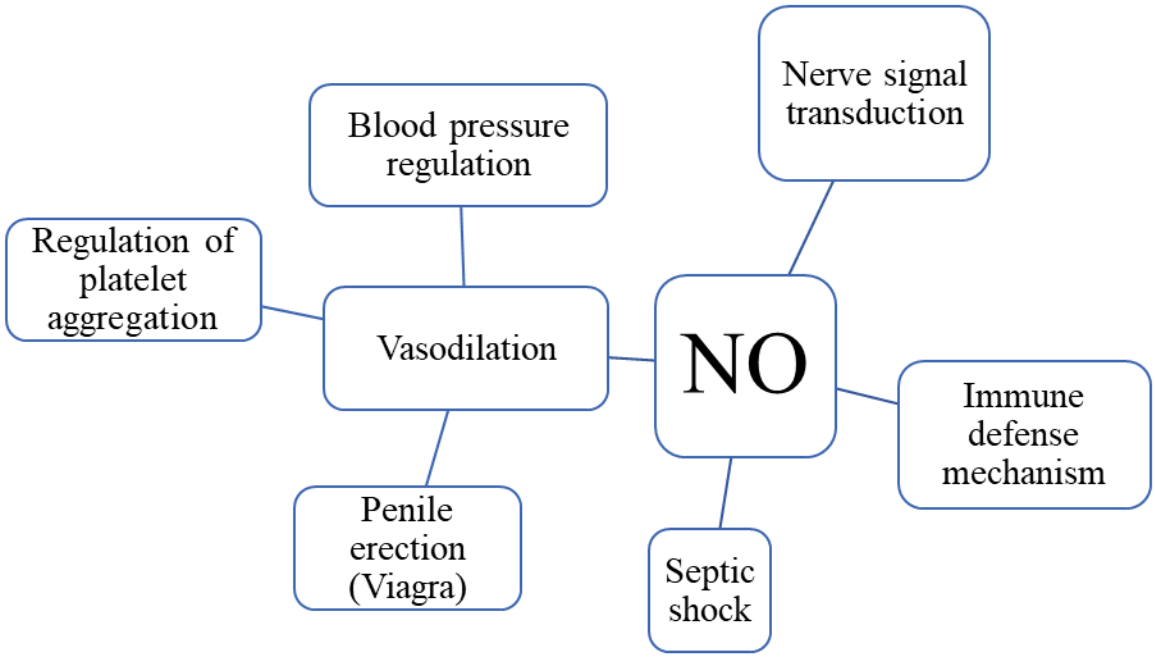

Figure 1.1 Overview of the key physiological roles attributed to NO.

can in fact be generated under physiological conditions, which was controversial for a long time. Recent data supports HNO generation from the interaction of NO with hydrogen sulfide (H_2S)[12], another signaling molecule that has received intense interest in recent years, with signaling pathways that are intertwined with those of NO and HNO.[13-17] Alternatively, NO can undergo proton-coupled nucleophilic attack by physiologically relevant alcohols, including ascorbate and tyrosine, to generate HNO under physiological conditions.[18]

The primary targets of NO and HNO signaling *in vivo* are thiols and metal centers, including heme and non-heme iron, as well as iron-sulfur clusters. For example, the propensity for HNO to bind to thiols is utilized in the alcohol deterrent drug cyanamide[19], which releases HNO and results in the inactivation of aldehyde dehydrogenase via an active site cysteine-thiol oxidation facilitated by HNO.[20] This results in an accumulation of the alcohol metabolite, acetaldehyde, which induces bad hangovers in patients who consume alcohol while taking the drug. Notably, this drug also generates cyanide[19]; however, it is generated at low enough

concentrations to avoid toxicity, showcasing the potent thiophillicity of HNO, even at extremely low concentrations. NO has also been utilized for its vasodilation effects in other drugs – most notably Viagra, which was initially designed to reduce the blood pressure in patients (via the formation of the secondary messenger cGMP, as described above) with heart disease.

On the other hand, NO is known to break down iron-sulfur clusters by generating dinitrosyl iron complexes (DNICs).[21-24] While this has been proposed as one route of NO toxicity towards pathogenic bacteria, NO is also capable of deleterious break down of iron-sulfur clusters in the human body. For example, NO can react with the [4Fe4S] cluster of aconitase, a crucial component in metabolic citrate regulation, resulting in inhibition of the enzyme, causing NO toxicity.[25] In addition to the formation of DNICs in iron-sulfur proteins, it has also been demonstrated that DNICs can form from the labile iron pool in the presence of thiols like cysteine (CysSH) and glutathione (GSH). For example, stopped-flow kinetics studies[26, 27] complimented by DFT calculations[26] have shown that low molecular weight thiols like CysSH and GSH can bind to labile Fe^{II} in the presence of NO to make a transient 3-coordinate $\{FeNO\}^7$ species in an initial slow phase of the reaction. This species then decays via thiyl (RS•) radical loss, affording a proposed $\{FeNO\}^8$ intermediate that rapidly binds an additional thiol and NO to afford a $\{Fe(NO)_2\}^9$ DNIC. Based on thiolate concentration and pH, this DNIC exists in equilibrium with its corresponding Roussin's red salt ester (Scheme 1.1). Importantly, DNICs can serve as a storage pool for NO and are chemically capable of delivering NO to targets like heme centers.[28] An alternate form of mobile NO storage arises from the oxidation of NO in the presence of cellular thiols like glutathione (GSH) and cysteine (Cys) to make S-nitrosothiols (RSNOs).[29-31] Recent work has demonstrated that copper centers serve as a possible route towards the controlled release of NO from S-nitrosothiols.[32] For example, CuZnSOD, an abundant source of Cu in red blood

cells, is capable of reducing GSNO to release NO in red blood cells.[33] This process serves as one route towards NO release, leading to the vasodilatory effects ascribed to NO.

Scheme 1.1 Proposed mechanism for DNIC formation from the labile iron pool with low molecular weight thiol (CysSH, GSH) and NO.

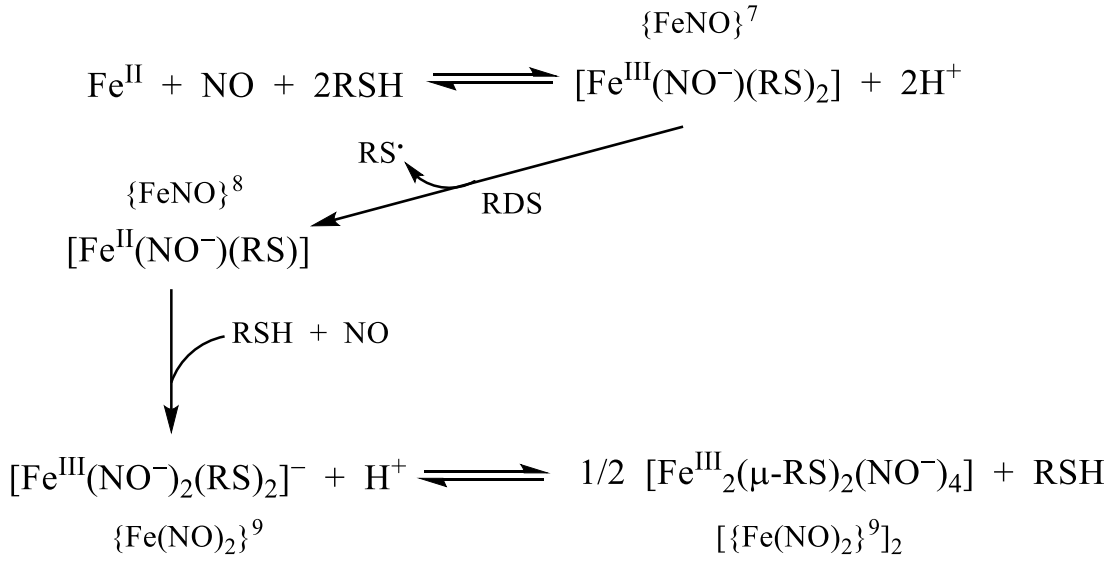

NO and HNO also interact with heme and non-heme iron centers in biology. Due to the non-innocent nature of NO in metal nitrosyl complexes, the Enemark-Feltham notation is typically utilized to indicate the oxidation state of the entire metal-nitrosyl unit, denoted as $\{M(NO)_x\}^n$.[34] Here, the subscript *x* corresponds to the number of NO ligands and *n* corresponds to the total number of valence electrons originating from the metal d- and NO π* electrons. Since the metal spin state also plays a key role in the electronic structure and reactivity of metal-nitrosyls, this thesis will also include a hs- (high-spin) or ls- (low-spin) prefix when necessary. The nitric oxide reductase (NOR) group of enzymes (discussed in detail in section 1.2) all contain proposed iron-nitrosyl $\{FeNO\}^7$ and iron-nitroxyl $\{FeNO\}^8$/$\{FeHNO\}^8$ intermediates (hs or ls, depending on the system) in their catalytic cycles, though the $\{FeNO\}^8$ species have remained elusive in enzyme studies and have only been characterized with model systems. Farmer and coworkers have

prepared a unique ls-{FeHNO}^{8} complex in myoglobin, and characterized it using ^{1}H-NMR, resonance Raman and X-ray absorption spectroscopy (XAS).[8, 35, 36] Here, the N-protonated hydrogen resonance at 14 ppm in ^{1}H-NMR becomes a doublet upon substitution with ^{15}NO with a characteristic coupling constant J_{NH} of 75 Hz. However, the generation of this species from the starting ls-{FeNO}^{7} complex required a negative reduction potential that sits at the edge of the physiologically feasible range at -630 mV, making it unlikely that this species could be generated under physiological conditions via the simple reduction of a ls-{FeNO}^{7} complex. One of the major questions remaining in the field is whether non-heme systems can generate and stabilize {FeNO}^{8}/{FeHNO}^{8} adducts. Importantly, non-heme iron model systems tend to have more positive {FeNO}$^{7/8}$ redox couples compared to their heme analogs[37, 38] owing to the fact non-heme iron complexes tend to be high spin and therefore, contain lower-energy unoccupied acceptor d-orbitals than the corresponding low-spin heme systems.[39] The electronic structure and reactivity of iron nitrosyl complexes is discussed further in section 1.3.

1.2 Nitric Oxide Reductases

The reduction of NO via iron-nitrosyl complexes as intermediates is carried out by three classes of nitric oxide reductases (NORs). Soil dwelling bacteria and fungi utilize several enzymes in the stepwise reduction of nitrate and nitrite to dinitrogen in anaerobic respiration, the so-called denitrification pathway.[40, 41] As an intermediate step in this process, NORs[42] carry out the two-electron reduction of two NO molecules to nitrous oxide (N_2O):

$$2\ NO + 2\ e^- + 2\ H^+ \rightarrow N_2O + H_2O \qquad (1)$$

Fungi carry out this reduction using fungal cytochrome P450 nitric oxide reductase (P450nor), which contains a ferric heme P450 active site and a nearby NADH substrate (Figure

1.2).[43, 44] Here, NO binds to the ferric heme followed by a direct hydride transfer from the NADH cofactor to the ferric nitrosyl, generating a {FeHNO}^{8} intermediate.[45, 46] The mechanism (Figure

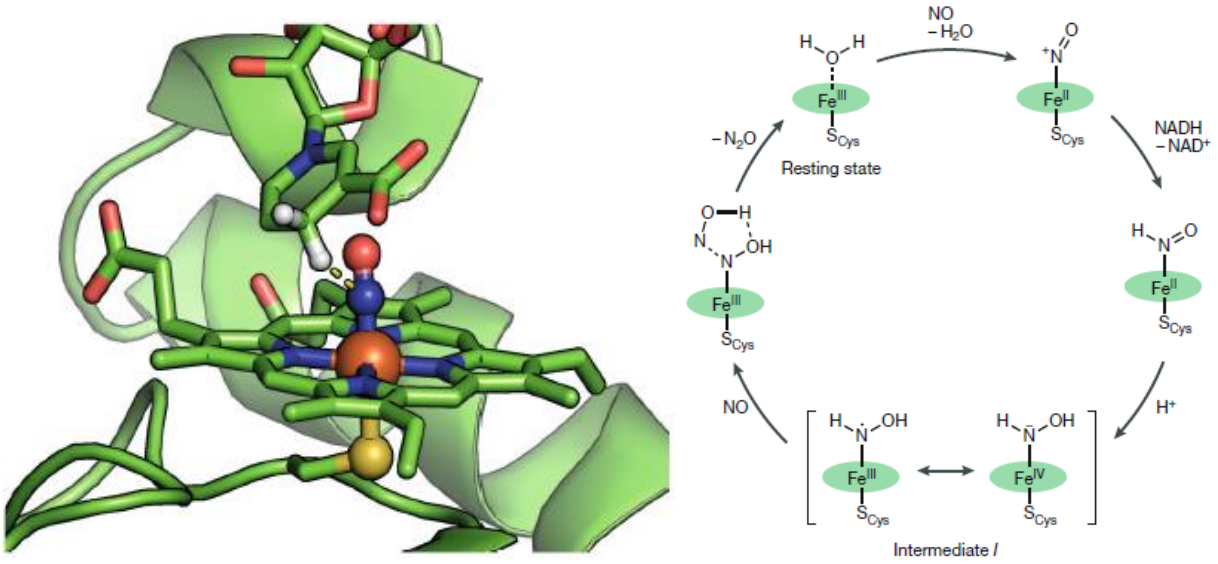

Figure 1.2 Left: Overlay of two cytochrome P450 nitric oxide reductase (Cyt P450nor) crystal structures, showing the ferric heme Fe–NO complex from one data set (Protein Data Bank identifier (PDB ID): 1CL6)[45], with the rest of the protein and a bound NAAD (a NADH analogue) obtained from another structure determination (PDB ID: 1XQD)[46]. All H atoms, except those at the C4 position of NAAD, are omitted for clarity. Right: Current mechanism proposed for CytP450nor.

1.2) by which this species proceeds to generate N_2O is still under investigation, and mechanistic studies are hampered by the limited lifetime of this intermediate.[47] The {FeHNO}^{8} complex could either directly couple with the second NO, followed by subsequent protonation, or first get protonated to a hydroxylamide ($NHOH^-$) type intermediate (as indicated in Figure 1.2), and then undergo coupling with the second NO to generate N_2O, H_2O, and the resting ferric heme. Recent studies coupled with density functional theory (DFT) calculations are in support of the doubly protonated hydroxylamide ($NHOH^-$) species as the reactive "Intermediate I" in the catalytic mechanism, as opposed to the singly protonated {FeHNO}^{8} complex. These mechanisms possibilities are discussed in detail in recent publications[39, 48-52] and will not be further commented on here.

Denitrifying bacteria carry out NO reduction using bacterial NO reductases (NorBC or cNOR). The active site of NorBC is bimetallic, consisting of a heme b_3 and a non-heme iron center termed Fe_B. In the crystal structure of the diferric resting state, the two iron centers contain a bridging μ-oxo ligand, with a Fe-Fe distance of 3.5Å and an otherwise typical coordination sphere around Fe_B, containing three histidine and one glutamate residues (Figure 1.3).[53-55] NorBC is a membrane-bound enzyme containing additional non-catalytic electron transfer hemes, and as such, detailed mechanistic and spectroscopic studies have been confounded.[56] Nonetheless, the enzyme active site has been successfully modeled by several groups[57] and three possible limiting mechanisms for N-N coupling have been established (Figure 1.3). The central pathway, termed

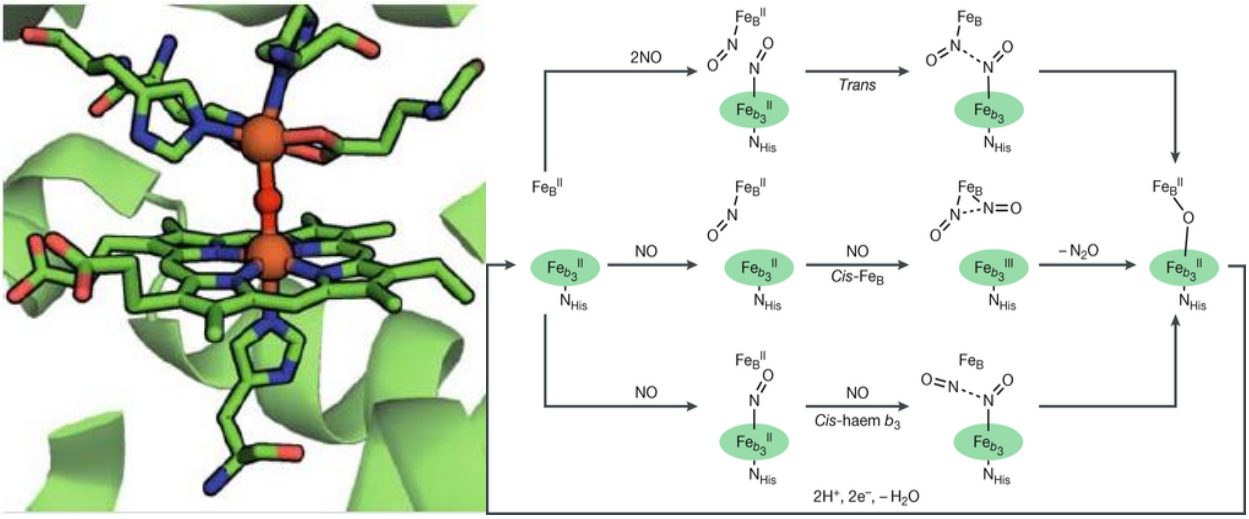

Figure 1.3 Left: Crystal structure of the bimetallic active site of bacterial NO reductase in the diferric resting state (PDB ID: 3O0R)[39]. Right: Mechanistic proposals for NO reductive coupling catalyzed by bacterial NO reductase.

"cis-Fe_B", involves the formation of a DNIC intermediate at the Fe_B center. This route is generally considered unlikely for two major reasons. To start, the heme-Fe has a significantly higher binding constant for NO (~10^{12}-10^{14})[58]. Secondly, the DNIC electronic structure is well established, consisting of a hs-Fe center antiferromagnetically coupled to two NO^- moieties, where all NO^- π^* electrons are spin-parallel. This results in a large barrier for N-N coupling between the two NO

units bound in DNICs, due to the spin-forbidden nature of this reaction.[59] The electronic structure of DNICs is discussed further in section 1.3. The upper pathway details the "trans" mechanism, which was initially proposed based on early UV-Vis, EPR, and enzyme kinetics data.[60] Here, NO binds to both the heme-Fe and the Fe_B center, which subsequently undergo a radical-type coupling to generate a trans-hyponitrite type intermediate. However, this intermediate has never been directly observed, and from a more fundamental point of view, both heme and non-heme $\{FeNO\}^7$ moieties tend to be very stable and unreactive.[61, 62] These findings are supported by DFT studies, predicting a prohibitively high activation barrier for N-N coupling via this route.[63] Evidence for this mechanism comes from studies on modified myoglobins that contain an engineered Fe_B site by Lu and coworkers and that are capable of N_2O production. Here, the generation of both heme and non-heme nitrosyl species under turnover was demonstrated spectroscopically, indirectly supporting this mechanism, though the N-N coupling is slow and therefore may not operate via the same mechanism as the native enzyme.[57, 64-66] Lastly, the lower pathway is termed the "cis heme b_3" mechanism.[67, 68] In this route, it is proposed that the heme FeNO adduct forms first and is subsequently attacked by a second free NO molecule. As initially proposed, the Fe_B center would simply act as a spectator here, while the second NO attacks the heme Fe-NO complex. Since these $\{FeNO\}^7$ species are stable to excess NO, this initial proposal is unfeasible; however, recent DFT data propose that the Fe_B center may instead act as a Lewis-acid activator that effectively polarizes the heme-bound NO and primes it for coupling with the second, incoming NO, while simultaneously stabilizing the hyponitrite intermediate.[63, 68] Interestingly, this hypothesis was also tested in Lu's modified myoglobin model by replacing the non-heme Fe_B with Cu^{II} and Zn^{II}. Importantly, the Cu^{II} analog polarizes the heme-NO unit, as evident from a decrease

in its ν_{NO} energy by 50 cm^{-1}, though this was insufficient to activate the heme-bound NO for N-N coupling.[69]

In contrast to the bacterial and fungal enzymes P450nor and NorBC that function in the respiratory chain, flavodiiron nitric oxide reductases (FNORs) are utilized by pathogenic bacteria as a means of detoxifying NO generated by the mammalian immune defense. These pathogens have developed a defense strategy against NO toxicity, whereby a transcription factor senses NO[70] and subsequently induces transcription of an FNOR, which then reduces NO to the much less toxic N_2O following eqn. 1.[71] This underlines the importance of the NO reduction reaction in Nature, which co-evolved using three completely different enzyme systems.

FNORs belong to the family of flavodiiron proteins (FDPs), which were first recognized for their ability to reduce O_2 to water in a purely protective, not metabolic, function.[72] Later, Gardner realized that some FDPs are designated NORs (flavodiiron NORs, or FNORs).[71] Further investigations have shown that all FDPs can catalyze the reduction of both NO and O_2 but that there is generally a catalytic preference – those that preferentially reduce NO are considered FNORs.[72] Here, different protein environments play a crucial role in determining the preference for NO or O_2, but the details are not well understood.[73-75] All structurally characterized FDPs, including FNORs, consist of similar active sites. Numerous FDPs from organisms such as *Desulfovibrio gigas, Rhodobacter capsulatus, Methanobacterium thermoautotrophicum*, and *Treponema denticola* have been studied.[74, 76-78] These FDPs exist as head-to-tail homodimers, where every monomer has a nonheme diiron site in the N-terminal domain and a flavin (FMN) binding site in the C-terminal domain. In the head-to tail arrangement of the homodimer, the diiron site of one subunit is only about 4−6 Å away from the FMN cofactor of the other subunit. In the diiron core of the *M. thermoacetica* and *T. maritima* enzymes, each iron center is coordinated by

two histidine ligands and a monodentate carboxylate as shown in Figure 1.4.[79, 80] In addition, the two irons are bridged by a hydroxide and a carboxylate ligand.[81] In contrast, the *D. gigas* FDP

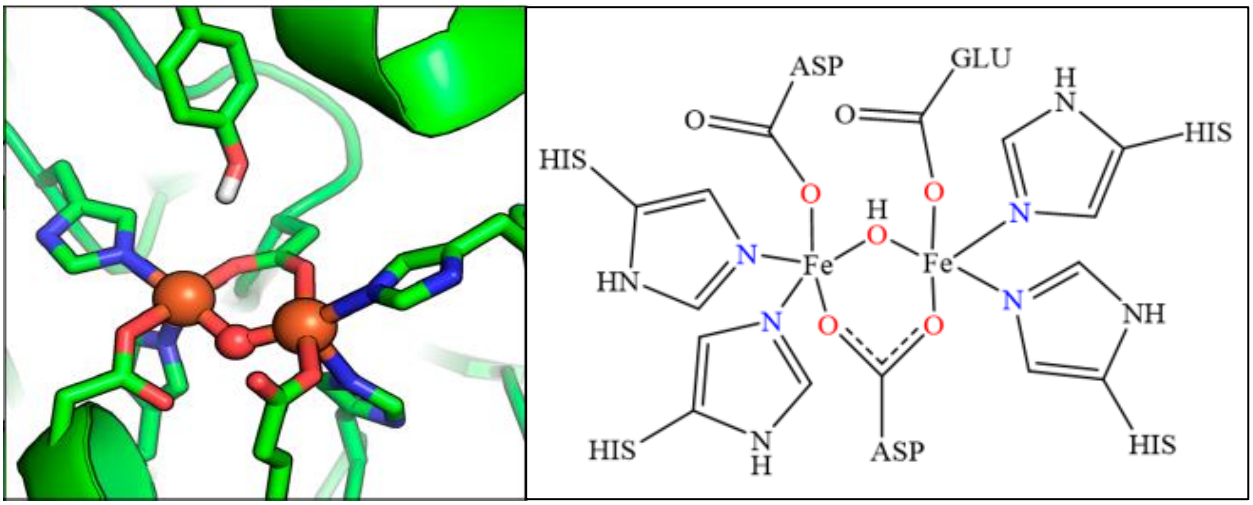

Figure 1.4 Left: Crystal structure of the non-heme diiron active site of FNORs (PDB ID: 1YCG)[79], including a potential secondary coordination sphere Y197.[82] Right: Chemdraw depiction of the FNOR active site.

shows a slightly more asymmetric diiron site, where one of the His ligands is replaced by a water molecule.[77] Interestingly, however, this difference in ligation between typical FDPs and the *D. gigas* enzyme does not seem to cause any difference in reactivity.[80] Despite these subtleties, all available crystal structures of FDPs generally show one open coordination site per iron center as indicated in Figure 1.4 adjacent to each other in a *cis* orientation. This allows two NO molecules to bind in proximity, which is a requirement for efficient N−N bond formation and N_2O generation.[83, 84] This is discussed further in chapters 2 and 3.

While the activation of NO by FNORs has been studied in both enzymes and in several synthetic model complexes, the mechanism by which NO is reduced to N_2O has been contested in the literature. Detailed rapid-freeze-quench Mössbauer and EPR studies on the flavinated and deflavinated *T. maritima* FDP by Kurtz and co-workers[85, 86] have shown that although a diiron mononitrosyl hs-Fe^{II}{FeNO}^{7} is generated in this enzyme upon sequential addition of NO equivalents, the diiron dinitrosyl complex, [hs-{FeNO}^{7}]$_2$, is the catalytically relevant

intermediate that accumulates before any N_2O is formed.[85, 87] From the diiron dinitrosyl intermediate, three different pathways for N−N coupling are feasible, all revolving around the question of how the FMN cofactor participates in catalysis (Scheme 1.2). These pathways have

Scheme 1.2 Proposed mechanisms for NO reduction in FNORs.

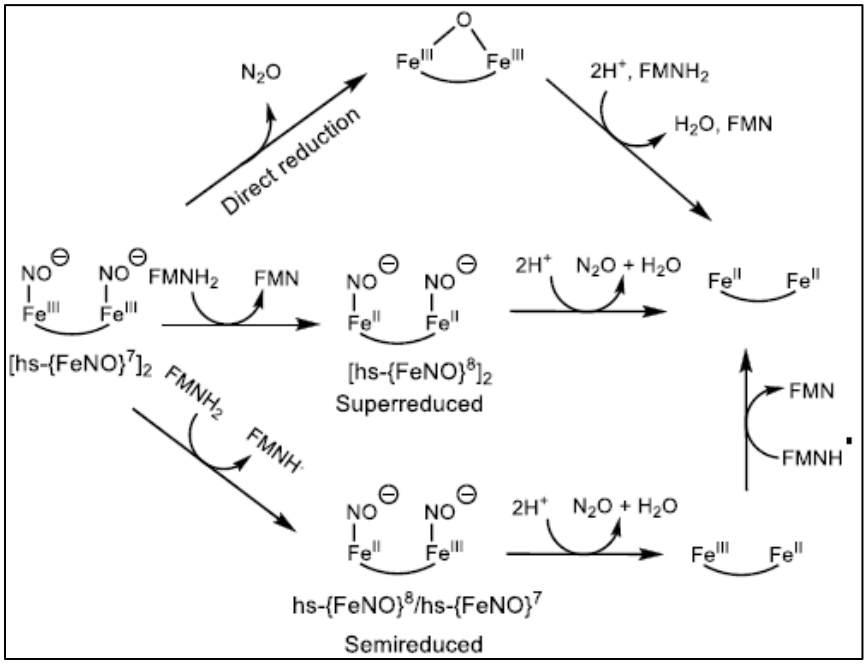

been termed (a) "direct reduction", where the [hs-{FeNO}^{7}]$_2$ intermediate can generate N_2O without the participation of the FMN cofactor (b) "semireduction", where the FMN cofactor must activate the [hs-{FeNO}^{7}]$_2$ dimer with one electron via a hs-{FeNO}^{7}/hs-{FeNO}^{8} intermediate, prior to N_2O formation; and (c) "superreduction", where the FMN cofactor delivers both of its reductive equivalents to activate the [hs-{FeNO}^{7}]$_2$ complex via a [hs-{FeNO}^{8}]$_2$ intermediate, prior to N_2O formation. In the "direct-reduction" pathway, the FMN would then serve solely as a means of re-reducing the active site for another turnover but would not actively participate in catalyzing NO reduction.

Interestingly, Kurtz and co-workers' detailed comparison between the flavinated and deflavinated *T. maritima* (*Tm*) FDP shows that even in the absence of the FMN cofactor, the *Tm*

FDP is still capable of a single turnover of 2NO to N_2O from the diferrous state.[85] However, this occurs at a slower rate compared to the flavinated FDP as monitored by stopped-flow UV− vis spectroscopy. Here, both reductive equivalents originate from the diferrous core in a direct reduction mechanism, implying that the FMN cofactor acts solely as a means of re-reducing the active site after N−N coupling. This seems surprising, given that numerous hs-{FeNO}^{7} model complexes have been synthesized and are stable towards N-N coupling in the solid state and in solution[84, 88-93] due to the high covalency of the Fe-NO bond.[94] However, a recent DFT study identified a secondary coordination sphere Y197 within H-bonding distance to NO at one of the irons in the diiron core (see Figure 1.4) and found that this H-bonding interaction to one of the iron-bound NOs reduces both the enthalpic and entropic penalties towards both N-N coupling and N-O cleavage along the N-N coupling pathway.[82] Native FNORs likely use a combination of electronic tuning and H-bonding assistance to accomplish their direct coupling mechanism of NO reduction.

In contrast to the above enzyme studies, preliminary studies on FNOR model complexes found that the hs-[{FeNO}^{7}]$_2$ core required additional assistance to facilitate NO reduction to N_2O. For example, Lippard's synthetic model complex $[Fe_2(\text{N-Et-HPTB})(O_2CPh)(NO)_2](BF_4)_2$ (N-Et-HPTB = N,N,N′,N′-tetrakis(2(1-ethylbenzimidazolyl))-2-hydroxy-1,3-diaminopropane) is capable of stabilizing a [hs-{FeNO}^{7}]$_2$ species that produces substoichiometric N_2O upon photocleavage of one of the Fe−NO bonds.[95] This generates a bridging mononitrosyl that is proposed to be attacked by the photocleaved NO, generating N_2O and a bridging μ-oxo product. While this mechanism is a chemically feasible coupling route, as discussed above, the diferrous dinitrosyl species is the catalytically competent intermediate for N-N coupling within the enzyme.

Our laboratory previously communicated the stable [hs-{FeNO}^{7}]$_2$ model complex, [Fe$_2$(BPMP)(OPr)(NO)$_2$](BPh$_4$)$_2$ (BPMP = 2,6-bis[(bis(2-pyridylmethyl)amino)methyl]-4-methylphenolate) which contains two coplanar hs-{FeNO}^{7} units in a *cis* orientation with an N−N distance of 2.803 Å. While the initial report[90] stated that two reductive equivalents were required to quantitatively reduce 2NO to N_2O, this complex suffered from poor solubility and Na/K BPh_4 impurities. Chapter 2 details the complete study of the more soluble and pure [Fe$_2$(BPMP)(OPr)(NO)$_2$](OTf)$_2$ analog, which quantitatively and rapidly generates N_2O in the presence of one reductive equivalent in support of the semireduced coupling pathway.[84] Recently, Majumdar's [Fe$_2$(*N*-Et-HPTB)(NO)$_2$(DMF)$_2$](BF$_4$)$_3$ (N-Et-HPTB$^-$ = N,N,N′,N′-tetrakis(2-(l-ethylbenzimidazolyl))-2-hydroxy-1,3-diaminopropane) complex similarly facilitates near quantitative semireduction and will be discussed further in Chapter 3.[96]

So far, no synthetic [hs-{FeNO}^{7}]$_2$ model complex is known that formally undergoes *intramolecular* superreduction. This is likely due to the efficiency of semireduction in the model systems studied experimentally thus far. Once the [hs-{FeNO}^{7}]$_2$ unit is reduced by one electron, fast intramolecular N_2O generation is observed before a second electron can be transferred. In agreement with this, DFT calculations on the complex [Fe$_2$(BPMP)(OPr)(NO)$_2$]$^{2+/1+/0}$ show that semireduction and superreduction have essentially identical barriers for N−N bond formation.[97] However, there are some examples of NO activation via *intermolecular* N−N coupling by the superreduced mechanism in non-heme mononitrosyl species. The first example is Goldberg's [Fe(NO)(N3PyS)]BF_4 complex[92], where N3PyS$^-$ is N-(2-(λ1-sulfaneyl)benzyl)-1,1di(pyridin-2-yl)-N-(pyridin-2-ylmethyl)methanamine, which can be chemically reduced to the hs-{FeNO}^{8} state. This species is metastable at room temperature ($t_{1/2}$ = 0.5 h) and slowly releases substiochiometric amounts of N_2O (27%) over 20 h.[98] Majumdar's diiron mononitrosyl complex[91],

$[Fe_2(N\text{-}Et\text{-}HPTB)(NO)(DMF)_3](BF_4)_3$, on the other hand, undergoes rapid and quantitative *intermolecular* N−N coupling upon reduction of the hs-Fe^{II}/hs-$\{FeNO\}^7$ to the hs-Fe^{II}/hs-$\{FeNO\}^8$ complex, affording N_2O in 45% yield within 5 min. This complex will be discussed in further detail in Chapter 3. Although these complexes do not directly model the FNOR mechanism, they further demonstrate that reduction is a potent means of activating otherwise stable non-heme hs$\{FeNO\}^7$ complexes for N−N coupling, and that superreduction is in principle possible.

While the above complexes either carry out *intramolecular* coupling via coplanar NO moieties or *intermolecular* coupling via two $\{FeNO\}^8$ species, Meyer's $[L\{Fe(NO)\}_2(\mu\text{−}OOCR)](X)_2$ [hs-$\{FeNO\}^7$]$_2$ model complex[99] (where L is a dinucleating pyrazole/triazacyclononane ligand, 4,4′-((1H-pyrazole-3,5diyl)bis(methylene))bis(1-methyl-1,4,7-triazonane), R is Me or Ph, and X^- is ClO_4^- or BPh_4^-) contains two hs-$\{FeNO\}^7$ units in *trans* orientation. This complex does not generate N_2O upon reduction, but instead, the one-electron reduced complex undergoes a redox and ligand disproportionation to form a $[\{Fe(NO)_2\}^9]_2$ di-DNIC and a diferrous complex, both characterized by X-ray crystallography. Based on these findings, as well as the data discussed in both chapters 2 and 3, the relative orientation of the Fe−N−O units in a dinuclear complex is proposed to be a key structural prerequisite for efficient N_2O formation by diiron complexes.

1.3 Non-heme Iron Nitrosyls: Overview of Electronic Structure and Reactivity

Pioneering work by Solomon and coworkers utilized a combination of EPR, MCD, SQUID, rRaman, and X-ray absorption techniques coupled to computations to determine that the ground state of hs-$\{FeNO\}^7$ complexes is best described as Fe^{III}-NO^-, where the hs-Fe^{III} (S = 5/2) is antiferromagnetically coupled to the $^3NO^-$ (S = 1) π^* electrons to give a S_t = 3/2 ground state (Figure 1.5).[94, 100] These studies are further supported with numerous recent

studies and reviews on other hs-{FeNO}^{7} complexes.[37, 101-104] Additional work from our laboratory

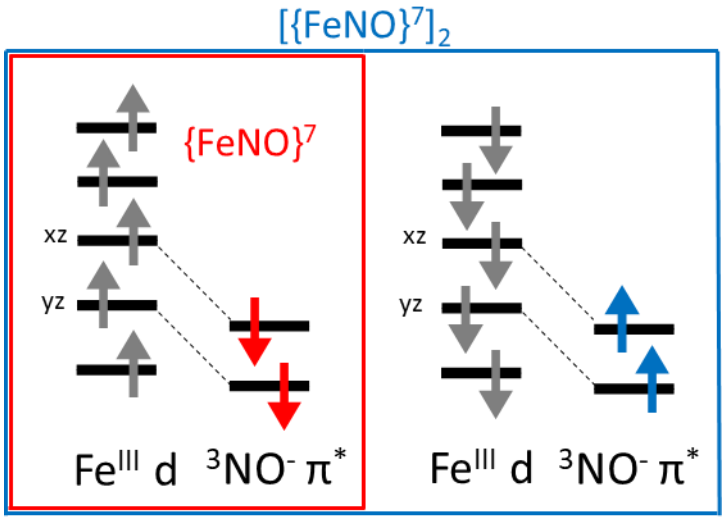

Figure 1.5 The electronic structure of a hs-{FeNO}^{7} monomer is shown on the left, illustrating antiferromagnetic coupling between the Fe-d and NO π* electrons. The whole diagram includes the expected antiferromagnetic coupling across the diiron core of a hs-{FeNO}^{7} dimer.

utilized NRVS and IR vibrational spectroscopies to correlate the Fe-NO and N-O stretching frequencies for a series of related ligand scaffolds of varying electron donicity.[38] Results from this study illustrate that the $^3NO^-$ ligand's primary bonding interaction is via π-donation from the π^* electrons, where the strength of this donation is inversely correlated to the electron donicity of the ligand scaffold. Here, electron rich ligands weaken the $^3NO^-$ π-bonding to the Fe center, resulting in weaker Fe-NO bonds and an increase in π^* electron density, thus weakening the N-O bonds as well. Based on a large body of reported hs-{FeNO}^{7} model complexes, the Fe-NO bond is typically slightly bent, with increased linearity corresponding with increased π-donation.[38, 94, 105-109] Bond angles range from 174° to 147° and correlate[107] with N-O stretching frequencies between 1831 and 1689 cm^{-1}. Furthermore, as demonstrated by additional work from our laboratory on the first hs-{FeNO}$^{6-8}$ series containing the TMG_3tren (TMG_3tren = 1,1,1-tris{2-[N2-(1,1,3,3-tetramethylguanidino)]ethyl}amine)

coligand[88, 110, 111], this effect is also directly correlated to the formal nuclear charge at the metal center. Taking a similar approach to the Solomon group, MCD, NRVS, XANES, EXAFS, IR, and Mössbauer spectroscopy coupled to DFT were used to demonstrate a Fe-centered reduction and oxidation of the hs-$\{FeNO\}^7$ species to generate the hs-Fe^{II}-NO^- (hs-$\{FeNO\}^8$) and Fe^{IV}-NO^- (hs-$\{FeNO\}^6$) complexes, respectively. Both hs-$\{FeNO\}^8$ and hs-$\{FeNO\}^6$ were successfully stabilized due to the steric protection afforded to the Fe-NO core by the TMG_3tren coligand. This series has N-O stretching frequencies of 1878, 1750, and 1618 cm^{-1} for the hs-$\{FeNO\}^6$, hs-$\{FeNO\}^7$, and hs-$\{FeNO\}^8$ complexes, respectively. In contrast, the TMG_2dien analog[112], where one of sterically bulky tetramethylguanidino groups is removed from the coligand, does not stabilize a hs-$\{FeNO\}^8$ state and instead, undergoes rapid disproportionation to generate a $\{Fe(NO)_2\}^{10}$ DNIC and a Fe^{II} species. The reactivity of hs-$\{FeNO\}^8$ species will be discussed in additional detail below. Since hs-$\{FeNO\}^{7\text{-}8}$ systems are the focus of this thesis, the electronic structure and reactivity of hs-$\{FeNO\}^6$ systems will not be commented on further here.

As discussed in section 1.2, non-heme hs-Fe^{II}/hs-$\{FeNO\}^7$ and hs-$[\{FeNO\}^7]_2$ systems and their reduced hs-$\{FeNO\}^8$ counterparts have recently emerged as a topic of intense research in NOR chemistry. The electronic structures of these systems are closely related to those of the mono-iron complexes introduced above. For hs-$\{FeNO\}^7$ complexes, the hs-Fe^{III} ($S = 5/2$) is antiferromagnetically coupled to the $^3NO^-$ ($S = 1$) ligand to afford $S_t = 3/2$ spin states with an additional weak antiferromagnetic coupling, dependent on the nature of the bridging ligands, between the two iron centers in a dimeric complex. For hs-Fe^{II}/hs-$\{FeNO\}^7$ systems, this results in antiferromagnetic coupling between the hs-Fe^{II} ($S = 2$) and the hs-$\{FeNO\}^7$ ($S = 3/2$) unit, affording an $S_t = ½$ ground state. In the same vein, hs-$[\{FeNO\}^7]_2$ complexes have an $S_t = 0$

ground state (see Figure 1.5). Typical exchange J-coupling constants for these systems[84, 89, 91, 96, 99, 113, 114] range from -5 to -20 cm^{-1} using the Spin Hamiltonian:

$$\underline{H} = -2J \bullet \underline{S_A} \bullet \underline{S_B}$$

Due to the highly covalent nature of the Fe-NO bond in hs-{FeNO}^{7} complexes[94], many of these complexes are stable indefinitely in the solid state and stable on the order of hours to indefinitely in solution, with NO loss being the primary means of decomposition.

In contrast, the one-electron reduction of hs-{FeNO}^{7} complexes to stable hs-{FeNO}^{8} species has, until recently, been experimentally challenging. As alluded to above, the first reported hs-{FeNO}^{8} complex was generated using the sterically bulky TMG_3tren coligand.[88, 111] This complex exhibits N-O and Fe-NO stretching frequencies of 1618 and 435 cm^{-1}, respectively, consistent with weakened Fe-NO and N-O bonds owing to the increased charge density at the iron center. Importantly, MCD, Mössbauer, and EXAFS spectroscopies support a S_t = 1 hs-Fe^{II}-NO^- ground state arising from antiferromagnetic coupling between the hs-Fe^{II} (S = 2) and the $^3NO^-$ (S = 1) ligand. More recently, Goldberg's [Fe(NO)(N_3PyS)](BF_4) (N_3PyS^- = *N*-[2-phenylthiomethyl-*N*-(2-pyridinylmethyl-*N*,*N*-bis(2-pyridinylmethyl)methylamine)]) complex[92] has been shown to undergo one electron reduction at low temperatures to generate a metastable hs-{FeNO}^{8} complex. Characterization by rRaman spectroscopy shows an N-O stretching frequency close to that of the TMG_3tren analog at 1641 cm^{-1}, supporting a Fe^{II}-NO^- ground state. These electronic structure assignments are also supported by Fujisawa and coworkers [Fe(L3)(NO)] (L3 = hydrotris(3-tertiary-butyl-5-isopropylpyrazolyl)borate) system[115], as well as Meyer's [Fe($TIMEN^{Mes}$)(NO)]($BF)_4$ (TIMENMes = tris[2-(3-mesitylimidazol-2-ylidene)ethyl]-amine)) system[116], both of which have been crystallized and structurally characterized by single-crystal X-ray diffraction.

While these systems have successfully utilized steric protection to inhibit hs-{FeNO}^{8} reactivity, the one-electron reduction of most hs-{FeNO}^{7} complexes tends to ultimately proceed via two limiting routes: N_2O or DNIC formation. N_2O formation via reduction of hs-{FeNO}^{7} species is discussed in detail in section 1.2, and as such, DNIC formation, electronic structure, and reactivity will be discussed further here.

Mono- and di-iron DNICs have classically either been synthesized via substitution of carbonyl ligands in the iron dicarbonyl dinitrosyl precursor $[Fe(NO)_2(CO)_2]$ with other desired ligands to make $[Fe(NO)_2(L)_2]$ type complexes, or they are generated via chemical reduction of a hs-{FeNO}^{7} complex. Several stable mononuclear DNICs have been isolated and characterized in both the {Fe(NO)$_2$}$^{9/10}$ oxidation states. All reported DNICs thus far share similar spectroscopic and electronic properties. The ground state of mononuclear {Fe(NO)$_2$}^{9} DNICs is best described as hs-Fe^{III} (S = 5/2) antiferromagnetically coupled to two NO^- ligands (S = 1 each), resulting in a S_t = 1/2 ground state that gives rise to a strong g ~ 2 signal by EPR spectroscopy (Figure 1.6).[22, 28, 59, 117] As revealed first by NMR studies, reduction to the {Fe(NO)$_2$}^{10} state gives rise to a S_t = 0 diamagnetic ground state.[118] Detailed spectroscopic and theoretical work by Lippard and

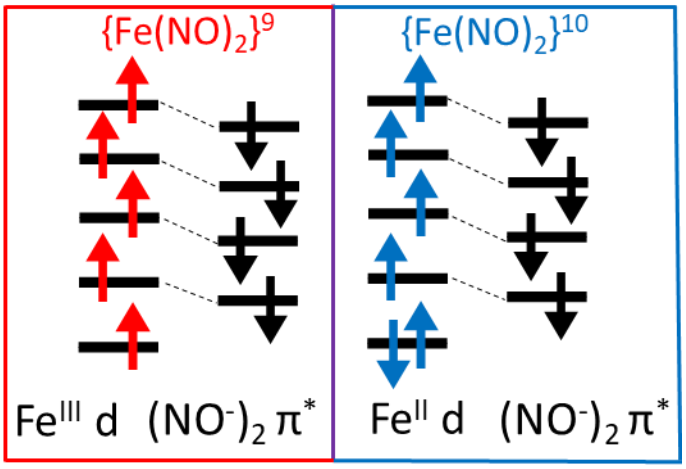

Figure 1.6 The electronic structures of 4-coordinate {Fe(NO)$_2$}^{9} and {Fe(NO)$_2$}^{10} DNICs[7]

coworkers on the $\{Fe(NO)_2\}^{9/10}$ complexes $[Fe(ar\text{-}nacnac)(NO)_2]^{0/-1}$ illustrates that this reduction is iron centered[117], and more interestingly, their experimental Mössbauer data coupled to Ye and Neese's DFT results[119] suggest that the Fe-NO bond strength *increases* upon reduction due to a significant enhancement of π-backbonding. This was later experimentally confirmed by our laboratory, using NRVS measurements coupled to QCC-NCA and DFT calculations on $[Fe(dmp)(NO)_2]^{+/0}$ (dmp = 2,9-dimethyl-1,10-phenanthroline) in the $\{Fe(NO)_2\}^{9/10}$ oxidation states.[59] Vibrationally, $\{Fe(NO)_2\}^9$ DNICs have symmetric and antisymmetric N-O stretching frequencies ranging from 1705-1766 and 1755-1840 cm^{-1} for the symmetric and antisymmetric N-O stretches, respectively.[59, 117, 118, 120, 121] Consistent with increased π-backbonding, the $\{Fe(NO)_2\}^{10}$ DNICs contain lower energy N-O stretching frequencies ranging from 1583-1688 and 1639-1714 cm^{-1} for their respective symmetric and antisymmetric stretches.[59, 117, 118, 121-123] In terms of reactivity, the two NO moieties contain spin-parallel π* electrons, and therefore, have a significant barrier towards N-N coupling and N_2O formation, due to the spin-forbidden nature of the N-N coupling step. Consequently, the primary means of decomposition for both $\{Fe(NO)_2\}^{9/10}$ complexes is NO loss, where the reported $\{Fe(NO)_2\}^9$ complexes, with few exceptions, decay much more rapidly than their $\{Fe(NO)_2\}^{10}$ analogs, due to the stronger and more covalent Fe-NO bonds[59] in the latter oxidation state.

Recently, bimetallic DNICs have received renewed interest within the context of NOR model complexes. For example, a diiron di-DNIC was generated from a ligand and redox disproportionation upon one-electron reduction of Meyer's $[L\{Fe(NO)\}_2(\mu\text{−}OOCR)](X)_2$ hs-$[\{FeNO\}^7]_2$ system,[99] containing *trans*-NO units (discussed in section 1.2). The $[\{Fe(NO)_2\}^9]_2$ di-DNIC that formed was structurally characterized by single-crystal X-ray diffraction, but no further reactivity or characterization was performed. Interestingly, the Liaw group later reported the

mixed-valent $\{Fe(NO)_2\}^9\{Fe(NO)_2\}^{10}$ di-DNIC $[(NO)_2Fe(\mu\text{-bdmap})Fe(NO)_2(THF)]$ (bdmap = 1,3-bis(dimethylamino)-2-propanolate).[124] This complex is capable of carrying out NO reduction to N_2O in the presence of an additional equivalent of NO via a proposed bridging μ-NO intermediate, whereby the coordination of NO induces significant charge and spin polarization towards the N-atom of the bridging NO ligand (based on DFT). This intermediate facilitates a bimolecular radical N-N coupling between two bridging NO units to make a stable *trans*-$N_2O_2^{2-}$ intermediate that was crystallized and structurally characterized. Protonation of this intermediate leads to N_2O release. As illustrated in Scheme 1.3, this di-DNIC unit is purely structural in nature.

Scheme 1.3 Proposed N-N coupling mechanism in the reaction of $[(NO)_2Fe(\mu\text{-bdmap})Fe(NO)_2(THF)]$ with NO(g).

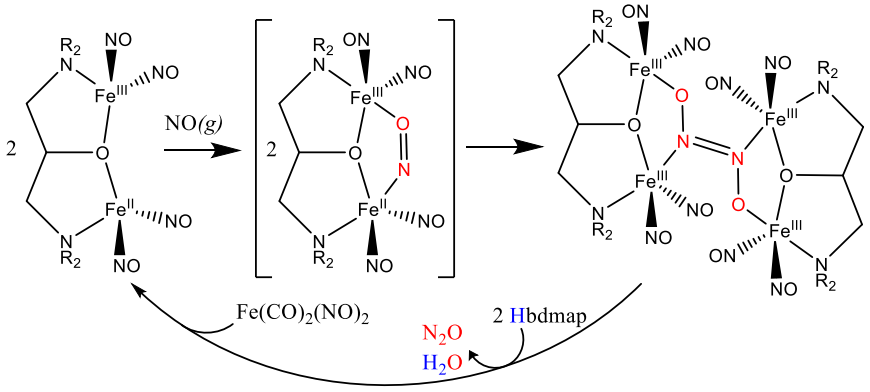

Nevertheless, this system is important in understanding and characterizing the N-N coupling intermediates preceding N_2O release in NORs. Finally, Layfield and coworkers published new data on the $\{Fe(NO)_2\}^{10}$ DNIC $[(NacNac^{Ar})Fe(NO)_2]$, where Ar = mesityl, or 2,6-diisopropylphenyl, that is capable of forming an end-on bridging nitrosyl (Fe-(N-O)$_2$-MCp*$_2$) complex, in the presence of Cp_2*M, where M = Y, Gd.[125] In the more sterically encumbering Ar = 2,6-diisopropylphenyl case, the Cp_2*M-bridged $\{Fe(NO)_2\}^{10}$ decays over multiple days to generate qualitative N_2O, as determined by gas chromatography. The authors propose that the Lewis acidity of the metal coupled to the steric bulk of the Ar enables this system to overcome the spin-forbidden barrier towards N-N coupling. However, since no intermediates of the reaction

could be identified, it is not clear whether a rearrangement of the Fe-$(N\text{-}O)_2$-MCp^*_2 core occurs prior to N-N coupling. Whether other di-iron systems can carry out this chemistry remains to be seen, and this is of mechanistic importance in the general field of NOR chemistry. Characterization of a BPMP DNIC is discussed further in Chapter 4.

There are also many low-spin non-heme iron-nitrosyl complexes that have been studied in the past years. These systems tend to have intermediate-to-strongly electron donating square planar or trigonal pyramidal ligand spheres. Two such examples are Lippard's $[Fe(TAML)(NO)]^-$ (TAML = tetraamidomacrocyclic ligand) system[126] and Meyer's $[Fe(^{NHC}L)(NO)](OTf)_2$ (where ^{NHC}L is a strongly donating tetracarbene ligand).[127] While these complexes are formally "non-heme" systems, their electronic structure largely mirrors that of ls-heme systems. For example, Lippard's $[Fe(TAML)(NO)]^-$ complex, formally a $\{FeNO\}^6$, is a low-spin (S = 0) species,[128] in line with most heme-$\{FeNO\}^6$ complexes. Accordingly, the Fe-NO bond is near linear at 172° and the complex has an N-O stretch of 1797 cm^{-1}. Another class of low-spin non-heme iron nitrosyls comes from spin-crossover complexes. These complexes tend to have more classic intermediate-field ligands that are capable of interconverting between hs and ls states depending on external conditions like temperature, pressure, or even the solvation sphere (coordinating/non-coordinating solvents). This behavior was first reported for the [Fe(salen)(NO)] ($salen^{2-}$ = N,N'-ethylenebis(salicylideneiminato)) complex[129], formally a $\{FeNO\}^7$ species, which undergoes a temperature-dependent interconversion between hs (S = 3/2) and ls (S =1/2) states. This is reflected in distinct shifts in the Fe-NO bond angle and N-O stretching frequencies, shifting from 147° to 127° and 1710 cm^{-1} to 1610 cm^{-1} upon conversion from the hs to ls state. More recently, Goldberg's hs-$\{FeNO\}^7$ system $[Fe(NO)(N_3PyS)](BF_4)$[130] discussed above undergoes a similar temperature-dependent conversion to ls upon cooling below 150K. Moreover, oxidation to the

{FeNO}^{6} state results in a contraction in Fe-ligand bonds, and correspondingly, an increase in ligand field strength, resulting in a ls-{FeNO}^{6} system. Aside from the select cases that are highlighted above, there are still many other interesting non-heme low-spin iron-nitrosyl systems that utilize unique ligand scaffolds to enforce unusual electronic structures, and correspondingly, reactivity, on the Fe-NO unit.[131-133] However, since the reactivity of hs-{FeNO}$^{7-8}$ systems is the focus of my thesis, the aforementioned systems will not be discussed further here.

1.4 Scope of Thesis

This thesis focuses on understanding how the geometric and electronic structures of diiron centers in FNOR model complexes affect the process of N-N coupling. In Chapter 2, a [hs-{FeNO}^{7}]$_2$ FNOR model complex, [Fe_2(BPMP)(OPr)$(NO)_2$]$(OTf)_2$, is reported. The complete spectroscopic characterization of this complex as well as its chemical and electrochemical reduction are discussed. Importantly, this is the first model complex reported where only one reductive equivalent is required to facilitate rapid and quantitative N-N coupling in a semireduced mechanism. The low temperature S = ½ intermediate of this process is captured and characterized by EPR and Mössbauer spectroscopies. The data presented in this chapter are published and adapted from: White, C. J., Speelman, A. L., Kupper, C., Demeshko, S., Meyer, F., Shanahan, J. P., Alp, E. E., Hu, M., Zhao, J.;Lehnert, N. The Semireduced Mechanism for Nitric Oxide Reduction by Non-Heme Diiron Complexes: Modeling Flavodiiron Nitric Oxide Reductases. *J. Am. Chem. Soc.* **2018**, *140*, 2562-2574.

In Chapter 3, collaborative work with the Majumdar group (Indian Association for the Cultivation of Science, Kolkata, India) on their diiron mononitrosyl and diiron dinitrosyl complexes [Fe_2(N-Et-HPTB)(NO)$(DMF)_3$]$(BF_4)_3$ and [Fe_2(N-Et-HPTB)$(NO)_2(DMF)_2$]$(BF_4)_3$, respectively, is presented. First, the dinitrosyl complex is the second example of a complex that

undergoes facile *intra*molecular semireduction, second to the BPMP complex discussed in Chapter 2. More importantly, the mixed-valent product that forms after N-N coupling was isolated and structurally characterized by X-Ray crystallography, revealing the formation of a tetrairon dimer linked via μ-oxo/hydroxo bridges. This compliments my Chapter 2 EPR characterization on the semireduction product of $[Fe_2(BPMP)(OPr)(NO)_2](OTf)_2$, supporting the formation of a monomeric S = ½ mixed-valent product at low temperatures that dimerizes or further oligomerizes upon warming, leading to an EPR silent species. Next, N_2O-formation studies on the mononitrosyl complex reveal the second reported example for a system that undergoes *inter*molecular superreduction, and the first complex to carry out this superreduction at a rapid timescale (~ 5 min). Work discussed herein supports the necessity of holding the two NO units in close proximity to carry out facile N-N coupling, leading to intramolecular semireduction. In the absence of a nearby second NO molecule, additional activation is needed to enablethe Fe-NO moieties to undergo an intermolecular superreduction. This chapter is adapted from the following two publications: (1) Jana, M., Pal, N., White, C. J., Kupper, C., Meyer, F., Lehnert, N.;Majumdar, A. Functional Mononitrosyl Diiron(II) Complex Mediates the Reduction of NO to N_2O with Relevance for Flavodiiron NO Reductases. *J. Am. Chem. Soc.* **2017**, *140*, 14380-14383. (2) Jana, M., White, C. J., Pal, N., Demeshko, S., Cordes, C., Meyer, F., Lehnert, N.;Majumdar, A. Functional Models for the Mono- and Dinitrosyl Intermediates of FNORs: Semireduction versus Superreduction of NO. *J. Am. Chem. Soc.* **2020**, *142*, 6600-6616.

In Chapter 4, new model systems are described where the bridging OPr^- ligand in $[Fe_2(BPMP)(OPr)(NO)_2](OTf)_2$ is replaced with monodentate ligands of varying bulk to promote non-coplanar NO binding to the diiron core. The rationale for investigating these complexes is twofold. First, since $[Fe_2(BPMP)(OPr)(NO)_2](OTf)_2$ carries out rapid N-N coupling, intermediates

preceding N_2O release could not be trapped and characterized, even at -80° C. In perturbing the (O)N-Fe-Fe-N(O) dihedral angle, the coupling may be inhibited, allowing for spectroscopic characterization of new intermediates. Second, studies of this perturbation will shed light onto the relevance of the bridging carboxylate for facile N-N coupling. The structural characterization of $[Fe_2(BPMP)(X)_2(NO)_2]^{3+/1+}$ (X = triflate, 1-methylimidazole, methanol) is presented and the reduction of this series of complexes is investigated. Importantly, the increased (O)N-Fe-Fe-N(O) dihedral angles for this series reduces the rate of N-N coupling at rapid t = 5-minute timescale, and furthermore, leads to parallel N_2O and DNIC formation. Interestingly, at longer t = 2 hr timescales, the DNIC products slowly decompose, with a corresponding increase in N_2O yields, implying that the DNIC facilitates this N-N coupling. The dinuclear systems are then compared to a mononuclear model system, $[Fe(BMPA)(OTf)_2(NO)]$ that not only can generate and model the DNIC intermediates from $[Fe_2(BPMP)(X)_2(NO)_2]^{3+/1+}$ well, but also generates stable DNIC products that do not generate any N_2O. This finding suggests that the presence of a tethered Fe^{II} in proximity to the DNIC products within the dinuclear systems contributes to this N-N coupling. A manuscript is in preparation for the data presented in this chapter.

In Chapter 5, the primary coordination sphere of the $BPMP^-$ ligand system is modified to include more electron-donating aliphatic carboxylate and aromatic benzoate arms, in order to tune the reduction potentials of our model system to be closer to those of native FNORs. First, unsuccessful synthetic strategies for the syntheses of these ligands are reviewed, followed by the development of a new synthetic route to conveniently synthesize symmetric aliphatic carboxylate- and benzoate-containing ligand scaffolds from a common branching point. Next, the separate synthesis of asymmetric ligands is also discussed. Lastly, the metallation, nitrosylation, and characterization of symmetric benzoate- and aliphatic carboxylate-containing BPMP ligand

derivatives are discussed. Based on cyclic voltammetry, both benzoate and aliphatic carboxylate analogs sit ~200 - 300 mV more positive in reduction potential than the $Fe^{III}Fe^{II}/Fe^{II}Fe^{II}$ couple of native FNORs. Importantly, while the aliphatic carboxylate ligand derivative stabilizes the dinitrosyl complex in the solid state, in solution the NO band of this complex decays over the course of 2 hrs with the formation of sub-stoichiometric amounts of N_2O, supporting a slow direct-coupling route. However, both aliphatic carboxylate and benzoate derivatives suffer from poor solubility in aprotic solvents, limiting solution IR studies of these species. Preliminary optimization of the synthesis of alkylated ligand-backbone derivatives is discussed, and alternate, commercially available pyridine and carboxylate derivatives are proposed for future syntheses of more soluble ligand derivatives.

1.5 References and Notes

(1) Portions of this chapter are adapted with permission from references 40 and 42.

(2) Boucher, J. L., Moali, C.;Tenu, J. P. Nitric oxide biosynthesis, nitric oxide synthase inhibitors and arginase competition for L-arginine utilization. *Cell Mol. Life Sci.* **1999**, *55*, 1015-1028.

(3) Montfort, W. R., Wales, J. A.;Weichsel, A. Structure and Activation of Soluble Guanylyl Cyclase, the Nitric Oxide Sensor. *Antioxid. Redox Signal* **2017**, *26*, 107-121.

(4) Philipp, L., Georg, H.;Josef, R. Inducible Nitric Oxide Synthase - Time for Reappraisal. *Inflamm. Allergy Drug Targets* **2002**, *1*, 89-108.

(5) Miranda, K. M. The chemistry of nitroxyl (HNO) and implications in biology. *Coord. Chem. Rev.* **2005**, *249*, 433-455.

(6) Fukuto, J. M., Cisneros, C. J.;Kinkade, R. L. A comparison of the chemistry associated with the biological signaling and actions of nitroxyl (HNO) and nitric oxide (NO). *J. Inorg. Biochem.* **2013**, *118*, 201-208.

(7) Fukuto, J. M., Dutton, A. S.;Houk, K. N. The Chemistry and Biology of Nitroxyl (HNO): A Chemically Unique Species with Novel and Important Biological Activity. *ChemBioChem* **2005**, *6*, 612-619.

(8) Kumar, M. R., Pervitsky, D., Chen, L., Poulos, T., Kundu, S., Hargrove, M. S., Rivera, E. J., Diaz, A., Colon, J. L.;Farmer, P. J. Nitrosyl Hydride (HNO) as an O_2 Analogue: Long-Lived HNO Adducts of Ferrous Globins. *Biochemistry* **2009**, *48*, 5018-5025.

(9) Fukuto, J. M. A recent history of nitroxyl chemistry, pharmacology and therapeutic potential. **2019**, *176*, 135-146.

(10) Bartberger, M. D., Liu, W., Ford, E., Miranda, K. M., Switzer, C., Fukuto, J. M., Farmer, P. J., Wink, D. A.;Houk, K. N. The reduction potential of nitric oxide (NO) and its importance to NO biochemistry *Proc. Natl. Acad. Sci. USA* **2002**, *99*, 10958–10963.

(11) Shafirovich, V.;Lymar, S. V. Nitroxyl and its anion in aqueous solutions: Spin states, protic equilibria, and reactivities toward oxygen and nitric oxide. *Proc. Natl. Acad. Sci. USA* **2002**, *99*, 7340-7345.

(12) Eberhardt, M., Dux, M., Namer, B., Miljkovic, J., Cordasic, N., Will, C., Kichko, T. I., de la Roche, J., Fischer, M., Suárez, S. A., Bikiel, D., Dorsch, K., Leffler, A., Babes, A., Lampert, A., Lennerz, J. K., Jacobi, J., Martí, M. A., Doctorovich, F., Högestätt, E. D., Zygmunt, P. M., Ivanovic-Burmazovic, I., Messlinger, K., Reeh, P.;Filipovic, M. R. H2S and NO cooperatively regulate vascular tone by activating a neuroendocrine HNO–TRPA1–CGRP signalling pathway. *Nature Commun.* **2014**, *5*, 4381.

(13) Bianco, C. L.;Fukuto, J. M. Examining the reaction of NO and H₂S and the possible cross-talk between the two signaling pathways. *Proc. Natl. Acad. Sci. USA* **2015**, *112*, 10573-10574.

(14) Ono, K., Akaike, T., Sawa, T., Kumagai, Y., Wink, D. A., Tantillo, D. J., Hobbs, A. J., Nagy, P., Xian, M., Lin, J.;Fukuto, J. M. Redox chemistry and chemical biology of H2S, hydropersulfides, and derived species: Implications of their possible biological activity and utility. *Free Rad. Biol. Med.* **2014**, *77*, 82-94.

(15) Fukuto, J. M., Carrington, S. J., Tantillo, D. J., Harrison, J. G., Ignarro, L. J., Freeman, B. A., Chen, A.;Wink, D. A. Small Molecule Signaling Agents: The Integrated Chemistry and Biochemistry of Nitrogen Oxides, Oxides of Carbon, Dioxygen, Hydrogen Sulfide, and Their Derived Species. *Chem. Res. Toxicol.* **2012**, *25*, 769-793.

(16) Saund, S. S., Sosa, V., Henriquez, S., Nguyen, Q. N. N., Bianco, C. L., Soeda, S., Millikin, R., White, C., Le, H., Ono, K., Tantillo, D. J., Kumagai, Y., Akaike, T., Lin, J.;Fukuto, J. M. The chemical biology of hydropersulfides (RSSH): Chemical stability, reactivity and redox roles. *Arch. Biochem. Biophys.* **2015**, *588*, 15-24.

(17) Millikin, R., Bianco, C. L., White, C., Saund, S. S., Henriquez, S., Sosa, V., Akaike, T., Kumagai, Y., Soeda, S., Toscano, J. P., Lin, J.;Fukuto, J. M. The chemical biology of protein hydropersulfides: Studies of a possible protective function of biological hydropersulfide generation. *Free Rad. Biol. Med.* **2016**, *97*, 136-147.

(18) Suarez, S. A., Neuman, N. I., Muñoz, M., Álvarez, L., Bikiel, D. E., Brondino, C. D., Ivanović-Burmazović, I., Miljkovic, J. L., Filipovic, M. R., Martí, M. A.;Doctorovich, F. Nitric Oxide Is Reduced to HNO by Proton-Coupled Nucleophilic Attack by Ascorbate, Tyrosine, and Other Alcohols. A New Route to HNO in Biological Media? *J. Am. Chem. Soc.* **2015**, *137*, 4720–4727.

(19) Paolocci, N., Jackson, M. I., Lopez, B. E., Miranda, K., Tocchetti, C. G., Wink, D. A., Hobbs, A. J.;Fukuto, J. M. The pharmacology of nitroxyl (HNO) and its therapeutic potential: not just the Janus face of NO. *Pharmacol Ther* **2007**, *113*, 442-458.

(20) DeMaster, E. G., Kaplan, E., Shirota, F. N.;Nagasawa, H. T. Metabolic activation of cyanamide by liver mitochondria, a requirement for the inhibition of aldehyde dehydrogenase enzymes. *Biochem. Biophys. Res. Comm.* **1982**, *107*, 1333-1339.

(21) Venkateswara, P.;Holm, R. H. Synthetic Analogs of the Active Sites of Iron-Sulfur Proteins. *Chem. Rev.* **2004**, *104*, 527-559.

(22) Lewandowska, H., Kalinowska, M., Brzoska, K., Wojciuk, K., Wojciuka, G.;Kruszewskia, M. Nitrosyl iron complexes—synthesis, structure and biology. *Dalton Trans.* **2011**, *40*, 8273-8289.

(23) Tsai, M. L., Tsou, C. C.;Liaw, W. F. Dinitrosyl Iron Complexes (DNICs): From Biomimetic Synthesis and Spectroscopic Characterization towards Unveiling the Biological and Catalytic Roles of DNICs. *Acc. Chem. Res.* **2015**, *48*, 1184-1193.

(24) Foster, M. W.;Cowan, J. A. Chemistry of Nitric Oxide with Protein-Bound Iron Sulfur Centers. Insights on Physiological Reactivity. *J. Am. Chem. Soc.* **1999**, *121*, 4093-4100.

(25) Tórtora, V., Quijano, C., Freeman, B., Radi, R.;Castro, L. Mitochondrial aconitase reaction with nitric oxide, S-nitrosoglutathione, and peroxynitrite: Mechanisms and relative contributions to aconitase inactivation. *Free Rad. Biol. Med.* **2007**, *42*, 1075-1088.

(26) Truzzi, D. R., Augusto, O., Iretskii, A. V.;Ford, P. C. Dynamics of Dinitrosyl Iron Complex (DNIC) Formation with Low Molecular Weight Thiols. *Inorg. Chem.* **2019**, *58*, 13446-13456.

(27) Pereira, J. C. M., Iretskii, A. V., Han, R.-M.;Ford, P. C. Dinitrosyl iron complexes with cysteine. Kinetics studies of the formation and reactions of DNICs in aqueous solution. *J. Am. Chem. Soc.* **2014**, *137*, 328-336.

(28) Tonzetich, Z. J., Héroguel, F., Do, L. H.;Lippard, S. J. Chemistry of Nitrosyliron Complexes Supported by a β-Diketiminate Ligand. *Inorg. Chem.* **2011**, *50*, 1570-1579.

(29) Broniowska, K. A.;Hogg, N. The chemical biology of S-nitrosothiols. *Antioxid. Redox Signal.* **2012**, *17*, 969-980.

(30) Keszler, A., Zhang, Y.;Hogg, N. Reaction between nitric oxide, glutathione, and oxygen in the presence and absence of protein: How are S-nitrosothiols formed? . *Free Rad. Biol. Med.* **2010**, *48*, 55-64.

(31) Foster, M. W., Hess, D. T.;Stamler, J. S. Protein *S*-nitrosylation in health and disease: a current perspective. *Trends Mol. Med.* **2009**, *15*, 391-404.

(32) Zhang, S., Çelebi-Ölçüm, N., Melzer, M. M., Houk, K. N.;Warren, T. H. Copper(I) Nitrosyls from Reaction of Copper(II) Thiolates with *S*-Nitrosothiols: Mechanism of NO Release from RSNOs at Cu. *J. Am. Chem. Soc.* **2013**, *135*, 16746-16749.

(33) Jourd'heuil, D., Laroux, F. S., Miles, A. M., Wink, D. A.;Grisham, M. B. Effect of Superoxide Dismutase on the Stability of S-Nitrosothiols. *Arch. Biochem. Biophys.* **1999**, *361*, 323-330.

(34) Enemark, J. H.;Feltham, R. D. Principles of Structure, Bonding, and Reactivity for Metal Nitrosyl Complexes. *Coord. Chem. Rev.* **1974**, *13*, 339-406.

(35) Farmer, P. J.;Sulc, F. Coordination chemistry of the HNO ligand with hemes and synthetic coordination complexes. *J. Inorg. Biochem.* **2005**, *99*, 166-184.

(36) Sulc, F., Fleischer, E., Farmer, P. J., Ma, D. J.;La Mar, G. N. ^{1}H NMR structure of the heme pocket of HNO-myoglobin. *J. Biol. Inorg. Chem.* **2003**, *8*, 348–352.

(37) Berto, T. C., Speelman, A., Zheng, S.;Lehnert, N. Mono- and Dinuclear Non-Heme Iron-Nitrosyl Complexes: Models for Key Intermediates in Bacterial Nitric Oxide Reductases. *Coord. Chem. Rev.* **2013**, *257*, 244-259.

(38) Berto, T. C., Hoffman, M. B., Murata, Y., Landenberger, K. B., Alp, E. E., Zhao, J.;Lehnert, N. Structural and Electronic Characterization of Non-Heme Fe(II)-Nitrosyls as Biomimetic Models of the Fe_B Center of Bacterial Nitric Oxide Reductase (NorBC). *J. Am. Chem. Soc.* **2011**, *133*, 16714–16717.

(39) Speelman, A.;Lehnert, N. Heme versus Non-Heme Iron-Nitroxyl $\{FeN(H)O\}^8$ Complexes: Electronic Structure and Biologically Relevant Reactivity. *Acc. Chem. Res.* **2014**, *47*, 1106-1116.

(40) Lehnert, N., Dong, H. T., Harland, J. B., Hunt, A. P.;White, C. J. Reversing Nitrogen Fixation. *Nat. Rev. Chem.* **2018**, *2*, 278-289.

(41) Wasser, I. M., de Vries, S., Moënne-Loccoz, P., Schröder, I.;Karlin, K. D. Nitric Oxide in Biological Denitrification: Fe/Cu Metalloenzymes and Metal Complex NO_x Redox Chemistry. *Chem. Rev.* **2002**, *102*, 1201-1234.

(42) Lehnert, N., Fujisawa, K., Camarena, S., Dong, H. T.;White, C. J. Activation of Non-Heme Iron-Nitrosyl Complexes: Turning up the Heat. *ACS Catal.* **2019**, *9*, 10499-10518.

(43) Shimizu, H., Park, S. Y., Lee, D. S., Shoun, H.;Shiro, Y. Crystal structures of cytochrome P450nor and its mutants (Ser286 Val, Thr) in the ferric resting state at cryogenic temperature: a comparative analysis with monooxygenase cytochrome P450s. *J. Inorg. Biochem.* **2000**, *81*, 191-205.

(44) Shimizu, H., Park, S.-Y., Shiro, Y.;Adachi, S.-I. Crystal Structure of Nitric Oxide Reductase (Cytochrome P450nor) at Atomic Resolution. *Acta Crystallogr. D* **2002**, *58*, 81.

(45) Shimizu, H., Park, S.-Y., Gomi, Y., Arakawa, H., Nakamura, H., Adachi, S.-I., Obayashi, E., Iizuka, T., Shoun, H.;Shiro, Y. Proton Delivery in NO Reduction by Fungal Nitric-oxide Reductase. Cryogenic Crystallography, Spectroscopy, and Kinetics of Ferric-NO Complexes of Wild-Type and Mutant Enzymes. *J. Biol. Chem.* **2000**, *275*, 4816-4826.

(46) Oshima, R., Fushinobu, S., Su, F., Zhang, L., Takaya, N.;Shoun, H. Structural evidence for direct hydride transfer from NADH to cytochrome P450nor. *J. Mol. Biol.* **2004**, *342*, 207-217.

(47) Shiro, Y., Fujii, M., Iizuka, T., Adachi, S., Tsukamoto, K., Nakahara, K.;Shoun, H. Spectroscopic and Kinetic Studies on Reaction of Cytochrome P450nor with Nitric Oxide. *J. Biol. Chem.* **1995**, *270*, 1617-1623.

(48) McQuarters, A. B., Wolf, M. W., Hunt, A. P.;Lehnert, N. 1958-2014: After 56 Years of Research, Cytochrome P450 Reactivity Finally Explained. *Angew. Chem. Int. Ed.* **2014**, *53*, 4750-4752.

(49) McQuarters, A. B., Wirgau, N. E.;Lehnert, N. Model Complexes of Key Intermediates in Fungal Cytochrome P450 Nitric Oxide Reductase (P450nor). *Curr. Op. Chem. Biol.* **2014**, *19*, 82-89.

(50) Riplinger, C.;Neese, F. The Reaction Mechanism of Cytochrome P450 NO reductase: A Detailed Quantum Mechanics/Molecular Mechanics Study. *Chem. Phys. Chem.* **2011**, *12*, 3192-3203.

(51) Kramos, B., Menyhard, D. K.;Olah, J. Direct Hydride Shift Mechanism and Stereoselectivity of P450nor Confirmed by QM/MM Calculations. *J. Phys. Chem. B* **2012**, *116*, 872−885.

(52) Lehnert, N., Praneeth, V. K. K.;Paulat, F. Electronic Structure of Iron(II)-Porphyrin Nitroxyl Complexes: Molecular Mechanism of Fungal Nitric Oxide Reductase (P450nor) *J. Comp. Chem.* **2006**, *27*, 1338-1351.

(53) Zumft, W. G. Nitric Oxide Reductases of Prokaryotes with Rmphasis on the Respiratory, Heme–Copper Oxidase Type. *J. Inorg. Biochem.* **2005**, *99*, 194-215.

(54) Shiro, Y. Structure and Function of Bacterial Nitric Oxide Reductases. *Biochim. Biophys. Acta* **2012**, *1817*, 1907-1913.

(55) Hino, T., Matsumoto, Y., Nagano, S., Sugimoto, H., Fukumori, Y., Murata, T., Iwata, S.;Shiro, Y. Structural Basis of Biological N_2O Generation by Bacterial Nitric Oxide Reductase. *Science* **2010**, *330*, 1666-1670.

(56) Lin, Y.-W. Rational design of metalloenzymes: From single to multiple active sites. *Coordination Chemistry Reviews* **2017**, *336*, 1-27.

(57) Yeung, N., Lin, Y. W., Gao, Y. G., Zhao, X., Russell, B. S., Lei, L., Miner, K. D., Robinson, H.;Lu, Y. Rational design of a structural and functional nitric oxide reductase. *Nature* **2009**, *462*, 1079-1082.

(58) Kadish, K. M., Smith, K. M.;Guilard, R. *The Handbook of Porphyrin Science*; World Scientific: New Jersey, 2011.

(59) Speelman, A. L., Zhang, B., Silakov, A., Skodje, K. M., Alp, E. E., Zhao, J., Hu, M. Y., Kim, E., Krebs, C.;Lehnert, N. Unusual Synthetic Pathway for an $\{Fe(NO)_2\}^9$ Dinitrosyl Iron Complex (DNIC) and Insight into DNIC Electronic Structure via Nuclear Resonance Vibrational Spectroscopy. *Inorg. Chem.* **2016**, *55*, 5485-5501.

(60) Girsch, P.;de Vries, S. Purification and initial kinetic and spectroscopic characterization of NO reductase from *Paracoccus denitrificans*. *Biochim. Biophys. Acta* **1997**, *1318*, 202-216.

(61) Praneeth, V. K. K., Näther, C., Peters, G.;Lehnert, N. Spectroscopic Properties and Electronic Structure of Five- and Six-Coordinate Iron(II) Porphyrin NO Complexes: Effect of the Axial N-Donor Ligand *Inorg. Chem.* **2006**, *45*, 2795-2811.

(62) Berto, T. C., Xu, N., Lee, S. R., McNeil, A. J., Alp, E. E., Zhao, J., Richter-Addo, G. B.;Lehnert, N. Characterization of the Bridged Hyponitrite Complex $\{[Fe(OEP)]_2(\mu\text{-}N_2O_2)\}$: Reactivity of Hyponitrite Complexes and Biological Relevance. *Inorg. Chem.* **2014**, *53*, 6398-6414.

(63) Blomberg, M. R. A. Can Reduction of NO to N_2O in Cytochrome c Dependent Nitric Oxide Reductase Proceed through a Trans-Mechanism? *Biochem.* **2017**, *56*, 120-131.

(64) Matsumura, H., Chakraborty, S., Reed, J., Lu, Y.;Moënne-Loccoz, P. Effect of Outer-Sphere Side Chain Substitutions on the Fate of the trans Iron–Nitrosyl Dimer in Heme/Nonheme Engineered Myoglobins (FeBMbs): Insights into the Mechanism of Denitrifying NO Reductases. *Biochemistry* **2016**, *55*, 2091-2099.

(65) Bhagi-Damodaran, A., Petrik, I.;Lu, Y. Using Biosynthetic Models of Heme-Copper Oxidase and Nitric Oxide Reductase in Myoglobin to Elucidate Structural Features Responsible for Enzymatic Activities. *Isr. J. Chem.* **2016**, *56*, 773-790.

(66) Matsumura, H., Hayashi, T., Chakraborty, S., Lu, Y.;Moënne-Loccoz, P. The Production of Nitrous Oxide by the Heme/Nonheme Diiron Center of Engineered Myoglobins (Fe_BMbs) Proceeds through a *trans*-Iron-Nitrosyl Dimer. *J. Am. Chem. Soc.* **2014**, *136*, 2420-2431.

(67) Blomberg, L. M., Blomberg, M. R. A.;Siegbahn, P. E. M. A theoretical study on nitric oxide reductase activity in ba_3-type heme-copper oxidase. *Biochim. Biophys. Acta* **2006**, *1757*, 31-46.

(68) Blomberg, M. R. A.;Siegbahn, P. E. M. Mechanism for N_2O Generation in Bacterial Nitric Oxide Reductase: A Quantum Chemical Study. *Biochem.* **2012**, *51*, 5173-5186.

(69) Hayashi, T., Miner, K. D., Yeung, N., Lin, Y.-W., Lu, Y.;Moënne-Loccoz, P. Spectroscopic Characterization of Mononitrosyl Complexes in Heme–Nonheme Diiron Centers within the Myoglobin Scaffold (Fe_BMbs): Relevance to Denitrifying NO Reductase. *Biochemistry* **2011**, *50*, 5939-5947.

(70) Gardner, A. M., Gessner, C. R.;Gardner, P. R. Regulation of the Nitric Oxide Reduction Operon (norRVW) in *Escherichia coli*. Role of NorR and σ^{54} in the Nitric Oxide Stress Response. *J. Biol. Chem.* **2003**, *278*, 10081-10086.

(71) Gardner, A. M., Helmick, R. A.;Gardner, P. R. Flavorubredoxin, an Inducible Catalyst for Nitric Oxide Reduction and Detoxification in *Escherichia coli*. *J. Biol. Chem.* **2002**, *277*, 8172-8177.

(72) Kurtz, D. M., Jr. Flavo-Diiron Enzymes: Nitric Oxide or Dioxygen Reductases? *Dalton Trans.* **2007**, 4115-4121.

(73) Vicente, J. B.;Teixeira, M. Redox and Spectroscopic Properties of the *Escherichia coli* Nitric Oxide-detoxifying System Involving Flavorubredoxin and Its NADH-oxidizing Redox Partner. *J. Biol. Chem.* **2005**, *280*, 34599-34608.

(74) Romão, C. V., Vicente, J. B., Borges, P. T., Frazão, C.;Teixeira, M. The Dual Function of Flavodiiron Proteins: Oxygen and/or Nitric Oxide Reductases. *J. Bio. Inorg. Chem.* **2016**, *21*, 39-52.

(75) Gonçalves, V. L., Vicente, J. B., Pinto, L., Romão, C. V., Frazão, C., Sarti, P., Giuffrè, A.;Teixeira, M. Flavodiiron Oxygen Reductase from Entamoeba histolytica: Modulation of Substrate Preference by Tyrosine 271 and Lysine 53. *J. Biol. Chem.* **2014**, *289*, 28260-28270.

(76) Frederick, R. E., Caranto, J. D., Masitas, C. A., Gebhardt, L. L., MacGowan, C. E., Limberger, R. J.;Kurtz, D. M., Jr. Dioxygen and Nitric Oxide Scavenging by *Treponema denticola* Flavodiiron Protein: A Mechanistic Paradigm for Catalysis. *J. Biol. Inorg. Chem.* **2015**, *20*, 603-613.

(77) Frazão, C., Silva, G., Gomes, C. M., Matias, P., Coelho, R., Sieker, L., Macedo, S., Liu, M. Y., Oliveira, S., Teixeira, M., Xavier, A. V., Rodrigues-Pousada, C., Carrondo, M. A.;Le Gall, J. Structure of a Dioxygen Reduction Enzyme From *Desulfovibrio gigas*. *Nat. Struct. Biol.* **2000**, *7*, 1041-1045.

(78) Wasserfallen, A., Ragettli, S., Jouanneau, J.;Leisinger, T. A Family of Flavoproteins in the Fomains Archaea and Bacteria. *Eur. J. Biochem.* **1998**, *254*, 325-332.

(79) Silaghi-Dumitrescu, R., Kurtz, D. M., Jr., Ljungdahl, L. G.;Lanzilotta, W. N. X-ray Crystal Structures of Moorella thermoacetica FprA. Novel Diiron Site Structure and Mechanistic Insights into a Scavenging Nitric Oxide Reductase. *Biochemistry* **2005**, *44*, 6492-6501.

(80) Fang, H., Caranto, J. D., Mendoza, R., Taylor, A. B., Hart, P. J.;Kurtz, D. M. Histidine Ligand Variants of a Flavo-Diiron Protein: Effects on Structure and Activities. *J. Bio. Inorg. Chem.* **2012**, *17*, 1231-1239.

(81) Weitz, A. C., Giri, N., Caranto, J. D., Kurtz, D. M., Bominaar, E. L.;Hendrich, M. P. Spectroscopy and DFT Calculations of a Flavo-diiron Enzyme Implicate New Diiron Site Structures. *J. Am. Chem. Soc.* **2017**, *139*, 12009-12019.

(82) Lu, J., Bi, B., Lai, W.;Chen, H. Origin of Nitric Oxide Reduction Activity in Flavo-Diiron NO Reductase: Key Roles of the Second Coordination Sphere. *Angew. Chem. Int. Ed.* **2019**, *58*, 3795-3799.

(83) Khatua, S.;Majumdar, A. Flavodiiron Nitric Oxide Reductases: Recent Developments in the Mechanistic Study and Model Chemistry for the Catalytic Reduction of NO. *J. Inorg. Biochem.* **2015**, *142*, 145-153.

(84) White, C. J., Speelman, A. L., Kupper, C., Demeshko, S., Meyer, F., Shanahan, J. P., Alp, E. E., Hu, M., Zhao, J.;Lehnert, N. The Semireduced Mechanism for Nitric Oxide Reduction by Non-Heme Diiron Complexes: Modeling Flavodiiron Nitric Oxide Reductases. *J. Am. Chem. Soc.* **2018**, *140*, 2562-2574.

(85) Caranto, J. D., Weitz, A., Giri, N., Hendrich, M. P.;Kurtz, D. M. J. A Diferrous-Dinitrosyl Intermediate in the N_2O-Generating Pathway of a Deflavinated Flavo-Diiron Protein. *Biochemistry* **2014**, *53*, 5631–5637.

(86) Hayashi, T., Caranto, J. D., Wampler, D. A., Kurtz, D. M., Jr.;Moënne-Loccoz, P. Insights into the Nitric Oxide Reductase Mechanism of Flavodiiron Proteins from a Flavin-Free Enzyme. *Biochemistry* **2010**, *49*, 7040−7049.

(87) Caranto, J. D., Weitz, A., Hendrich, M. P.;Kurtz, D. M., Jr. The Nitric Oxide Reductase Mechanism of a Flavo-Diiron Protein: Identification of Active-Site Intermediates and Products. *J. Am. Chem. Soc.* **2014**, *136*, 7981–7992.

(88) Speelman, A. L., White, C. J., Zhang, B., Alp, E. E., Zhao, J., Hu, M., Krebs, C., Penner-Hahn, J.;Lehnert, N. Non-heme High-Spin $\{FeNO\}^{6-8}$ Complexes: One Ligand Platform Can Do It All. *J. Am. Chem. Soc.* **2018**, *140*, 11341-11359.

(89) Feig, A. L., Bautista, M. T.;Lippard, S. J. A Carboxylate-Bridged Non-heme Diiron Dinitrosyl Complex. *Inorg. Chem.* **1996**, *35*, 6892-6898.

(90) Zheng, S., Berto, T. C., Dahl, E. W., Hoffman, M. B., Speelman, A. L.;Lehnert, N. The Functional Model Complex $[Fe_2(BPMP)(OPr)(NO)_2](BPh_4)_2$ Provides Insight into the Mechanism of Flavodiiron NO Reductases. *J. Am. Chem. Soc.* **2013**, *135*, 4902−4905.

(91) Jana, M., Pal, N., White, C. J., Kupper, C., Meyer, F., Lehnert, N.;Majumdar, A. Functional Mononitrosyl Diiron(II) Complex Mediates the Reduction of NO to N_2O with Relevance for Flavodiiron NO Reductases. *J. Am. Chem. Soc.* **2017**, *140*, 14380-14383.

(92) Confer, A. M., McQuilken, A. C., Matsumura, H., Moënne-Loccoz, P.;Goldberg, D. P. A Nonheme, High-Spin $\{FeNO\}^8$ Complex that Spontaneously Generates N_2O. *J. Am. Chem. Soc.* **2017**, *139*, 10621-10624.

(93) Confer, A. M., Sabuncu, S., Siegler, M. A., Moënne-Loccoz, P.;Goldberg, D. P. Mononuclear, Nonheme, High-Spin $\{FeNO\}^{7/8}$ Complexes Supported by a Sterically Encumbered N_4S-Thioether Ligand. *Inorg. Chem.* **2019**, *58*, 9576-9580.

(94) Brown, C. A., Pavlosky, M. A., Westre, T. E., Zhang, Y., Hedman, B., Hodgson, K. O.;Solomon, E. I. Spectroscopic and Theoretical Description of the Electronic Structure of S = 3/2 Iron-Nitrosyl Complexes and Their Relation to O_2 Activation by Non-Heme Iron Enzyme Active Sites *J. Am. Chem. Soc.* **1995**, *117*, 715-732.

(95) Jiang, Y., Hayashi, T., Matsumura, H., Do, L. H., Majumdar, A., Lippard, S. J.;Moënne-Loccoz, P. Light-Induced N_2O Production from a Non-heme Iron–Nitrosyl Dimer. *J. Am. Chem. Soc.* **2014**, *136*, 12524-12527.

(96) Jana, M., White, C. J., Pal, N., Demeshko, S., Cordes, C., Meyer, F., Lehnert, N.;Majumdar, A. Functional Models for the Mono- and Dinitrosyl Intermediates of FNORs: Semireduction versus Superreduction of NO. *J. Am. Chem. Soc.* **2020**, *142*, 6600-6616.

(97) Van Stappen, C.;Lehnert, N. Mechanism of N-N Bond Formation by Transition Metal-Nitrosyl Complexes: Modeling Flavodiiron Nitric Oxide Reductases. *Inorg. Chem.* **2018**, *57*, 4252-4269.

(98) Note: N_2O yields are reported with respect to different reference points (maximum N_2O yield, [reductant], [complex]) in different publications. In order to minimize confusion, all reported N_2O yields in this chapter are reported with respect to the concentration of the complex that generated N_2O.

(99) Kindermann, N., Schober, A., Demeshko, S., Lehnert, N.;Meyer, F. Reductive Transformations of a Pyrazolate-Based Bioinspired Diiron−Dinitrosyl Complex. *Inorg. Chem.* **2016**, *55*, 11538-11550.

(100) Zhang, Y., Pavlosky, M. A., Brown, C. A., Westre, T. E., Hedman, B., Hodgson, K. O.;Solomon, E. I. Spectroscopic and Theoretical Description of the Electronic Structure of the S = 3/2 Nitrosyl Complex of Non-heme Iron Enzymes. *J. Am. Chem. Soc.* **1992**, *114*, 9189-9191.

(101) Jackson, T. A., Yikilmaz, E., Miller, A.-F.;C., B. T. Spectroscopic and Computational Study of a Non-Heme Iron $\{Fe{-}NO\}^7$ System: Exploring the Geometric and Electronic Structures of the Nitrosyl Adduct of Iron Superoxide Dismutase. *J. Am. Chem. Soc.* **2003**, *125*, 8348-8363.

(102) Diebold, A. R., Brown-Marshall, C. D., Neidig, M. L., Brownlee, J. M., Moran, G. R.;Solomon, E. I. Activation of α-Keto Acid-Dependent Dioxygenases: Application of an $\{FeNO\}^7/\{FeO_2\}^8$ Methodology for Characterizing the Initial Steps of O_2 Activation. *J. Am. Chem. Soc.* **2011**, *133*, 18148–18160.

(103) Ye, S., Price, J. C., Barr, E. W., Green, M. T., Bollinger, J. M., Krebs, C.;Neese, F. Cryoreduction of the NO-Adduct of Taurine:α-Ketoglutarate Dioxygenase (TauD) Yields an Elusive$\{FeNO\}^8$ Species. *J. Am. Chem. Soc.* **2010**, *132*, 4739−4751.

(104) Banerjee, A., Li, J., Speelman, A. L., White, C. J., Pawlak, P. L., Brennessel, W. W., Lehnert, N.;Chavez, F. A. A Structural Model for the Iron-Nitrosyl Adduct of Gentisate Dioxygenase. *Eur. J. Inorg. Chem.* **2018**, 4797-4804.

(105) Radon, M., Broclawik, E.;Pierloot, K. Electronic Structure of Selected {FeNO}7 Complexes in Heme and Non-Heme Architectures: A Density Functional and Multireference ab Initio Study. *J. Phys. Chem. B* **2010**, *114*, 1518-1528.

(106) Pohl, K., Wieghardt, K., Nuber, B.;Weiss, J. Preparation and magnetism of the binuclear iron(II) complexes $[\{Fe(C_9H_{21}N_3)X_2\}_2]$(X = NCS, NCO, or N_3) and their reaction with NO. Crystal structures of $[\{Fe(C_9H_{21}N_3)(NCS)_2\}_2]$ and $[Fe(C_9H_{21}N_3)(NO)(N_3)_2]$. *J. Chem. Soc. Dalton Trans.* **1987**, 187-192.

(107) Li, J., Banerjee, A., Pawlak, P. L., Brennessel, W. W.;Chavez, F. A. Highest Recorded N–O Stretching Frequency for 6-Coordinate {Fe-NO}^{7} Complexes: An Iron Nitrosyl Model for His_3 Active Sites. *Inorg. Chem.* **2014**, *53*, 5414–5416.

(108) Dong, H. T., Speelman, A. L., Kozemchak, C. E., Sil, D., Krebs, C.;Lehnert, N. The $Fe_2(NO)_2$ Diamond Core: A Unique Structural Motif in Non-Heme Iron-NO Chemistry. *Angew. Chem. Int. Ed.* **2019**, *58*, asap.

(109) Chiou, Y.-M.;Que Jr, L. Model Studies of. alpha.-Keto Acid-Dependent Nonheme Iron Enzymes: Nitric Oxide Adducts of [FeII(L)(O_2CCOPh)](ClO_4) Complexes. *Inorg. Chem.* **1995**, *34*, 3270-3278.

(110) Speelman, A., Zhang, B., Krebs, C.;Lehnert, N. Structural and Spectroscopic Characterization of a High-Spin {FeNO}^{6} Complex with an Iron(IV)-NO^- Electronic Structure. *Angew. Chem. Int. Ed.* **2016**, *55*, 6685-6688.

(111) Speelman, A. L.;Lehnert, N. Characterization of a High-Spin Non-Heme {FeNO}^{8} Complex: Implications for the Reactivity of Iron Nitroxyl Species in Biology. *Angew. Chem. Int. Ed.* **2013**, *52*, 12283-12287.

(112) Speelman, A. L. "Investigation of the Electronic Structure and Reactivity of Non-Heme Iron Nitrosyl and Nitroxyl Complexes". Ph.D. Thesis, University of Michigan, Ann Arbor, MI, **2016**.

(113) Haskin, C. J., Ravi, N., Lynch, J. B., Muenck, E.;Que, L., Jr. Reaction of NO with the Reduced R2 Protein of Ribonucleotide Reductase from *Escherichia coli*. *Biochemistry* **1995**, *34*, 11090-11098.

(114) Herold, S.;Lippard, S. J. Carboxylate-Bridged Diiron(II) Complexes: Synthesis, Characterization, and O2-Reactivity of Models for the Reduced Diiron Centers in Methane Monooxygenase and Ribonucleotide Reductase. *J. Am. Chem. Soc.* **1997**, *119*, 145-156.

(115) Fujisawa, K., Soma, S., Kurihara, H., Ohta, A., Dong, H. T., Minakawa, Y., Zhao, J., Alp, E. E., Hu, M. Y.;Lehnert, N. Stable Ferrous Mononitroxyl {FeNO}^{8} Complex with a Hindered Hydrotris(pyrazolyl)borate Coligand: Structure, Spectroscopic Characterization, and Reactivity Toward NO and O_2. *Inorg. Chem.* **2019**, *58*, 4059-4062.

(116) Keilwerth, M., Hohenberger, J., Heinemann, F. W., Sutter, J. r., Scheurer, A., Fang, H., Bill, E., Neese, F., Ye, S.;Meyer, K. A Series of Iron Nitrosyl Complexes {Fe–NO}$^{6-9}$ and a Fleeting {Fe–NO}^{10} Intermediate en Route to a Metalacyclic Iron Nitrosoalkane. *J. Am. Chem. Soc.* **2019**, *141*, 17217-17235.

(117) Tonzetich, Z. J., Do, L. H.;Lippard, S. J. Dinitrosyl Iron Complexes Relevant to Rieske Cluster Nitrosylation. *J. Am. Chem. Soc.* **2009**, *131*, 7964-7965.

(118) Tran, C. T., Skodje, K. M.;Kim, E. Monomeric Dinitrosyl Iron Complexes: Synthesis and Reactivity; Karlin, K. D., Ed.; John Wiley & Sons, Inc. : Hoboken, NJ, 2014, p 339.

(119) Ye, S.;Neese, F. The Unusual Electronic Structure of Dinitrosyl Iron Complexes. *J. Am. Chem. Soc.* **2010**, *132*, 3646–3647.

(120) Hung, M.-C., Tsai, M.-C., Lee, G.-H.;Liaw, W.-F. Transformation and Structural Discrimination between the Neutral {Fe(NO)2}10 Dinitrosyliron Complexes (DNICs) and the Anionic/Cationic {Fe(NO)2}9 DNICs. *Inorg. Chem.* **2006**, *45*, 6041-6047.

(121) Atkinson, F. L., Blackwell, H. E., Brown, N. C., Connelly, N. G., Crossley, J. G., Orpen, A. G., Rieger, A. L.;Rieger, P. H. Synthesis of the 17-electron cations [FeL(L′)(NO)2]+(L, L′= PPh3, OPPh3): structure and bonding in four-co-ordinate metal dinitrosyls, and implications for the identity of paramagnetic iron dinitrosyl complex catalysts. *J. Chem. Soc. Dalton Trans.* **1996**, 3491-3502.

(122) Hess, J. L., Hsieh, C.-H., Reibenspies, J. H.;Darensbourg, M. Y. N-Heterocyclic Carbene Ligands as Mimics of Imidazoles/Histidine for the Stabilization of Di- and Trinitrosyl Iron Complexes. *Inorg. Chem.* **2011**, *50*, 8541-8552.

(123) Wang, R., Wang, X., Sundberg, E. B., Nguyen, P., Grant, G. P. G., Sheth, C., Zhao, Q., Herron, S., Kantardjieff, K. A.;Li, L. Synthesis, Structures, Spectroscopic and Electrochemical Properties of Dinitrosyl Iron Complexes with Bipyridine, Terpyridine, and 1,10-Phenathroline. *Inorg. Chem.* **2009**, *48*, 9779-9785.

(124) Wu, W.-Y., Hsu, C.-N., Hsieh, C.-H., Chiou, T.-W., Tsai, M.-L., Chiang, M.-H.;Liaw, W.-F. NO-to-[N2O2]2−-to-N2O Conversion Triggered by {Fe(NO)2}10-{Fe(NO)2}9 Dinuclear Dinitrosyl Iron Complex. *Inorg. Chem.* **2019**, *58*, 9586-9591.

(125) Bar, A. K., Heras Ojea, M. J., Tang, J.;Layfield, R. A. Coupling of Nitric Oxide and Release of Nitrous Oxide from Rare-Earth-Dinitrosyliron Complexes. *J. Am. Chem. Soc.* **2020**, *142*, 4104-4107.

(126) Pluth, M. D.;Lippard, S. J. Reversible binding of nitric oxide to an Fe(III) complex of a tetra-amido macrocycle. *Chem. Commun.* **2012**, *48*, 11981-11983.

(127) Kupper, C., Rees, J. A., Dechert, S., DeBeer, S.;Meyer, F. Complete Series of $\{FeNO\}^8$, $\{FeNO\}^7$, and $\{FeNO\}^6$ Complexes Stabilized by a Tetracarbene Macrocycle. *J. Am. Chem. Soc.* **2016**, *138*, 7888-7898.

(128) Hong, S., Yan, J. J., Karmalkar, D. G., Sutherlin, K. D., Kim, J., Lee, Y.-M., Goo, Y., Mascharak, P. K., Hedman, B.;Hodgson, K. O. A mononuclear nonheme $\{FeNO\}^6$ complex: synthesis and structural and spectroscopic characterization. *Chem Sci* **2018**, *9*, 6952-6960.

(129) Haller, K. J., Johnson, P. L., Feltham, R. D., Enemark, J. H., Ferraro, J. R.;Basile, L. J. Effects of Temperature and Pressure on the Molecular and Electronic Structure of N,N′-ethylenebis(salicylideneiminato)nitrosyliron, Fe(NO)(salen). *Inorg. Chim. Acta* **1979**, *33*, 119-130.

(130) Dey, A., Confer, A. M., Vilbert, A. C., Moënne-Loccoz, P., Lancaster, K. M.;Goldberg, D. P. A Nonheme Sulfur-Ligated $\{FeNO\}^6$ Complex and Comparison with Redox-Interconvertible $\{FeNO\}^7$ and $\{FeNO\}^8$ Analogues. *Angew. Chem. Int. Ed.* **2018**, *57*, 13465-13469.

(131) Chalkley, M. J.;Peters, J. C. A Triad of Highly Reduced, Linear Iron Nitrosyl Complexes: $\{FeNO\}^{8\text{-}10}$. *Angew. Chem. Int. Ed.* **2016**, *55*, 11995-11998.

(132) Pecak, J., Stöger, B., Mastalir, M., Veiros, L. F., Ferreira, L. P., Pignitter, M., Linert, W.;Kirchner, K. Five-Coordinate Low-Spin $\{FeNO\}^7$ PNP Pincer Complexes. *Inorg. Chem.* **2019**, *58*, 4641-4646.

(133) Foi, A., Di Salvo, F., Doctorovich, F., Roy, T. G., Stirnat, K., Biewer, C.;Klein, A. Tracing the Iron Nitrosyl Complex $[Fe(2, 2′\text{-bipyridine})(CN)_3(NO)]^-$. *Euro. J. Inorg. Chem.* **2015**, *2015*, 1033-1040.

Chapter 2[1]

The Semireduced Mechanism of N-N Coupling

As discussed in Chapter 1, our initially reported synthesis of $[Fe_2(BPMP)(OPr)(NO)_2](BPh_4)_2$ suffers from several drawbacks. In the original procedure, the precursor complex $[Fe_2(BPMP)(OPr)](BPh_4)_2$ is obtained via a salt metathesis step of the initially formed triflate complex $[Fe_2(BPMP)(OPr)](OTf)_2$ with $NaBPh_4$. The following reaction with NO then gives $[Fe_2(BPMP)(OPr)(NO)_2](BPh_4)_2$. While some batches of this complex yielded N_2O quantitatively, more typical yields were in the 60-80% range. Elemental analyses of the precursor complex showed that this was largely due to varying amounts of salt impurities in the bulk material, due to the salt metathesis step. Additionally, the tetraphenylborate salts of the complexes exhibit low solubility in organic solvents and are insoluble in water, likely due to the tetraphenylborate counterion.

In this chapter, I discuss the synthesis of the triflate complex $[Fe_2(BPMP)(OPr)](OTf)_2$ (**1**),[2] which can be obtained in consistent, high purity, as evidenced by elemental analysis, and Mössbauer, IR and UV-Vis spectroscopy. Accordingly, the nitrosylated complex $[Fe_2(BPMP)(OPr)(NO)_2](OTf)_2$ (**2a**) consistently gives quantitative N_2O yields, and is completely soluble in CH_2Cl_2, CH_3CN, and MeOH. Since the synthesis of $[Fe_2(BPMP)(OPr)(NO)_2](BPh_4)_2$ had numerous issues described above, an analog containing the non-coordinating $^{-}BF_4$ counterion, $[Fe_2(BPMP)(OPr)(NO)_2](BF_4)_2$ (**3**), is also reported and its reduction was investigated. Portions of

this work were performed in collaboration with the Meyer laboratory at the University of Göttingen in Germany. Stopped-flow IR measurements were performed by myself during my time working in their laboratory from June-August 2016, while Mössbauer and SQUID data were collected by Claudia Kupper and Serhiy Dehmeshko.

2.1 Synthesis and Characterization of $[Fe_2(BPMP)(OPr)(NO)_2](X)_2$

Synthesis of $[Fe_2(BPMP)(OPr)(NO)_2](X)_2$

As discussed above, our initial communication on $[Fe_2(BPMP)(OPr)(NO)_2](BPh_4)_2$ suffered from several drawbacks. In order to mitigate these drawbacks and expand on our initial communication, two new complexes containing $^{-}$OTf and $^{-}BF_4$ counterions and their isotopologs will be discussed in detail here (Table 2.1).

Table 2.1 A list of all BPMP complexes and their corresponding sample codes discussed in this chapter.

Complex	Code
$[Fe_2(BPMP)(OPr)](OTf)_2$	**1**
$[Fe_2(BPMP)(OPr)(NO)_2](OTf)_2$	**2a**
$[Fe_2(BPMP)(OPr)(^{15}NO)_2](OTf)_2$	**2b**
$[Fe_2(BPMP)(OPr)(^{15}N^{18}O)_2](OTf)_2$	**2c**
$[^{57}Fe_2(BPMP)(OPr)(NO)_2](OTf)_2$	**2d**
$[^{57}Fe_2(BPMP)(OPr)(^{15}N^{18}O)_2](OTf)_2$	**2e**
$[Fe_2(BPMP)(OPr)(NO)_2](BF_4)_2$	**3**
$[Fe_2(BPMP)(OPr)_2](OTf)$	**4**
$[Zn_2(BPMP)(OPr)_2](OTf)(CH_2Cl_2)$	**5a**
$[Zn_2(BPMP)(OAc)_2](OTf)$	**5b**

H[BPMP] can be metallated under inert conditions in the presence of one equivalent of base (KOMe), a bridging carboxylate (propionate, $^{-}$OPr), and a ferrous-counterion salt, $Fe(OTf)_2{\cdot}2CH_3CN$ or $Fe(BF_4)_2{\cdot}2.5CH_3CN$, to generate $[Fe_2(BPMP)(OPr)](X)_2$. Upon mixing under a headspace of NO(g), the corresponding dinitrosyl products $[Fe_2(BPMP)(OPr)(NO)_2](OTf)_2$ (**2a**) and $[Fe_2(BPMP)(OPr)(NO)_2](BF_4)_2$ (**3**) are formed. The ^{15}NO and $^{15}N^{18}O$ isotopologs, **2b** and **2c**, respectively, were also generated in this manner, while

the ^{57}Fe isotopologs **2d** and **2e** first required the *in-situ* generation of $^{57}FeOTf_2$ via the salt metathesis of $^{57}FeCl_2$ with AgOTf following a previously published protocol.[11] A general reaction scheme for the metalation and nitrosylation of H[BPMP] is provided in Scheme 2.1.

Scheme 2.1 General reaction scheme for the metallation and nitrosylation of H[BPMP]

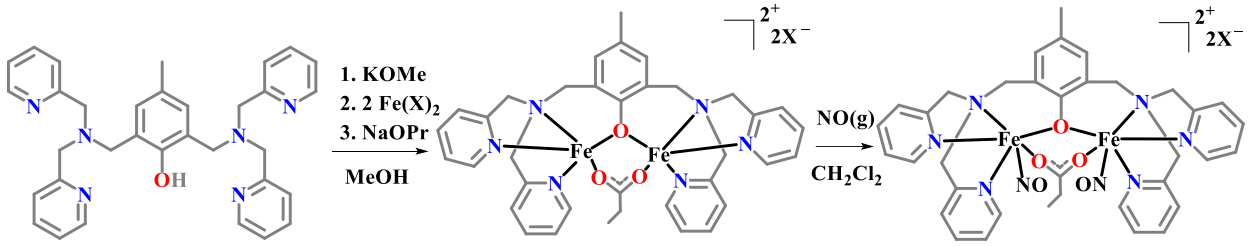

Characterization of $[Fe_2(BPMP)(OPr)(NO)_2](X)_2$

The diferrous precursor $[Fe_2(BPMP)(OPr)](OTf)_2$ (**1**) is a bright yellow complex, which displays a moderately strong absorption band at 400 nm (ε = 2000 $M^{-1}cm^{-1}$; see Figure 2.1) in its UV-Vis spectrum, assigned to an iron(II)-to-pyridine metal-to-ligand charge transfer (MLCT) band.[3] Mössbauer experiments performed on powder samples of **1** show a single quadrupole doublet, indicative of electronically identical iron sites in **1**. Figure 2.2 shows the experimental data along with a fit, delivering an isomer shift of 1.19 mm/s and a quadrupole splitting ΔE_q of 2.89 mm/s, indicative of high-spin iron(II) centers. The spin state of the iron(II) centers is further confirmed by magnetic susceptibility data, shown in Figure 2.2. The data are fit assuming two high-spin Fe(II) centers (S = 2 each), using the Spin Hamiltonian, where S_A and S_B are the spin

$$\underline{H} = -2J \bullet \underline{S_A} \bullet \underline{S_B} \qquad (1)$$

operators for centers A and B, and J is the exchange coupling constant. A fit of the data in Figure 2.2 gives a coupling constant of J = -3.6 cm^{-1}, indicating weak antiferromagnetic coupling between

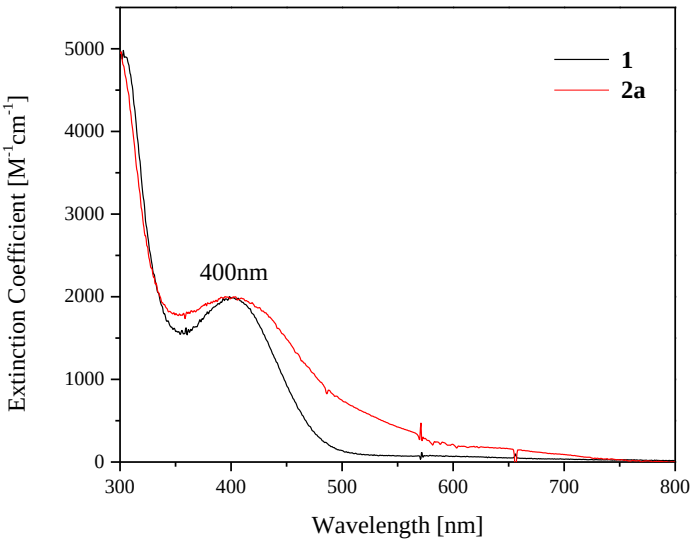

Figure 2.1 UV-Visible spectra of $[Fe_2(BPMP)(OPr)](OTf)_2$ (**1,** black) and $[Fe_2(BPMP)(OPr)(NO)_2](OTf)_2$ (**2a**, red) .

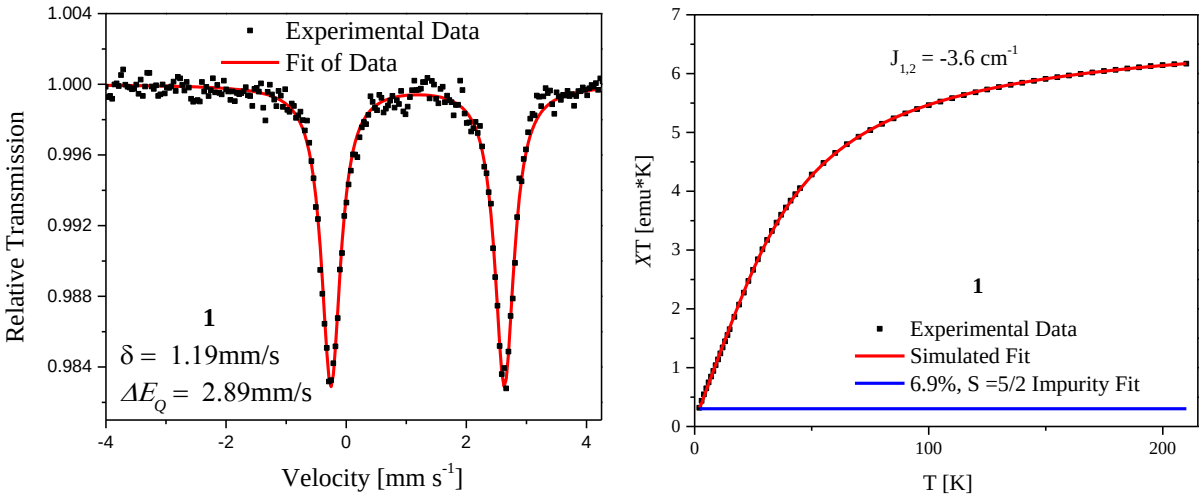

Figure 2.2 Left: Mössbauer spectra of **1** taken on a powder sample at 80K. The isomer shift and quadrupole splitting are consistent with a hs-Fe^{II} center. Right: Magnetic susceptibility data of **1**, simulated using the *julX* program.[29] **1** exhibits weak antiferromagnetic coupling between the iron centers with a $J_{1,2}$ coupling constant of -3.6cm^{-1}.

the two Fe(II) ions. Note that this data required fitting a 7% S = 5/2 hs-Fe^{III} impurity to be best fit. The cyclic voltammetry data for **1** illustrates two redox events at $E_{1/2}$ = 0.260 V and 1.020 V vs Fc^+/Fc corresponding to the $Fe^{III}Fe^{II}/Fe^{II}Fe^{II}$ and $Fe^{III}Fe^{III}/Fe^{III}Fe^{II}$ couples, respectively. The oxidation to the diferric state is only quasi-reversible, resulting in a new decomposition redox couple on the reverse (reductive sweep) at 0.650 V vs Fc^+/Fc (Figure 2.3)

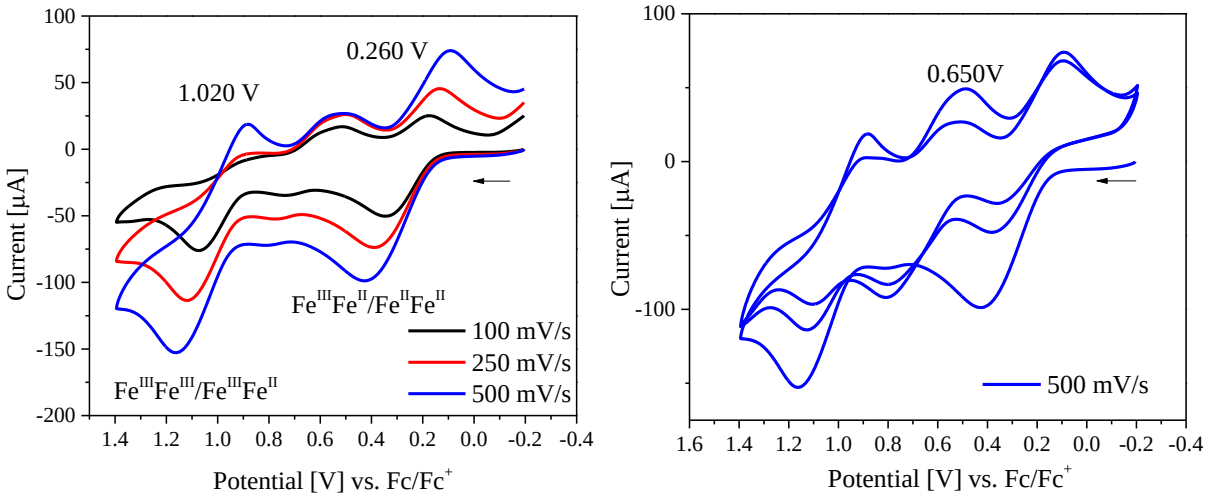

Figure 2.3 Left: The cyclic voltammogram of **1** shows two clean oxidation events at $E_{1/2}$ = 0.260 and 1.020 V vs. Fc^+/Fc. Right: The final oxidation to $Fe^{III}Fe^{III}$ is quasi-reversible, resulting in a new feature appearing at 0.650 V on the reverse scan.

Upon nitrosylation of **1** to form $[Fe_2(BPMP)(OPr)(NO)_2](OTf)_2$ (**2a**), there is an immediate color change of the solution to dark brown. The UV-Vis absorption spectrum of **2a** shows a broad band at 400 nm (ε = 2000 $M^{-1}cm^{-1}$; see Figure 2.1). As mentioned in Chapter 1, non-heme high-spin $\{FeNO\}^7$ centers are best described as Fe(III)-NO^-, where a high-spin Fe(III) center (S = 5/2) is coordinated to a $^3NO^-$ ligand (S = 1), and the spins are antiferromagnetically coupled (S_t = 3/2). These complexes typically exhibit relatively weak NO^- to Fe(III) ligand-to-metal charge transfer (LMCT) transitions in the 400 – 500 nm range[4-6], and we assign the 400 nm feature of **2a** to a corresponding LMCT transition. SQUID data for **2a** are shown in Figure 2.4. These data reveal two $\{FeNO\}^7$ centers with S = 3/2 spin states that are antiferromagnetically coupled, confirming that the $\{FeNO\}^7$ units are in the high-spin state. A fit of the data to equation (1) gives an exchange coupling constant *J* of -7.0 cm^{-1}. The increase in the magnitude of *J* from **1** to **2a** is attributed to the partial oxidation of the iron centers upon nitrosylation from Fe^{II} to Fe^{III}-NO^-, resulting in slightly increased antiferromagnetic coupling. This is further illustrated in the Mössbauer data for **2a** (Figure 2.4), containing a single quadrupole doublet with an isomer shift of 0.70 mm/s and a

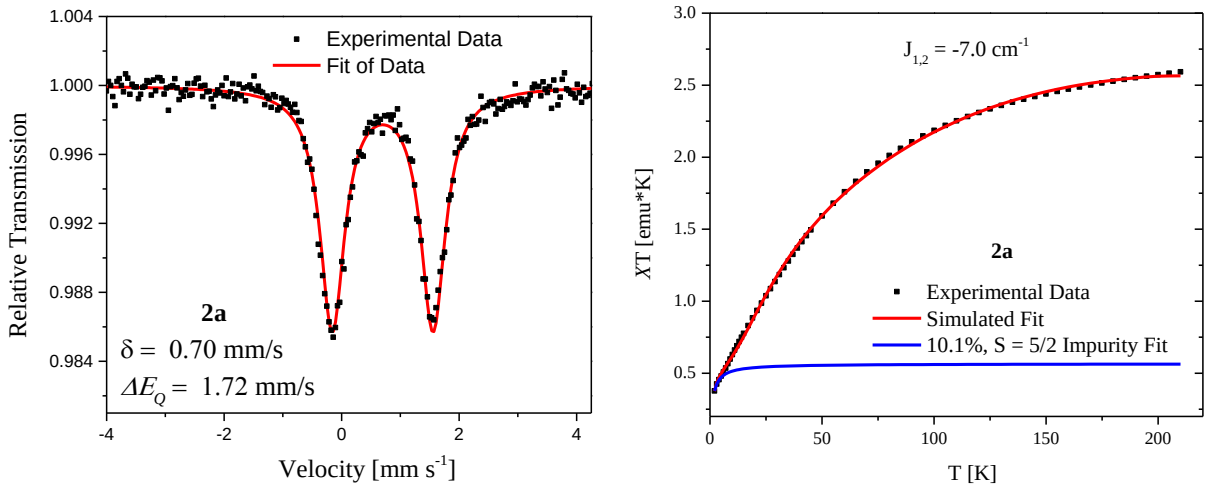

Figure 2.4 Left: Mössbauer spectra of **2a** taken on a powder sample at 80K. The isomer shift and quadrupole splitting are consistent with a hs-{FeNO}^{7} center. Right: Magnetic susceptibility data of **2a**, simulated using the *julX* program.[2] **2a** exhibits weak antiferromagnetic coupling between the iron centers with a $J_{1,2}$ coupling constant of -7.0 cm^{-1}.

quadrupole splitting of 1.72 mm/s. These parameters are consistent with similar, reported non-heme hs-{FeNO}^{7} complexes in the literature.[7-9] Importantly, the isomer shift is directly correlated with the Fe s-electron density, and correspondingly, the Fe oxidation state. Non-heme hs-{FeNO}^{7} complexes have isomer shifts that sit between typical hs-Fe^{II} isomer shifts (~1.0 – 1.3 mm/s) and hs-Fe^{III} isomer shifts (~0.4 – 0.6 mm/s), consistent with the idea that binding of NO to a high-spin iron(II) leads to an oxidation of the iron center affording a ground state Fe^{III}-NO$^-$ electronic structure.[21,22,41] In turn, the fact that the isomer shift is larger compared to analogous Fe(III) complexes with the BPMP$^-$ ligand,[10] reflects the large amount of electron density that is donated from the NO$^-$ ligand back to the Fe(III) center by forming two strong π-donor bonds.[11, 12]

The FT-IR spectrum of **2a** contains an intense N-O stretching band at 1768 cm^{-1}, which shifts to 1734 and 1695 cm^{-1} upon ^{15}NO and ^{15}N^{18}O labeling, respectively (Figure 2.5). The frequency of the N-O stretch is consistent with other mono- and dinuclear non-heme high-spin {FeNO}^{7} model complexes,[7, 13,34] which generally exhibit the N-O stretch between 1710 – 1810 cm^{-1}. In comparison, the NO adduct of RNR contains an N-O stretch at 1742 cm^{-1},[14, 15] and,

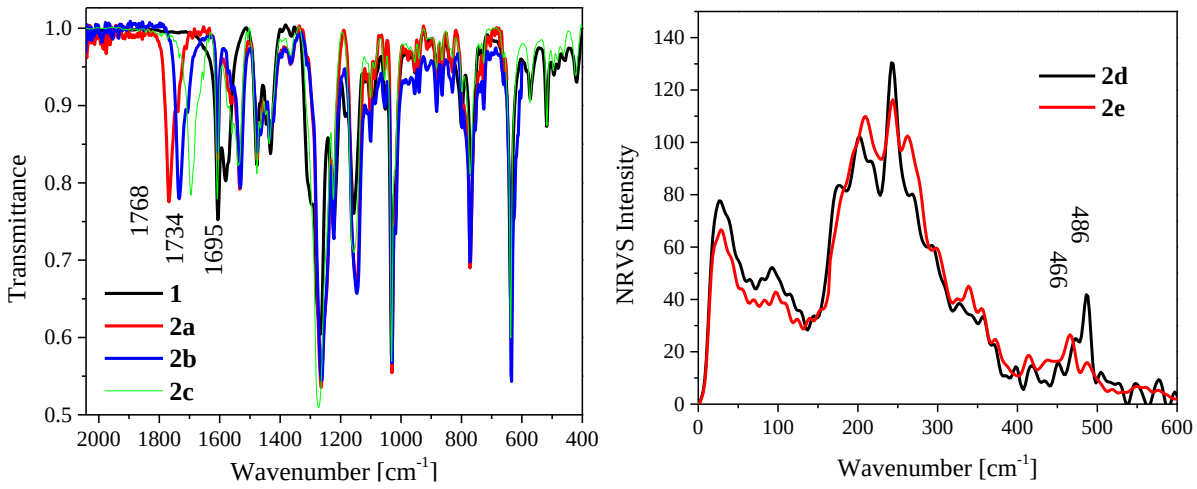

Figure 2.5 Left: Overlay of the room temperature IR (KBr) spectra of the metallated precursor **1** and its nitrosylated isotopologs, **2a**, **2b**, and **2c**. The N-O stretch of **2a** is observed at 1768 cm^{-1} which shifts to 1734 cm^{-1} and 1695 cm^{-1} upon labelling with ^{15}NO and $^{15}N^{18}O$, respectively. Right: Comparison of the NRVS data for the ^{57}Fe isotopologs of **2a** containing natural abundance NO (**2d**) and $^{15}N^{18}O$ (**2e**). We attribute the isotope sensitive band at 486 cm^{-1} to the Fe-NO stretch. Spectra were taken in 0.25 meV steps and represent the sum of 6 scans.

importantly, the N-O stretching frequency of **2a** compares very well to that of the dinitrosyl adduct of *Tm* FDP, reported at 1749 cm^{-1}.[16] In order to measure the Fe-NO stretch of **2a**, nuclear resonance vibrational spectroscopy (NRVS) of the ^{57}Fe analogue of this complex (**2d** and **2e**) was applied. As shown in Figure 2.5, NRVS exhibits an isotope-sensitive band at 486 cm^{-1} that downshifts to 466 cm^{-1} upon $^{15}N^{18}O$ labelling. We assign this feature to the Fe-NO stretch of **2a**. In comparison, the Fe-NO stretching frequencies of the mono- and dinitrosyl adducts of the deflavinated *T. maritima* FDP are reported at lower energies of 451 cm^{-1} and 459 cm^{-1}, respectively, indicating that the electronic environment of the Fe centers in the enzyme is more electron-rich compared to our model complex.[16, 17]

We have previously established a correlation between the N-O and the Fe-NO stretching frequencies for mononuclear high-spin $\{FeNO\}^7$ complexes with the TMPA (tris(2-pyridylmethyl)amine) and BMPA-Pr$^-$ (N-propano-ate-N,N-bis(2-pyridylmethyl)amine) coligands (Figure 2.6).[11] These serve as model complexes for the non-heme Fe_B site of bacterial

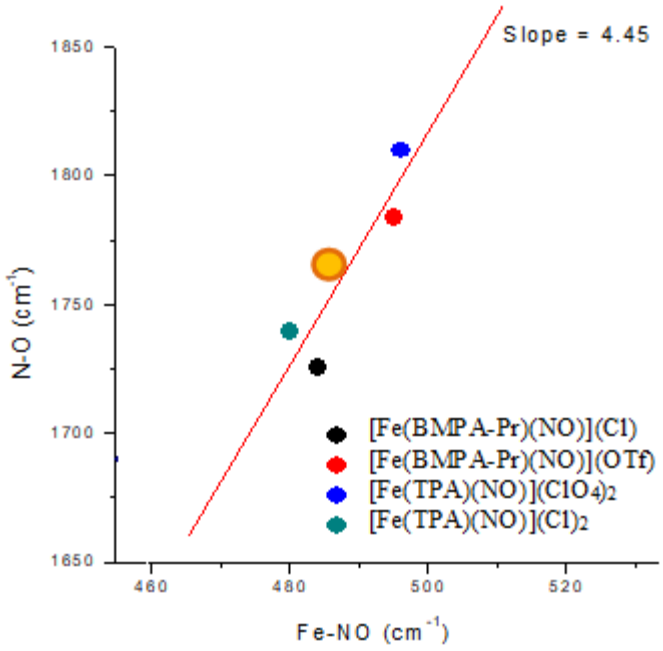

Figure 2.6 Correlation curve between the N-O and Fe-NO stretching frequencies of selected mononuclear $\{FeNO\}^7$ complexes and complex **2a** (orange).

NO reductase, with N_4 and N_3O coordination spheres, respectively. Complex **2a** lies right on the correlation line that was previously established for the mononuclear compounds. This is not surprising, considering the very similar coordination spheres of the iron centers in **2a** and the mononuclear hs-$\{FeNO\}^7$ complexes used to establish the correlation. However, what this shows is that the individual $\{FeNO\}^7$ units in **2a** have very similar electronic structures compared to the mononuclear compounds, and that the hs-$\{FeNO\}^7$ units in **2a** are not strongly electronically coupled.

Finally, cyclic voltammetry of **2a** displays an irreversible reductive wave at -1.15 V vs. Fc/Fc^+ (Figure 2.7) consistent with reduction of the $\{FeNO\}^7$ complex and the subsequent fast, irreversible transformation of NO to N_2O. A new wave forms at -0.45 V (vs. Fc/Fc^+) after reduction, which we attribute to the reduction product formed under the CV conditions. These data are essentially identical to the electrochemical data reported previously for the analog

$[Fe_2(BPMP)(OPr)(NO)_2](BPh_4)_2$. With this redox potential in mind, the chemical and electrochemical reduction of **2a** was performed.

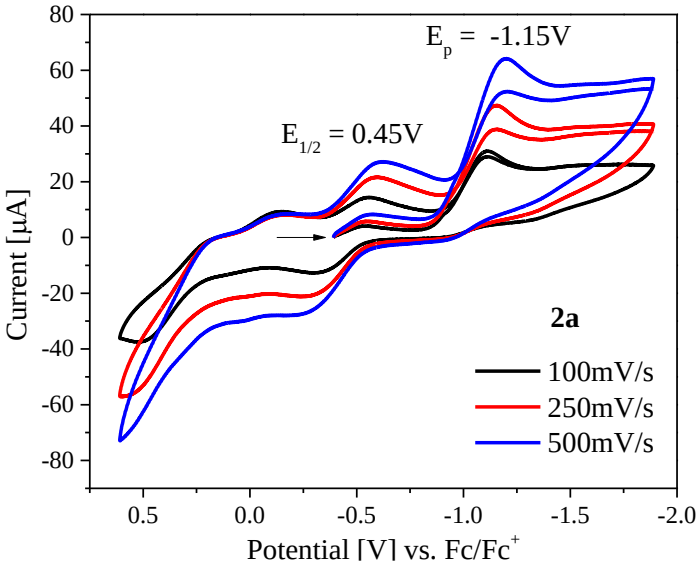

Figure 2.7 Cyclic voltammetry of ~5mM **2a** in CH_2Cl_2 with ~0.1M tetrabutylammonium triflate added as the electrolyte. The data show an irreversible reductive wave at -1.15V. The measurement was conducted using a glassy carbon working electrode, a platinum counter electrode, and an Ag wire pseudoreference electrode. Potentials are referenced to an Fc/Fc^+ standard.

2.2 Chemical and Electrochemical Reduction of $[Fe_2(BPMP)(OPr)(NO)_2](X)_2$

Chemical Reduction: Semi- vs. Super-reduction

For our initially reported complex $[Fe_2(BPMP)(OPr)(NO)_2](BPh_4)_2$, we observed quantitative N_2O generation after the addition of two equivalents of reductant (cobaltocene, $CoCp_2$, $E_{1/2}$ = -1.33 V vs. Fc^+/Fc).[13] This was initially interpreted as evidence that the complex uses a superreduced mechanism for N_2O formation. In any case, it provided clear evidence that reduction of otherwise stable hs-$\{FeNO\}^7$ complexes serves as a potent means to activate them and make them more reactive. In support of this finding, data published for the $[Fe(TMG_3tren)(NO)]$ hs-$\{FeNO\}^{6\text{-}8}$ series demonstrates that reduction leads to a decrease in the covalency of the Fe-NO bond and increases the negative charge and radical character on the $^3NO^-$ ligand.[12, 18]

Quantification of N_2O yields were carried out using a N_2O calibration curve (Figure 2.8) that was generated by dissolving Piloty's acid in 2.5 mL of a NaOH solution (pH 13). Piloty's acid acts as an HNO donor under basic conditions, which dimerizes after release and quantitatively decomposes into N_2O and H_2O. The Piloty's acid solution was stirred in a sealed 25 mL round bottom flask with a 14/20 septum. After 2 hours, the gas headspace was transferred into an evacuated Pike HT gas-IR cell (190 milliTorr) via cannula transfer for exactly 20 s, and the IR spectrum was measured. After subtraction of a solvent blank taken under the exact same conditions, the full band of the N-N stretching mode of N_2O in the absorption IR spectrum was integrated from 2150 cm-1 to 2275 cm-1, using a straight-line baseline correction.

The $[Fe_2(BPMP)(OPr)(NO)_2](OTf)_2$ dimer **2a** studied here also generates N_2O quantitatively upon addition of two equivalents of $CoCp_2$, determined by IR gas-headspace analysis (Figure 2.9), consistent with our initial communication. However, the complex not only

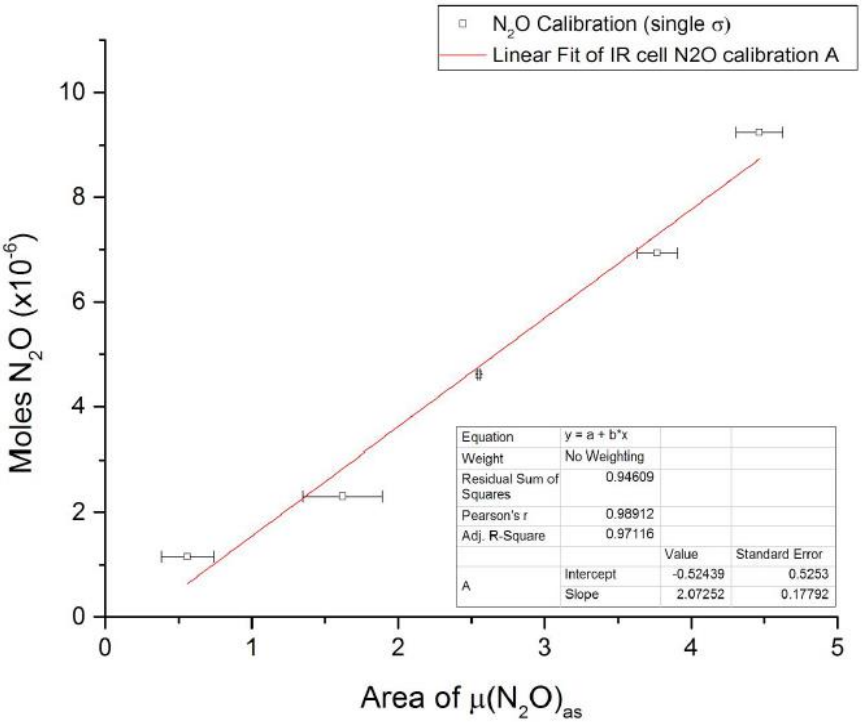

Figure 2.8 Gas-headspace N_2O calibration curve generated from the decomposition of 2 – 20 μmol of Piloty's Acid under basic conditions.

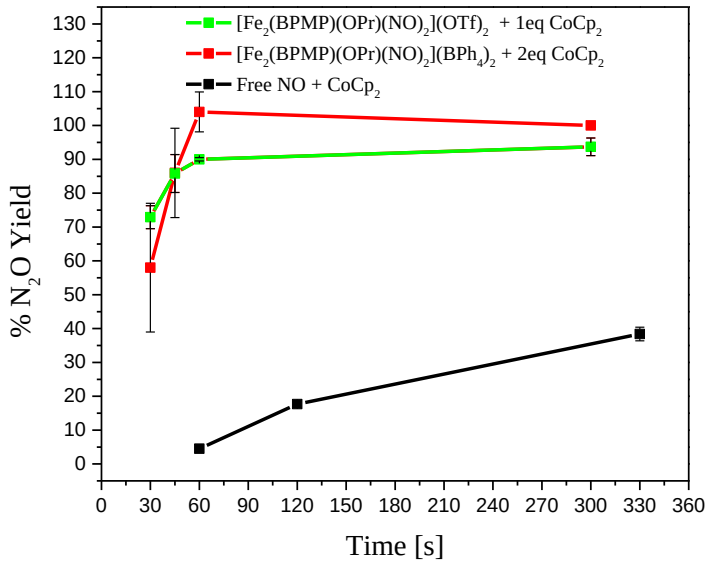

Figure 2.9 N_2O yield comparison for the reduction of $[Fe_2(BPMP)(OPr)(NO)_2](X)_2$ complexes with one and two equivalents of reductant illustrates quantitative N_2O yield in both cases after 60 s. As a control, the reduction of free NO gas is included.

generates quantitative amounts of N_2O in the presence of only one equivalent of $CoCp_2$, the rate of N_2O production, as determined by IR gas-headspace analysis, is also identical to the case where two equivalents of reductant are used (Figure 2.9). First, this result demonstrates that **2a** actually uses a "semireduced" mechanism for N_2O generation. The second equivalent of reductant is not needed for N_2O formation and does not influence the overall reaction rate. This further implies that the one-electron reduced hs-$\{FeNO\}^7/\{FeNO\}^8$ dimer is in fact activated for N-N coupling, releasing N_2O and forming a mixed-valent reaction product:

$$[\{FeNO\}^7]_2 + e^- \rightarrow [\{FeNO\}^7/\{FeNO\}^8] \rightarrow \text{"Fe(II)-O-Fe(III)"} + N_2O \qquad (2)$$

This poses the question of how the second electron is consumed when two equivalents of reductant are added to **2a**. To investigate this, a redox titration where **2a** was added stepwise to a solution of 110 μM of $CoCp_2$ was performed. The data in Figure 2.10 show that consumption of up to 0.55 equivalents of **2a** (60 μM) leads to the appearance of a new absorption band at 435nm, with an isosbestic point at 382 nm. Addition of further equivalents of **2a** simply shows the absorption

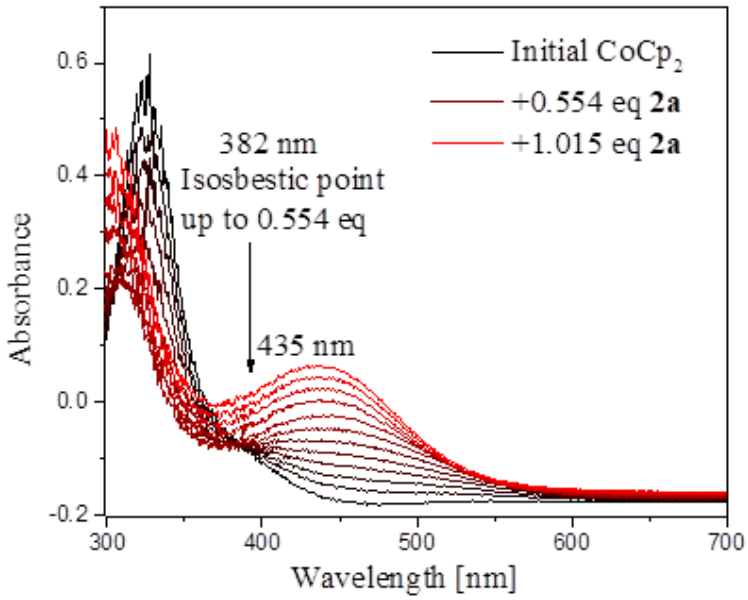

Figure 2.10 Room temperature UV-Vis dip probe titration of 110 μM of $CoCp_2$ in CH_2Cl_2 with **2a**, showing an isosbestic point at 382nm up to the addition of 0.554 equivalents (60 μM) of **2a**. This is consistent with the consumption of two equivalents of reductant per complex **2a**, as previously reported.

spectrum of **2a** appear on top of the spectrum of the reduced reaction product. Therefore, complex **2a** is in fact able to consume a total of two equivalents of reductant, as reported in our initial communication.[13] The second reductive equivalent is then consumed by reducing the initially formed mixed-valent reaction product:

$$\text{“Fe(II)-O-Fe(III)”} + e^- \rightarrow \text{“Fe(II)/Fe(II)”} \qquad (3)$$

While we considered this unlikely, one additional possibility as to why **2a** carries out semireduction as opposed to the $^-BPh_4$ analog's (reported) superreduction is due to the coordinating nature of the ^-OTf counterion. In order to test this idea and simultaneously avoid the difficulties associated with the $^-BPh_4$ complex, the non-coordinating $^-BF_4$ complex $[Fe_2(BPMP)(OPr)(NO)_2](BF_4)_2$ (**3**) was synthesized and its chemical reduction was investigated. Importantly, N_2O was again generated quantitatively with the addition of just *one* equivalent of reductant, confirming that the nature of the counter ion does not influence the reaction of $[Fe_2(BPMP)(OPr)(NO)_2]^{2+}$ with reductant. Hence, we conclude that

$[Fe_2(BPMP)(OPr)(NO)_2](BPh_4)_2$ also proceeds via the same semireduced mechanism as **2a** and **3**, with the second reductive equivalent being consumed by the mixed-valent product generated after N_2O release. In line with this, the formation of a diferrous reaction product after the addition of two equivalents of $CoCp_2$ to a solution of $[Fe_2(BPMP)(OPr)(NO)_2](BPh_4)_2$ was confirmed in the initial communication.[13]

Kinetics of N_2O Generation

In order to evaluate the kinetics of N_2O generation and to identify putative intermediates, like the hs-$\{FeNO\}^7\{FeNO\}^8$ dimer, the reduction of **2a** was first monitored by IR spectroelectrochemistry (IR-SEC). Upon applying a potential of -1.3 V vs. Ag wire to a solution of **2a**, the N-O stretching band at 1765 cm^{-1} decreases in intensity, with a concomitant increase of the product N_2O band at 2222 cm^{-1} and a shift of the bridging carboxylate band at 1541 cm^{-1} to higher energy, towards the pyridine band at 1605 cm^{-1} (Figure 2.11). The intensities of the NO and N_2O bands were normalized and plotted as a function of time (Figure 2.11), showing no delay between the consumption of **2a** (decrease in intensity of the NO band) and the rise of the N_2O band. The reaction therefore proceeds at a faster rate than the IR-SEC timescale, and no intermediate hs-$\{FeNO\}^7\{FeNO\}^8$ species was detected. This is surprising, given that this experiment shares a similar timescale to the N_2O gas-headspace analysis experiments (see Figure 2.9), which show quantitative N_2O formation occurring only after ~60 seconds. In retrospect, the delay in N_2O quantification in the gas-headspace experiments monitors that rate at which N_2O diffuses from solution into the gas phase and is not a suitable means to measure the rates of fast reactions. Moving forward, the reaction of **2a** with one equivalent of $CoCp_2$ was probed by stopped- flow IR spectroscopy. Upon mixing of **2a** with one equivalent of $CoCp_2$ at room temperature, the NO band completely disappears with the instant formation of the N_2O band in the

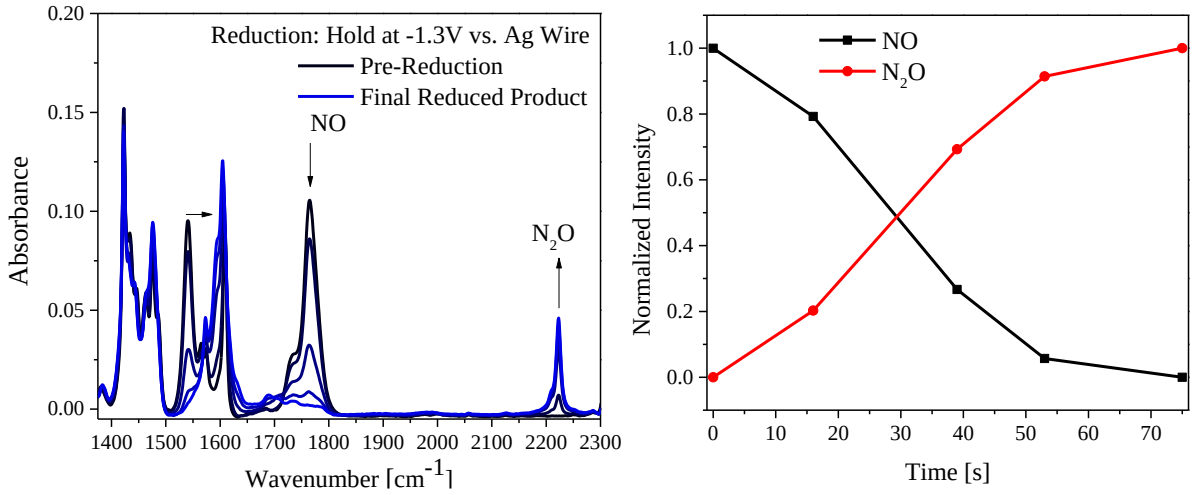

Figure 2.11 Left: IR spectroelectrochemistry monitoring of the reduction of ~5mM **2a** upon applying a potential of -1.3V vs. Ag wire, showing the loss of the N-O stretching band at 1765 cm^{-1} along with an increase of the N-N stretch of N_2O at 2222 cm^{-1} over time. Right: The plot of the normalized intensities of the NO and N_2O bands over time illustrates the direct conversion of NO to N_2O without the formation of any observable intermediates on the IR-SEC timescale. Spectra were recorded for a ~5mM solution of **2a** in CH_2Cl_2 with ~0.1M tetrabutylammonium triflate as the supporting electrolyte, using a thin layer SEC cell with a Pt mesh as the working and counter electrodes and an Ag wire as the pseudoreference electrode.

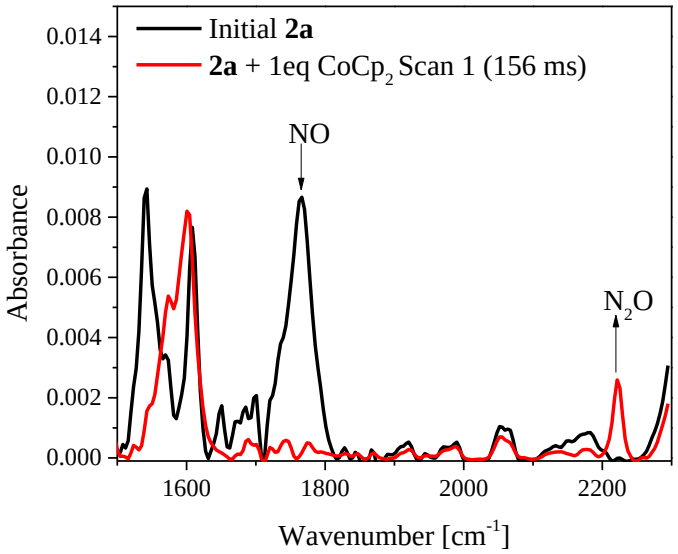

Figure 2.12 Stopped-flow IR experiment monitoring the reduction of 8.1mM **2a** in CH_2Cl_2 with one equivalent of $CoCp_2$. The data show that completion of the N-N coupling process and N_2O release occur within the 156 ms mixing dead time of the instrument.

first scan (Figure 2.12), revealing that the reduction proceeds remarkably fast, within the 156 ms dead time of the stopped-flow IR instrument. Based on this result, the first order rate constant k_{obs} for N-N coupling and N_2O release is estimated to be $>10^2$ s^{-1}, assuming a >95% conversion

occurred in the 156 ms time frame. This further assumes that the reduction of **2a** is instantaneous, and that the following generation of N_2O is rate limiting. In contrast, a similar non-heme diiron dinitrosyl complex with a cis NO orientation, $[Fe_2(Et\text{-}HPTB)(O_2CPh)(NO)_2](BF_4)_2$, photoreduces NO to N_2O with a first order rate constant of 0.2 min^{-1}.[7] Kinetic studies on 70μM of the *T. maratima* FDP,[8, 19] which is primarily an O_2 reductase *in vivo*, have shown an accumulation of the $[\{FeNO\}^7]_2$ intermediate, preceding a decay of this species to a diferric product and N_2O over the course of ~120 s.

Due to the rapid reaction of **2a** with $CoCp_2$ and quick N_2O release, the concentration dependence on the rate constant for the reaction could not be measured. In order to determine if **2a** undergoes an *intra*molecular N-N coupling, as the *Tm.* FDP does, an isotope scrambling experiment was performed. Here, a 1:1 mixture of the natural abundance complex **2a** and the ^{15}NO complex **2b** were reacted with one equivalent of $CoCp_2$ and the isotopic scrambling of N_2O was evaluated by gas-headspace IR. Initially, this reaction was carried out at room temperature, and afforded a mixture of $^{14,14}N_2O$, $^{14,15}N_2O$, and $^{15,15}N_2O$ products (Figure 2.13). However, this does not immediately imply that *inter*molecular N-N coupling is occurring. By solution IR, the N-O stretch of a 5mM solution of **2b** shifts to that of **2a** over 15 minutes upon addition of natural abundance NO(g) to the solution, suggesting that the NO ligands are labile and capable of exchanging at room temperature (Figure 2.13). In order to mitigate ligand exchange in solution, the reduction of a 1:1 mixture of **2a** and **2b** was instead carried out at -80°C and the gas-headspace was similarly analyzed for isotopic scrambling in N_2O (Figure 2.13). In this case only $^{14,14}N_2O$ and $^{15,15}N_2O$ were formed, suggesting that the coupling occurred *intra*molecularly, consistent with the rapid timescale of the reaction as determined by stopped-flow IR.

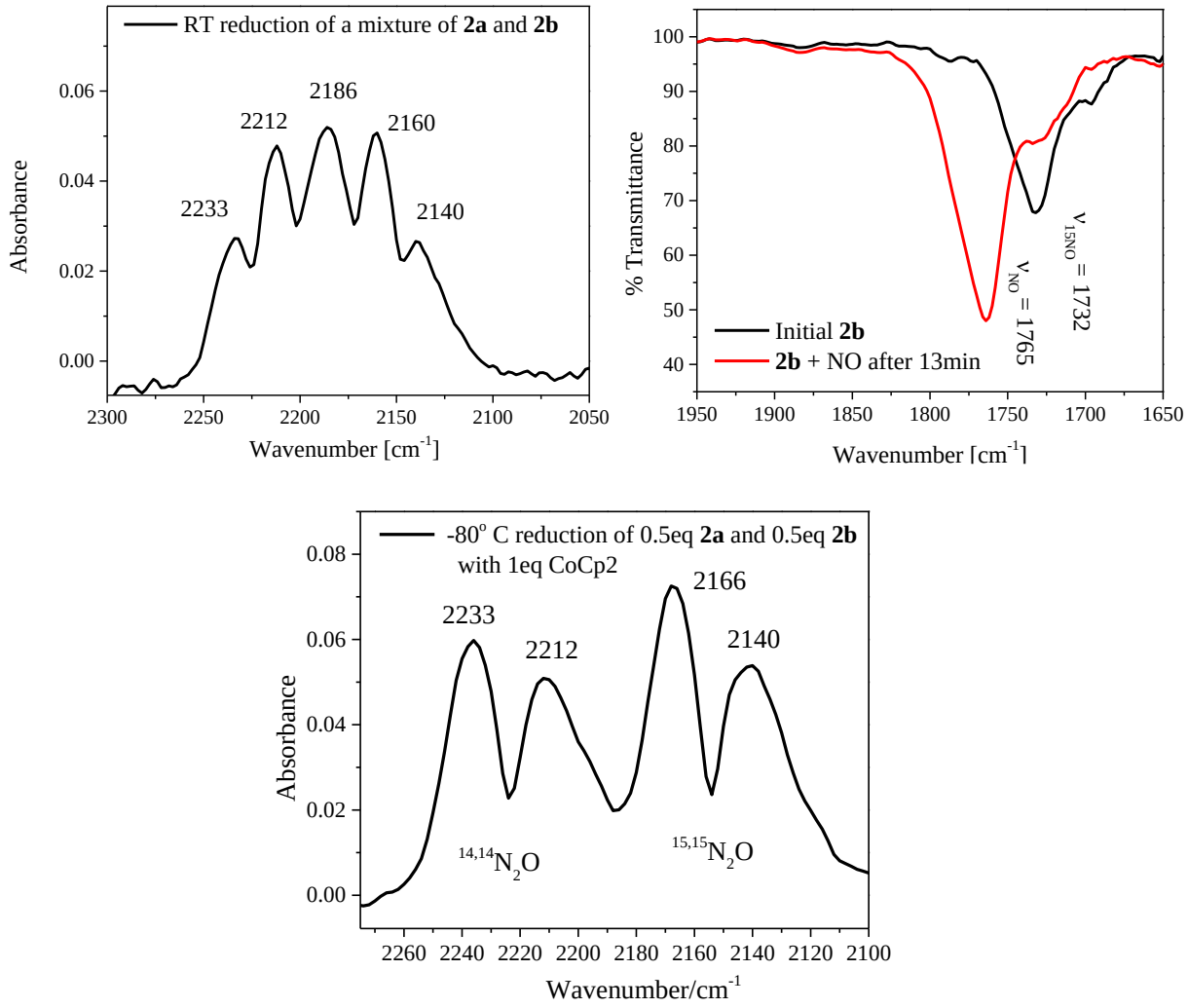

Figure 2.13 Top Left: IR gas-headspace analysis of the room temperature reduction of a mixture of **2a** and **2b**, showing isotopic scrambling in the N_2O product. Top Right: Solution IR of ^{15}NO-labelled **2b** before and after the addition of natural abundance NO, illustrating facile NO exchange in solution at room temperature. Bottom: At low temperature, NO exchange is mitigated, and the reduction of a mixture of **2a** and **2b** affords the intramolecular $^{14,14}N_2O$ and $^{15,15}N_2O$ coupling products.

In order to potentially trap intermediates of the NO reduction reaction of **2a**, the reduction of this complex with one equivalent $CoCp_2$ was also monitored at -80° C via a UV-Vis dip probe setup. Interestingly, the reduction product of **2a** at -80° C exhibits an absorption band at 437 nm, which is stable if the temperature is held at -80° C but decays to a shoulder at 425 nm when warmed to room temperature. The product formed when **2a** is directly reduced at room temperature also shows a 425 nm shoulder, implying that an intermediate species is trapped at -80°C. (Figure 2.14) However, solution IR spectroscopy of the -80° C solution reveals the complete decay of the NO

band with the complete formation of N_2O (Figure 2.14). Hence, the 437 nm intermediate forms after N-N coupling and N_2O release, and therefore, corresponds to the mixed-valent product of the reaction. This will be discussed further in section 2.3. Overall, the generation of N_2O at -80° C combined with the rapid kinetics of the reaction suggest that there is a remarkably low activation barrier for N-N bond formation in the semireduced pathway. Based on the stopped-flow IR data, the lower limit for the rate constant is estimated to be 100 s^{-1}. The low-temperature studies

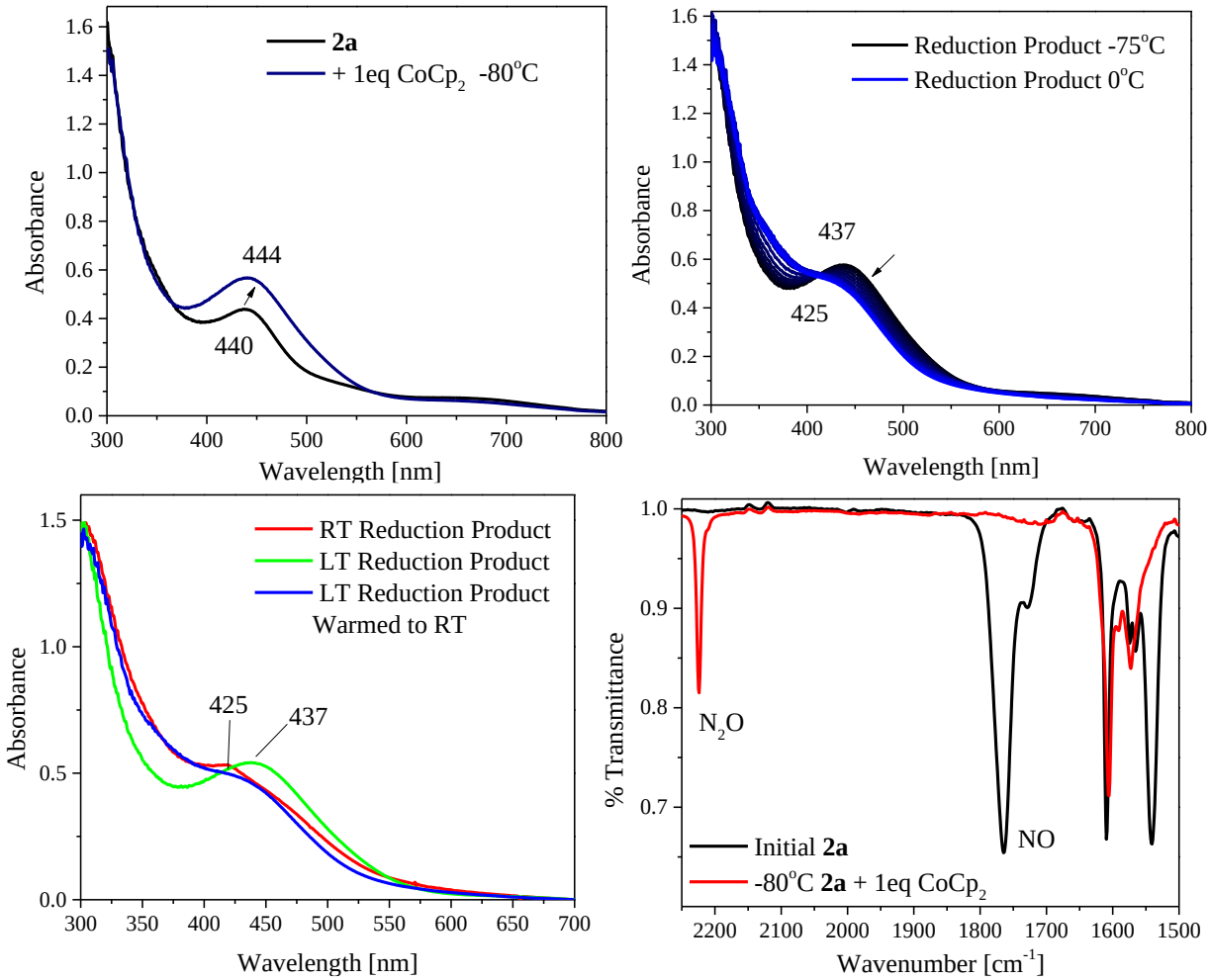

Figure 2.14 Top Left: Low-temperature reduction of 180μM **2a** in CH_2Cl_2 leads to the immediate formation of a new species with an absorption band at 437 nm. Top Right: This species decays upon warming to room temperature to a species with a shoulder at 425nm. Bottom Left: Upon reduction at room temperature, a similar spectrum with a 425 nm shoulder forms. Bottom Right: Low-temperature solution IR of the 437 nm species shows that the NO band has decayed with the complete formation of N_2O, implying that this 437 nm species occurs after N-N coupling and N_2O release.

demonstrate that N_2O can be generated at -80° C, consistent with an extremely low activation barrier for the reaction at room temperature (< 3 kcal/mol). An interesting mechanistic detail is the relative orientation of the two hs-$\{FeNO\}^7$ units in the dimer. In **2a** and as proposed for FNORs, the hs-$\{FeNO\}^7$ units are coplanar, allowing for very efficient N-N coupling to occur. In contrast, in Meyer's complex $[L\{Fe(NO)\}_2(\mu\text{-}OOCR)](X)_2$, where L is a dinucleating pyrazole/triazacyclononane ligand (R is Me or Ph, and X^- is ClO_4^- or BPh_4^-), the NO ligands are in a trans geometry, and correspondingly, this complex does not produce N_2O upon reduction, but instead, disproportionation of the $\{FeNO\}^8$ units is observed.[9] The relative orientation of the hs-$\{FeNO\}^7$ units is therefore a crucial factor for FNOR catalysis and will be discussed further in Chapter 4.

2.3 Characterization of the Reduction Product: Mechanistic Insights

Since the two-electron reduction of NO to N_2O by **2a** only requires the addition of one equivalent of reductant following the semireduced mechanism, the mixed-valent, oxo-bridged Fe^{II}-O^{2-}-Fe^{III} species is the expected reaction product. Whereas **1** and **2a** are EPR silent, the putative mixed-valent product contains a non-integer spin and should be EPR active. Interestingly, this is the case for the reaction product generated at -80° C, containing an intense EPR signal with g-values of 1.96, 1.92, and 1.81 (Figure 2.15). This is indicative of the formation of a mixed-valent species with $S_t = 1/2$ arising from antiferromagnetic coupling between the hs-Fe^{II} (S = 2) and hs-Fe^{III} (S = 5/2) centers. Antiferromagnetic coupling is quite common for mixed-valent Fe(II)/Fe(III)

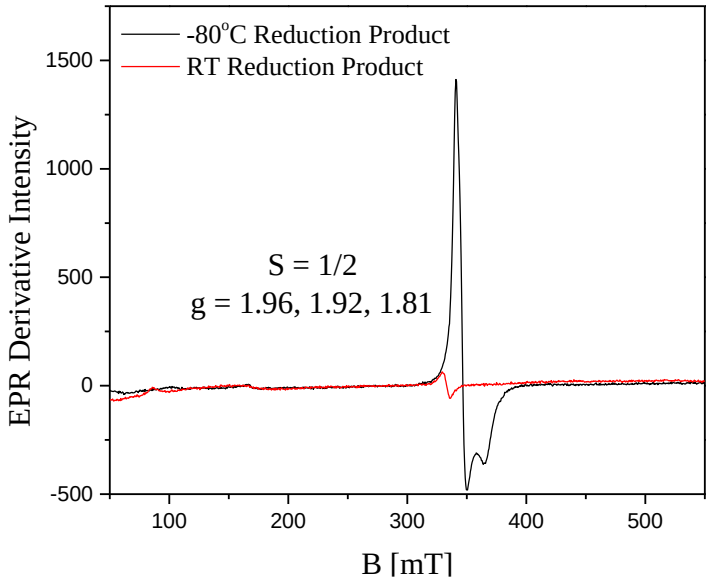

Figure 2.15 EPR spectra of (a) the -80° C reduction product, taken on a ~2mM sample at 7K with 20mW power and a 1G modulation amplitude, and (b) of the room temperature reduction product, taken on a ~2mM sample at 4K with 20mW power and 1G modulation amplitude. The low temperature spectrum is consistent with an S=1/2 species that originates from the antiferromagnetic coupling of an Fe^{III} (S=5/2) and an Fe^{II} (S=2) center. While it is unclear why the room temperature product is EPR silent, this is consistent with the formation of a new species upon warming the low-temperature product to room temperature, as observed by UV-Vis spectroscopy (see Figure 2.14).

dimers with bridging ligands, and this has been observed for several similar dinuclear model complexes,[20, 21] including $[Fe_2(BPMP)(OPr)_2]^{2+}$,[10, 22] and also for the mixed-valent form of *T. maritima* FDP. In contrast, the product generated at room temperature is EPR silent, as shown in Figure 2.15. This could be due to numerous factors. Notably, it has been reported that in some cases, similar mixed-valent diiron species are EPR silent under standard X-band EPR conditions.[23, 24] Alternatively, the low temperature species could originate from a diferrous complex containing a bridging phenoxy radical that then relaxes to the mixed-valent complex upon warming. In the same vein, the complex may exist as a mixed-valent, diiron monomer at low temperature and further oligomerize upon warming, for example, by the formation of a mixed-valent, tetrairon dimer at room temperature, which would then be EPR silent. Lastly, the low-temperature product could also undergo a redox disproportionation at room temperature to generate a diferrous and diferric species, both of which would be EPR silent

The first of these hypotheses that was tested is whether the bridging phenol could act as a non-innocent ligand and form a phenoxy radical at low temperatures. In order to probe whether the phenol could be oxidized in place of Fe, the structurally analogous complex $[Zn_2(BPMP)(OPr)_2](OTf)$ (**5a**), containing non-redox active Zn^{2+} centers, was synthesized and structurally characterized via X-Ray Crystallography (Figure 2.16). Initial crystallographic data of **5a** contained substantial disorder in the terminal carbon atom of the bridging propionate ligands. As such, the corresponding acetate bridged analog $[Zn_2(BPMP)(OPr)_2](OTf)$ (**5b**) was also synthesized solely for crystallization purposes, showing a Zn−Zn distance of 3.384 Å, similar to the 3.360 Å Fe−Fe distance in the diferrous complex **4**. Cyclic voltammetry measurements of **5a** reveal two semi-reversible waves at 0.625 and 0.850 V vs. Fc^+/Fc (Figure 2.16), both of which are significantly more positive (by 0.4 and 0.6 V, respectively) than the $Fe^{II}Fe^{II}/Fe^{II}Fe^{III}$ couple in **1** (0.260 V). Hence, formation of a bridging phenoxy radical is improbable and a mixed-valent type species is the expected product.

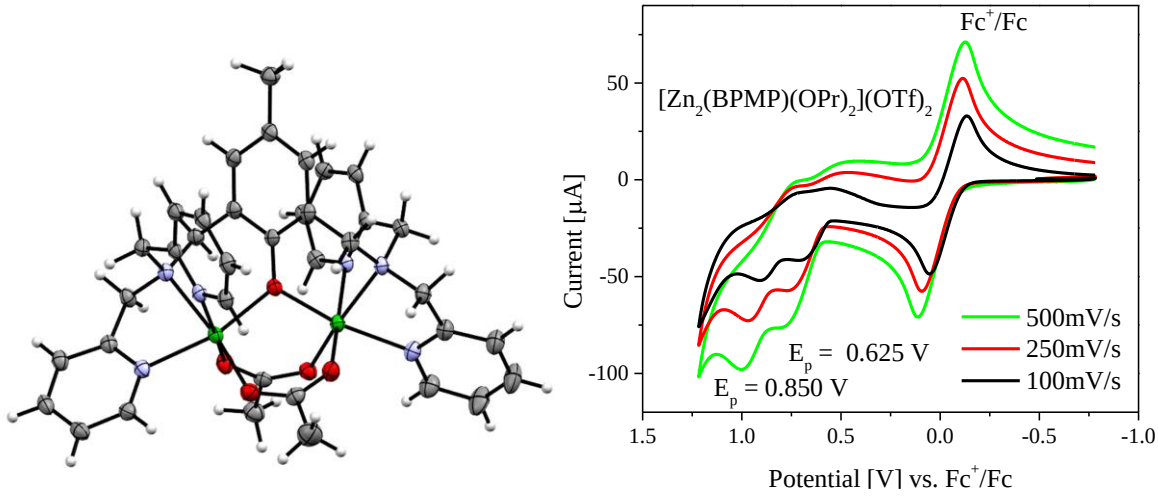

Figure 2.16 Left: The crystal structure of **5b**, obtained by vapor diffusion of diethyl ether into a solution of **5b** in methanol at -30 °C. Right: The cyclic voltammogram of ~5mM **5a** in CH_2Cl_2 with ~0.1M tetrabutylammonium triflate added as an electrolyte shows two semi-reversible waves at 0.625V and 0.850V attributed to the BPMP phenolate oxidation. The measurement was conducted using a glassy carbon working electrode, a platinum counter electrode, and an Ag wire pseudoreference electrode. Potentials are referenced to an internal Fc^+/Fc standard.

The room temperature reaction product was then structurally and spectroscopically characterized. Crystals were obtained by layering hexanes onto a solution of the room temperature product in tetrahydrofuran. Interestingly, X-ray crystallographic analysis of the crystals obtained in this way over four days identified them as the diferrous bis-propionate bridged complex $[Fe_2(BPMP)(OPr)_2](OTf)$ (**4**) (Figure 2.17). This suggests that the mixed-valent product undergoes a redox disproportionation into the differrous product **4** and an unidentified ferric species. However, the question remains whether the low-temperature mixed-valent product directly undergoes redox disproportionation to form this species or if there is a distinct room temperature precursor [**X**] that decays over the course of 4 days to generate **4**. To determine this, **4** was synthesized independently and was characterized in tandem with the room temperature reaction product [**X**]. Cyclic voltammograms taken of the RT reduction product [**X**] immediately after its formation show three different reversible waves; two small signals with $E_{1/2}$ at 0.683 V and -0.030 V, and one large signal at -0.983 V (all vs. Fc^+/Fc, Figure 2.18). The couples at 0.683 V and -0.030 V belong to the diferrous bis-propionate complex **4**, as evident from the literature,[10,22]

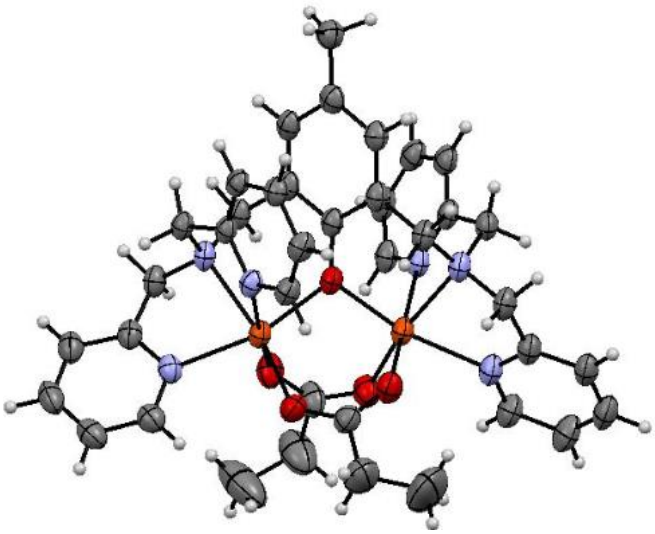

Figure 2.17 Crystal structure of **4**, obtained by layering the room temperature reaction product in tetrahydrofuran solution with hexanes. This leads to the formation of the diferrous bis-propionate complex **4**.

and further confirmed by the CV of our independently synthesized complex **4** (see Figure 2.18). The main signal in the CV at -0.983 V vs. Fc^+/Fc must then belong to the initially formed room temperature product. It is important to note that this potential is lower than that of $CoCp_2$ and explains our results in section 2.2 showing that two equivalents of $CoCp_2$ are in fact consumed, despite the fact that only one equivalent of $CoCp_2$ is necessary for N-N coupling and N_2O formation. The presence of only small amounts of **4** in the initial CV in Figure 2.18 further indicates that the disproportionation of [**X**] is slow. This is further evidenced by the M*össbauer* spectrum of [**X**], which contains a 49.6% ferric species with an isomer shift of 0.66 mm/s and quadrupole splitting of 1.34 mm/s, and 50.4% ferrous species with an isomer shift of 1.13 mm/s and quadrupole splitting of 2.93 mm/s (Figure 2.19)**.** Importantly, the ferrous signal is unique from that of our independently synthesized **4**, so we attribute this M*össbauer* spectrum to [**X**] prior to disproportionation. A summary of all Mössbauer parameters presented in this chapter is listed in Table 2.2.

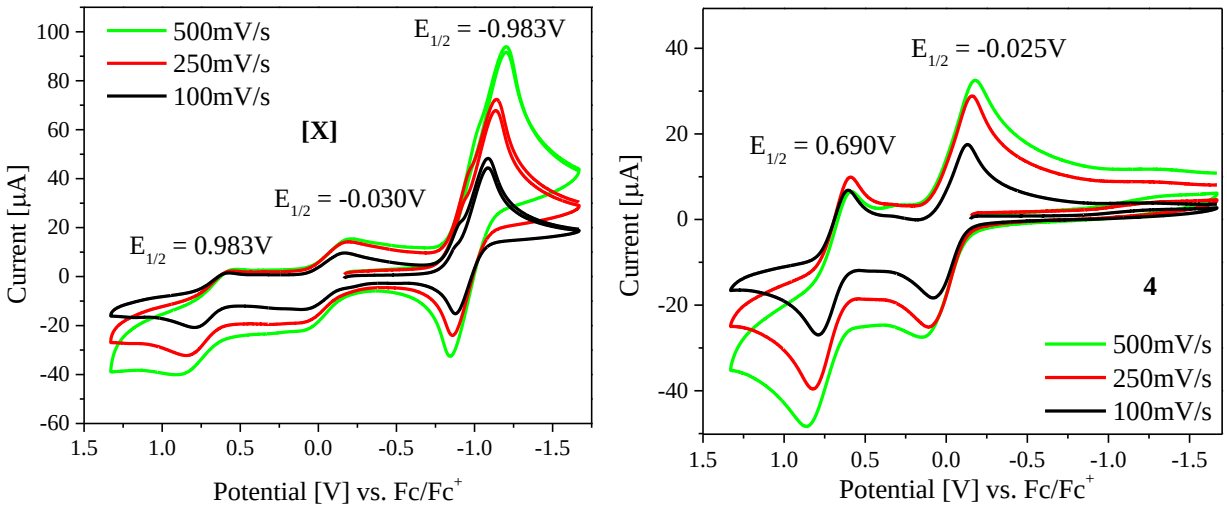

Figure 2.18 Left: The cyclic voltammogram of a ~5 mM solution of the room temperature reaction product [**X**] in CH_2Cl_2 shows a main, reversible redox feature at -0.983V. The two other reversible signals at -0.030V and 0.683V correspond to the diferrous bis-propionate complex, **4**, which forms via a slow disproportionation process. Right: **4** was independently synthesized and its cyclic voltammogram measured, showing consistent $Fe^{III}Fe^{II}/Fe^{II}Fe^{II}$ and $Fe^{III}Fe^{III}/Fe^{III}Fe^{II}$ redox couples. All potentials are referenced to a Fc^+/Fc standard.

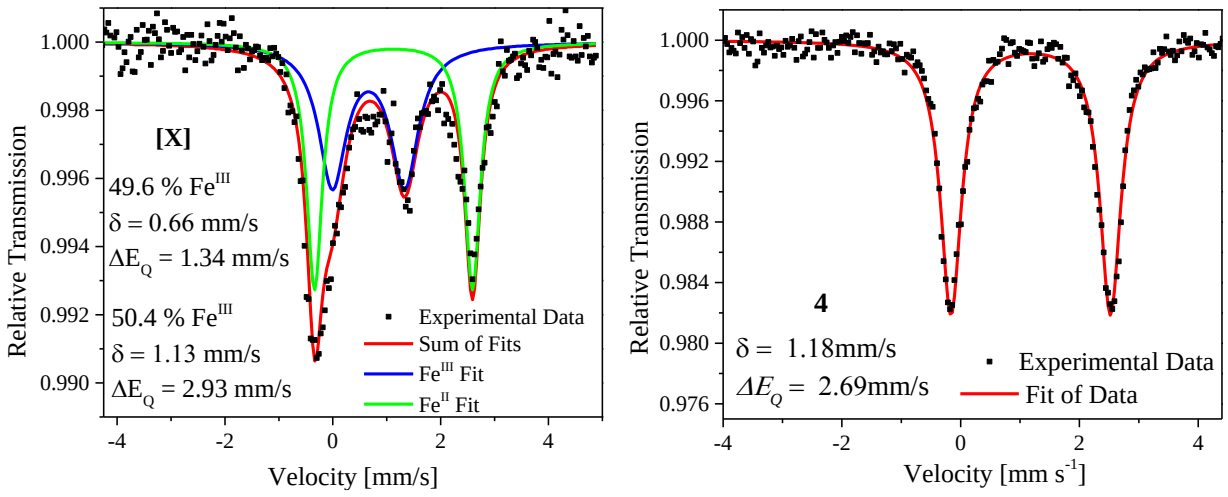

Figure 2.19 Left: The Mössbauer spectrum of the room-temperature reduction product [**X**] taken on a powder sample at 80 K contains a 1:1 integration of Fe^{II} and Fe^{III} species. *Right: The M*össbauer spectrum of **4** taken on a powder sample at 80 K contains distinct Fe^{II} *M*össbauer parameters compared to [**X**].

Table 2.2 Comparison of all Mössbauer parameters presented in this chapter.

Complex	δ (mm/s)	ΔE_q (mm/s)	Integration (%)
1	1.19	2.89	100
2a	0.70	1.72	100
4	1.18	2.69	100
[X]	0.66 1.13	1.34 2.93	49.6 50.4

With these combined results in hand, a reaction scheme for the semireduction of **2a** is shown in Scheme 2.2. Complex **2a** can be reduced at -80° C and at RT with one equivalent of $CoCp_2$, leading to intramolecular N-N coupling of the NO units to generate a quantitative yield of N_2O. At -80° C, a mixed-valent species is formed as shown by EPR spectroscopy. Based on the stoichiometry of the reaction, we propose that this is the mixed-valent oxo-bridged dimer. This species then rearranges upon warming of the reaction mixture to RT, forming an EPR silent species [**X**]. Given that the species trapped at -80° C is formed after N_2O release, and that the mixed-valent diiron core cannot oxidize the ligand, we suspect that this may be due to the formation of a tetramer or oligomer when warming the reaction mixture from low to room temperature. This would then

template the complex to undergo a slow redox and ligand disproportionation to form **4**, and is further supported by data collected on Dr. Majumdar's related $[Fe_2(N\text{-Et-HPTB})(NO)_2(DMF)_2](BF_4)_3$ complex, which is discussed in detail in Chapter 3. Furthermore, we have demonstrated via cyclic voltammetry and UV-Vis titrations that [**X**] can draw an additional electron to form a diferrous species, consistent with our initial communication.

Scheme 2.2 Reaction scheme summarizing the key findings presented in this chapter, including a proposed tetrairon structure for [X].

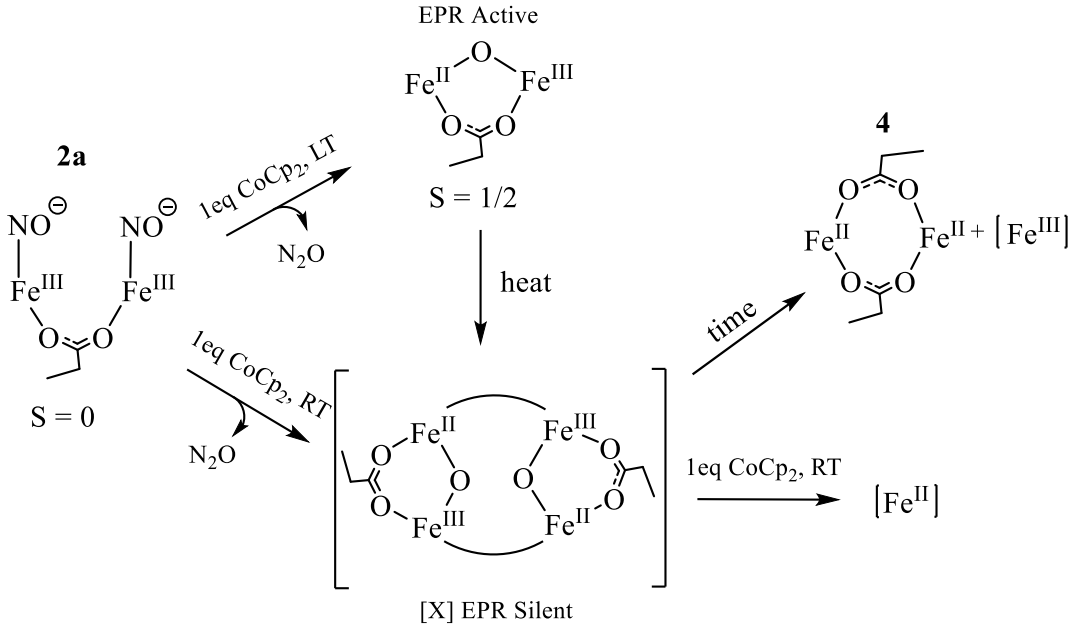

2.4 Experimental Section

General Considerations

Air sensitive materials were prepared under a dinitrogen atmosphere in either an MBraun glovebox, or using standard Schlenk techniques. Unless specified otherwise, low temperature experiments were conducted in an Inert Technologies glovebox modified with a cold well. All solvents were dried using standard techniques, freeze-pump-thawed to remove dioxygen, and stored over molecular sieves. All reagents were purchased from commercial sources and were used as received, unless noted below. $Fe(OTf)_2$ was recrystallized from ~10 mL of acetonitrile

with ~70 mL of diethyl ether and dried under high vacuum to give $[Fe(OTf)_2](CH_3CN)_2$.[25] Cobaltocene ($CoCp_2$) was sublimed under static vacuum and stored at -35° C in the glovebox freezer. Nitric oxide was passed over an Ascarite II column and subsequently through a -80° C cold trap to remove higher N_xO_y impurities. Nitric oxide-$^{15}N^{18}O$ and ^{15}NO were used without any further purification.

Synthesis of BPMP Complexes

$[Fe(BF_4)_2]\cdot 2.5(CH_3CN)$. Under an inert atmosphere, 103 mg (1.8 mmol) of Fe powder and 399 mg (3.4 mmol) of $NOBF_4$ were combined in a Schlenk flask and dissolved in 12 mL of acetonitrile. The reaction mixture was then stirred on the Schlenk line under static vacuum, while periodically refilling and evacuating the headspace with argon, always leaving the flask under a static vacuum. After 6 hours, the solvent was removed under high vacuum and the flask was brought into the glovebox. The precipitate was then re-dissolved in 5 mL of acetonitrile and filtered through a 0.2 μm PTFE syringe filter to remove excess iron powder. The filtrate was precipitated with 50 mL of diethylether and stored at -35° C overnight. The product was then filtered off, yielding an off-white precipitate, which was dried under high vacuum overnight. Yield: 480 mg (1.4 mmol, 85%) of the dried product was collected as a white powder. Characterization: Elemental anal. Calcd for $C_{5/2}H_{7/2}B_2F_8FeN_{5/2}$: C, 17.93; H, 2.26; N, 10.46; found (%): C, 18.16; H, 2.59; N, 10.40. IR (KBr) $\nu(CH_3CN)$ 2317, 2289 cm^{-1}.

2,6-bis[[bis(2-pyridylmethyl)amino]methyl]-4-methylphenol (H[BPMP]). H[BPMP] was generated via a modified literature procedure.[10, 26] In a dry 3-neck flask under a dinitrogen atmosphere, equipped with a dropping funnel and a condenser, 1mL (5.6 mmol) of di-2-picolylamine and 1 mL (7.17 mmol) of triethylamine were combined in 12 mL anhydrous tetrahydrofuran. 608 mg (2.9 mmol) of 2,6-bis(chloromethyl)-4-methylphenol were dissolved in

12 mL anhydrous tetrahydrofuran, loaded in the dropping funnel, and added slowly to the 0° C chilled reaction mixture. The reaction was then heated to reflux for 5 hrs before cooling the solution back to RT and filtering off the triethylammonium chloride. The filtrate was concentrated under reduced pressure to a yellow oil, which was then taken up in minimal dichloromethane and precipitated with hexanes. The resulting cloudy solution was immediately filtered through a celite plug and the filtrate was allowed to precipitate at -35° C overnight. The product was filtered off, giving 1.06 g (2.0mmol, 74 % yield) of a pale-yellow powder which was used without further purification. Characterization: ^{1}H NMR (400 MHz, Chloroform-*d*) δ 10.75 (s, 1H), 8.50 (dd, 4H), 7.58 (td, 4H), 7.47 (d, 4H), 7.10 (t, 4H), 6.98 (s, 2H), 3.85 (s, 8H), 3.76 (s, 4H), 2.22 (s, 3H).

[Fe$_2$(BPMP)(OPr)](OTf)$_2$ (1). Under an inert atmosphere, 235 mg (0.45 mmol) of H[BPMP] and 35 mg (0.50 mmol) of KOMe were combined in a Schlenk flask and dissolved in 3 mL of MeOH. 370 mg (0.88 mmol) of [Fe(OTf)$_2$](CH$_3$CN)$_2$ dissolved in 1 mL of MeOH were added and the solution was stirred for 5 min before slowly adding 43 mg (0.45 mmol) NaOPr dissolved in 1 mL of methanol, giving a yellow-orange solution. The solution was stirred for 1hr before precipitating it overnight at -35° C with 70 mL of diethylether. The resulting yellow precipitate was filtered through a frit and washed with dichloromethane until only the white KOTf/NaOTf salt remained on the frit. The filtrate was then precipitated with 30 mL of hexanes, and the yellow powder was separated with a frit, giving 392 mg (0.39 mmol, 88% yield) of the final product. Characterization: Elemental anal. calcd for $C_{38}H_{38}F_6Fe_2N_6O_9S_2$: C, 45.08; H, 3.78; N, 8.30; found (%): C, 44.83; H, 3.78; N, 8.23. M*ö*ssbauer (80K, powder) δ = 1.19 mm/s, ΔE_Q = 2.89 mm/s. UV-Vis (CH_2Cl_2) 400 nm.

[Fe$_2$(BPMP)(OPr)(NO)$_2$](OTf)$_2$ (2a). Under an inert atmosphere, 335 mg (0.331 mmol) of (**1**) was dissolved in 3 mL CH_2Cl_2, and the solution was stirred in a Schlenk flask under a headspace

of NO gas for 15 min. 24 mL of hexanes were syringed in to precipitate the product, and the flask was stored at -35° C overnight. The solution was filtered through a frit, making sure to stop the vacuum while there was still a small layer of solvent remaining to prevent NO loss. 291 mg (0.271 mmol, 82% yield) of the product, as a brown powder, were collected after the residual solvent had evaporated. Characterization: IR (KBr) ν(NO) 1768 cm^{-1}. M*ö*ssbauer (80K, powder) δ = 0.70 mm/s, ΔE_Q = 1.72 mm/s. UV-Vis (CH_2Cl_2) 400 nm.

[Fe$_2$(BPMP)(OPr)((^{15}NO)$_2$](OTf)$_2$ (2b). A 50 mL Schlenk flask was equipped with a T-joint and connected to the NO tank and the Schlenk line, with an additional T-joint with a 3-way stopcock in-between the Schlenk flask and the Schlenk line leading to a balloon to monitor the pressure of the system. The balloon was purged in 30 quick cycles of evacuation and refilling with Ar, and was then held under a positive pressure while the Schlenk flask was purged five times with 30 minute evacuation cycles. The balloon was then evacuated and the three way stopcock was turned to be open to the balloon and the NO tank. At this point, **1** dissolved in minimal CH_2Cl_2 was syringed into the Schlenk flask and the NO tank was opened until the balloon was under a positive pressure. The flask was briefly manually shaken under ^{15}NO pressure and then taken into the glovebox to stir for an additional hour before precipitating the product with ~20 mL of hexanes at -35° C overnight. The reaction mixture was filtered through a frit, taking care to stop the vacuum while there was still a small layer of solvent above the precipitate. Characterization: IR (KBr) ν(NO) 1734 cm^{-1}.

[Fe$_2$(BPMP)(OPr)((^{15}N^{18}O)$_2$](OTf)$_2$ (2c). The same procedure was followed as for **2b**. Characterization: IR (KBr) ν(NO) 1695 cm^{-1}.

[Fe$_2$(BPMP)(OPr)(NO)$_2$](BF$_4$)$_2$ (3). Under an inert atmosphere, 84.5 mg (0.16 mmol) of H[BPMP] and 12.7 mg (0.18 mmol) of KOMe were combined in 2 mL of MeOH. 110.0 mg (0.31

mmol) of $[Fe(BF_4)_2]\cdot 2.5(CH_3CN)$ dissolved in 1 mL of methanol were then added to the solution, followed by the slow addition of 16.6 mg (0.17 mmol) NaOPr in 1 mL of MeOH, yielding a yellow-orange solution. This solution was then stirred under a headspace of NO gas for 15 min before precipitating the crude product with 24 mL of diethyl ether at -35° C overnight. The resulting brown powder was filtered off with a frit and the precipitate was washed with CH_2Cl_2, being careful to apply minimal vacuum to avoid NO loss. The filtrate was precipitated with hexanes at -35° C overnight. The powder was again filtered off with a frit, yielding 71.0 mg (0.02 mmol, 46.8% yield) of the final product. Characterization: IR (ATR) ν(NO) 1760 cm^{-1}.

$[Fe_2(BPMP)(OPr)_2](OTf)$ (4). Under an inert atmosphere, 233 mg (0.45 mmol) of H[BPMP] and 40.1 mg (0.57 mmol) of KOMe were combined in a Schlenk flask and dissolved in 3 mL of MeOH. 375 mg (0.89 mmol) of $[Fe(OTf)_2](CH_3CN)_2$ dissolved in 1 mL of MeOH were added and the solution was stirred for 5 min before slowly adding 89.1 mg (0.93 mmol) NaOPr dissolved in 1 mL of MeOH, giving an orange solution. The solution was stirred for 1 hr before precipitating it overnight at -35° C with 70 mL of diethyl ether. The resulting solution was filtered through a frit and the precipitate was washed with dichloromethane until only the white KOTf/NaOTf salt remained. The filtrate was then precipitated with 30 mL of hexanes, and the resulting orange powder was filtered off, giving 248 mg (0.26 mmol, 59% yield) of product. Characterization: Elemental anal. calcd for $C_{40}H_{44}F_3Fe_2N_6O_8S$: C, 51.24; H, 4.73; N, 8.96; found (%): C, 51.01; H, 4.71; N, 9.10. Mössbauer (80 K, powder) δ = 1.18 mm/s, ΔE_Q = 2.69 mm/s. UV-Vis (λ_{max}) 444 nm. ^{1}H NMR (400 MHz, Acetonitrile-d_3, broad singlets) δ 185.10, 176.19, 142.00, 79.95, 73.56, 62.59, 46.78, 42.33, 41.46, 35.91, 31.61, 27.13, 24.42, 12.85, 11.70, 10.80, 5.45, 3.42, 2.14, 1.95, 1.29, 1.14, 0.89.

[Zn_2(BPMP)$(OPr)_2$]$(OTf)(CH_2Cl_2)$ (5a). This complex was synthesized in an analogous manner as **4** from $Zn(OTf)_2$. Characterization: Elemental anal. calcd for $C_{41}H_{47}Cl_2F_3N_6O_8SZn_2$: C, 47.23; H, 4.54; N, 8.06; found (%): C, 47.45; H, 4.06; N, 8.36. ^{1}H NMR (400 MHz, Acetonitrile-*d3*, broad singlets) δ 8.80, 8.56, 8.23, 7.94, 7.50, 7.44, 7.31, 7.02, 6.66, 6.47, 6.42, 5.45, 4.51, 4.03, 3.91, 3.49, 3.42, 3.21, 2.28, 2.02, 1.29, 0.95, 0.89.

[Zn_2(BPMP)$(OAc)_2$](OTf) (5b). Due to disorder in the terminal propionate carbon atoms of **5a**, its crystal structure could not be completely refined. The acetate analog **5b** was made as described for **5a** using NaOAc in place of NaOPr. Crystals suitable for X-ray diffraction were obtained by vapor diffusiong of diethyl ether into a -30 ºC solution of **5b** dissolved in MeOH.

Preparation of ^{57}Fe Samples (2d, 2e): ^{57}Fe-labelled complexes of **1** and **2a** were synthesized in the same manner as the unlabeled complexes from $^{57}Fe(OTf)_2$, generated *in situ* from the metathesis of $^{57}FeCl_2$ with Ag(OTf) as previously described.[11]

Physical Measurements

UV-Vis/Immersion Probe: Spectra were taken using an Analytik Jena Specord S-600 UV-Vis spectrometer. Dip probe experiments used the same spectrometer, with a Helma low-temperature immersion probe.

IR (ATR/KBr/Gas): Spectra of solids were taken on PerkinElmer BX and GX, and on a Bruker Alpha-E FTIR spectrometer. Solution samples were measured in a thin-layer solution cell equipped with CaF_2 windows. Gas samples were measured using a Pike HT gas cell (10 cm) with CaF_2 windows on the same instruments.

^{1}H NMR: Measurements were conducted on a Varian MR 400 instrument at room temperature and were referenced against tetramethylsilane.

Cyclic Voltammetry*:* Cyclic voltammograms were obtained on a CH Instruments CHI600E electrochemical workstation with a glassy-carbon working electrode, platinum counter electrode, and silver wire psuedoreference electrode. All potentials were referenced to a ferrocene standard, taken before each experiment under the same experimental conditions. Data were collected on ~5 mM samples in CH_2Cl_2 with 0.1 M tetrabutylammonium triflate as the supporting electrolyte.

IR Spectroelectrochemistry*:* IR spectroelectrochemical experiments were conducted in a LabOmak UF-SEC thin layer cell, with Pt mesh working and counter electrodes, and an Ag wire pseudoreference electrode.

EPR*:* X-Band electron paramagnetic resonance spectra were obtained on a Bruker X-band EMX spectrometer equipped with an Oxford Instruments liquid helium cryostat. Spectra were recorded on ~2 mM frozen solutions using 20 mW microwave power and 100 kHz field modulation at a 1 G amplitude.

NRVS: Nuclear resonance vibrational spectroscopy (NRVS) data were obtained as described previously.[27] Spectra were taken at beamline 3ID at the Advanced Photon Source (APS) at Argonne National Laboratory. Powder samples were loaded into copper sample cells with a 4x7x1 mm sample compartment. Spectra were taken from 0 to 80 or to 120 meV (depending on the compound) in 0.25 meV steps, and represent the sum of 6 to 12 scans.

X-Ray Crystallography: Orange blocks of **4** were grown from layering a solution of the room temperature reduction product in tetrahydrofuran with hexanes at 22° C. A crystal of dimensions 0.20 x 0.04 x 0.03 mm was mounted on a Rigaku AFC10K Saturn 944+ CCD-based X-ray diffractometer equipped with a low temperature device and Micromax-007HF Cu-target micro-focus rotating anode (λ = 1.54187 Å) operated at 1.2 kW power (40 kV, 30 mA). The X-ray intensities were measured at 85(1) K with the detector placed at a distance of 42.00 mm from the

crystal. A total of 2028 images were collected with an oscillation width of 1.0° in ω. The exposure times were 1 sec. for the low angle images, 5 sec. for high angle. Rigaku d*trek images were exported to CrysAlisPro for processing and corrected for absorption. The integration of the data yielded a total of 36133 reflections to a maximum 2θ value of 138.70° of which 8598 were independent and 8072 were greater than 2σ(I). The final cell constants were based on the xyz centroids of 16330 reflections above 10σ(I). Analysis of the data showed negligible decay during data collection. The structure was solved and refined with the Bruker SHELXTL (version 2016/6) software package, using the space group P1bar with Z = 2 for the formula $C_{41}H_{51}N_6O_9F_3SFe$. All non-hydrogen atoms were refined anisotropically with the hydrogen atoms placed in idealized positions. Full matrix least-squares refinement based on F^2 converged at R1 = 0.0522 and wR2 = 0.1458 [based on I > 2sigma(I)], R1 = 0.0544 and wR2 = 0.1494 for all data. The SQUEEZE subroutine of the PLATON program suite was used to address a disordered THF solvate molecule present in the structure. Additional details are presented in the Supporting Information. Note that the crystal structure was deposited with the CCDC, deposition no. 1572848.

Yellow needles of **5b** were grown from a methanol/diethyl ether solution of the compound at -30 deg. C. A crystal of dimensions 0.15 x 0.02 x 0.02 mm was mounted as described above. The integration of the data yielded a total of 31369 reflections to a maximum 2θ value of 139.21° of which 7555 were independent and 7142 were greater than 2σ(I). The final cell constants were based on the xyz centroids 17240 reflections above 10σ(I). Analysis of the data showed negligible decay during data collection; the data were processed with CrystalClear 2.0 and corrected for absorption. The structure was solved and refined with the Bruker SHELXTL (version 2014/6) software package, using the space group P1bar with Z = 2 for the formula $C_{38}H_{39}N_6O_8F_3SZn_2$ + [solvent]. All non-hydrogen atoms were refined anisotropically with the hydrogen atoms placed

in idealized positions. Full matrix least-squares refinement based on F^2 converged at R1 = 0.0363 and wR2 = 0.0959 [based on I > 2sigma(I)], R1 = 0.0380 and wR2 = 0.0985 for all data. The SQUEEZE subroutine of the PLATON program suite was used to address the disordered solvent present in the structure. Note that the crystal structure was deposited with the CCDC, deposition no. 1816883.

Stopped-Flow IR*:* Stopped flow IR measurements were conducted at room temperature with a VERTEX 70 FTIR spectrometer with a liquid nitrogen cooled MCT detector at a $4cm^{-1}$ resolution with OPUS software in Rapid Scan mode. 5-10mM sample solutions were prepared in the glovebox and loaded into luer-lock plastic syringes. The syringes were connected to a TgK Scientific SF-16 syringe drive operated by KinetaDrive software, which was used to mix the solutions in a 100μm pathlength cell. The tubing was initially washed with degassed CH_2Cl_2, which was also used as a solvent blank before loading solutions of (**2a**) and/or $CoCp_2$.

Mössbauer Spectroscopy*:* Mössbauer spectra were recorded using an alternating constant *WissEl* Mössbauer spectrometer, consisting of an MR 360 Drive Unit, an MV-1000 velocity transducer, and an LND 45431 proportional counter mounted on an LINOS precision bench. The system was operated in a horizontal transmission geometry with source, absorber, and detector in a linear arrangement. The temperature was controlled and maintained using a Janis SHI closed-cycle helium cryostat. Data acquisition was performed using a 512 channel analyzer. Isomer shifts were referenced to α-iron metal foil at ambient temperatures. Simulation of experimental data was performed using the *Mfit* program.[28]

SQUID: Magnetic susceptibility measurements were conducted on a Quantum-Design MPMS XL-5 SQUID magnetometer, equipped with a 5 T magnet. Powder samples were loaded into a gelatin capsule, fixed in place using a polyfluorinated oil, and placed in a plastic straw sample

holder. The raw data were corrected for the diamagnetic contribution of the gelatin capsule as well as the diamagnetic contribution of the complex using Pascal constants. The data were fit using the *julX* program.[29]

Elemental Analysis: Elemental analyses were conducted by Atlantic Microlabs (Norcross, GA).

Chemical Reduction/N_2O tests: N_2O tests were performed as previously described.[13] Briefly, ~5 μmol of (**2a**) were dissolved in 2 mL of CH_2Cl_2 in a 25 mL round bottom flask with a septa. 1eq of $CoCp_2$ dissolved in 0.5 mL of CH_2Cl_2 was added and the reaction mixture was then stirred for various times before transferring the gas headspace into the evacuated gas-IR cell for exactly 20 s via a cannula. The N_2O band was integrated from 2150 to 2275 cm^{-1} after the subtraction of a CH_2Cl_2 blank taken under the exact same conditions, and the integration was compared to a standard curve.[2]

2.5 References and Notes

(1) This chapter is adapted from reference 2.

(2) White, C. J., Speelman, A. L., Kupper, C., Demeshko, S., Meyer, F., Shanahan, J. P., Alp, E. E., Hu, M., Zhao, J.;Lehnert, N. The Semireduced Mechanism for Nitric Oxide Reduction by Non-Heme Diiron Complexes: Modeling Flavodiiron Nitric Oxide Reductases. *J. Am. Chem. Soc.* **2018**, *140*, 2562-2574.

(3) Borovik, A. S., Hendrich, M. P., Holman, T. R., Munck, E., Papaefthymiou, V.;Que, L. Models for diferrous forms of iron-oxo proteins. Structure and properties of [Fe2BPMP(O2CR)2]BPh4 complexes. *J. Am. Chem. Soc.* **1990**, *112*, 6031-6038.

(4) Berto, T. C., Speelman, A. L., Zheng, S.;Lehnert, N. Mono- and dinuclear non-heme iron–nitrosyl complexes: Models for key intermediates in bacterial nitric oxide reductases. *Coord. Chem. Rev.* **2013**, *257*, 244-259.

(5) Jackson, T. A., Yikilmaz, E., Miller, A.-F.;Brunold, T. C. Spectroscopic and Computational Study of a Non-Heme Iron {Fe−NO}7 System: Exploring the Geometric and Electronic Structures of the Nitrosyl Adduct of Iron Superoxide Dismutase. *J. Am. Chem. Soc.* **2003**, *125*, 8348-8363.

(6) Brown, C. A., Pavlosky, M. A., Westre, T. E., Zhang, Y., Hedman, B., Hodgson, K. O.;Solomon, E. I. Spectroscopic and Theoretical Description of the Electronic Structure of S = 3/2 Iron-Nitrosyl Complexes and Their Relation to O2 Activation by Non-Heme Iron Enzyme Active Sites. *J. Am. Chem. Soc.* **1995**, *117*, 715-732.

(7) Feig, A. L., Bautista, M. T.;Lippard, S. J. A Carboxylate-Bridged Non-Heme Diiron Dinitrosyl Complex. *Inorg. Chem.* **1996**, *35*, 6892-6898.

(8) Caranto, J. D., Weitz, A., Hendrich, M. P.;Kurtz, D. M. The Nitric Oxide Reductase Mechanism of a Flavo-Diiron Protein: Identification of Active-Site Intermediates and Products. *J. Am. Chem. Soc.* **2014**, *136*, 7981-7992.

(9) Kindermann, N., Schober, A., Demeshko, S., Lehnert, N.;Meyer, F. Reductive Transformations of a Pyrazolate-Based Bioinspired Diiron–Dinitrosyl Complex. *Inorg. Chem.* **2016**, *55*, 11538-11550.

(10) Borovik, A. S., Papaefthymiou, V., Taylor, L. F., Anderson, O. P.;Que, L., Jr. Models for iron-oxo proteins. Structures and properties of $Fe^{II}Fe^{III}$, $Zn^{II}Fe^{III}$, and $Fe^{II}Ga^{III}$ complexes with (μ-phenoxo)bis(μ-carboxylato)dimetal cores. *J. Am. Chem. Soc.* **1989**, *111*, 6183-6195.

(11) Berto, T. C., Hoffman, M. B., Murata, Y., Landenberger, K. B., Alp, E. E., Zhao, J.;Lehnert, N. Structural and Electronic Characterization of Non-Heme Fe(II)–Nitrosyls as Biomimetic Models of the FeB Center of Bacterial Nitric Oxide Reductase. *J. Am. Chem. Soc.* **2011**, *133*, 16714-16717.

(12) Speelman, A. L., Zhang, B., Krebs, C.;Lehnert, N. Structural and Spectroscopic Characterization of a High-Spin {FeNO}6 Complex with an Iron(IV)−NO− Electronic Structure. *Angew. Chem. Int. Ed.* **2016**, *55*, 6685-6688.

(13) Zheng, S., Berto, T. C., Dahl, E. W., Hoffman, M. B., Speelman, A. L.;Lehnert, N. The Functional Model Complex [Fe2(BPMP)(OPr)(NO)2](BPh4)2 Provides Insight into the Mechanism of Flavodiiron NO Reductases. *J. Am. Chem. Soc.* **2013**, *135*, 4902-4905.

(14) Haskin, C. J., Ravi, N., Lynch, J. B., Muenck, E.;Que, L., Jr. Reaction of NO with the Reduced R2 Protein of Ribonucleotide Reductase from *Escherichia coli*. *Biochemistry* **1995**, *34*, 11090-11098.

(15) Lu, S., Libby, E., Saleh, L., Xing, G., Bollinger, J. M.;Moënne-Loccoz, P. Characterization of NO adducts of the diiron center in protein R2 of Escherichia coli ribonucleotide reductase and site-directed variants; implications for the O2 activation mechanism*. *J. Biol. Inorg. Chem.* **2004**, *9*, 818-827.

(16) Hayashi, T., Caranto, J. D., Wampler, D. A., Kurtz, D. M.;Moënne-Loccoz, P. Insights into the Nitric Oxide Reductase Mechanism of Flavodiiron Proteins from a Flavin-Free Enzyme. *Biochemistry* **2010**, *49*, 7040-7049.

(17) Hayashi, T., Caranto, J. D., Matsumura, H., Kurtz, D. M.;Moënne-Loccoz, P. Vibrational Analysis of Mononitrosyl Complexes in Hemerythrin and Flavodiiron Proteins: Relevance to Detoxifying NO Reductase. *J. Am. Chem. Soc.* **2012**, *134*, 6878-6884.

(18) Speelman, A. L.;Lehnert, N. Characterization of a High-Spin Non-Heme {FeNO}8 Complex: Implications for the Reactivity of Iron Nitroxyl Species in Biology. *Angew. Chem. Int. Ed.* **2013**, *52*, 12283-12287.

(19) Caranto, J. D., Weitz, A., Giri, N., Hendrich, M. P.;Kurtz, D. M. A Diferrous-Dinitrosyl Intermediate in the N2O-Generating Pathway of a Deflavinated Flavo-Diiron Protein. *Biochemistry* **2014**, *53*, 5631-5637.

(20) Payne, S. C.;Hagen, K. S. Steric Control of Reactivity of Non-Heme μ-Hydroxo Diiron(II) Complexes with Oxygen: Isolation of a Strongly Coupled μ-Oxo Fe(II)Fe(III) Dimer. *J. Am. Chem. Soc.* **2000**, *122*, 6399-6410.

(21) Majumdar, A., Apfel, U.-P., Jiang, Y., Moënne-Loccoz, P.;Lippard, S. J. Versatile Reactivity of a Solvent-Coordinated Diiron(II) Compound: Synthesis and Dioxygen Reactivity of a Mixed-Valent FeIIFeIII Species. *Inorg. Chem.* **2014**, *53*, 167-181.

(22) Masatatu, S., Akira, U., Hiroki, O., Kazutoyo, E., Makoto, Y., Sigeo, K.;Kazuo, S. Syntheses and Characterization of Dinuclear Iron(II, II) and Iron(II, III) Complexes with a Dinucleating Ligand, 2,6-Bis[bis(2-pyridylmethyl)aminomethyl]-4-methylphenolate (1—). *Bull. Chem. Soc. Jpn.* **1987**, *60*, 3547-3555.

(23) Borovik, A. S., Murch, B. P., Que, L., Papaefthymiou, V.;Munck, E. Models for iron-oxo proteins: a mixed valence iron(II)-iron(III) complex. *J. Am. Chem. Soc.* **1987**, *109*, 7190-7191.

(24) Borovik, A. S.;Que, L. Models for the iron(II)iron(III) and iron(II)iron(II) forms of iron-oxo proteins. *J. Am. Chem. Soc.* **1988**, *110*, 2345-2347.

(25) Hagen, K. S. Iron(II) Triflate Salts as Convenient Substitutes for Perchlorate Salts: Crystal Structures of [Fe(H2O)6](CF3SO3)2 and Fe(MeCN)4(CF3SO3)2. *Inorg. Chem.* **2000**, *39*, 5867-5869.

(26) Masatatsu, S., Hajime, K.;Ichiro, M. Synthesis and Properties of Binuclear Cobalt(II) Oxygen Adduct With 2,6-bis[bis(2-pyridylmethyl)aminoethyl)-4-methylphenol. *Chem. Lett.* **1981**, *10*, 1745-1748.

(27) J T Sage, C. P., G R A Wyllie, W Sturhahn, S M Durbin, P M Champion, E E Alp, W R Scheidt Nuclear resonance vibrational spectroscopy of a protein active-site mimic. *J. Phys.: Condens. Matter* **2001**, *13*, 7707-7722.

(28) Bill, E. Mfit. *Mfit*, *Max-Planck Institute for Chemical Energy Conversion*, Germany.

(29) Bill, E. julX. *julX*, *Max-Planck Institute for Chemical Energy Conversion*, Germany.

Chapter 3

Reduction of Mono- and Dinitrosyl Non-Heme {FeNO}^{7} Complexes: Additional Mechanistic Insights[1]

As discussed in Chapter 1, multiple routes toward N-N coupling in FNORs have been proposed, centered on the question of if and how the FMN redox cofactor participates in the N-N coupling reaction. Detailed stopped-flow UV-Vis and rapid freeze-quench Mössbauer and EPR studies on the *Tm* FDP by Kurtz and coworkers[2-4] have demonstrated that nitrosylation of the diferrous core occurs stepwise, resulting in an intermediate hs-Fe^{II}{FeNO}^{7} species that forms preceding the catalytically competent hs-[{FeNO}^{7}]$_2$ species, and second, that the N-N coupling can occur in the absence of the FMN cofactor, in support of the direct-reduction pathway.[5]

This chapter focuses on a detailed comparison between the hs-Fe^{II}{FeNO}^{7} and hs-[{FeNO}^{7}]$_2$ intermediates along the N-N coupling pathway of FNORs. One synthetic challenge in FNOR model chemistry that has precluded a direct comparison between a mono- and dinitrosyl complex of the same ligand scaffold is achieving the selective nitrosylation of a single iron center within otherwise symmetric (or pseudosymmetric) dinuclear complexes. While there are now numerous reported diiron dinitrosyl model complexes[6-9], only two diiron mononitrosyl complexes[10] had been reported preceding the work presented here.[8, 11] Lippard and coworkers have reported the complex [Fe$_2$(N-Et-HPTB)(NO)$_{0.6}$(DMF)$_{3.4}$](BF$_4$)$_3$,[10] which effectively contains a mixture of ~ 60 % hs-Fe^{II}{Fe(NO)}^{7} and ~ 40 % hs-Fe$^{II}_2$ complexes. No reductive reactivity was

reported for this species. Lippard and coworkers also reported a related hs-Fe^{III}{Fe(NO)}^{7} complex, $[Fe_2$(N-Et-HPTB)(NO)(OH)$(DMF)_2](BF_4)_3$,[10] that was inactive towards photoreduction of N_2O, though no chemical or electrochemical reduction studies were reported.

In this chapter, the selective synthesis of mono- and dinitrosyl complexes that utilize the same, symmetric N-Et-HPTB ligand system ($[Fe_2$(N-Et-HPTB)(NO)$(DMF)_3](BF_4)_3$ and $[Fe_2$(N-Et-HPTB)$(NO)_2(DMF)_2](BF_4)_3$, $\mathbf{1}^{3+}$ and $\mathbf{2}^{3+}$, respectively) is discussed and their reactivity landscape is directly compared via experimental and DFT methods.[8, 11] The data presented in this chapter represent the first direct comparison of a diiron mono- and dinitrosyl complex within the same ligand scaffold and expands on the list of model complexes that undergo facile super- and semireduction. This study also supplements Chapter 2 by providing a structural characterization and identification of the product of semireduction in this system (referred to as **[X]** in Chapter 2). The synthesis and structural characterization of these complexes was carried out by Nabhendu Pal and Manish Jana in the Majumdar laboratory at the Indian Association for the Cultivation of Science (Kolkata, India), while the Mössbauer and SQUID data were collected and fit by Drs. Claudia Kupper and Serhiy Demeshko in the Meyer laboratory at the Georg-August-Universität Göttingen, Institut für Anorganische Chemie, Germany. My contribution to this work is the characterization of these complexes via X-band EPR and IR-spectroelectrochemistry, the determination of gas-headspace N_2O yields, and DFT studies on the hs-{FeNO}$^{7/8}$ oxidation states of the mono- and dinitrosyl complexes ($\mathbf{1}^{3+/2+}$ and $\mathbf{2}^{3+/2+}$). These results are discussed within this chapter.

3.1 Selective Synthesis and Characterization of the hs-Fe^{II}{FeNO}^{7} and hs-[{FeNO}^{7}]$_2$ Complexes (Majumdar Laboratory)

Synthesis of hs-Fe^{II}{FeNO}^{7} and hs-[{FeNO}^{7}]$_2$

The selective asymmetric mono-nitrosylation of [Fe_2(N-Et-HPTB)(CH_3COS)](BF_4)$_2$ was carried out by Majumdar and coworkers, and is achieved using a redox-controlled synthetic approach. Here, the thioacetate bound diiron precursor complex, [Fe_2(N-Et-HPTB)(CH_3COS)](BF_4)$_2$, is stirred in the presence of the nitrosonium donor (NO)(BF_4).[11] The NO^+ released by (NO)(BF_4) can oxidize the thioacetate to the thiyl radical via S-nitrosylation of thioacetate, followed by homolytic cleavage of the S-NO bond, resulting in the controlled release of $NO^{\bullet}$ near the S-bound Fe while the O-atom of $CH_3COS^{\bullet}$ still remains bound at the other Fe-center, thereby promoting asymmetric and selective ligation of NO at a single Fe atom. Two equivalents of $CH_3COS^{\bullet}$ can then undergo radical coupling to generate the corresponding disulfide, which is displaced by DMF in the final mononitrosyl complex [Fe_2(N-Et-HPTB)(NO)($DMF)_3$](BF_4)$_3$ (**1**$^{3+}$) (Scheme 3.1).[11] In contrast, the corresponding dinitrosyl

Scheme 3.1 Synthetic scheme for the selective mono-nitrosylation of [Fe_2(N-Et-HPTB)(CH_3COS)](BF_4)$_2$ to make [Fe_2(N-Et-HPTB)(NO)($DMF)_3$](BF_4)$_3$. Structures represented in brackets highlight possible reactive species that could lead to selective mono-nitrosylation. The synthesis below was designed by Majumdar and coworkers.

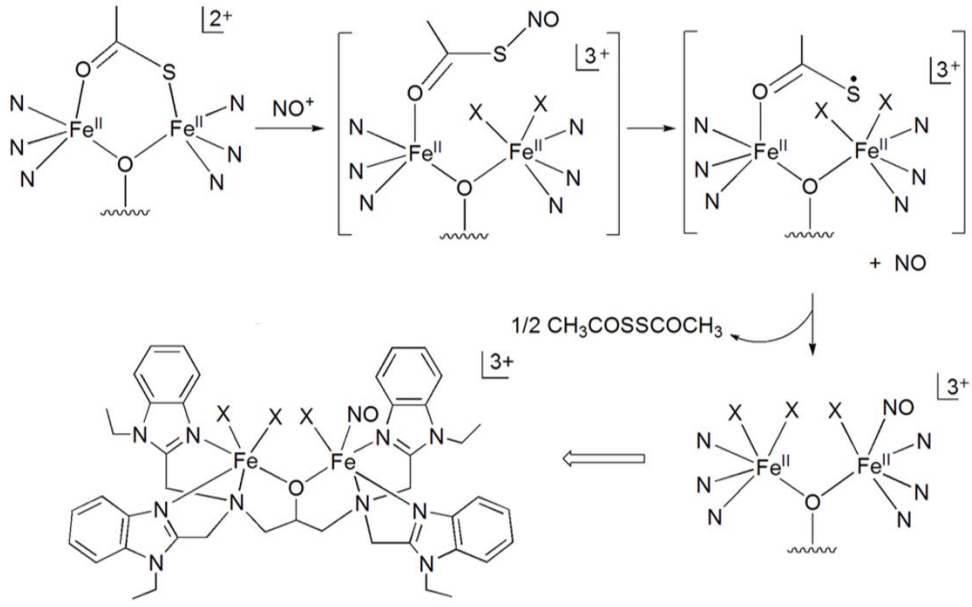

complex can be generated in a more classic manner by stirring the diferrous precursor complex without a bridging thioacetate, $[Fe_2(N\text{-}Et\text{-}HPTB)(DMF)_4](BF_4)_3$,[12] with excess NO either as NO(g), or via the NO-donor tritylnitrosothiol[13, 14] (Ph_3CSNO) to afford an analytically pure $[Fe_2(N\text{-}Et\text{-}HPTB)(NO)_2(DMF)_2](BF_4)_3$ (**2**$^{3+}$) dinitrosyl complex.

Characterization of hs-Fe^{II}{FeNO}^{7} and hs-[{FeNO}^{7}]$_2$

The electronic absorption spectrum of the mononitrosyl complex **1**$^{3+}$ consists of at least five distinct transitions, with a broad feature at 625 nm ($\varepsilon = 160 \pm 2$ $M^{-1}cm^{-1}$) attributed to a spin-forbidden d-d transition. **1**$^{3+}$ exhibits an additional band at 510 nm ($\varepsilon = 220 \pm 5$ $M^{-1}cm^{-1}$), with a shoulder at 428 nm ($\varepsilon = 640 \pm 50$ $M^{-1}cm^{-1}$) and two underlying shoulders in the UV-region at 340 nm ($\varepsilon = 2407 \pm 175$ $M^{-1}cm^{-1}$) and 310 nm ($\varepsilon = 2820 \pm 145$ $M^{-1}cm^{-1}$) (Figure 3.1). These four

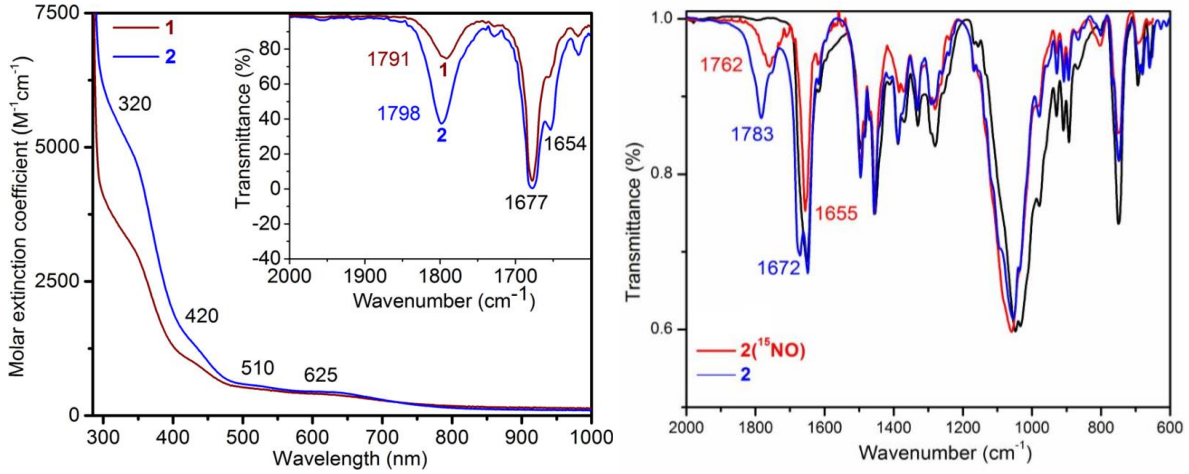

Figure 3.1 Left: Electronic absorption and (Inset) solution IR spectra of **1**$^{3+}$ and **2**$^{3+}$ in CH_3CN taken by Majumdar and coworkers. The IR bands at 1677 and 1654 cm^{-1} correlate to free-DMF and metal-coordinated DMF, respectively. Conditions: [**1**$^{3+}$] = [**2**$^{3+}$] = 0.2 mM (UV-Vis) and 2 mM (solution IR). Right: IR (KBr) overlay of the $[Fe_2(N\text{-}Et\text{-}HPTB)(DMF)_4](BF_4)_3$ precursor (black) with its natural abundance (blue) and ^{15}NO (red) nitrosylated isotopologs.

bands are attributed to $NO^- \pi^*$ to Fe^{III} charge transfer transitions, as previously identified in related nonheme hs-{FeNO}^{7} complexes.[15-18] The FTIR spectrum of **1**$^{3+}$ shows an N-O stretching

frequency of ν_{NO} = 1768 cm^{-1} (KBr)/1791 cm^{-1} (CH_3CN), conforming to typical N-O stretching frequencies for non-heme hs-{FeNO}^{7} systems.[19-23] The dinitrosyl analog $\mathbf{2^{3+}}$ contains a near identical UV-spectrum with a broad feature at 625 nm ($\varepsilon = 505 \pm 70$ $M^{-1}cm^{-1}$) and four additional features at 510 nm ($\varepsilon = 558 \pm 80$ $M^{-1}cm^{-1}$), 425 nm ($\varepsilon = 1785 \pm 160$ $M^{-1}cm^{-1}$), and 320 nm ($\varepsilon = 4763 \pm 700$ $M^{-1}cm^{-1}$), with increased extinction coefficients consistent with additional $NO^- \pi^*$ to Fe^{III} charge transfer associated with the presence of the additional NO ligand. The FTIR spectrum of $\mathbf{2^{3+}}$ exhibits an N-O stretch at ν_{NO} = 1778-1783 cm^{-1} (KBr)/1798 cm^{-1} (CH_3CN), with the ^{15}NO isotopolog exhibiting ν_{NO} at 1762 cm^{-1} (KBr) (Figure 3.1). Both $\mathbf{1^{3+}}$ and $\mathbf{2^{3+}}$ are stable towards NO loss in solution in the absence of a reductant, similar to $[Fe_2(N\text{-}Et\text{-}HPTB)(PhCOO)(NO)_2]^{2+}$,[15] $[Fe_2(N\text{-}Et\text{-}HPTB)(OH)(NO)(DMF)_2]^{3+}$,[10] and $[Fe_2(BPMP)(OPr)(NO)_2](OTf)_2$,[7] as well as the dinitrosyl adducts of ribonucleotide reductase and methane monooxygenase.[16, 24, 25]

The cyclic voltammogram of $\mathbf{1^{3+}}$ shares distinct similarities with that of the complex $[Fe_2(BPMP)(OPr)(NO)_2](OTf)_2$ (Chapter 2), which exhibits an irreversible redox event at E_p = -1.15 V vs Fc^+/Fc with a new reversible wave at $E_{1/2}$ -0.45 V associated with the oxidation/reduction of the product immediately formed after N_2O release. Similarly, $\mathbf{1^{3+}}$ exhibits a single semi-reversible reductive event at E_p = -1.01 V vs Fc^+/Fc, which in turn, generates a new redox event appearing at $E_{1/2}$ = -0.62 V that does not occur when scanning solely in the -0.32 to -0.82 V range (Figure 3.2). This suggests that the reduction to hs-{FeNO}^{8} may similarly lead to irreversible N_2O formation in this system and the formation of an oxo bridged diferrous product (Fe^{II}-O-Fe^{II}), where the $E_{1/2}$ at -0.62 V is associated with the oxidation/reduction of this product. Interestingly, there is a scan rate dependent re-oxidation of the hs-{FeNO}^{8} back to the hs-{FeNO}^{7} complex, located at -0.93 V at faster scan rates, suggesting that it may be possible to spectroscopically trap a hs-{FeNO}^{8} type species,

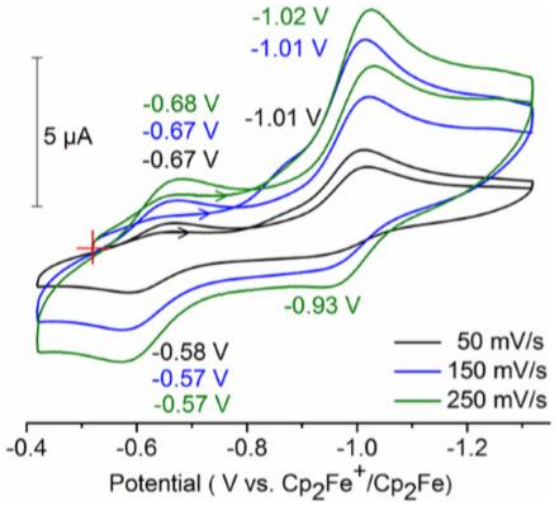

Figure 3.2 Cyclic voltammetric traces for $\mathbf{1}^{3+}$ (two consecutive scans for each scan rate) in DMF taken by Majumdar and coworkers illustrate a semireversible reduction of the hs-{FeNO}^{7} complex at -1.02 V leading to the formation of the presumptive oxo-bridged diferous product which exhibits a reversible redox couple at $E_{1/2}$ = -0.62 V vs. Fc^+/Fc.

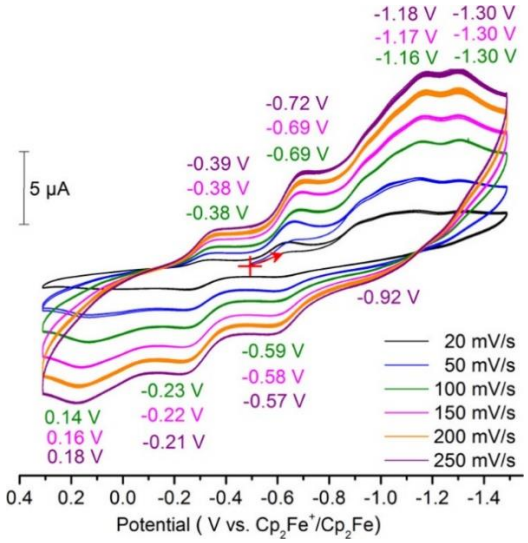

Figure 3.3 Cyclic voltammetry traces for $\mathbf{2}^{3+}$ (two scans at each scan rate) in DMF taken by Majumdar and coworkers illustrate electronically coupled and irreversible hs-[{FeNO}^{7}]$_2$ reduction events at -1.17 V and -1.30 V vs. Fc^+/Fc.

$\mathbf{1}^{2+}$. The cyclic voltammogram of $\mathbf{2}^{3+}$ contains two electronically coupled reduction events at -1.17 V and -1.30 V vs. Fc^+/Fc with a current ratio near unity (0.98), presumably irreversibly generating the diferrous oxo-bridged product (Fe^{II}-O-Fe^{II}) and N_2O (Figure 3.3). In the reverse scan new oxidative and reductive events appear at $E_{1/2}$ = -0.63 V, which are not present when solely

scanning in the -0.5 V to -0.95 V window, and which are therefore attributed to the initial oxidation/reduction of the Fe^{II}-O-Fe^{II} product upon N_2O release. The two additional quasi- and irreversible oxidation events at -0.22 V and 0.16 V, respectively, are attributed to the oxidation of the hs-{FeNO}^{7} units.

The Mössbauer spectroscopic data for $[Fe_2(N\text{-Et-HPTB})(CH_3COS)](BF_4)_2$ show two distinct quadrupole doublets associated with Fe^{II}_2 centers, with nearly identical isomer shifts (δ = 1.02 and 1.05 mm s^{-1}) but distinctly different quadrupole splitting values (ΔE_Q = 2.97, 3.33 mm s^{-1}) as a result of the different coordination environments of the two Fe(II) sites. Upon mono-

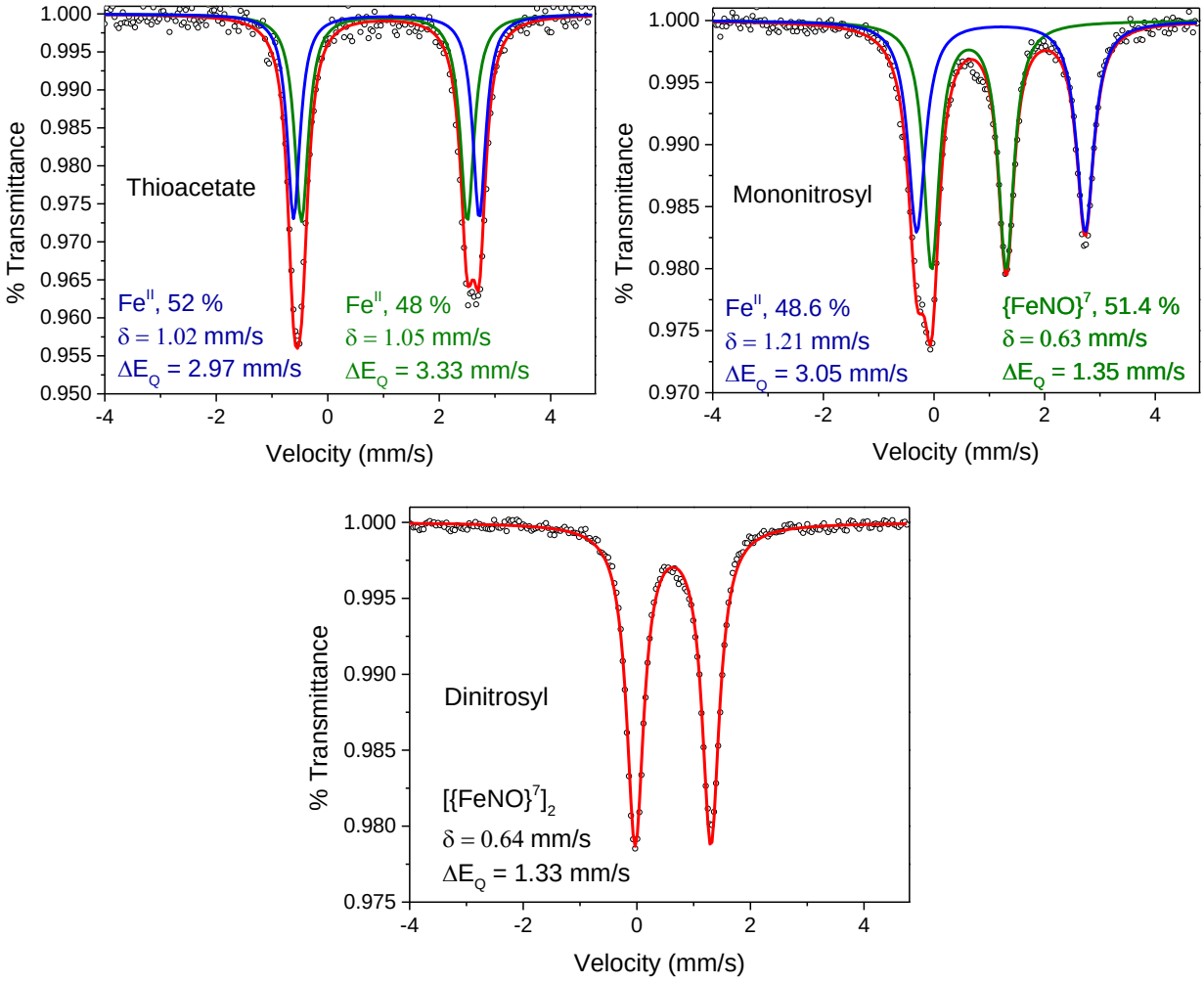

Figure 3.4 Mössbauer spectroscopic data for $[Fe_2(N\text{-Et-HPTB})(CH_3COS)](BF_4)_2$ (top left), $\mathbf{1}^{3+}$ (top right), and $\mathbf{2}^{3+}$ (bottom) taken on powder samples at 80K by Meyer and coworkers.

nitrosylation to $\mathbf{1}^{3+}$ a new hs-{FeNO}^{7} quadrupole doublet arises with an isomer shift $\delta = 0.63$ mm s^{-1} and a quadrupole splitting $\Delta E_Q = 1.35$ mm s^{-1}, while the Fe^{II} quadrupole doublet shifts slightly to $\delta = 1.21$ mm s^{-1} and $\Delta E_Q = 3.05$ mm s^{-1} (Figure 3.4). Similar isomer shifts have been observed for the hs-{FeNO}^{7} units in other N-Et-HPTB complexes such as [Fe$_2$(N-Et-HPTB)(PhCOO)(NO)$_2$](BF$_4$)$_2$ and [Fe$_2$(N-Et-HPTB)(NO)(OH)(DMF)$_2$](BF$_4$)$_3$,[10, 15] as well as in [Fe$_2$(BPMP)(OPr)(NO)$_2$](OTf)$_2$.[7] Superconducting quantum interference device (SQUID)

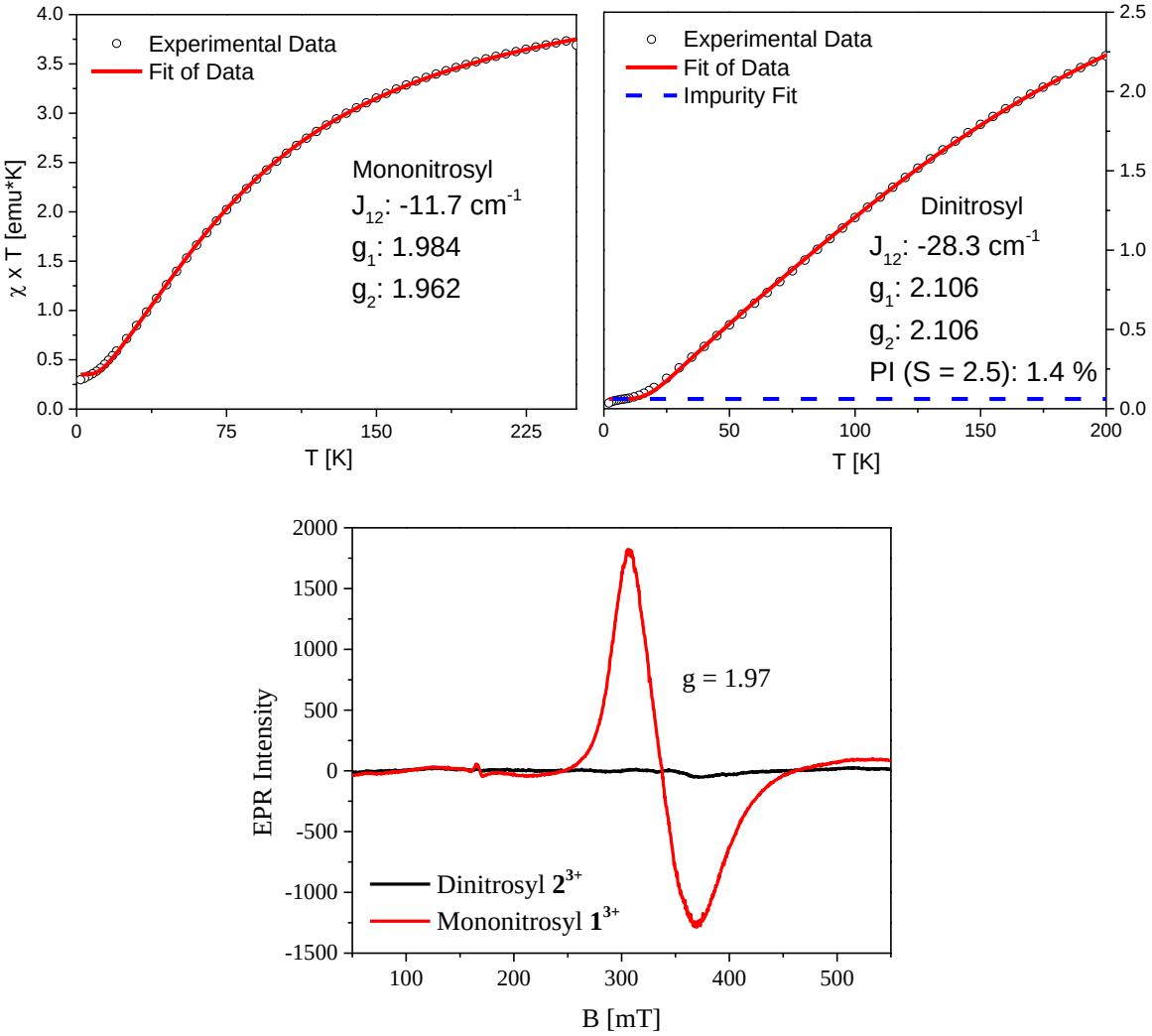

Figure 3.5 Top: SQUID data and fits for $\mathbf{1}^{3+}$ (top left) and $\mathbf{2}^{3+}$ (top right), taken on powder samples by Meyer and coworkers, reveal an antiferromagnetically coupled diiron core in each case, resulting in a $S_t = ½$ and $S_t = 0$ ground state for $\mathbf{1}^{3+}$ and $\mathbf{2}^{3+}$, respectively. Consistent with this formulation, EPR (bottom) taken on $\mathbf{1}^{3+}$ exhibits a broad signal at g ~ 1.97 while $\mathbf{2}^{3+}$ is EPR silent. Conditions: [$\mathbf{1}^{3+}$] = 2mM in CH_3CN, 9.302 GHz microwave frequency, 20.46 mW microwave power, 5 G modulation amplitude; [$\mathbf{2}^{3+}$] = 4.1 mM in CH_2Cl_2, 9.326 GHz microwave frequency, 20.510 microwave power, 1 G modulation amplitude.

magnetometry on $\mathbf{1}^{3+}$ reveals a weak antiferromagnetic coupling of $J_{1,2}$ = -11.7 cm^{-1} between the hs-{FeNO}^{7} and hs-Fe^{II} sites (Figure 3.5). In line with this, $\mathbf{1}^{3+}$ displays an EPR signal with g ~1.97 at 4 K and is consistent with a hs-[Fe^{II}{FeNO}^{7}] formulation for $\mathbf{1}^{3+}$, where an S_t = 1/2 system results from the antiferromagnetic coupling of a hs-Fe^{II} ion (S = 2) with a hs-{FeNO}^{7} unit (S = 3/2) (Figure 3.5). In comparison, the Mössbauer spectroscopic characterization of $\mathbf{2}^{3+}$ exhibits nearly identical {FeNO}^{7} quadrupole doublets compared to $\mathbf{1}^{3+}$ with δ = 0.65 mm s^{-1} and ΔE_Q = 1.33 mm s^{-1} (Figure 3.4). SQUID magnetometry measurements of $\mathbf{2}^{3+}$ reveal an increase in the antiferromagnetic coupling between the two hs-{FeNO}^{7} units with $J_{1,2}$ = -28.3 cm^{-1} (Figure 3.5). Consistent with this, $\mathbf{2}^{3+}$ is EPR silent, arising from the antiferromagnetic coupling between the two S = 3/2 hs-{FeNO}^{7} units to give a S_t = 0 ground state. The SQUID and Mössbauer data for both $\mathbf{1}^{3+}$ and $\mathbf{2}^{3+}$ support the typical Fe^{III}-NO^- formulation for these hs-{FeNO}^{7} species, in line with Solomon's early detailed electronic structure characterization of hs-{FeNO}^{7} complexes discussed in Chapter 1.[20, 26] Upon nitrosylation, the Fe^{II} is partially oxidized, supported by both an increase in J-coupling constants in $\mathbf{2}^{3+}$ compared to $\mathbf{1}^{3+}$ and a decrease in the isomer shift from δ = 1.21 mm s^{-1} (hs-Fe^{II}) to 0.65 mm s^{-1} (hs-{FeNO}^{7}).

3.2 Reduction of hs-Fe^{II}{FeNO}^{7} and hs-[{FeNO}^{7}]$_2$

Chemical and Electrochemical Reduction of $\boldsymbol{1}^{3+}$

As discussed in section 3.1, the CV of $\mathbf{1}^{3+}$ exhibits a scan-rate dependence in the reversibility of the hs-{FeNO}$^{7/8}$ redox couple, suggesting that a hs-{FeNO}^{8} species could feasibly be trapped at rapid timescales. In order to evaluate whether this hs-{FeNO}^{8} species can be spectroscopically captured, an IR-SEC experiment was performed on a 5.3 mM CH_2Cl_2 solution of $\mathbf{1}^{3+}$ containing ~ 0.1 M of $(Et_4N)(BF_4)$ as the supporting electrolyte. Upon holding the potential

at -1.6 V vs Ag wire for 100 s, the decay of the NO band was monitored, resulting in the direct formation of N_2O without the formation of any detectable $\{FeNO\}^8$ intermediates on this timescale (Figure 3.6). This is further illustrated by plotting the normalized intensities of the NO and N_2O

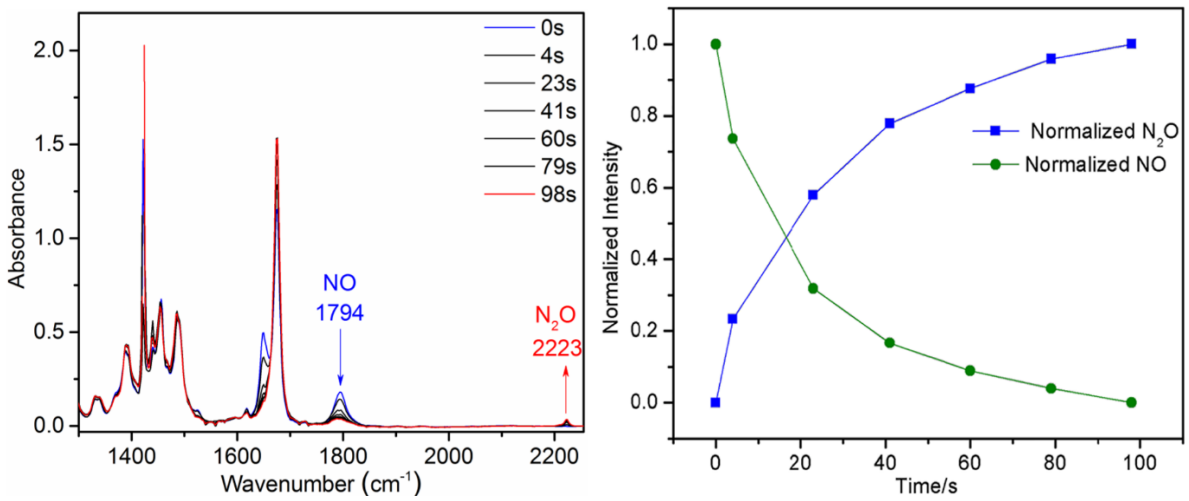

Figure 3.6 Left: The IR-SEC reduction of a $\mathbf{1}^{3+}$ results in the direct generation of N_2O via NO reduction. Conditions: Hold at -1.6 V vs. Ag wire, 5.3 mM in CH_2Cl_2 with 0.1 M $(Et_4N)(BF_4)$ as the supporting electrolyte. Right: A plot of the normalized intensities of the NO and N_2O bands vs. time illustrates the direct conversion from NO to N_2O.

bands (scaled to their maximum intensity, set to 1), showing a direct conversion from NO to N_2O with no lag phase preceding N_2O formation. During the reduction of NO to N_2O in this system, the band at ~1655 cm^{-1} (bound DMF) also decreases with an increase of the band at ~1675 cm^{-1} (free DMF), implying that coordinated DMF is released concomitant with the reduction. The rapid production of N_2O was further confirmed by IR spectroscopic analysis of the reaction headspace upon the reduction of $\mathbf{1}^{3+}$ with one equivalent of $CoCp_2$ using the N_2O calibration curve presented in Chapter 2.[7] Here, $\mathbf{1}^{2+}$ generates an average of 45% N_2O yield (with respect to $[\mathbf{1}^{3+}]$)[27] within 5 minutes (Figure 3.7), in line with a bimolecular reaction of two molecules of the reduced hs-$[Fe^{II}\{FeNO\}^8]$ intermediate (the *super*reduced mechanism):

$$2Fe^{II}\{FeNO\}^7 + 2e^- \rightarrow [2Fe^{II}\{FeNO\}^8] \rightarrow Fe^{II}Fe^{II}\text{-}O\text{-}Fe^{II}Fe^{II} + N_2O$$

In order to test whether this system could undergo semi-reduction, $\mathbf{1}^{3+}$ was reacted with 0.5 equivalents of $CoCp_2$, resulting in an average yield of 25.5% N_2O (with respect to [$\mathbf{1}^{3+}$]), indicating that in this case the reaction still proceeds via a bimolecular superreduction whereby a 2:1 ratio of $CoCp_2$:N_2O is necessary (as opposed to still generating a ~50% yield, which would imply a bimolecular semireduction). While generation of N_2O by diiron dinitrosyl complexes is not unprecedented, this is only the second example of *super*reduction from a mononitrosyl hs-{FeNO}^{8} complex, and the first system that is capable of near-quantitative and rapid N_2O generation. In contrast, Goldberg's hs-{FeNO}^{8} complex [Fe(NO)(N3PyS)]BF_4[28] is metastable at room temperature ($t_{1/2}$ = 30 min) with 27% N_2O formed with respect to [hs-{FeNO}^{8}] after 20 hrs.

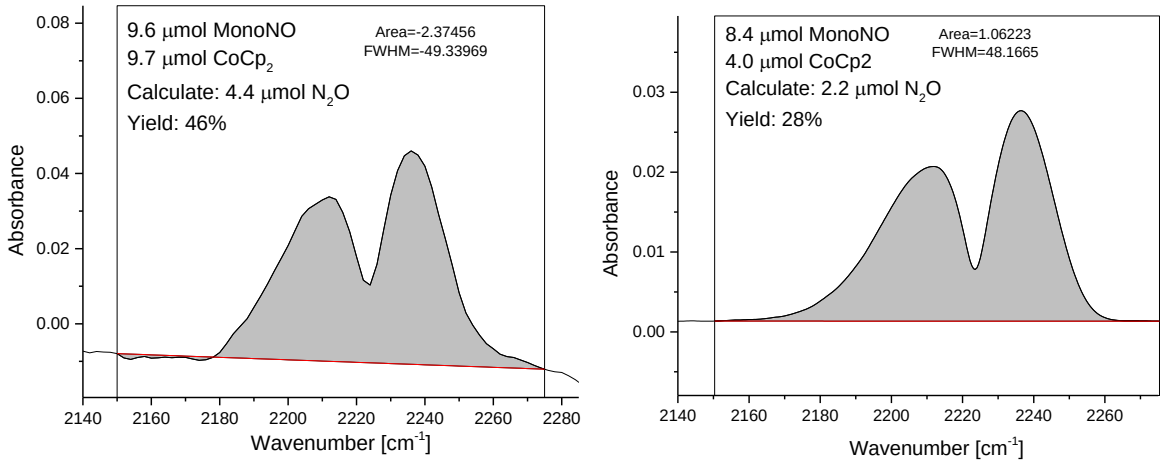

Figure 3.7 Representative gas-headspace N_2O analysis for the reduction of $\mathbf{1}^{3+}$ with (left) ~1 eq $CoCp_2$ and (right) ~0.5 eq $CoCp_2$.

Chemical and Electrochemical Reduction of $\boldsymbol{2}^{3+}$

The chemical and electrochemical reduction of $\mathbf{2}^{3+}$ was monitored in the same manner as in the case of $\mathbf{1}^{3+}$. IR-SEC measurements on $\mathbf{2}^{3+}$ and its ^{15}NO isotopolog were taken on 7.7 mM and 11.4 mM samples in CH_2Cl_2, respectively, using 0.1 M $(Et_4N)(BF_4)$ as the supporting electrolyte (Figure 3.8). Upon holding the potential at -1.6 V vs. Ag wire for ~2 minutes, the NO

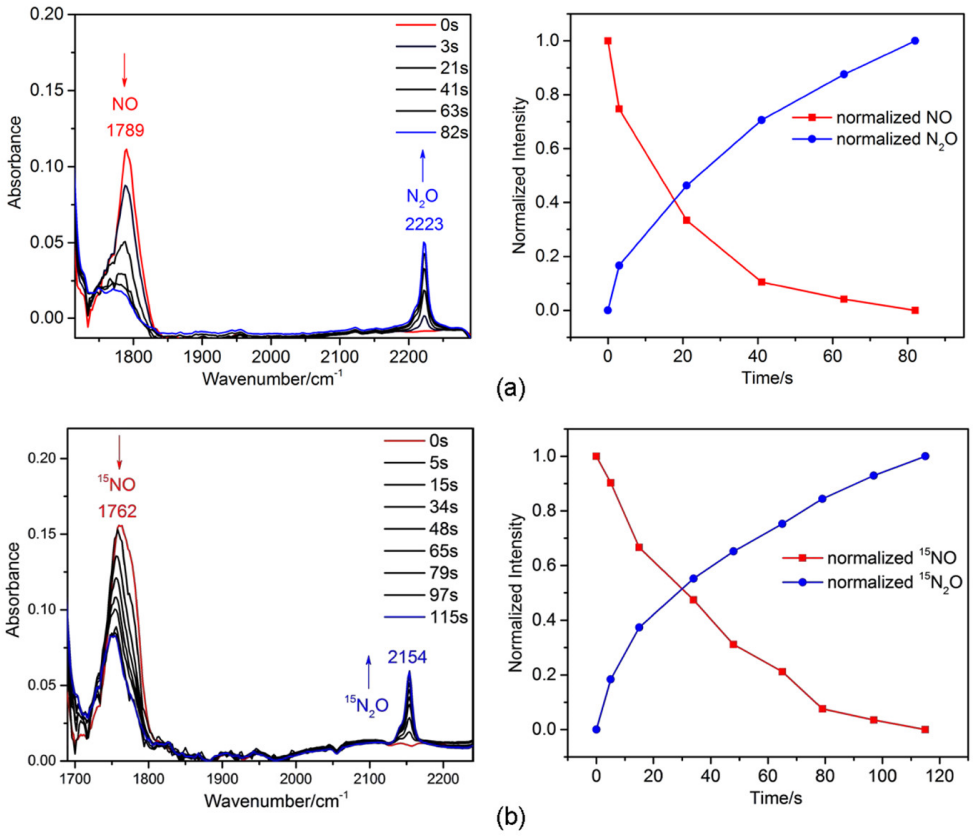

Figure 3.8 Top: The IR-SEC reduction of natural abundance $\mathbf{2}^{3+}$ results in the direct generation of N_2O, identified by the rising N-N stretch at 2223 cm^{-1}, via NO reduction. Conditions: Hold at a potential of -1.6 V vs. Ag wire, 7.7 mM $\mathbf{2}^{3+}$ in CH_2Cl_2 was used with 0.1 M $(Et_4N)(BF_4)$ as the supporting electrolyte. Bottom: The IR-SEC reduction of the ^{15}NO isotopolog of $\mathbf{2}^{3+}$ similarly directly generates $^{15,15}N_2O$ (N-N stretch at 2154 cm^{-1}). Conditions: Hold at a potential of -1.6 vs. Ag wire, 11.4 mM complex in CH_2Cl_2 with 0.1 M $(Et_4N)(BF_4)$ as the supporting electrolyte.

band decayed with the direct formation of N_2O. No intermediates preceding N-N coupling were observed on the IR-SEC timescale.

The rapid production of N_2O was further confirmed by IR spectroscopic analysis of the reaction gas headspace. In the presence of two equivalents of $CoCp_2$, an average yield of 96 % N_2O (with respect to the concentration of $\mathbf{2}^{3+}$) was obtained within 5 minutes of the addition of $CoCp_2$. Interestingly, it was observed that even 1 eq of $CoCp_2$ was sufficient for near quantitative N_2O production, resulting in an average 89% N_2O yield (Figure 3.9). In contrast, the reduction of $\mathbf{1}^{3+}$ with 1 eq of $CoCp_2$ generated a 45% yield of N_2O. These results indicate an interesting

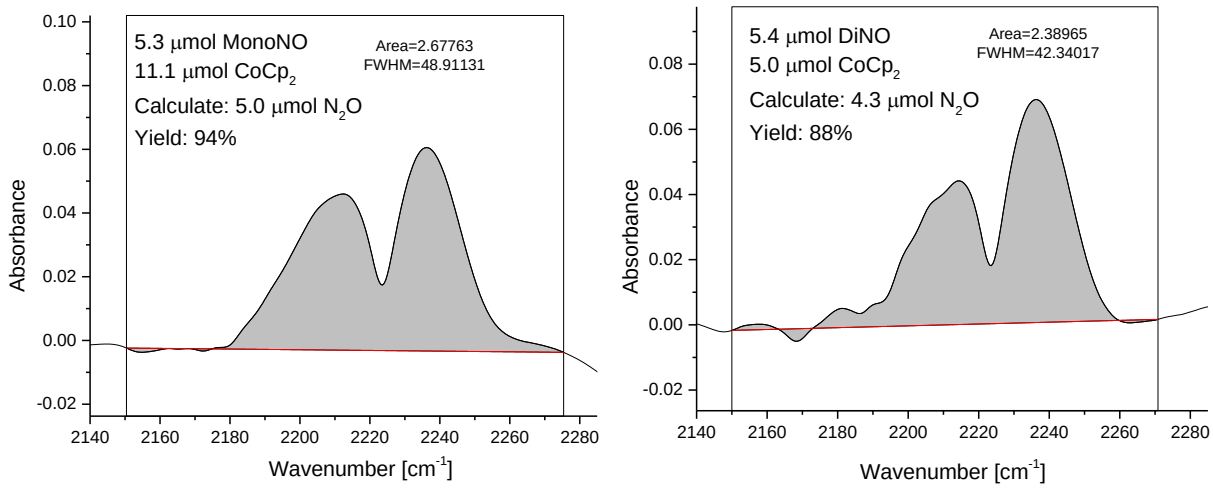

Figure 3.9 Representative gas-headspace N_2O analyses for the reduction of $\mathbf{2}^{3+}$ with (left) ~2 eq $CoCp_2$ and (right) ~1 eq $CoCp_2$.

difference between $\mathbf{1}^{3+}$and $\mathbf{2}^{3+}$: whereas the mononitrosyl complex uses an *inter*molecular superreduced mechanism to generate N_2O, the dinitrosyl complex is the second model complex after $[Fe_2(BPMP)(OPr)(NO)_2](OTf)_2$ that uses a semireduced mechanism to achieve facile NO reduction. Based on the isotopic scrambling data presented for $[Fe_2(BPMP)(OPr)(NO)_2](OTf)_2$ in Chapter 2, we speculate that $\mathbf{2}^{3+}$ similarly undergoes *intra*molecular semireduction.

Characterization of the Reduction Products

Based on the interesting difference in the mechanism by which $\mathbf{1}^{3+}$ and $\mathbf{2}^{3+}$ generate N_2O, attempts were made to isolate and characterize the reaction product in each case. Complex $\mathbf{1}^{3+}$ exists in a S_t = ½ ground state and contains a broad g ~ 1.97 signal in acetonitrile solution. Upon chemical reduction with excess $CoCp_2$ at -40° C this signal is essentially quenched (Figure 3.10), thus indicating the formation of a significant amount of EPR-silent species during N_2O generation from $\mathbf{1}^{3+}$. The residual g ~ 1.97 signal with significantly lower intensity may arise from the poor solubility of $CoCp_2$ at low temperature in CH_3CN, thereby leaving behind a small amount of unreacted $\mathbf{1}^{3+}$ in the reaction mixture. Minimal spectroscopic changes occur upon warming to RT

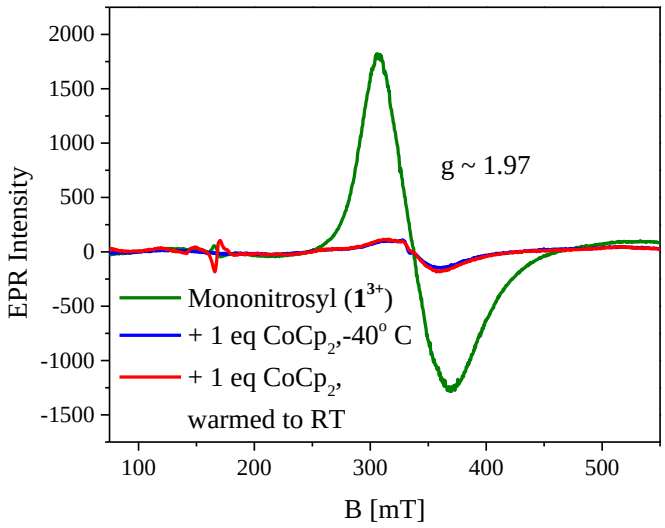

Figure 3.10 EPR study for the reaction of $\mathbf{1}^{3+}$ with excess $CoCp_2$ in CH_3CN. Conditions: [$\mathbf{1}^{3+}$] = 2 mM, [$CoCp_2$] = 4 mM, 9.355 GHz microwave frequency, 20.510 mW microwave power, 1G modulation amplitude.

suggesting that the LT and RT products are similar. These EPR data are consistent with a bimolecular superreduced mechanism whereby an EPR silent Fe^{II}-O-Fe^{II} oxo-bridged dimer is the expected byproduct.

In contrast, $\mathbf{2}^{3+}$ is initially EPR silent, with an S_t = 0 ground state, as expected for an antiferromagnetically coupled hs-[{FeNO}^{7}]$_2$ dimer. Upon mixing $\mathbf{2}^{3+}$ with one equivalent of $CoCp_2$ in CH_2Cl_2, a broad S = ½ signal appears (Figure 3.11). This EPR signal is best fit with g = 1.55, 1.79, and 2.03, but because of the broadness of the signal, this does not constitute a unique fit. Notably, the S = ½ signal is significantly higher when the reduction is conducted at RT compared to -80° C. The formation of a S = ½ signal suggests that a mixed-valent diiron(II,III) species is formed upon one-electron reduction of $\mathbf{2}^{3+}$, which is consistent with a semireduced N-N coupling mechanism whereby one reductive equivalent is provided externally via $CoCp_2$ while the second one originates from the diferrous core. Interestingly, there is a temperature dependence of the intensity of the S = ½ signal, suggesting that the reduction product may exist in an equilibrium of diiron (EPR active) and oligomeric (EPR silent) oxo-bridged species. The broadness of the

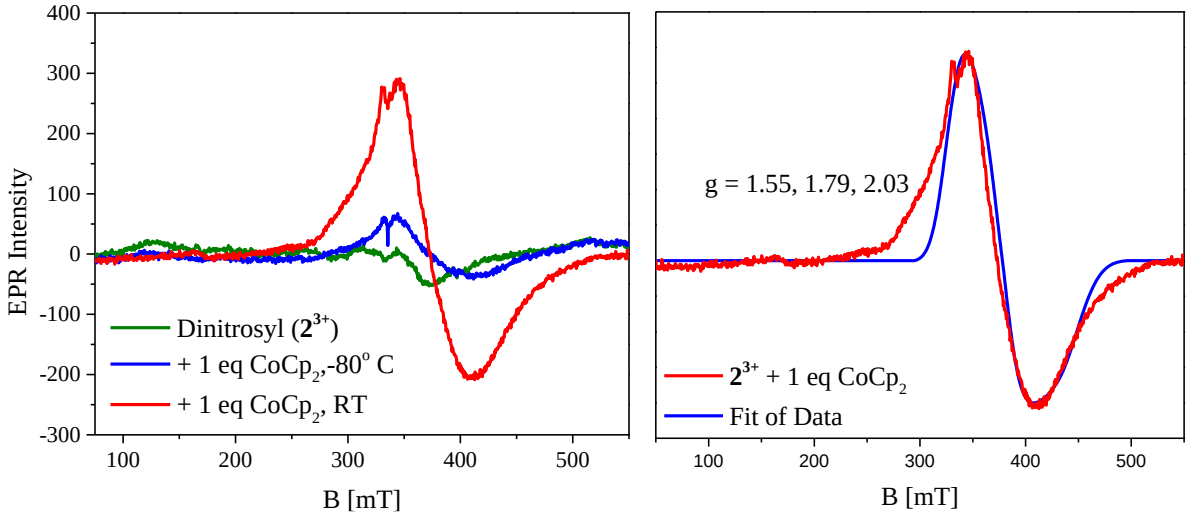

Figure 3.11 Left: EPR study for the reaction of $\mathbf{2}^{3+}$ (green, 4.1 mM) with 1 eq of $CoCp_2$ in CH_2Cl_2. RT Conditions: [$\mathbf{2}^{3+}$] = 5.1 mM, [$CoCp_2$] = 5.5 mM, 9.326 GHz microwave frequency, 20.460 mW microwave power, 1G modulation amplitude. LT Conditions: [$\mathbf{2}^{3+}$] = 5.4 mM, [$CoCp_2$] = 5.5 mM, 9.336 GHz microwave frequency, 20.510 mW microwave power, 1G modulation amplitude. Right: Spin Count simulation of the EPR spectrum generated from the RT reduction of $\mathbf{2}^{3+}$. Due to the broadness of the signal, the fit shown is not a unique solution. Simulation paramaters: g_x = 1.55, g_y = 1.79, g_z = 2.03; sg_x = 0.07, sg_y = 0.07, sg_z = 0.08.

resulting EPR signal also suggests that multiple S = ½ species may be present. Indeed, mass spectrometric data collected by Majumdar and coworkers contain several fragments suggestive of an equilibria of monomeric (diiron) μ-oxo and dimeric (tetrairon) μ-oxo products with m/z = 446.16 and 425.64, corresponding to $[Fe_2(N\text{-}Et\text{-}HPTB)(\mu\text{-}O)(MeCN)]^{2+}$ and $[Fe_2(N\text{-}Et\text{-}HPTB)(\mu\text{-}O)]^{2+}$, as well as m/z = 455.41 and 434.90, corresponding to $[Fe_4(N\text{-}Et\text{-}HPTB)_2(\mu\text{-}OH)_4(MeCN)_2]^{4+}$ and $[Fe_4(N\text{-}Et\text{-}HPTB)_2(\mu\text{-}OH)_4]^{4+}$. Majumdar and coworkers further crystallized the bulk one electron reduction product of $\mathbf{2}^{3+}$ and identified the product as $[Fe_4(N\text{-}Et\text{-}HPTB)_2(\mu OH)_2(\mu\text{-}O)](BF_4)_4$ (Figure 3.12). This complex features two mixed-valent diiron(II,III) units linked together by two hydroxyl bridges (average Fe-O distance = 1.995 Å) and one oxo bridge (Fe-O distance = 1.815 Å). This tetrairon reduction product could not be isolated as an analytically pure sample, and therefore, bulk characterization of this species was not accomplished. Nevertheless, the isolation of this crystal coupled with the EPR study above strongly indicate that N_2O and the mixed valent diiron(II,III) species are the direct products after treating $\mathbf{2}^{3+}$ with 1 eq

of $CoCp_2$, followed by dimerization in the presence of H_2O to generate $[Fe_4(N\text{-}Et\text{-}HPTB)_2(\mu OH)_2(\mu\text{-}O)](BF_4)_4$.

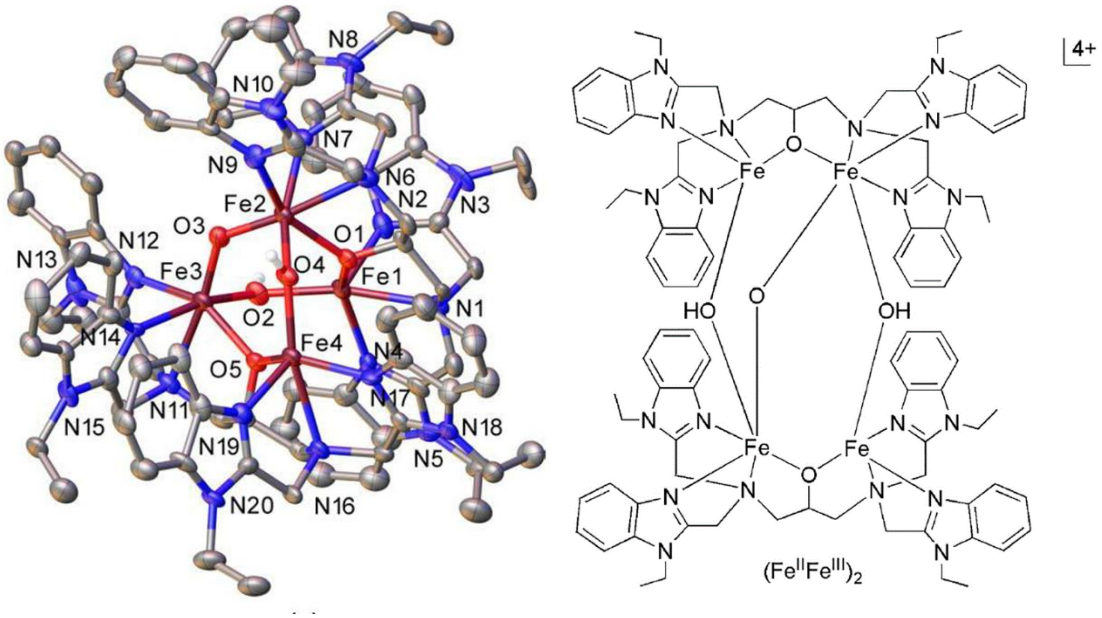

Figure 3.12 Molecular structure of the mixed-valent tetrairon dimer that was crystallized by Majumdar and coworkers from the bulk reduction of $\mathbf{2}^{3+}$ with 1 eq of $CoCp_2$. 30% probability thermal ellipsoids and partial atom labeling are shown. Hydrogen atoms and counterions (except for μ_2-OH) are omitted for clarity. Selected distances (Å): Fe1−O2 = 2.018(9), Fe3−O2 = 1.980(8), Fe2−O4 = 1.999(9), Fe4−O4 = 1.985(8), Fe2−O3 = 1.814(8), Fe3−O3 = 1.816(8).

As discussed in Chapter 2, it has been observed that the semireduction of $[Fe_2(BPMP)(OPr)(NO)_2](OTf)_2$ leads to the formation of an EPR-active mixed valent S = ½ product when the reduction is carried out at -80° C. However, when the reaction mixture is warmed to RT or the reaction is directly conducted at RT, the product becomes EPR silent, a surprising finding that could not be fully explained in the initial report. The results presented above provide an elegant explanation for this finding: the initially formed mixed-valent (and EPR-active) Fe^{II}-O-Fe^{III} product dimerizes at higher temperatures, likely producing a similar tetrameric product as observed here that is then EPR silent (referred to as **[X]** in Chapter 2). This result could therefore have general implications for the behavior of mixed-valent reaction products formed from NO reduction in diiron model complexes. Despite several reports on NO reduction by diiron

complexes in the literature, this is the first time that the oligomerized tetrameric products from these reactions could be unambiguously characterized.

DFT Comparison of the hs-Fe^{II}{FeNO}^{8} and hs-{FeNO}^{7}{FeNO}^{8} forms

The fact that $\mathbf{1}^{3+}$ can only produce N_2O using an intermolecular superreduced mechanism while $\mathbf{2}^{3+}$ is capable of undergoing facile semireduction results in an interesting dichotomy considering that $\mathbf{1}^{3+}$ and $\mathbf{2}^{3+}$ contain the same coligand, and hence, the hs-{FeNO}$^{7/8}$ units in these complexes have very similar structural and electronic properties. As such a DFT study was employed to better understand the differences between the reduced analogs of these complexes ($\mathbf{1}^{2+}$ and $\mathbf{2}^{2+}$). Density functional theory (DFT) optimized structures of $\mathbf{1}^{3+}$ and $\mathbf{2}^{3+}$ were obtained with Gaussian 09[30] using the B3LYP functional[31, 32] and 6-311G(d) basis set.[33, 34] These structures contain quite typical hs-{FeNO}^{7} units with Fe−NO and N−O bond lengths of 1.79 and 1.16 Å, respectively, and Fe−N−O bond angles of 170° in $\mathbf{1}^{3+}$ and 165° and 168° in $\mathbf{2}^{3+}$, in good agreement with structural parameters reported for these complexes by X-ray crystallography (Table 3.1). In contrast, the frequency calculations overestimate the N-O stretching frequencies[35], predicting values of 1863 cm^{-1} for $\mathbf{1}^{3+}$ and antisymmetric/symmetric stretches at 1846 and 1873 cm^{-1} for $\mathbf{2}^{3+}$. Such an overestimate of the N-O stretch is typically observed with hybrid functionals such as B3LYP that contain exact Hartree-Fock exchange.[35] Nonetheless, across the series of $\mathbf{1}^{3+/2+}$ and $\mathbf{2}^{3+/2+}$, these calculations can be employed to evaluate the differences in electronic structure between these complexes. In the calculations, reduction of $\mathbf{2}^{3+}$ to $\mathbf{2}^{2+}$ results in a significant decrease in the N-O stretching frequency of the resulting hs-{FeNO}^{8} unit to 1694 cm^{-1}. Orca 4.0.1.2[36] single-point calculations on the optimized structure suggest that the added electron populates the d_{xy} orbital (Figure 3.13), which is nonbonding with respect to the Fe-NO unit. The

Table 3.1 Comparison of experimental and DFT-calculated structural parameters (in Å or °) and N-O stretching frequencies (in cm^{-1}) for $\mathbf{1}^{3+/2+}$ and $\mathbf{2}^{3+/2+}$.

	Mononitrosyl				Dinitrosyl[b]			
	$Fe^{II}\{FeNO\}^7$		$Fe^{II}\{FeNO\}^8$		$[\{FeNO\}^7]_2$		$\{FeNO\}^7\{FeNO\}^8$	
	Expt.[a]	DFT[b]	Expt.	DFT	Expt.	DFT	Expt.	DFT
Fe-N(O) (Å)	1.775(5)	1.79	--	1.90	1.748(7) 1.729(7)	1.79 1.79	--	1.79 1.81
N-O (Å)	1.066(7)	1.16	--	1.23	1.147(8) 1.123(8)	1.16 1.16	--	1.16 1.20
Fe-N-O (°)	160.5(7)	170	--	130	164.9(7) 174.9(8)	165 168	--	168 158
ν(NO) (cm^{-1})	1768[c] 1791[d] 1794[e]	1863	--	1545	1782[c] 1798[d] 1794[e]	1846 1873	--	1859 1694
ON-NO (Å)	--	--	--	--	3.178(0)	3.07	--	2.91

[a] From ref.: Jana et al., *J. Am. Chem. Soc.* **2017**, *139*, 14380-14383. [b] From ref.: Jana et al., *J. Am. Chem. Soc*. **2020**, *142*, 6600-6616. [c] KBr pellet. [d] In CH_3CN. [e] In CH_2Cl_2.

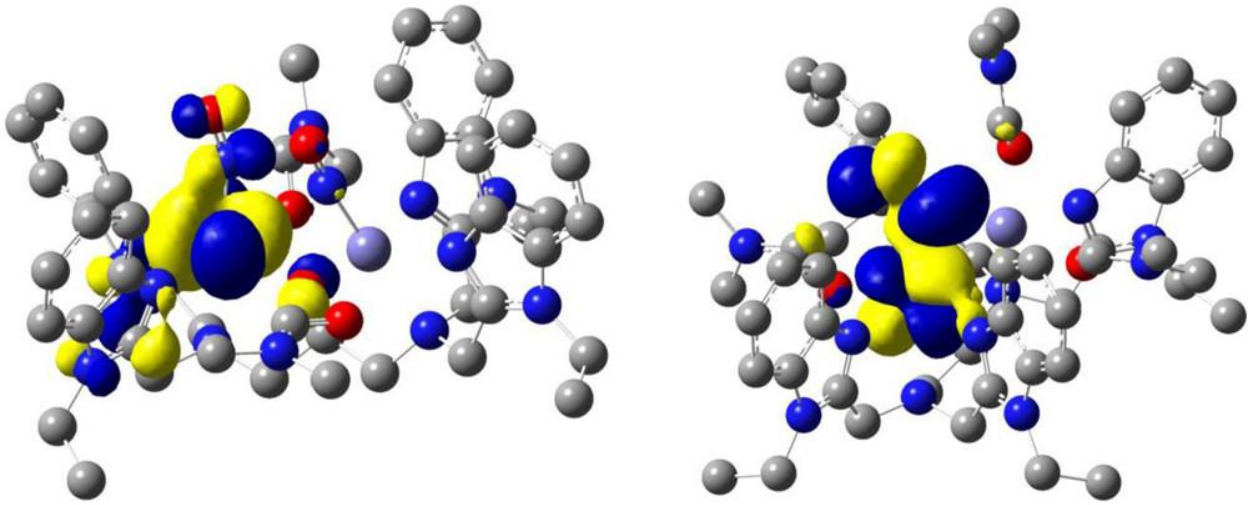

Figure 3.13 (Left) Contour plot of the nonbonding d_{xy} orbital (with respect to NO) that is occupied upon one-electron reduction of $\mathbf{2}^{3+}$ to $\mathbf{2}^{2+}$**.** Note that, since the coordination environment of the two hs-$\{FeNO\}^7$ units in $\mathbf{2}^{3+}$ is identical, with the amine groups trans to NO in both cases, reduction of the other iron center gives the same result. (Right) Contour plot of the antibonding d_{xz} orbital (with respect to NO) that is occupied upon reduction of $\mathbf{1}^{3+}$ to $\mathbf{1}^{2+}$.

additional electron density at the iron center leads to an increase of the effective nuclear charge at the Fe and, in this way, weakens the Fe-NO bond[19, 37] resulting in the observed decrease in the N-O stretching frequency. In the case of $\mathbf{2}^{3+/2+}$, it is therefore the proximity of the two Fe-NO units

that facilitates *intra*molecular N-N bond formation and N_2O generation via attack of the reduced hs-{FeNO}^{8} unit on the proximal hs-{FeNO}^{7} unit following the semireduced mechanism.[35]

If the two NO units are not held in proximity, as is the case for the mononitrosyl $\mathbf{1}^{3+/2+}$, further activation is required. Here, attack of one hs-{FeNO}^{8} species at the hs-{FeNO}^{7} center of a second complex is not enough to induce N-N bond formation and N_2O release. Only reaction of two hs-{FeNO}^{8} species allows the reaction to proceed via *inter*molecular superreduction. This finding has mechanistic implications for FNORs, arguing against a mononitrosyl mechanism, whereby the attack of a second free NO on the activated hs-{FeNO}$^{7/8}$ unit was proposed to induce N-N bond formation. This mechanistic scenario is unlikely, and the reaction most favorably proceeds via coordination of the two NO molecules, thereby holding them in close proximity for further reaction. Interestingly, single point calculations on the optimized structure of $\mathbf{1}^{2+}$ suggest that upon reduction of the mononitrosyl complex, the extra electron occupies the antibonding d_{xz}/π^*_x orbital of the Fe-NO unit (Figure 3.13). Accordingly, this induces elongation of the Fe-NO and N-O bonds to 1.90 and 1.23 Å, respectively, as well as a significant increase in Fe-N-O bending, from 170° to 130°. This is further reflected in an increase in spin density on the NO unit in $\mathbf{1}^{2+}$ compared to $\mathbf{1}^{3+}$, consistent with the decreased covalency of the Fe-NO bond (Table 3.2).

Table 3.2 Loewdin spin populations of the Fe-NO units of $\mathbf{1}^{3+/2+}$ and $\mathbf{2}^{3+/2+}$.

	Mononitrosyl Complex[a]		**Dinitrosyl Complex[b]**	
	Fe1 {Fe2N2O2}^{7}	**Fe1 {Fe2N2O2}^{8}**	**{Fe1N1O1}^{7} {Fe2N2O2}^{7}**	**{Fe1N1O1}^{7} {Fe2N2O2}^{8}**
Fe1	3.77	3.77	3.83	3.80
N1	--	--	-0.61	-0.56
O1	--	--	-0.56	-0.53
Fe2	-3.83	-3.49	-3.82	-3.42
N2	0.63	0.67	0.60	0.82
O2	0.57	0.96	0.57	0.64

[a] Fe1 corresponds to the Fe^{II} center and Fe2N2O2 corresponds to the hs-{FeNO}$^{7/8}$ unit.
[b] Fe1N1O1 corresponds to the first hs-{FeNO}^{7} unit and Fe2N2O2 corresponds to the second hs-{FeNO}$^{7/8}$ unit.

Because of the decrease in Fe-NO covalency, the N-O stretching frequency in $\mathbf{1}^{2+}$ is significantly lower than that of $\mathbf{2}^{2+}$, at 1545 cm^{-1}, indicative of a more activated hs-{FeNO}^{8} moiety in the mononitrosyl complex. Nonetheless, this complex experimentally still requires superreduction to generate N_2O, further highlighting the necessity of having two NO units bound in close proximity in order to achieve facile N-N coupling.

Conclusions

In summary, this work provides a detailed description of the synthesis, characterization, and reactivity of a mononitrosyl diiron(II) and a dinitrosyl diiron(II) complex, which may be considered as functional models for the mono- and dinitrosyl intermediates observed in the catalytic cycle of FNORs. Both the mono- and dinitrosyl diiron(II) complexes demonstrate facile N_2O generation upon chemical and electrochemical reduction following a superreduced and semireduced mechanism, respectively. This difference in reactivity points to the importance of binding two molecules of NO in close proximity for fast and efficient N_2O generation. The end products generated after N_2O release from such model complexes have been characterized by EPR spectroscopic methods and, for the first time, by single-crystal X-ray structure determination, which shows the surprising formation of tetranuclear iron complexes as the final products that use the oxo/hydroxo groups produced by N_2O release as bridging ligands. This provides a general trend for the fate of functional model complexes of FNORs after the generation of N_2O, and provides an elegant explanation for the nature of [**X**] in Chapter 2.

3.3 Experimental Section

Computational Methods. Optimization and frequency calculations on $\mathbf{1}^{3+/2+}$ and $\mathbf{2}^{3+/2+}$ were performed with Gaussian 09[30] using the B3LYP functional[31, 32] and 6-311G(d) basis set.[33, 34] Both of these complexes contain two antiferromagnetically coupled iron centers. These were treated by generating three fragments, one fragment containing the ligand scaffold, and the other two fragments containing one each of the Fe or Fe-NO units.[35] An initial guess is performed in Gaussian09 by making one of the Fe-containing fragments antiferromagnetically coupled to the other Fe. This guess is then utilized to begin single point and geometry optimization calculations. Once optimized, a frequency calculation is performed, and the final optimized structure is used in a subsequent Orca[36] 4.0.1.2 single point calculation to visualize the electronic structure. This single point is performed on the Gaussian09 B3LYP optimized structure (without fragments) utilizing the B3LYP/G functional and 6-311G(d) basis set with the def2/J auxiliary basis set.[38] The ferromagnetic single point is first calculated, and the spins at one of the Fe-NO units are then flipped using the SpinFlip option.

General Physical Methods. Mössbauer spectra were recorded using an alternating constant *WissEl* Mössbauer spectrometer, consisting of an MR 360 Drive Unit, an MV-1000 velocity transducer, and an LND 45431 proportional counter mounted on an LINOS precision bench. The system was operated in a horizontal transmission geometry with source, absorber, and detector in a linear arrangement. The temperature was controlled and maintained using a Janis SHI closed-cycle helium cryostat. Measurements were performed at 80 K. Data acquisition was performed using a 512 channel analyzer. Isomer shifts were referenced versus α-iron metal foil at ambient temperatures. The simulation of experimental data was performed using the *Mfit* program. Magnetic susceptibility measurements were conducted on a Quantum-Design MPMS XL-5 SQUID magnetometer, equipped with a 5 T magnet. Powder samples were loaded into a Teflon

bucket (for **1**) or into a gelatin capsule (with addition of a polyfluorinated oil to prevent crystal reorientation, for **2**) and placed in a plastic straw. The raw data were corrected for the diamagnetic contribution of the sample holder (and of the oil in case of **2**) as well as the diamagnetic contribution of the complexes using $\chi_M^{dia}(\text{sample}) = -0.5 \cdot M \cdot 10^{-6}$ cm^3·mol^{-1}. The data were fit with the *julX* program[39] using the appropriate Heisenberg-Dirac-van-Vleck (HDvV) spin Hamiltonian for isotropic exchange coupling and Zeeman splitting, equation (1).

$$\hat{H} = -2J\hat{S}_1\hat{S}_2 + g\mu_B\vec{B}(\vec{S}_1 + \vec{S}_2) \quad (1)$$

EPR spectra were recorded using a Bruker X-band EMX spectrometer equipped with an Oxford liquid helium cryostat. Spectra were recorded on ~2mM frozen solutions using 20mW microwave power and 100kHz field modulation at a 5G amplitude. IR spectroelectrochemistry experiments were performed using a LabOmak UF-SEC thin layer cell, with Pt mesh working and counter electrodes, and an Ag wire pseudo-reference electrode. N_2O yield experiments were carried out on samples of **1** and **2** as described in the experimental section of Chapter 2.[7]

3.4 References and Notes

(1) This chapter is adapted from references 8 and 11.

(2) Silaghi-Dumitrescu, R., Kurtz, D. M., Jr., Ljungdahl, L. G.;Lanzilotta, W. N. X-ray Crystal Structures of Moorella thermoacetica FprA. Novel Diiron Site Structure and Mechanistic Insights into a Scavenging Nitric Oxide Reductase. *Biochemistry* **2005**, *44*, 6492-6501.

(3) Hayashi, T., Caranto, J. D., Wampler, D. A., Kurtz, D. M., Jr.;Moënne-Loccoz, P. Insights into the Nitric Oxide Reductase Mechanism of Flavodiiron Proteins from a Flavin-Free Enzyme. *Biochemistry* **2010**, *49*, 7040−7049.

(4) Hayashi, T., Caranto, J. D., Matsumura, H., Kurtz, D. M., Jr.;Moënne-Loccoz, P. Vibrational Analysis of Mononitrosyl Complexes in Hemerythrin and Flavodiiron Proteins: Relevance to Detoxifying NO Reductase. *J. Am. Chem. Soc.* **2012**, *134*, 6878-6884.

(5) Caranto, J. D., Weitz, A., Giri, N., Hendrich, M. P.;Kurtz, D. M. J. A Diferrous-Dinitrosyl Intermediate in the N_2O-Generating Pathway of a Deflavinated Flavo-Diiron Protein. *Biochemistry* **2014**, *53*, 5631–5637.

(6) Kindermann, N., Schober, A., Demeshko, S., Lehnert, N.;Meyer, F. Reductive Transformations of a Pyrazolate-Based Bioinspired Diiron−Dinitrosyl Complex. *Inorg. Chem.* **2016**, *55*, 11538-11550.

(7) White, C. J., Speelman, A. L., Kupper, C., Demeshko, S., Meyer, F., Shanahan, J. P., Alp, E. E., Hu, M., Zhao, J.;Lehnert, N. The Semireduced Mechanism for Nitric Oxide Reduction by Non-Heme Diiron Complexes: Modeling Flavodiiron Nitric Oxide Reductases. *J. Am. Chem. Soc.* **2018**, *140*, 2562-2574.

(8) Jana, M., White, C. J., Pal, N., Demeshko, S., Cordes, C., Meyer, F., Lehnert, N.;Majumdar, A. Functional Models for the Mono- and Dinitrosyl Intermediates of FNORs: Semireduction versus Superreduction of NO. *J. Am. Chem. Soc.* **2020**, *142*, 6600-6616.

(9) Jiang, Y., Hayashi, T., Matsumura, H., Do, L. H., Majumdar, A., Lippard, S. J.;Moënne-Loccoz, P. Light-Induced N_2O Production from a Non-heme Iron–Nitrosyl Dimer. *J. Am. Chem. Soc.* **2014**, *136*, 12524-12527.

(10) Majumdar, A.;Lippard, S. J. Non-Heme Mononitrosyldiiron Complexes: Importance of Iron Oxidation State in Controlling the Nature of the Nitrosylated Products. *Inorg. Chem.* **2013**, *52*, 13292-13294.

(11) Jana, M., Pal, N., White, C. J., Kupper, C., Meyer, F., Lehnert, N.;Majumdar, A. Functional Mononitrosyl Diiron(II) Complex Mediates the Reduction of NO to N_2O with Relevance for Flavodiiron NO Reductases. *J. Am. Chem. Soc.* **2017**, *140*, 14380-14383.

(12) Majumdar, A., Apfel, U.-P., Jiang, Y., Moënne-Loccoz, P.;Lippard, S. J. Versatile Reactivity of a Solvent-Coordinated Diiron(II) Compound: Synthesis and Dioxygen Reactivity of a Mixed-Valent FeIIFeIII Species. *Inorg. Chem.* **2014**, *53*, 167-181.

(13) Harrop, T. C., Tonzetich, Z. J., Reisner, E.;Lippard, S. J. Reactions of Synthetic [2Fe-2S] and [4Fe-4S] Clusters with Nitric Oxide and Nitrosothiols. *J. Am. Chem. Soc.* **2008**, *130*, 15602-15610.

(14) Arulsamy, N., Bohle, D. S., Butt, J. A., Irvine, G. J., Jordan, P. A.;Sagan, E. Interrelationships between Conformational Dynamics and the Redox Chemistry of S-Nitrosothiols. *J. Am. Chem. Soc.* **1999**, *121*, 7115-7123.

(15) Feig, A. L., Bautista, M. T.;Lippard, S. J. A Carboxylate-Bridged Non-heme Diiron Dinitrosyl Complex. *Inorg. Chem.* **1996**, *35*, 6892-6898.

(16) Berto, T. C., Speelman, A., Zheng, S.;Lehnert, N. Mono- and Dinuclear Non-Heme Iron-Nitrosyl Complexes: Models for Key Intermediates in Bacterial Nitric Oxide Reductases. *Coord. Chem. Rev.* **2013**, *257*, 244-259.

(17) Borovik, A. S.;Que, L. Models for the iron(II)iron(III) and iron(II)iron(II) forms of iron-oxo proteins. *J. Am. Chem. Soc.* **1988**, *110*, 2345-2347.

(18) Speelman, A. L., White, C. J., Zhang, B., Alp, E. E., Zhao, J., Hu, M., Krebs, C., Penner-Hahn, J.;Lehnert, N. Non-heme High-Spin $\{FeNO\}^{6-8}$ Complexes: One Ligand Platform Can Do It All. *J. Am. Chem. Soc.* **2018**, *140*, 11341-11359.

(19) Berto, T. C., Hoffman, M. B., Murata, Y., Landenberger, K. B., Alp, E. E., Zhao, J.;Lehnert, N. Structural and Electronic Characterization of Non-Heme Fe(II)-Nitrosyls as Biomimetic Models of the Fe_B Center of Bacterial Nitric Oxide Reductase (NorBC). *J. Am. Chem. Soc.* **2011**, *133*, 16714–16717.

(20) Brown, C. A., Pavlosky, M. A., Westre, T. E., Zhang, Y., Hedman, B., Hodgson, K. O.;Solomon, E. I. Spectroscopic and theoretical description of the electronic structure of S= 3/2 iron-nitrosyl complexes and their relation to O2 activation by non-heme iron enzyme active sites. *J. Am. Chem. Soc.* **1995**, *117*, 715-732.

(21) Radon, M., Broclawik, E.;Pierloot, K. Electronic Structure of Selected {FeNO}7 Complexes in Heme and Non-Heme Architectures: A Density Functional and Multireference ab Initio Study. *J. Phys. Chem. B* **2010**, *114*, 1518-1528.

(22) Pohl, K., Wieghardt, K., Nuber, B.;Weiss, J. Preparation and magnetism of the binuclear iron(II) complexes $[\{Fe(C_9H_{21}N_3)X_2\}_2]$(X = NCS, NCO, or N_3) and their reaction with NO. Crystal structures of $[\{Fe(C_9H_{21}N_3)(NCS)_2\}_2]$ and $[Fe(C_9H_{21}N_3)(NO)(N_3)_2]$. *J. Chem. Soc. Dalton Trans.* **1987**, 187-192.

(23) Li, J., Banerjee, A., Pawlak, P. L., Brennessel, W. W.;Chavez, F. A. Highest Recorded N–O Stretching Frequency for 6-Coordinate {Fe-NO}^{7} Complexes: An Iron Nitrosyl Model for His_3 Active Sites. *Inorg. Chem.* **2014**, *53*, 5414–5416.

(24) Coufal, D. E., Tavares, P., Pereira, A. S., Hyunh, B. H.;Lippard, S. J. Reactions of Nitric Oxide with the Reduced Non-Heme Diiron Center of the Soluble Methane Monooxygenase Hydroxylase. *Biochemistry* **1999**, *38*, 4504-4513.

(25) Haskin, C. J., Ravi, N., Lynch, J. B., Muenck, E.;Que, L., Jr. Reaction of NO with the Reduced R2 Protein of Ribonucleotide Reductase from *Escherichia coli*. *Biochemistry* **1995**, *34*, 11090-11098.

(26) Zhang, Y., Pavlosky, M. A., Brown, C. A., Westre, T. E., Hedman, B., Hodgson, K. O.;Solomon, E. I. Spectroscopic and Theoretical Description of the Electronic Structure of the S = 3/2 Nitrosyl Complex of Non-heme Iron Enzymes. *J. Am. Chem. Soc.* **1992**, *114*, 9189-9191.

(27) Note: N_2O yields are reported with respect to different reference points (maximum N_2O yield, [reductant], [complex]) in different publications. In order to minimize confusion, all reported N_2O yields in this chapter are reported with respect to the concentration of the complex that generated N_2O.

(28) Confer, A. M., McQuilken, A. C., Matsumura, H., Moënne-Loccoz, P.;Goldberg, D. P. A Nonheme, High-Spin {FeNO}^{8} Complex that Spontaneously Generates N_2O. *J. Am. Chem. Soc.* **2017**, *139*, 10621-10624.

(29) Chuang, C. H., Liaw, W. F.;Hung, C. H. Conversion of Nitric Oxide into Nitrous Oxide as Triggered by the Polarization of Coordinated NO by Hydrogen Bonding. *Angew. Chem. Int. Ed.* **2016**, *55*, 5190-5194.

(30) Frisch, M. J., Trucks, G. W., Schlegel, H. B., Scuseria, G. E., Robb, M. A., Cheeseman, J. R., Scalmani, G., Barone, V., Mennucci, B., Petersson, G. A., Nakatsuji, H., Caricato, M., Li, X., Hratchian, H. P., Izmaylov, A. F., Bloino, J., Zheng, G., Sonnenberg, J. L., Hada, M., Ehara, M., Toyota, K., Fukuda, R., Hasegawa, J., Ishida, M., Nakajima, T., Honda, Y., Kitao, O., Nakai, H., Vreven, T., Montgomery, J. A., Jr., Peralta, J. E., Ogliaro, F., Bearpark, M., Heyd, J. J., Brothers, E., Kudin, K. N., Staroverov, V. N., Kobayashi, R., Normand, J., Raghavachari, K., Rendell, A., Burant, J. C., Iyengar, S. S., Tomasi, J., Cossi, M., Rega, N., Millam, J. M., Klene, M., Knox, J. E., Cross, J. B., Bakken, V., Adamo, C., Jaramillo, J., Gomperts, R., Stratmann, R. E., Yazyev, O., Austin, A. J., Cammi, R., Pomelli, C., Ochterski, J. W., Martin, R. L., Morokuma, K., Zakrzewski, V. G., Voth, G. A., Salvador, P., Dannenberg, J. J., Dapprich, S., Daniels, A. D., Farkas, O., Foresman, J. B., Ortiz, J. V., Cioslowski, J.;Fox, D. J.; Gaussian, Inc.: Wallingford, CT, 2009.

(31) Becke, A. D. Density-functional thermochemistry. III. The role of exact exchange. *J. Chem. Phys.* **1993**, *98*, 5648-5652.

(32) Lee, C., Yang, W.;Parr, R. G. Development of the Colle-Salvetti correlation-energy formula into a functional of the electron density. *Phys. Rev. B* **1988**, *37*, 785-789.

(33) Perdew, J. P., Burke, K.;Wang, Y. Generalized gradient approximation for the exchange-correlation hole of a many-electron system. *Phys. Rev. B* **1996**, *54*, 16533-16539.

(34) Wachters, J. H. Gaussian basis set for molecular wavefunctions containing third-row atoms. *J. Chem. Phys.* **1970**, *52*, 1033.

(35) Van Stappen, C.;Lehnert, N. Mechanism of N-N Bond Formation by Transition Metal-Nitrosyl Complexes: Modeling Flavodiiron Nitric Oxide Reductases. *Inorg. Chem.* **2018**, *57*, 4252-4269.

(36) Neese, F. Software update: the ORCA program system, version 4.0; Wiley Interdisciplinary Reviews: Computational Molecular Science, 2018; Vol. 8, p e1327. .

(37) Speelman, A. L.;Lehnert, N. Characterization of a High-Spin Non-Heme {FeNO}^{8} Complex: Implications for the Reactivity of Iron Nitroxyl Species in Biology. *Angew. Chem. Int. Ed.* **2013**, *52*, 12283-12287.

(38) Weigend, F. Accurate Coulomb-fitting basis sets for H to Rn. *Phys. Chem. Chem. Phys.* **2006**, *8*, 1057-1065.

(39) Bill, E. julX, Program for Simulation of Molecular Magnetic Data; Max-Planck Institute for Chemical Energy Conversion: Mülheim/ Ruhr, Germany, 2008.

(40) APEX II, 2009 ed.; Bruker Analytical X-ray Systems Inc.: Madison, WI, 2009. .

(41) Spek, A. L. Single-crystal structure validation with the program PLATON. *J. Appl. Crystallogr.* **2003**, *36*, 7-13.

(42) Spek, A. L. Structure validation in chemical crystallography. *Acta Cryst., Sect. D.: Biol. Cryst.* **2009**, *65*, 148-155.

(43) Sheldrick, G. M. A short history of SHELX. *Acta Crystallographica Section A* **2008**, *64*, 112-122.

(44) Dolomanov, O. V., Bourhis, L. J., Gildea, R. J., Howard, J. A. K.;Puschmann, H. OLEX2: a complete structure solution, refinement and analysis program. *J. Appl. Crystallogr.* **2009**, *42*, 339-341.

Chapter 4

Perturbations of ON-NO Distances and Dihedral Angles: Unusual Reactivity and Inhibition of N-N Coupling

In Chapter 3, the degrees of activation that are necessary to generate N_2O via unimolecular coupling from a [hs-{FeNO}^{7}]$_2$ complex or bimolecular coupling between two hs-Fe^{II}{FeNO}^{7} complexes were compared.[1, 2] The results from Chapter 3 show that the coupling of two NO in close proximity within the [hs-{FeNO}^{7}]$_2$ complex proceeds via facile *semi*reduction, whereas the coupling between two hs-Fe^{II}{FeNO}^{7} complexes requires *super*reduction, emphasizing that the binding of two NO ligands in close proximity strongly aides in facile N-N coupling. This chapter takes a step further to expand on our understanding of the structural prerequisites for N-N coupling within the context of diiron dinitrosyl complexes. We had initially proposed that the near coplanar binding of the NO ligands, enforced by the bridging OPr^- ligand in [Fe$_2$(BPMP)(OPr)(NO)$_2$](OTf)$_2$, presented in Chapter 2[3], is essential in its ability to carry out such rapid N-N coupling. In support of this hypothesis, Meyer and coworkers reported a [hs-{FeNO}^{7}]$_2$ complex with a dinucleating pyrazole/triazacyclononane coligand with completely trans (180^o) NO ligands that is unable to generate N_2O.[4] Instead, upon the addition of one reductive equivalent, the complex disproportionates into a [hs-{Fe(NO)$_2$}^{9}]$_2$ di-DNIC and a diferrous product. Preliminary studies on the complex [Fe$_2$(BPMP)(OTf)$_2$(NO)$_2$](OTf) without a bridging carboxylate ligand, carried out by Dr. Amy Speelman, demonstrated (1) that in the absence of the

bridging carboxylate, the two NO bind in a non-coplanar geometry with an ON-NO dihedral angle of 26.4° and (2) that N_2O generation was significantly inhibited.[5] This chapter expands on Amy's preliminary work and presents a series of BPMP complexes containing different monodentate ligands in place of the bridging carboxylate: $[Fe_2(BPMP)(X)_2(NO)_2]^{3+/1+}$, where X = N-methylimidazole (NMeIm); Methanol (MeOH), or trifluoromethanesulfonate ($^{-}$OTf). These complexes were structurally characterized either by X-Ray crystallography or their structures were optimized by DFT, and their reactivities towards NO reduction and N_2O formation are compared.

4.1 Synthesis and Characterization of $[Fe_2(BPMP)(X)_2(NO)_2]^{3+/1+}$

Synthesis of $[Fe_2(BPMP)(X)_2(NO)_2]^{3+/1+}$

The synthesis and purification of BPMP complexes with two monodentate ligands (instead of a bridging carboxylate) can be directly adapted from the Chapter 2 procedure for the synthesis of $[Fe_2(BPMP)(OPr)(NO)_2]^{2+}$, where the bridging $^{-}$OPr is either substituted for two equivalents of the monodentate ligand for the X = NMeIm complex, or where no monodentate ligand is added for the X = MeOH or $^{-}$OTf complexes.[3] In these cases, the metallation is still carried out in MeOH followed by precipitation with Et_2O. The precipitate is then filtered off and washed with CH_2Cl_2 to remove Na/KOTf salt byproducts. To generate the $^{-}$OTf complex, the CH_2Cl_2 filtrate is directly precipitated with hexanes to afford the complex $[Fe_2(BPMP)(OTf)_2](OTf)$. In order to make the MeOH complex, the CH_2Cl_2 filtrate must first be evaporated and the residue re-dissolved in MeOH and precipitated with Et_2O to generate the $[Fe_2(BPMP)(MeOH)_2](OTf)_3$ analog. The nitrosylations of these three complexes are adapted from the general nitrosylation procedure in Chapter 2, where the X = $^{-}$OTf and NMeIm derivatives are nitrosylated in CH_2Cl_2 and precipitated with hexanes

and the X = MeOH derivative is nitrosylated in MeOH and precipitated with Et_2O. The complexes discussed in this chapter and their sample codes are listed in Table 4.1.

Attempts to crystallize and structurally characterize both the metallated precursors and NO complexes across this series of complexes was met with various degrees of success. Importantly, the $[Fe_2(BPMP)(NMeIm)_2(OTf)](OTf)_2$ precursor was successfully crystallized (Figure 4.1),

Table 4.1 Sample codes for the three dinuclear BPMP complexes containing monodentate ligands that are discussed in this chapter, and a mononuclear ligand (BMPA) used to model the BPMP N_{tert} and two N_{py} coordination within a mononuclear system.

Complex	Code
$[Fe_2(BPMP)(OTf)_2(NO)_2](OTf)$	**1**
$[Fe_2(BPMP)(NMeIm)_2(NO)_2](OTf)_3$	**2**
$[Fe_2(BPMP)(MeOH)_2(NO)_2](OTf)$	**3**
$[Fe(BMPA)(CH_3CN)_2(NO)](OTf)_2$	**4**

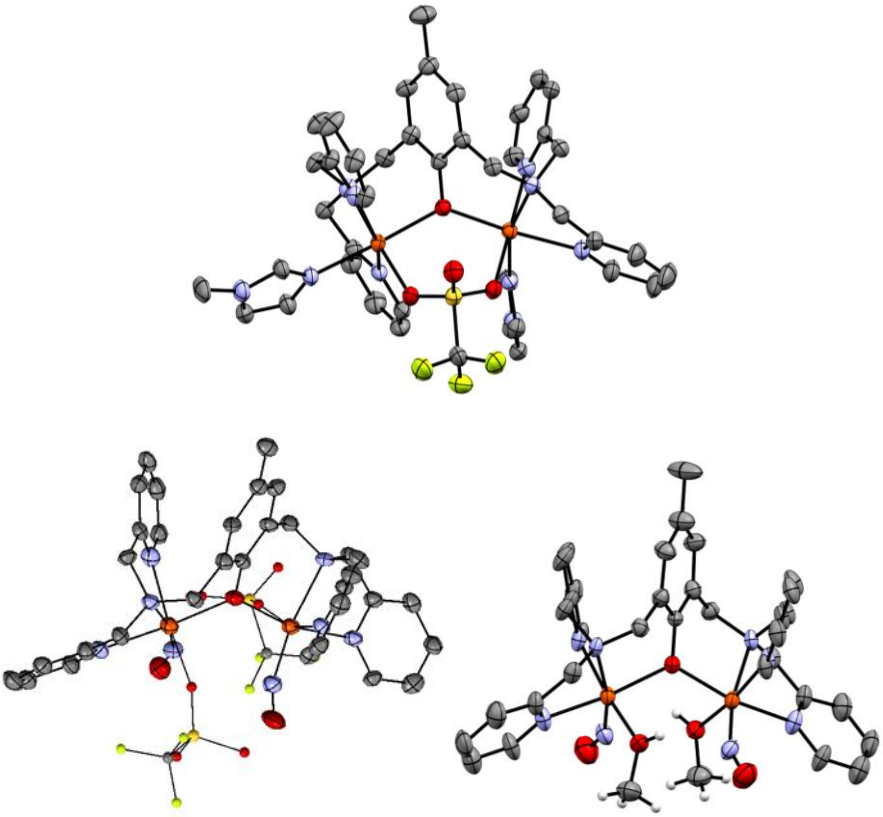

Figure 4.1 Top: Crystal structure of $[Fe_2(BPMP)(NMeIm)_2(OTf)](OTf)_2$ obtained by room-temperature vapor diffusion of Et_2O into a methanolic solution of $[Fe_2(BPMP)(NMeIm)_2(OTf)](OTf)_2$. Bottom Left: Crystal structure of **1** obtained by Dr. Amy Speelman via the room-temperature vapor diffusion of Et_2O into a concentrated CH_3CN solution of **1**.[5] Bottom Right: Crystal structure of **3** obtained by vapor diffusion of Et_2O into a concentrated MeOH solution of $[Fe_2(BPMP)(MeOH)_2(NO)_2](OTf)_3$ complex.

containing non-coplanar NMeIm ligation with a NMeIm-Fe-Fe-NMeIm dihedral angle of 58.3°. Unfortunately, the NO complex with NMeIm coligands (**2**) was typically quite oily and was never successfully crystallized. Nonetheless, crystal structures of both **1** and **3** were successfully obtained (Figure 4.1). Dr. Amy Speelman crystallized **1** and provided a preliminary characterization of this complex, showing a ON-NO dihedral angle of 26.4°.[5] The MeOH complex **3** was fortuitously crystallized (Figure 4.1) from my initial attempts to metallate BPMP with 2,4,6-trimethylpyridine (TMP) as another monodentate ligand. Upon vapor diffusion of Et_2O into a MeOH solution of the "TMP" complex, crystals of **3** containing two bound MeOH ligands formed instead, with a ON-NO dihedral angle of 90.4°. In order to verify that the MeOH complex **3** was in fact the bulk product made from the metallation with TMP, an IR (KBr) of the crystals formed from the supposed "TMP" complex was taken and compared to the intentionally synthesized MeOH complex discussed above (see Figure 4.2), showing that these are both in fact the same complex. We suspect that the 2,6-methyl substituents of TMP sterically hinder this ligand from binding, although additional attempts at metallating with 4-methylpyridine (pMePy) were also

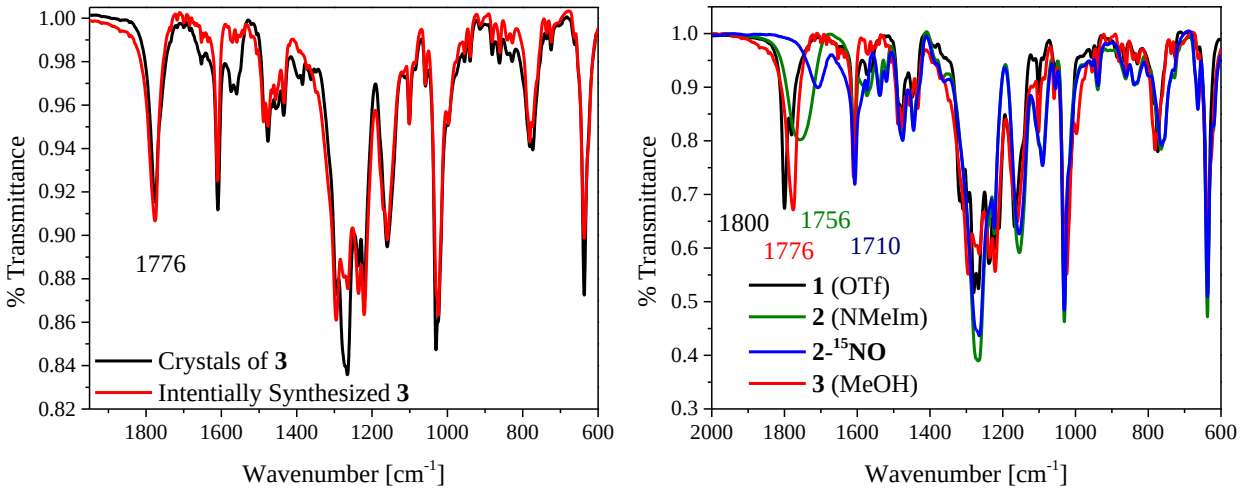

Figure 4.2 Left: Overlay of the IR spectra (KBr) of $[Fe_2(BPMP)(MeOH)_2(NO)_2](OTf)_3$ (**3**) used to generate the X-Ray crystal structure shown in Figure 4.1 and the bulk product of intentionally synthesized **3**. Right: Overlay of the IR spectra of the series of complexes **1-3** and **2-^{15}NO**, emphasizing their discrete NO stretching frequencies.

unsuccessful, instead resulting in the formation of the OTf complex **1**, as determined by elemental analysis. While DFT modelling clearly shows that TMP is sterically unable to bind, resulting in a significantly elongated Fe-N(TMP) distance to minimize steric repulsion with the 2,6-dimethyl substituents of TMP, it is unclear why a pMePy-ligated complex was unable to be isolated, since this steric congestion does not exist with this ligand (Figure 4.3). An IR (KBr) comparison of all three isolated NO-complexes **1-3** is shown in Figure 4.2, as well as the ^{15}NO analog of **2** (**2-^{15}NO**), with all three derivatives containing discrete N-O stretching frequencies in accordance with the ligation of three discrete monodentate ligands X.

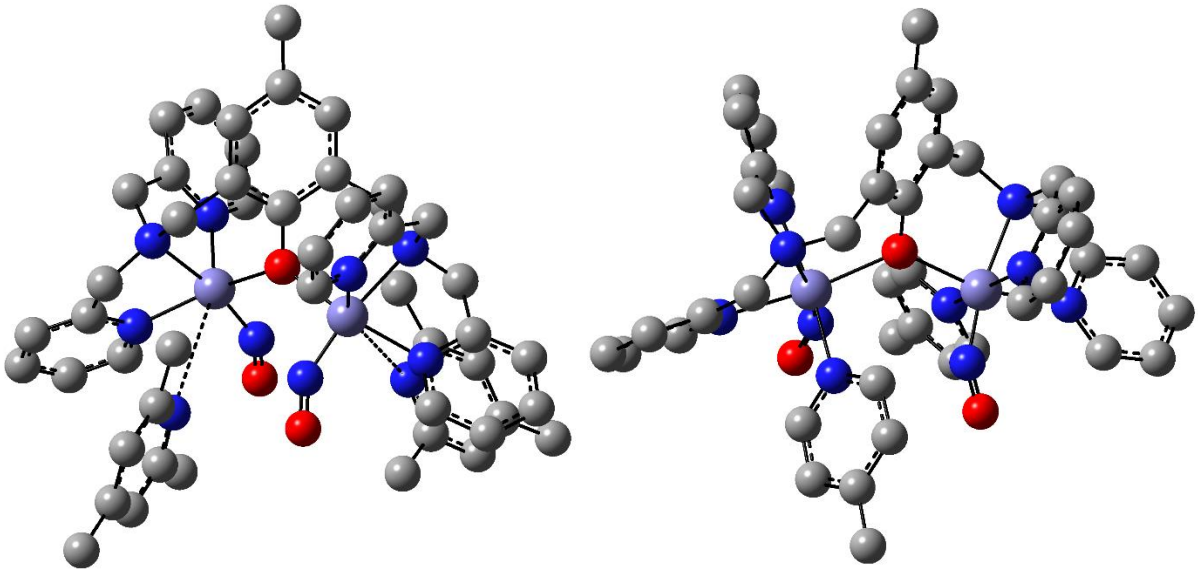

Figure 4.3 Left: Partially optimized (BP86/6-311G) structure of $[Fe_2(BPMP)(TMP)_2(NO)_2]^{3+}$, highlighting the elongated Fe-N(TMP) bond distance (4.02 Å). Right: In contrast, the structure of the optimized (BP86/6-311G(d) complex $[Fe_2(BPMP)(pMePy)_2(NO)_2$ contains a typical Fe-N(pMePy) bond distance of 2.21 Å.

Since the structures of the [hs-{FeNO}^{7}]$_2$ cores are of importance in correlating NO binding geometries and N-N distances to the N-N coupling reactivity, DFT optimizations and frequency calculations were employed to supplement the X-Ray crystallographic data discussed above. Using the crystal structures of both **1** and **3** as starting points, Gaussian 09[6] optimizations were performed on **1** and **3** using both BP86[7]/6-311G(d)[8-10] and BP86/TZVP[11, 12], following the

methods described in Chapter 3, to evaluate how well these methods predict the relevant core structural features of these complexes. The fully optimized structures reproduce the key Fe-Fe, Fe-N(O), and N-O distances, as well as the Fe-N-O angles with high fidelity. For **1**, the N-Fe-Fe-N and O-N-N-O dihedral angles are reproduced well (see Table 4.2), whereas larger deviations are observed for **3**, but the agreement is still reasonable. As such, **2** was similarly optimized, using the crystal structure of **1** as a starting geometry. Lastly, the frequency calculations on **1-3** reproduce the trend in experimental NO stretching frequencies in Figure 4.3 well, with **1** containing the highest predicted frequency at 1789 and 1765 cm^{-1} for the symmetric/asymmetric stretches, followed by **3** at 1765 and 1747 cm^{-1}, and **2** at 1738 and 1713 cm^{-1}. Overall, the DFT results reproduce the relevant structural and vibrational data with decent accuracy and show that the series of complexes **1-3** contains a distribution of ON-NO dihedral angles due to the binding geometries of the different monodentate ligands.

Table 4.2 Overview of key experimental and DFT-optimized structural and vibrational parameters for complexes **1-3**.

	1 (OTf)			**2 (NMeIm)**			**3 (MeOH)**		
	TZVP	**6311G(d)**	**Expt**	**TZVP**	**6311G(d)**	**Expt**	**TZVP**	**6311G(d)**	**Expt**
Fe-Fe (Å)	3.74	3.69	3.66	3.90	3.85	--	3.86	3.81	3.72
Fe-N (Å)	1.75	1.73, 1.74	1.75, 1.78	1.74	1.73	--	1.73	1.72	1.76
N-O (Å)	1.17	1.17	1.14, 1.17	1.18	1.18	--	1.17	1.18	1.18
Fe-N-O (º)	150.7, 147.2	148.4, 146.2	153.5 155.9	147.5	146.6	--	149.0	147.4	153.7
ON-NO (Å)	3.04	2.90	3.13	3.78	3.73	--	3.36	3.34	3.96
Dihedral N-Fe-Fe-N (º)	51.5	50.9	56.2	76.8	79.2	--	64.7	67.13	85.1
Dihedral O-N-N-O (º)	21.3	26.4	26.4	18.2	20.51	--	72.2	79.5	90.4
ν(NO) (cm^{-1})	1789, 1765	1784, 1761	1800	1728, 1713	1729, 1715	1756	1765, 1747	1745, 1729	1776

4.2 Chemical and Electrochemical Reduction: N_2O Yields and Mechanistic Studies

Chemical and Electrochemical Reduction of 1-3: Mechanistic Insights

Cyclic voltammograms of **1-3** (Figure 4.4) reveal similar reductive features for **1** and **3**, both of which exhibit at least three reductive events at -0.77, -1.05, and -1.40 V for **1** and -0.65, -0.80, and -1.12 V (all vs. Fc^+/Fc) for **3** with minimal reversibility in the subsequent oxidative sweep. In contrast, **2** contains two quasi-reversible redox events at -0.90 and -1.12 V. As discussed further in section 4.3, both **1** and **3** can generate increased N_2O yields compared to **2**, in line with

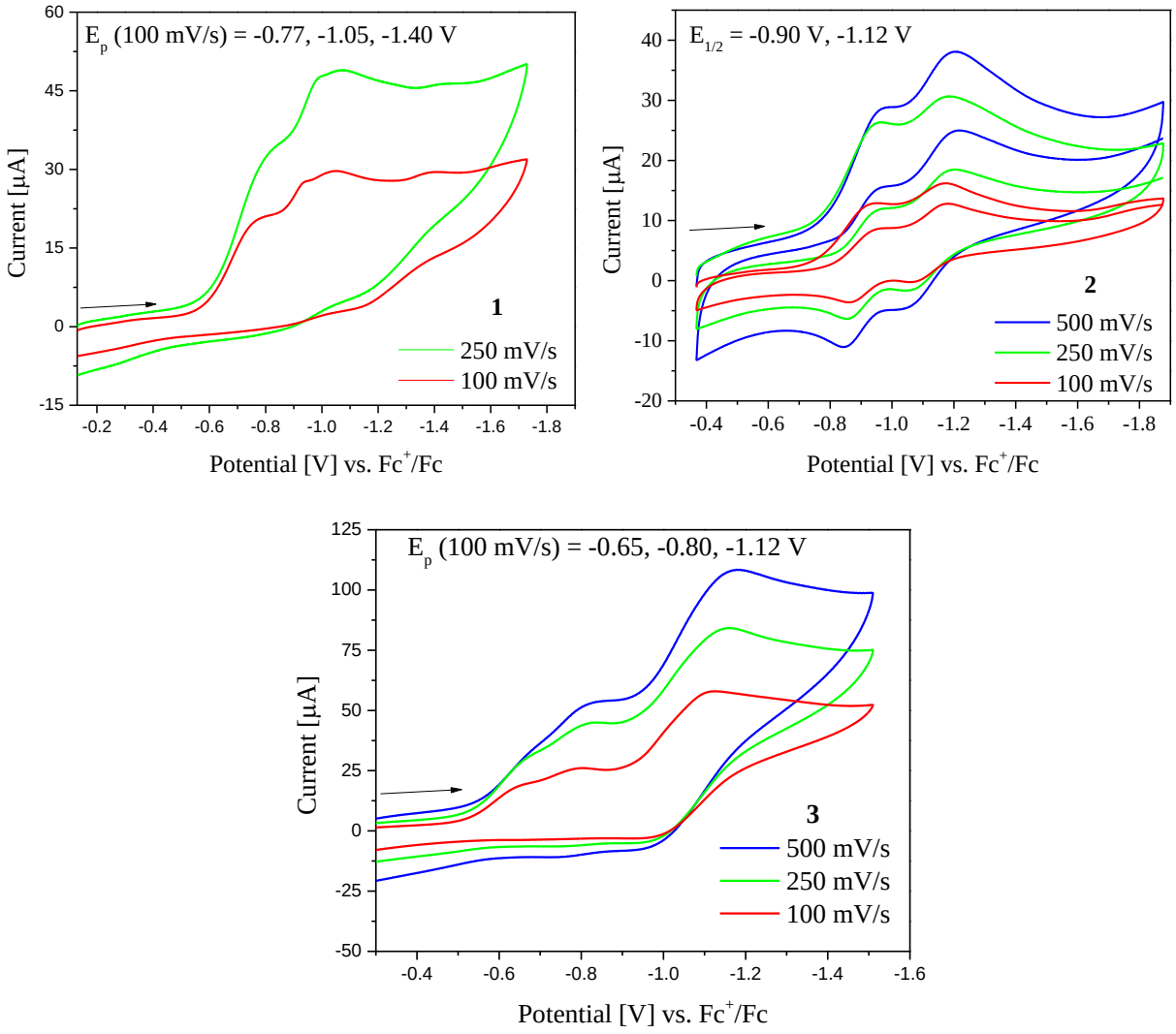

Figure 4.4 Cyclic voltammograms of **1** (top left), **2** (top right), and **3** (bottom). Conditions: ~5 mM **1-3** with 0.1 M [TBA][OTf] as the supporting electrolyte. **1** and **2** were taken in CH_2Cl_2 and **3** was taken in MeOH.

there being no oxidative current drawn in the reverse scan. In contrast, the reduction of **2** leads to a more stable product, with quasi-reversible reductive events at -0.90 and -1.12 V. The nature of these reduced products is discussed further below.

Based on the reduction potentials determined by CV, the chemical and electrochemical reductions of these complexes were performed. We initially carried out an IR-SEC reduction on a ~5 mM solution of **2** in CH_2Cl_2, containing ~0.1 M [TBA][OTf] as the supporting electrolyte. Upon holding the cell at a potential of -1.4 V vs. Ag wire, the initial N-O stretching bands of **2** at 1766 and 1747 cm^{-1} decayed with the formation of numerous new bands, first at 1789 and 1716 cm^{-1} and shortly after at 1682 and 1620 cm^{-1}, accompanied by the formation of N_2O at 2222 cm^{-1} as the reduction proceeded (Figure 4.5). While this was initially difficult to rationalize, the data clearly indicate that numerous reduced species were formed upon the electrochemical reduction of the $[hs\text{-}\{FeNO\}^7]_2$ complex, that these species are still capable of generating N_2O, and that N-N coupling was substantially inhibited for this complex when contrasted with the analogous IR-SEC

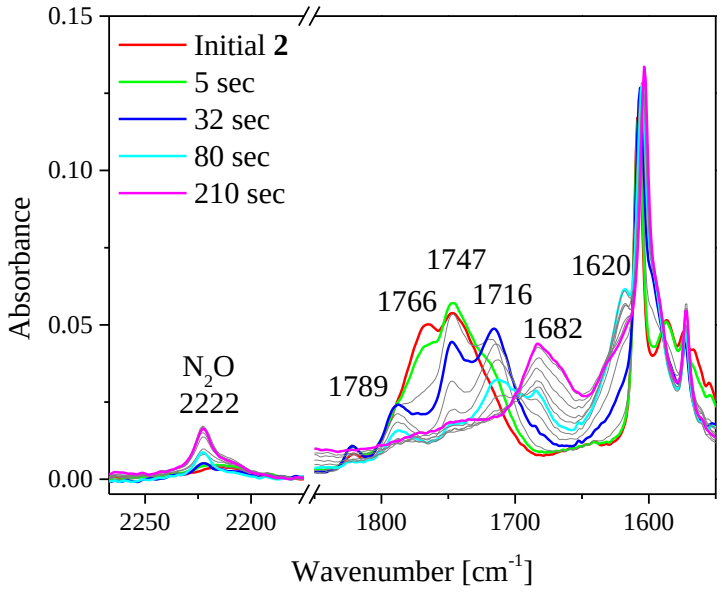

Figure 4.5 IR-SEC reduction of a ~5 mM solution of **2** containing ~0.1 M [TBA][OTf], carried out by holding the potential at -1.4 V vs. Ag wire over the course of 210 seconds.

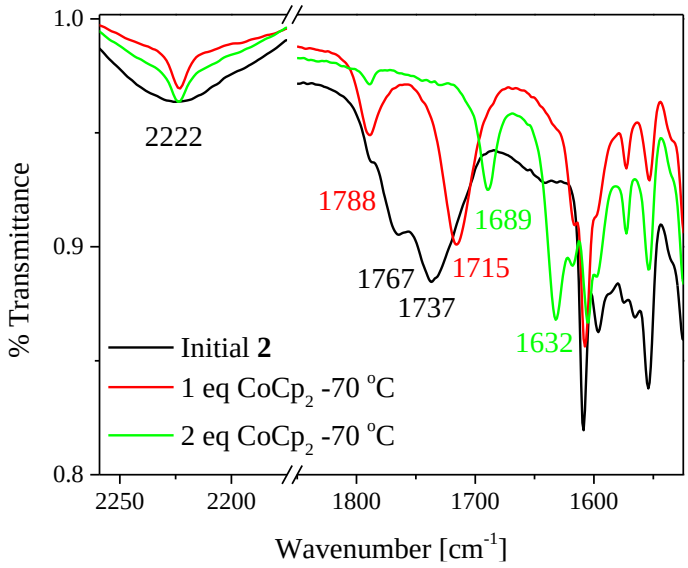

Figure 4.6 Solution-IR overlay of the initial dinitrosyl **2** and its reduced $\{Fe(NO)_2\}^{9/10}$ products upon chemical reduction with either one or two equivalents of $CoCp_2$ at -70 °C in CH_2Cl_2.

data for $[Fe_2(BPMP)(OPr)(NO)_2](OTf)_2$ from Chapter 2.[3] The nature of the new compounds responsible for the new N-O stretching bands observed upon reduction was clarified by carrying out a bulk chemical reduction of **2** with either one or two equivalents of $CoCp_2$ at -70 °C in CH_2Cl_2, and by characterizing the reduced products by solution IR spectroscopy (Figure 4.6). In this experiment, upon the addition of one equivalent of $CoCp_2$ to **2**, two new NO-bands form at 1788 and 1715 cm^{-1} that shift down to 1689 and 1632 cm^{-1} upon addition of the second reductive equivalent. These two-band signals are a fingerprint of DNICs and suggest that a hs-$\{Fe(NO)_2\}^9$ and a hs-$\{Fe(NO)_2\}^{10}$ species are sequentially formed upon addition of one and two equivalents of reductant, respectively, as well as some N_2O. There are also some examples of mononuclear hs-$\{FeNO\}^7$ complexes that form DNIC products upon chemical reduction[13, 14], though at 50% efficiency, following the eqns:

$$2\{FeNO\}^7 + e^- \rightarrow \{Fe(NO)_2\}^9 + Fe^{II}$$

$$2\{FeNO\}^7 + 2e^- \rightarrow \{Fe(NO)_2\}^{10} + Fe^{II}$$

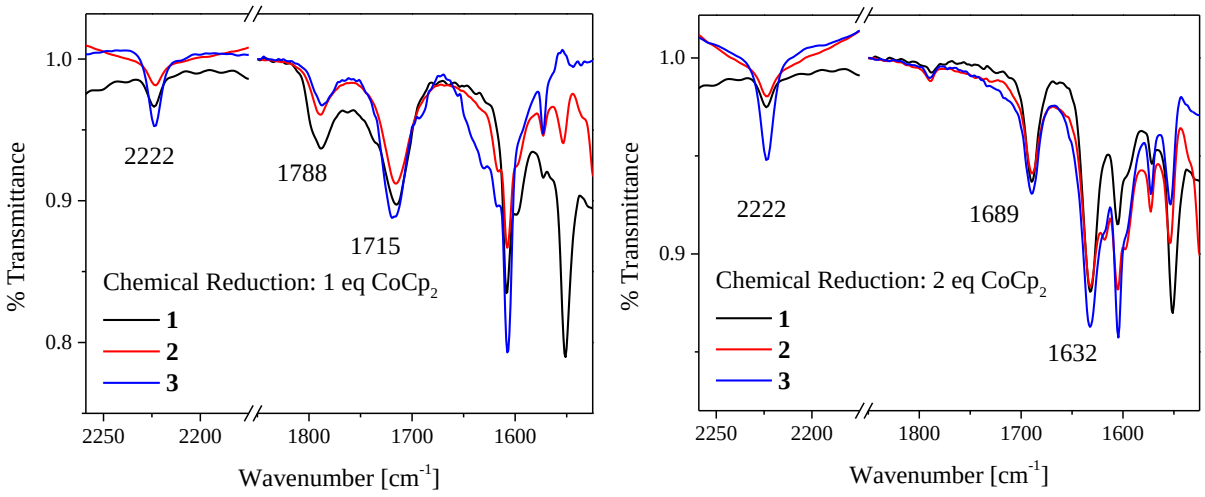

Figure 4.7 Left: Solution IR overlay of the $\{Fe(NO)_2\}^9$ DNIC product, with NO-bands at 1788 and 1715 cm^{-1}, that forms upon bulk one-electron reduction of **1-3** at -70 °C in CH_2Cl_2. Right: Solution IR overlay of the $Fe(NO)_2\}^{10}$ DNIC product, with NO-bands at 1689 and 1632 cm^{-1}, that forms upon bulk two-electron reduction of **1-3** at -70 °C in CH_2Cl_2.

We propose that the DNICs formed here follow a related, unimolecular mechanism from a hs-[{FeNO}^{7}{FeNO}^{8}] diiron dinitrosyl intermediate to generate the respective hs-Fe^{II}{Fe(NO)$_2$}$^{9/10}$ DNICs. More interestingly, the series of complexes **1-3** generate the exact same DNICs, as evident from identical N-O stretching bands for both the one- and two-electron reductions carried out at -70 °C in CH_2Cl_2 (Figure 4.7), implying that the monodentate ligands X are no longer coordinated to the DNIC-containing iron center. This is not entirely unexpected since the starting [hs-{FeNO}^{7}]$_2$ complexes all start out with six-coordinate (6c) iron centers, and would require at least displacement of one ligand to house a second NO ligand. While there are a few special cases of 6c DNICs reported in the literature[4, 15-17], the body of DNIC literature by and large consists of numerous four-coordinate[5, 15] (4c) and five-coordinate[16, 18] (5c) DNICs, supporting the loss of at least both monodentate ligands from the DNIC-containing Fe center. With a large body of reported 4c and 5c DNICs, one diagnostic feature that is commonly used to distinguish between 4c/5c/6c DNICs is the splitting between the symmetric and antisymmetric N-O stretching bands ($\Delta\nu_{NO}$) of the DNIC[15]. 6c DNICs have a $\Delta\nu_{NO}$ of ~110 cm^{-1}, while cationic 5c

Scheme 4.1 Proposed mechanism for the sequential one and two electron reduction of **1-3**, including key spectroscopic parameters for all experimentally captured intermediates.

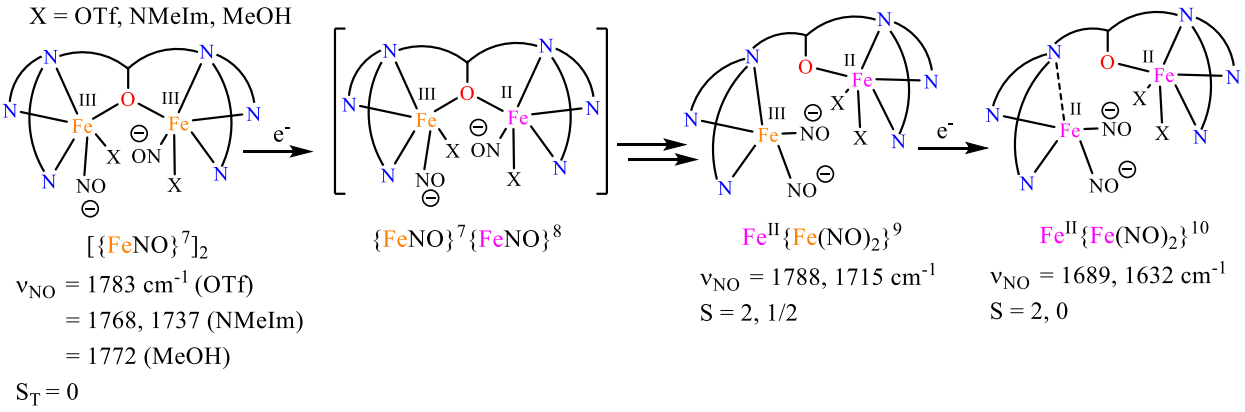

hs-{Fe(NO)$_2$}^{9} DNIC complexes have $\Delta\nu_{NO}$ of 73 cm^{-1} and neutral 4c hs-{Fe(NO)$_2$}^{10} DNICs have $\Delta\nu_{NO}$ values ranging from 45-60 cm^{-1}.[15] Based on this, we propose that the DNICs formed from the chemical reduction of **1-3** above are a 5c hs-Fe^{II}{Fe(NO)$_2$}^{9} and 4c hs-Fe^{II}{Fe(NO)$_2$}^{10} (Scheme 4.1). EPR spectroscopy lends additional support to these formulations. The [hs-{FeNO}^{7}]$_2$ starting material contains two antiferromagnetically coupled S = 3/2 centers, giving a S_t = 0 ground state electronic structure. The proposed hs-Fe^{II}{Fe(NO)$_2$}^{10} intermediate contains a S = 2 hs-Fe^{II} and a S = 0 {Fe(NO)$_2$}^{10} fragment, both of which are similarly EPR silent. However, the hs-Fe^{II}{Fe(NO)$_2$}^{9} intermediate contains a S = 2 hs-Fe^{II} and a S = ½ {Fe(NO)$_2$}^{9} fragment, and should therefore be EPR active. Indeed, upon one-electron reduction of **2** at -70 °C in CH_2Cl_2, a large g = 2.037 signal appears (Figure 4.8). Importantly, the g = 2.037 signal implies that the S = ½ hs-{Fe(NO)$_2$}^{9} fragment is *uncoupled* from the S = 2 hs-Fe^{II} fragment (the coupled system would either have a S= 5/2 or 3/2 ground state), suggesting that the phenolate bridge has been broken and likely shifts to a monodentate coordination of the hs-Fe^{II} fragment. This would then generate a 5c DNIC as predicted based on the $\Delta\nu_{NO}$ value of 73 cm^{-1}, with BPMP coordination to the DNIC from the N_{tert} (tertiary amine) and two N_{py} (pyridine) groups, and the two NO as the 4th and 5th ligands. We further propose that the monodentate ligand X shifts over to the hs-Fe^{II} center,

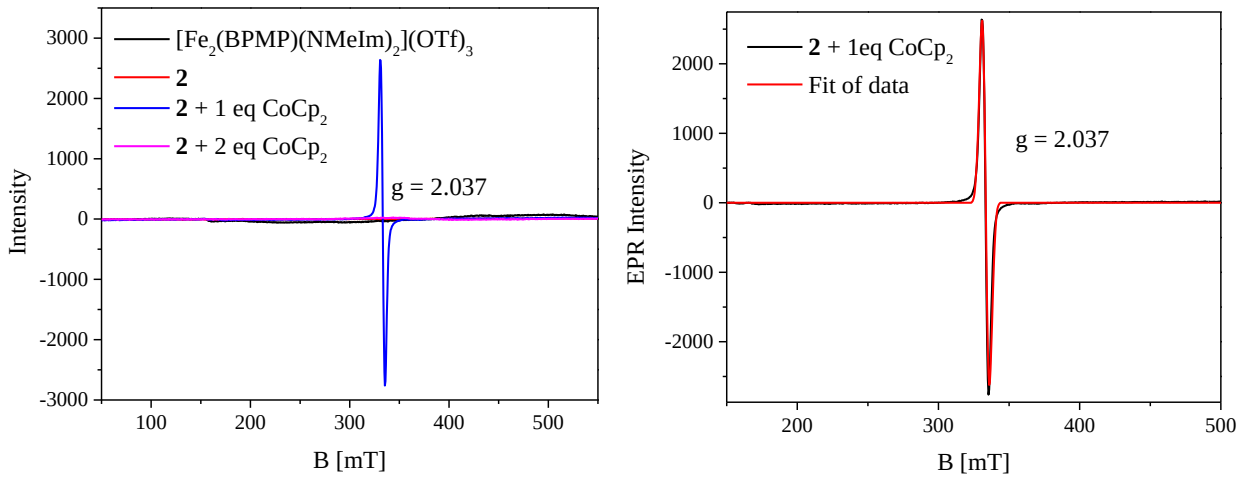

Figure 4.8 Left: Overlay of the EPR spectra of the metallated precursor $[Fe_2(BPMP)(NMeIm)_2](OTf)_3$, **2**, and of its one-/two-electron reduced hs-Fe^{II}{FeNO}$^{9/10}$ products. All species other than the hs-Fe^{II}{$Fe(NO)_2$}^{9} complex are EPR silent. Right: EPR spectrum and fit for the proposed hs-Fe^{II}{$Fe(NO)_2$}^{9} intermediate of **2** that forms upon the one-electron reduction at -70 °C in CH_2Cl_2. The large g = 2.037 signal corresponds to the S = ½, hs-{$Fe(NO)_2$}^{9} unit, uncoupled from the Fe^{II} center. Conditions: $[Fe_2(BPMP)(NMeIm)_2](OTf)_3$ = 2 mM dissolved inCH_2Cl_2 at RT; [**2**] = 2 mM dissolved in CH_2Cl_2 at RT; reaction of **2** + 1 or 2 eq $CoCp_2$ was carried out at -70 °C in CH_2Cl_2 and samples were immediately frozen in liquid nitrogen. Spectra were taken at 4-7 K, with 2 mW power, and 9.326 Gz frequency. The S = 1/2 data are simulated with $g_x = g_y = g_z$ = 2.0365 and $sg_x = sg_y = sg_z = 0.02$.

completing its coordination sphere. The g-value of 2.037 is within the typical range of mono-iron DNICs, which have isotropic g-values ranging from ~2.01-2.03 (in contrast to diiron RRE-type hs-{$Fe(NO)_2$}^{9}/hs-{$Fe(NO)_2$}^{10} DNICs, which tend to have axial signals)[15]. Within this bracket of g-values, 4c hs-{$Fe(NO)_2$}^{9} DNICs tend to have g ~ 2.03, whereas the reported 5c and 6c hs-{$Fe(NO)_2$}^{9} DNICs have g ~ 2.01-2.02, placing the g-value for **2** + 1 eq $CoCp_2$ slightly outside of the typical range for 5c DNICs. Nonetheless, the EPR data clearly point to the loss of the central phenolate bridge, the $\Delta\nu_{NO}$ of 73 cm^{-1} points to a 5c structure, and as will be discussed below, DFT modelling further supports our 5c assignment.

As an additional mechanistic subtlety, we found that the chemical reduction of **1-3** in CH_3CN results in the stabilization of the DNIC products (compared to CH_2Cl_2), at hour timescales when working at room-temperature. For **2**, the chemical reduction in CH_3CN results in identical hs-Fe^{II}{$Fe(NO)_2$}$^{9/10}$ products with NO bands at 1785 and 1709 cm^{-1} for the hs- Fe^{II}{$Fe(NO)_2$}^{9}

and 1689 and 1636 cm^{-1} for the hs-$Fe^{II}\{Fe(NO)_2\}^{10}$ complexes, respectively, as determined by a solution IR redox titration that was carried out over 1 hr at RT (Figure 4.9). The reduction of **2-^{15}NO** leads to a 35 cm^{-1} shift of the N-O stretch down to 1750 and 1675 cm^{-1} for the hs-$Fe^{II}\{Fe(NO)_2\}^9$ complex, and a 42 cm^{-1} shift of the N-O stretch to 1647 and 1594 cm^{-1} for the hs-

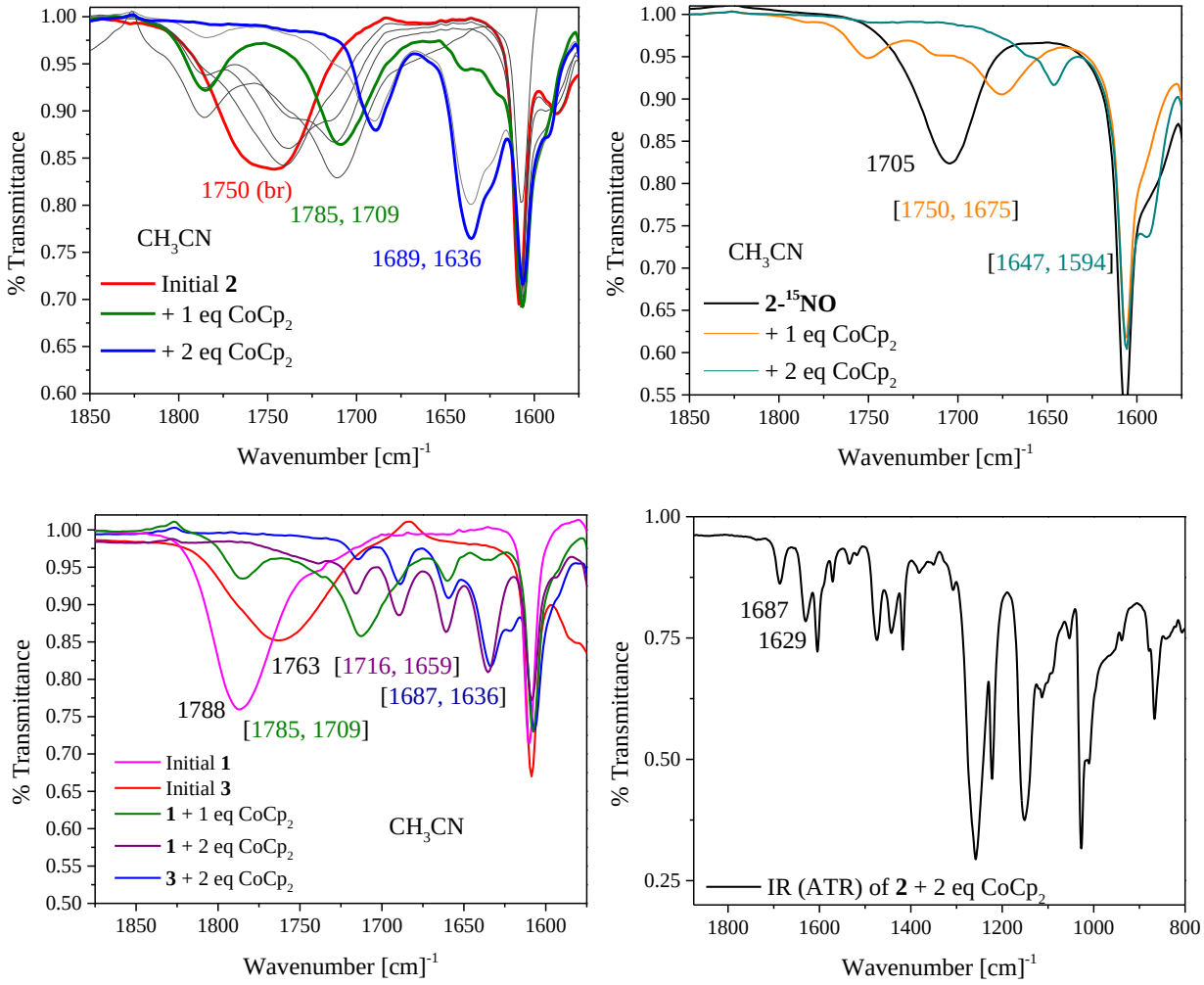

Figure 4.9 Top left: A room temperature redox titration of **2** with $CoCp_2$ in CH_3CN over the course of ~ 1 hr shows the sequential formation of hs-$Fe^{II}\{Fe(NO)_2\}^{9/10}$ intermediates that were previously only isolated at -70 °C in CH_2Cl_2. Top right: Solution IR of the **2-^{15}NO** complex and its one/two electron reduced hs-$\{Fe(NO)_2\}^{9/10}$ products. Bottom left: Reduction of **1** and **3** in CH_3CN with one equivalent of reductant similarly produces the same hs-$Fe^{II}\{Fe(NO)_2\}^9$ species observed at -70 °C in CH_2Cl_2. However, reduction of **1** and **3** with two equivalents of $CoCp_2$ in CH_3CN results in two discrete hs-$Fe^{II}\{Fe(NO)_2\}^{10}$ species: one set of signals at 1687 and 1636 cm^{-1} is identical to the DNIC bands observed at -70 °C, whereas the second set at 1716 and 1659 cm^{-1} is unique. Bottom Right: Single successful attempt at isolating the DNIC product(s) upon the chemical reduction of **2** at RT, showing quite strong $Fe^{II}\{Fe(NO)_2\}^{10}$ bands upon isolation. Note that this ATR spectrum was taken immediately upon filtration of the powder after removal of the solution from the -35° freezer.

$Fe^{II}\{Fe(NO)_2\}^{10}$ species (Figure 4.9) However, this is not the case for **1** or **3**, both of which make a similar hs-$Fe^{II}\{Fe(NO)_2\}^{9}$ DNIC containing symmetric/asymmetric N-O stretching frequencies at 1785 and 1709 cm^{-1}, but form two distinct hs-$Fe^{II}\{Fe(NO)_2\}^{10}$ DNICs with frequencies of 1716/1659 and 1687/1636 cm^{-1}(Figure 4.9), respectively. It is currently not clear why a second set of DNIC signals appears under these conditions. This finding is further discussed below (complex **4**). Attempts at isolating the DNIC products in the solid state were made by precipitating the bulk CH_3CN reduction products with Et_2O and immediately storing the product in the -35 ^oC glovebox freezer overnight to precipitate. While IR(ATR) spectra taken on the powder that was isolated immediately upon filtration resulted in an IR spectrum with strong hs-$Fe^{II}\{Fe(NO)_2\}^{10}$ DNIC bands on one occasion (Figure 4.9), the majority of isolation attempts resulted in weak DNIC IR-bands, likely due to its instability, even in the solid state.

In solution, while the hs-$Fe^{II}\{Fe(NO)_2\}^{9/10}$ DNICs are more stable in CH_3CN than in CH_2Cl_2, we also found that the hs- $Fe^{II}\{Fe(NO)_2\}^{9}$ DNIC decomposed much more rapidly in solution than its hs- $Fe^{II}\{Fe(NO)_2\}^{10}$ analog. As shown in Figure 4.10, the one electron reduction of **2** at RT in CH_3CN leads to the formation of the hs-$Fe^{II}\{Fe(NO)_2\}^{9}$ with bands at 1785 and 1709 cm^{-1}. This species largely decays over the course of ~ 35 mins, with minor additional decomposition up to 2 hrs. In contrast, the two-electron reduction of **2** leads to a stable hs-$Fe^{II}\{Fe(NO)_2\}^{10}$ with bands at 1689 and 1636 cm^{-1} that only minimally decay over 2 hrs. This finding is consistent with the electronic structure descriptions of these two states discussed in Chapter 1, which show that the Fe-NO bond strength *increases* upon the reduction of hs-$\{Fe(NO)_2\}^{9}$ to hs-$\{Fe(NO)_2\}^{10}$, owing to a significant enhancement of π-backbonding in the hs-$\{Fe(NO)_2\}^{10}$ state.[13, 19] This means that the lability of the NO ligand is larger in the hs-$\{Fe(NO)_2\}^{9}$ compared to the hs-$\{Fe(NO)_2\}^{10}$ state. As will be discussed below, this has implications for the

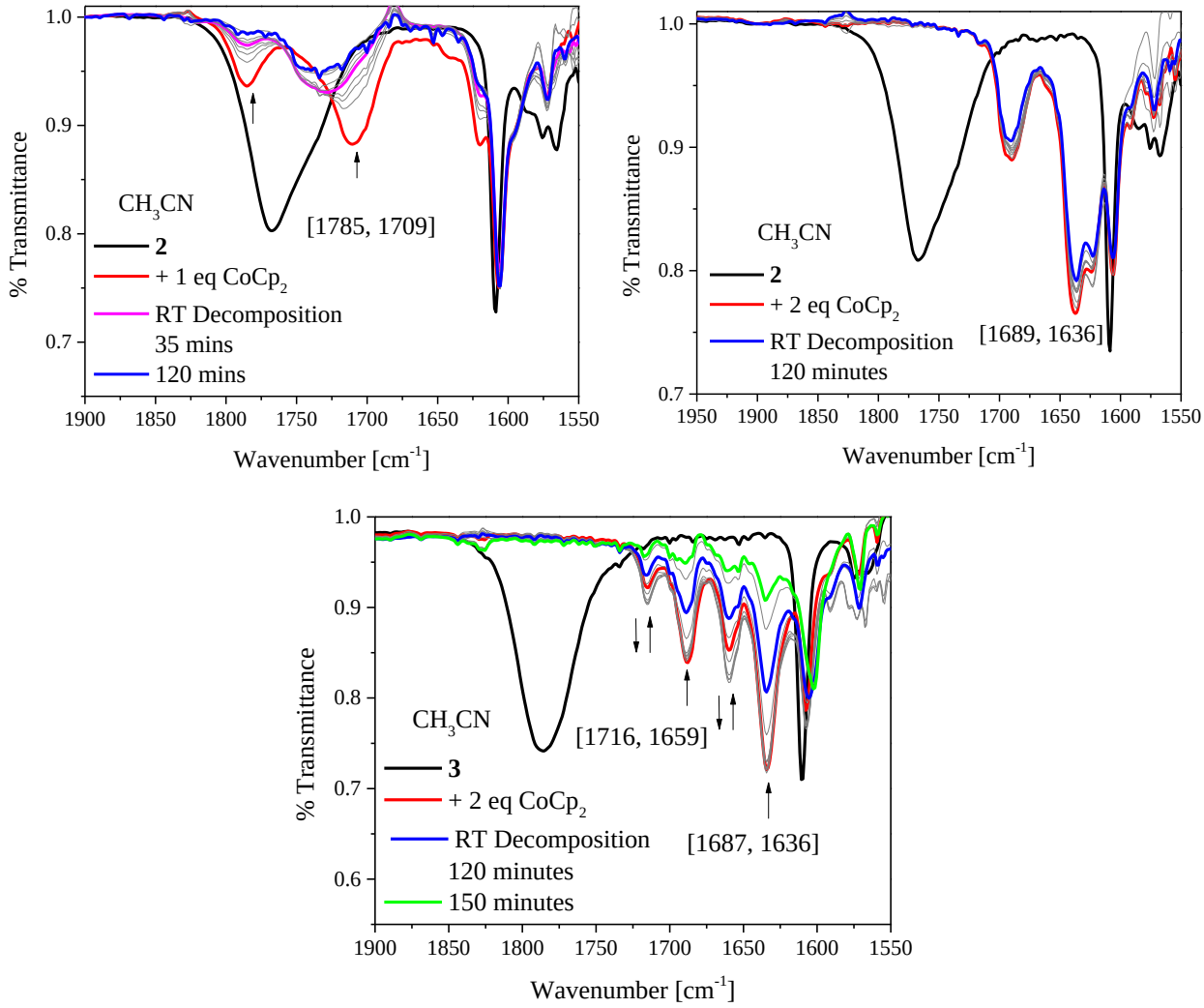

Figure 4.10 Top left: The one electron chemical reduction of **2** at RT in CH_3CN leads to the formation of a transient hs-$Fe^{II}\{Fe(NO)_2\}^9$ with bands at 1785 and 1709 cm^{-1} that decay rapidly over 35 minutes. Top right: In contrast, the two electron reduction of **2** affords a hs-$Fe^{II}\{Fe(NO)_2\}^{10}$ with bands at 1689 and 1636 cm^{-1} that only minimally decays over the course of 2 hours. Bottom: The analogous hs-$Fe^{II}\{Fe(NO)_2\}^{10}$ generated from **3** is unstable over 2 hours. Conditions: ~ 5 mM of **2** and **3** at RT in CH_3CN.

reactivity of these intermediates towards N-N coupling and N_2O release. Interestingly, when comparing the stabilities of the hs- $Fe^{II}\{Fe(NO)_2\}^{10}$ DNICs between **2** and **3**, the 1687/1636 cm^{-1} and 1716/1659 cm^{-1} hs-$Fe^{II}\{Fe(NO)_2\}^{10}$ bands of **3** decay much more rapidly over the course of 2 hrs compared to the corresponding features of the hs-$Fe^{II}\{Fe(NO)_2\}^{10}$ product of **2**. This suggests that the nature of the monodentate ligand X affects the stabilities of the hs-$Fe^{II}\{Fe(NO)_2\}^{10}$ DNIC products. Interestingly, in the case of **3**, as the 1687/1636 cm^{-1} bands decay, the 1716/1659 cm^{-1}

hs- $Fe^{II}\{Fe(NO)_2\}^{10}$ bands initially increase over the first 10 minutes, then subsequently decay over the course of 2 hours (Figure 4.10). This suggests that this second hs-$Fe^{II}\{Fe(NO)_2\}^{10}$ DNIC is either in equilibrium with the 1687/1636 cm^{-1} product, or it contributes to its decomposition

Chemical Reduction: N_2O yields

Gas-headspace N_2O yields provide an additional means of evaluating the reactivity of the DNIC intermediates under different conditions (solvent, time). While the N_2O calibration curve presented in Chapter 2 was used for analyzing N_2O yields in every other chapter in this thesis[3], the data collected here were taken after our gas-IR cell was modified with new windows. We determined that the cell had a lower leak rate, resulting in inaccurate N_2O yields when using the Chapter 2 calibration curve. As such, two new calibration curves were generated, one using a clean (by elemental analysis) batch of $[Fe_2(BPMP)(OAc)(NO)_2](OTf)_2$ as the standard, and the other using Piloty's Acid exactly as described in Chapter 2. N_2O yields in this chapter are reported

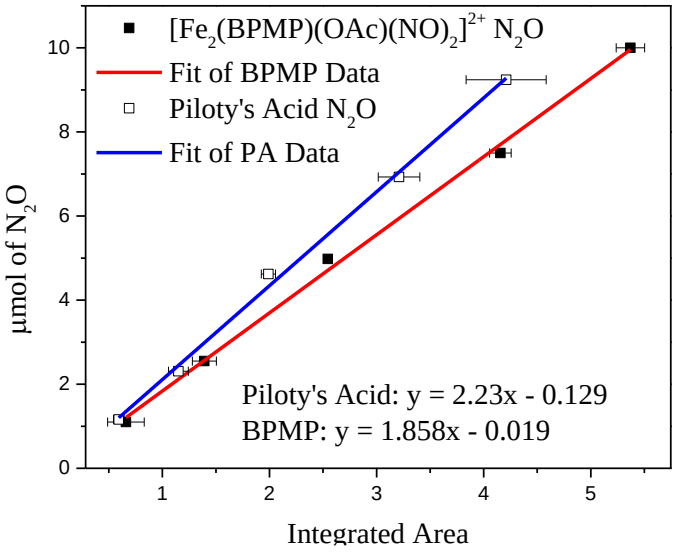

Figure 4.11 Gas-headspace N_2O calibration curves. After stirring between 1-10 µmol of $[Fe_2(BPMP)(OAc)(NO)_2](OTf)_2$ with 1 eq $CoCp_2$ in CH_2Cl_2 in a 14/20 septum-sealed 25 mL RBF for 15 minutes, the headspace was evacuated into the gas-IR cell (first evacuated on the Schlenk line to 150 mbar) for precisely 20 seconds. The gas-headspace IR data were collected and the N_2O band was integrated as described in Chapter 2. Data points were taken in triplicate and the data are presented with a ± 1 standard deviation error bar.

using the $[Fe_2(BPMP)(OAc)(NO)_2](OTf)_2$ calibration curve due to its linear fit having a y-intercept closest to 0, allowing for more accurate measurements to be taken at low concentrations of N_2O. A linear fit of the data (where y = μmol of N_2O and x = integrated area under the N_2O IR band) gives y = 1.858x – 0.019 (Figure 4.11). As a comparison, the Piloty's Acid data are also overlaid with this fit. Based on the different solution stabilities of the DNIC products from **1-3**, including in different solvent conditions, N_2O yields were measured in CH_2Cl_2 and CH_3CN, using either 1 or 2 eq of $CoCp_2$, and were collected after 5 minutes and 2 hours. These data are combined in Table 4.3 and visualized in Figure 4.12.

Table 4.3 Compiled N_2O yields for **1-3** taken under different experimental conditions. N_2O yield data for $[Fe_2(BPMP)(OPr)(NO)_2](OTf)_2$ is also included for comparison.

		% N_2O Yields[a] (± 1 STD)						
		1 eq $CoCp_2$				2 eq $CoCp_2$		
Solvent	Time	**1**	**2**	**3**	OPr[c]	**1**	**2**	**3**
CH_2Cl_2	5 min	61.8 ± 2.3	20.0 ± 0.7	64.8 ± 3.1	90.0 ± 0.6[c]	21.8 ± 0.4	16.8 ± 2.5	21.7 ± 0.5
	2 hr	106.3 ± 3.8	38.1 ± 1.7	103.7 ± 2.6	--	93.8 ± 12.8	28.3 ± 4.8	89.5 ± 2.3
CH_3CN	5 min	31.5 ± 6.0	4.7 ± 0.7	57.9 ± 12.1	--	7.4 ± 0.6	4.7 ± 0.7	8.7 ± 0.2[b]
	2 hr	77.0 ± 7.5	38.6 ± 3.2	82.3 ± 2.3[b]	--	14.4 ± 2.9	6.1 ± 1.3	71.1 ± 14.3[b]

[a]Unless otherwise noted, average of triplicate experiments. [b]Average of duplicate experiments. [c]Data collected on $[Fe_2(BPMP)(OPr)(NO)_2](OTf)_2$ after 1 minute

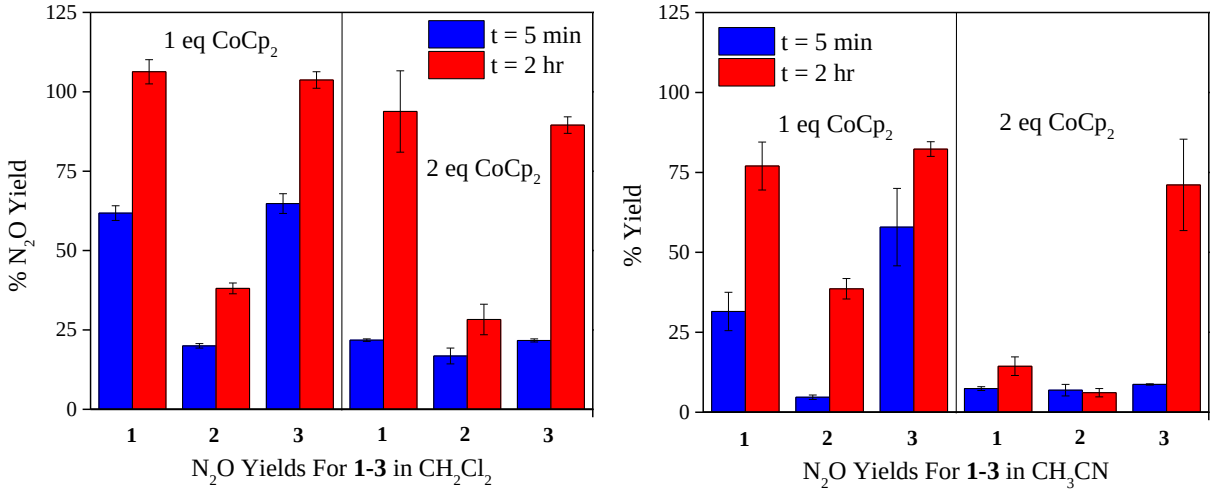

Figure 4.12 Graphical representation of the gas-headspace N_2O results for **1-3** with 1 or 2 eq of $CoCp_2$ after 5 minutes or 2 hours in (Left) CH_2Cl_2 and (Right) CH_3CN. Error bars represent ± 1 standard deviation.

Several comparisons can be made based on this set of data that directly support the spectroscopic findings discussed above. First, the N_2O generation occurs in two phases, where the N_2O yields after 5 minutes are substantially lower than that of $[Fe_2(BPMP)(OPr)(NO)_2](OTf)_2$ discussed in Chapter 2, with 64.8 % as the highest yield from **3** with 1 eq of $CoCp_2$ in CH_2Cl_2, followed by 61.8% for **1** and 31.5% for **2**. Additionally, in line with the enhanced stabilities of the DNIC products in CH_3CN (see Figures 4.7 and 4.10), the N_2O yields after 5 minutes were larger in CH_2Cl_2 than in CH_3CN, and are also larger with 1 eq CoCp than with 2 eq $CoCp_2$. For example, **1-3** generated 21.8, 16.8, and 21.7 % N_2O with 2 eq $CoCp_2$ in CH_2Cl_2 vs. 7.4, 4.7, and 8.7 % N_2O in CH_3CN. Similar trends occur between 1 and 2 eq $CoCp_2$. For example, in CH_2Cl_2 yields are 61.8, 20.0, and 64.8 %, while the corresponding yields in CH_3CN are 21.8, 16.8, and 21.7 for **1-3**, respectively. Counterintuitively, **3** sits as an outlier to the expected N_2O yield trend, with yields comparable to **1** despite containing the longest (O)N-N(O) distance and N-Fe-Fe-N dihedral angle. However, the crystal structure of **3** contains H-bonding interactions between the MeOH and adjacent NO ligand (MeOH--NO = 2.73 Å), potentially leading to an artificially expanded core structure within the crystal. In this regard, additional DFT modelling of the CH_3CN-bound structure will be carried out to evaluate whether the core structure contracts in the absence of this H-bonding interaction.

Second, despite forming the exact same DNIC products, the N_2O yields over 2 hours differ across the series of **1-3**. First and foremost this suggests that the DNIC itself facilitates N_2O formation slowly over the course of 2 hrs, a surprising finding based on the general stability of hs-$\{Fe(NO)_2\}^{9/10}$ species towards N-N coupling due to the spin-forbidden nature of the coupling. Here the N_2O generated upon addition of 1 eq of $CoCp_2$ after 2 hrs is larger across **1-3** compared to the N_2O yields upon addition of 2 eq of $CoCp_2$. For example, **1-3** generate 81.9, 38.1, and

103.7% N_2O with 1 eq $CoCp_2$ in CH_2Cl_2 after 2 hrs compared to 39.0, 28.3, and 89.5 % N_2O with 2 eq $CoCp_2$ under related conditions. This finding agrees with the electronic structure descriptions of these two electronic states. The hs-Fe^{II}{$Fe(NO)_2$}^{9} complex contains a weaker Fe-NO bond, and therefore decomposes more rapidly than the hs-Fe^{II}{$Fe(NO)_2$}.[10,13] Additionally, the N_2O yields after 2 hours follow a similar solvent trend as discussed above, with higher N_2O yields from reductions in CH_2Cl_2 than those in CH_3CN. For example, the 2 eq $CoCp_2$ reduction of **1-3** in CH_2Cl_2 results in 39.0, 28.3, and 89.5 % N_2O yields while the analogous reduction in CH_3CN results in 14.4, 6.1, and 71.1 % N_2O yields. This is in line with the different solution stabilities of these DNICs in the two solvent systems. Interestingly, despite generating identical DNIC products, the N_2O yields are inconsistent across the series of **1-3** with **3 > 1 > 2** for both of the t = 2 hr trends (CH_3CN/CH_2Cl_2 and 1 or 2 eq of $CoCp_2$) suggesting that the monodentate ligands X may still play a role in the generation of N_2O despite our proposal that they had shifted to the adjacent hs-Fe^{II} center. The mechanistic implications of these trends are discussed in detail below.

DFT Modelling of DNIC Products

Unfortunately, suitable crystals of both proposed 5c hs-Fe^{II}{$Fe(NO)_2$}^{9} and 4c hs-Fe^{II}{$Fe(NO)_2$}^{10} intermediates could not be obtained, so we turned towards DFT modelling to predict potential structures and vibrational frequencies of these intermediates. As a starting point for the B3LYP/TZVP optimization of the proposed 5c hs-Fe^{II}{$Fe(NO)_2$}^{9} species, one Fe center and half of the BPMP ligand (from the DFT optimized structure of **2**), consisting of one tertiary amine and two pyridines, were twisted away from the other hs-Fe^{II} center to significantly increase the DNIC Fe-O (of the central PhO^-) distance to 4.09 Å. The NMeIm on the new DNIC Fe center was replaced with the second NO ligand and at the remaining hs-Fe^{II} site, a second NMeIm was

placed in the now empty 6th coordination site. This structure was then optimized with three fragments consisting of the S = 0 BPMP and NMeIm ligands, a S = 2 hs-Fe^{II} center, and a S = 1/2 hs-$\{Fe(NO)_2\}^9$ center. The fully optimized structure of the 5c hs-$Fe^{II}\{Fe(NO)_2\}^9$ complex (Figure 4.13) was then used as a starting point for the corresponding hs-$Fe^{II}\{Fe(NO)_2\}^{10}$ optimization. In support of the formation of a 4c DNIC, the hs-$Fe^{II}\{Fe(NO)_2\}^{10}$ optimized structure contains an elongated DNIC Fe-N_{tert} distance of 2.43 Å, resulting in a pseudo-tetrahedral geometry.

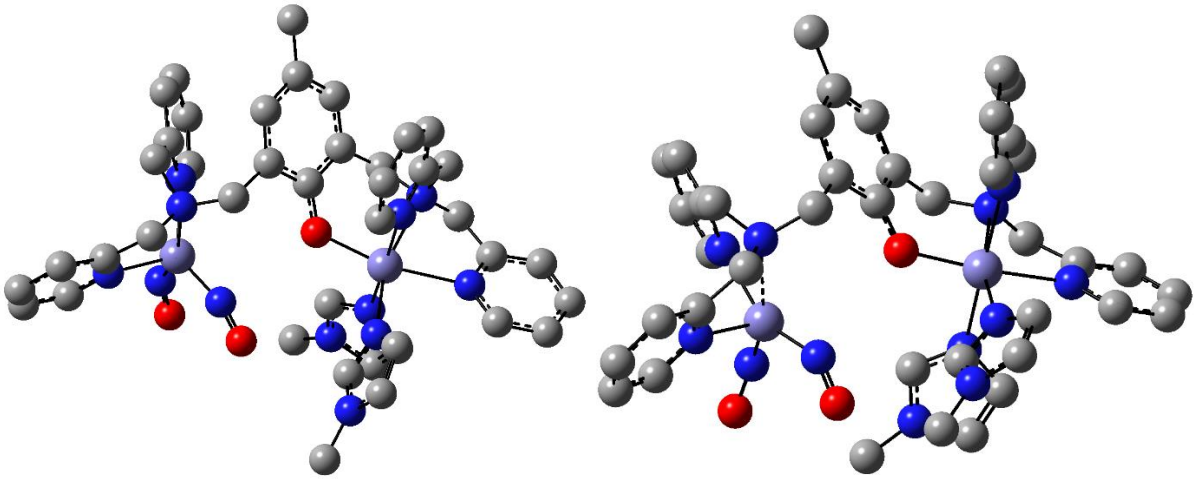

Figure 4.13 Left: DFT-optimized structure of the proposed five-coordinate hs-$Fe^{II}\{Fe(NO)_2\}^9$ intermediate with X = NMeIm, illustrating a quite large (DNIC)Fe-O(PhO) distance, in support of a five-coordinate geometry at the DNIC. Right: The analogous hs-$Fe^{II}\{Fe(NO)_2\}^{10}$ optimized structure contains an elongated Fe-N_{tert} bond, and takes on a pseuto-tetrahedral geometry, in accordance with the $\Delta\nu_{NO}$ for this species. As emphasized in Table 4.4, the Fe-N_{py} distances in this structure are quite asymmetric, since one NO sits nearly trans to one N_{py}. We suspect that the N_{tert} tether to both N_{py} units sterically hinders the complex for optimal N_{py} ligand re-organization to a pure tetrahedral geometry.

Interestingly, in the 5c hs-$Fe^{II}\{Fe(NO)_2\}^9$ state, the DNIC center is trigonal bipyramidal with one NO bound trans to N_{tert} and the other NO bound in the N_{py}-Fe-N_{py} trigonal plane. Upon reduction to the hs-$Fe^{II}\{Fe(NO)_2\}^{10}$ state, the ligand is unable to optimally conformationally adjust to a pure tetrahedral geometry, leaving one NO pseudo-trans to one N_{py}, and resulting in increased asymmetry between the two Fe-N_{py} bond distances (Δ = 0.15 Å), due to the *trans* effect of NO. Frequency calculations on these two DNICs predict symmetric and asymmetric stretching frequencies of 1842 and 1711 cm^{-1} for the 5c hs-$Fe^{II}\{Fe(NO)_2\}^9$ and 1625 and 1582 cm^{-1} for the

Table 4.4 Overview of key structural parameters for the DFT optimized hs-$Fe^{II}\{Fe(NO)_2\}^9$ and hs-$Fe^{II}\{Fe(NO)_2\}^{10}$ states.

	hs-$Fe^{II}\{Fe(NO)_2\}^9$		**hs-$Fe^{II}\{Fe(NO)_2\}^{10}$**	
	Fe^{II}	**$\{Fe(NO)_2\}^9$**	**Fe^{II}**	**$\{Fe(NO)_2\}^{10}$**
Fe-O (PhO) (Å)	2.03	3.83	1.98	3.71
Fe-N_{tert} (Å)	2.29	2.32	2.33	2.43
Fe-N_{py} (Å)	2.34, 2.25	2.17, 2.13	2.30, 2.27	2.27, 2.12
Fe-NMeIm (Å)	2.25, 2.20	--	2.25, 2.18	--
Fe-NO (Å)	--	1.82, 1.76	--	1.83, 1.81
(O)N-Fe-N(O) (º)	--	100.7	--	105.4
ν(NO) (cm^{-1})	--	1843, 1712	--	1625, 1582

4c hs-$Fe^{II}\{Fe(NO)_2\}^{10}$ complex. The key geometric and vibrational parameters of the two optimized structures are summarized in Table 4.4

*Chemical Modelling of the DNIC Products Using Complex **4***

In tandem with DFT studies, we also sought to chemically model the DNIC products. As proposed above, the dinuclear systems effectively contain a completely uncoupled hs-DNIC ligated by a N_{tert}, two N_{py}, and two NO ligands in the coordination sphere, with a tethered, albeit electronically uncoupled, hs-Fe^{II} center that contains the monodentate ligands X, as well as BPMP coordination from the central PhO^-, N_{tert} and two N_{py}. With this in mind, we targeted a purely mononuclear DNIC model that contains a similar coordination sphere, with a N_{tert} and two N_{py} ligands available for coordination to the iron center. As discussed in above, while the classical method of synthesizing DNIC complexes is via substitution of $[Fe(CO)_2(NO)_2]$ with the desired mono/bidentate ligands, there are also some examples of mononuclear hs-$\{FeNO\}^7$ complexes that form DNIC products upon chemical reduction with 0.5 or 1 eq of reductant to make hs-$\{Fe(NO)_2\}^{9/10}$ + Fe^{II} species. Following this route, the synthesis of a mononuclear hs-$\{FeNO\}^7$

complex containing two N_{py} and N_{tert} coordination was achieved by metalating iron(II) triflate with bis(2-methylpyridyl)amine (BMPA) in CH_3CN, followed by immediate nitrosylation, affording microcrystalline [Fe(BMPA)$(OTf)_2$(NO)] (**4**) (Scheme 4.2). This complex exhibits a strong ν_{NO} band at 1848 cm^{-1} by IR (KBr), while in the ^{15}NO isotopolog (**4-^{15}NO**) ν_{NO} shifts down by 34 cm^{-1} to 1814 cm^{-1}. In CH_3CN solution, the N-O band of **4** shifts to 1818 cm^{-1} (Figure 4.14). Such shifts in ν_{NO} between solid and solution IR spectra are not uncommon for these types of complexes,

Scheme 4.2 Schematic depiction of the metallation and nitrosylation of BMPA to make [Fe(BMPA)$(CH_3CN)_2$(NO)]$(OTf)_2$ (**4**).

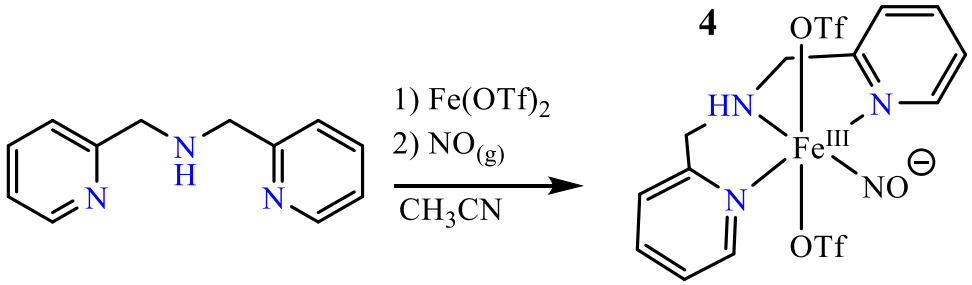

and related shifts in N-O frequencies between solid and solution states have been previously reported from our laboratory.[13, 20, 21] In this case, we propose that the shift is due to replacement of the triflate ligands by CH_3CN in solution. Owing to the quite electron poor ligand sphere, this is one of the highest N-O stretching frequencies reported so far for a hs-{FeNO}^{7} complex. In line with this, the preliminary X-Ray crystal structure of **4** reveals that the [Fe(BMPA)(NO)] core is square planar, containing a linear Fe-NO unit (Fe-N-O angle = 180°; due to symmetry constraints), with the two $^-$OTf counterions located at the remaining two axial positions (Figure 4.14). Importantly, the chemical reduction of this complex (0.5 eq $CoCp_2$) at room temperature in CH_2Cl_2 leads to the formation of a stable hs-{Fe$(NO)_2$}^{9} species with N-O stretching frequencies of 1789 and 1713 cm^{-1} (Figure 4.15), which has N-O frequencies that are shifted *only 4 cm^{-1} higher* than those observed for our hs-Fe^{II}{Fe$(NO)_2$}^{9} intermediate obtained for complexes **1-3** discussed above, indicating that this complex models the coordination sphere of the Fe^{II}{Fe$(NO)_2$}^{9}

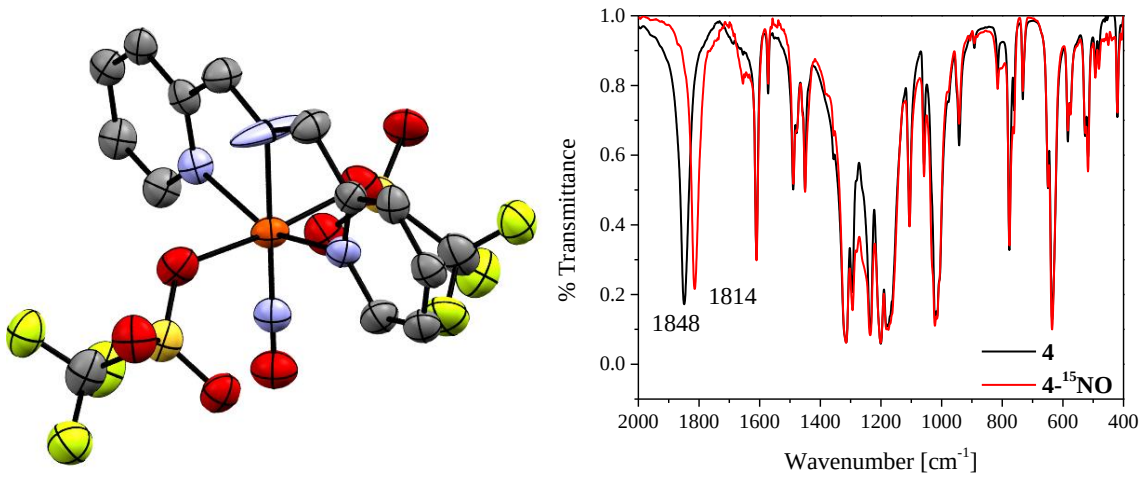

Figure 4.14 Left: X-Ray crystal structure of **4** illustrates the square planar Fe(BMPA)(NO) coordination sphere and completely linear Fe-NO bond (due to the C_2V symmetry of the molecule), in line with an extremely electron poor hs-{FeNO}^{7} complex. Right: IR(KBr) spectra of **4** and **4-^{15}NO**, illustrating a 34 cm^{-1} shift in the N-O stretching frequency upon labelling with ^{15}NO.

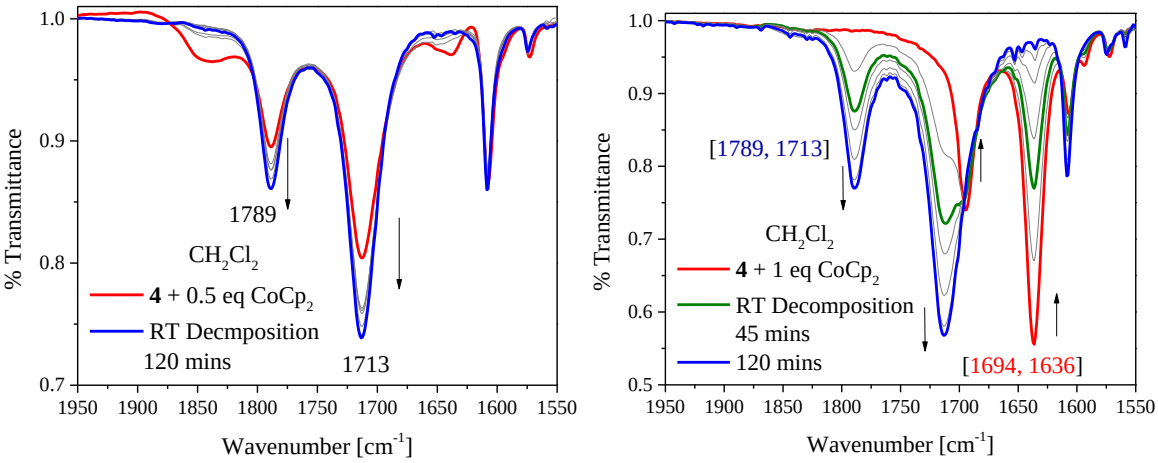

Figure 4.15 Left: Solution-IR measurements of the reduction of **4** (10 mM) in RT CH_2Cl_2 with 0.5 eq $CoCp_2$ to generate a hs-{Fe(NO)$_2$}^{9} DNIC with N-O frequencies of 1789 and 1713 cm^{-1}. Right: The analogous reduction with 1 eq $CoCp_2$ leads to the formation of a hs-{Fe(NO)$_2$}^{10} with N-O frequencies of 1694 and 1636 cm^{-1} that decays back to a hs-{Fe(NO)$_2$}^{9} over time.

intermediate very well. In this experiment, the hs-{Fe(NO)$_2$}^{9} bands increased over time. The hs-{FeNO}^{7} complex **4** is minimally soluble in CH_2Cl_2. The addition of $CoCp_2$ pulls some hs-{FeNO}^{7} into solution, however, over the course of the experiment, the hs-{FeNO}^{7} never completely dissolved. The increase in the N-O stretching bands is attributed to the slow dissolution of the hs-{FeNO}^{7} complex and subsequent reduction to hs-{Fe(NO)$_2$}^{9} over the course of the

experiment. An analogous chemical reduction of **4** in RT CH_2Cl_2 with 1 eq of $CoCp_2$ leads to the rapid formation of a hs-$\{Fe(NO)_2\}^{10}$ DNIC with bands similarly shifted *only 4 cm^{-1} higher* (at 1694 and 1636 cm^{-1}) than those of the hs-$Fe^{II}\{Fe(NO)_2\}^{10}$ from **1-3** (Figure 4.15), again indicating that the simple mononuclear complex models the hs-$Fe^{II}\{Fe(NO)_2\}^{10}$ intermediate very well. Unusually, this hs-$\{Fe(NO)_2\}^{10}$ is not stable, and over the course of 2 hrs forms the hs-$\{Fe(NO)_2\}^{9}$ product with bands at 1789 and 1713 cm^{-1}. Since the reduction of the starting hs-$\{FeNO\}^{7}$ should generate two fully reduced species: the hs-$\{Fe(NO)_2\}^{10}$ and Fe^{II}, it is unclear how this re-oxidation occurs. Nonetheless, the mononuclear DNIC products that are generated upon reduction of **4** with both 0.5 and 1 eq $CoCp_2$ are stable in CH_2Cl_2 with no discernable decomposition of the final hs-$\{Fe(NO)_2\}^{9}$ product or N_2O formation by solution IR, standing in contrast to the dinuclear analogs obtained from the reduction of **1-3**.

The same solution stability experiments were also carried out in CH_3CN to determine if **4** generates a single hs-$\{Fe(NO)_2\}^{9}$ and two hs-$\{Fe(NO)_2\}^{10}$ DNICs as observed with **1** and **3** under related conditions. Indeed, upon the addition of 0.5 eq $CoCp_2$ to a solution of **4** at RT in CH_3CN, a single hs-$\{Fe(NO)_2\}^{9}$ DNIC forms with bands at 1789 and 1713 cm^{-1} (Figure 4.16). Over the course of 2 hours, this DNIC is stable in solution, with negligible decomposition over this timeframe. Upon the addition of 1 eq $CoCp_2$ to **4** at RT in CH_3CN, there is an initial mixture of two hs-$\{Fe(NO)_2\}^{10}$ species with bands at 1714/1659 cm^{-1} and 1693/1637 cm^{-1} (Figure 4.16), where the 1714/1659 cm^{-1} hs-$\{Fe(NO)_2\}^{10}$ is the major product while the 1693/1637 cm^{-1} hs-$\{Fe(NO)_2\}^{10}$ is a minor species that decays within the first 15 minute scan. Interestingly, the minor 1693/1637 cm^{-1} hs-$\{Fe(NO)_2\}^{10}$ is similar to the major hs-$Fe^{II}\{Fe(NO)_2\}^{10}$ product from the two electron reduction of **1-3** at -70 ^{o}C in CH_2Cl_2 (and is also the major species that initially forms upon the 1 electron reduction of **4** in CH_2Cl_2, see Figure 4.15 above). In CH_3CN, **1** and **3** contain a

roughly 1:1 ratio between the two hs-$Fe^{II}\{Fe(NO)_2\}^{10}$ products whereas the product from **4** has a roughly 5:1 ratio. While it is unclear why there is a difference in the ratios of DNIC products formed from **4**, it is clear from these combined solution stability studies that the reactivity of **4** closely resembles the reactivity (in terms of DNIC products) of **1-3** under related experimental conditions. The conversion from the minor 1693/1637 cm^{-1} $\{Fe(NO)_2\}^{10}$ product of **4** to the1714/1659 cm^{-1} species indicates that these two DNICs are related species. Additionally, **4-**

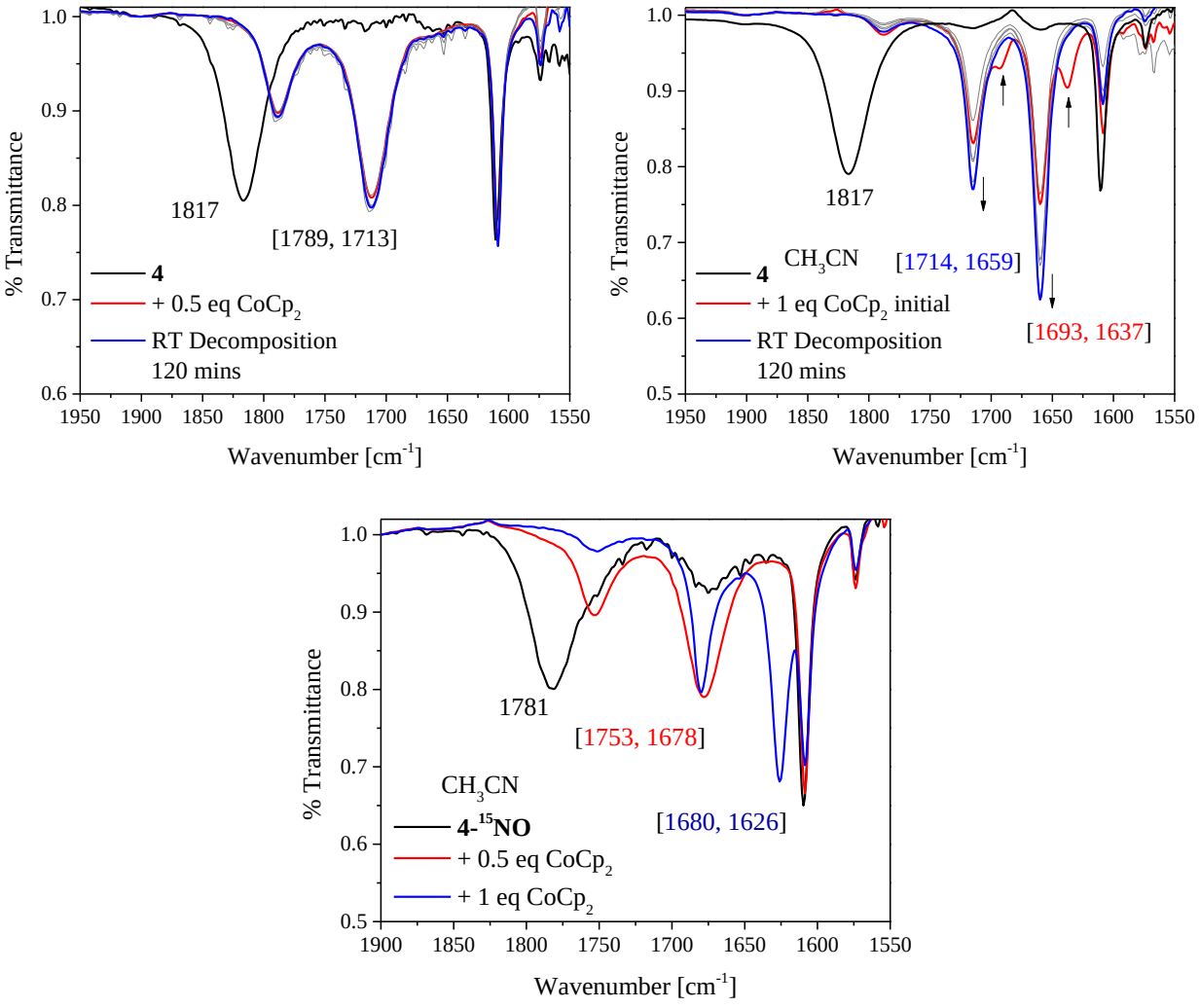

Figure 4.16 Top left: Solution-IR measurements of the reduction of **4** (10 mM) in RT CH_3CN with 0.5 eq $CoCp_2$ to generate a hs-$\{Fe(NO)_2\}^9$ DNIC with N-O stretching frequencies of 1789 and 1713 cm^{-1}. Top right: The analogous reduction with 1 eq $CoCp_2$ leads to the formation of two hs-$\{Fe(NO)_2\}^{10}$ species with N-O stretching frequencies of 1714/1659 and 1693/1637 cm^{-1}. The 1693/1637 cm^{-1} bands decay after the first 15-minute spectra is taken. Bottom: Overlay of **4-^{15}NO** and its reduced hs-$\{Fe(NO)_2\}^{9/10}$ analogs, illustrating a 36 cm^- shift between **4** and **4-^{15}NO** bands. In this experiment, the formation of the second DNIC product was not observed in the initial scan.

^{15}NO was chemically reduced with 0.5 and 1 eq $CoCp_2$ illustrating a 36 cm^{-1} shift in N-O frequencies between **4** and **4-^{15}NO** for all species present (Figure 4.16), with the initial NO complex starting at 1781 cm^{-1}, the hs-$\{Fe(NO)_2\}^9$ at 1753 and 1678 cm^{-1}, and the hs-$\{Fe(NO)_2\}^{10}$ at 1680 and 1626 cm^{-1}. A summary of the DNIC N-O stretching frequencies from the reductions of **1-4** with 0.5, 1, or 2 eq of $CoCp_2$ and in CH_2Cl_2 or CH_3CN is presented in Table 4.5. Due to the slight differences in amine ligation between **4** (R_2NH) and **1-3** (R_3N), the slight shifts in N-O

Table 4.5 Summary of N-O stretching frequencies (in cm^{-1}) for the DNIC products of **1-4**.

	$\{Fe(NO)_2\}^9$			$\{Fe(NO)_2\}^{10}$		
	1, 3	**2**	**4**	**1, 3**	**2**	**4**
CH_2Cl_2	1788, 1715	1788, 1715	1789, 1713	1689, 1632	1689, 1632	1694, 1636
CH_3CN	1785, 1709	1785, 1709	1789, 1713	[1716, 1659] [1687, 1636]	1689, 1636	[1714, 1659] [1693, 1637]

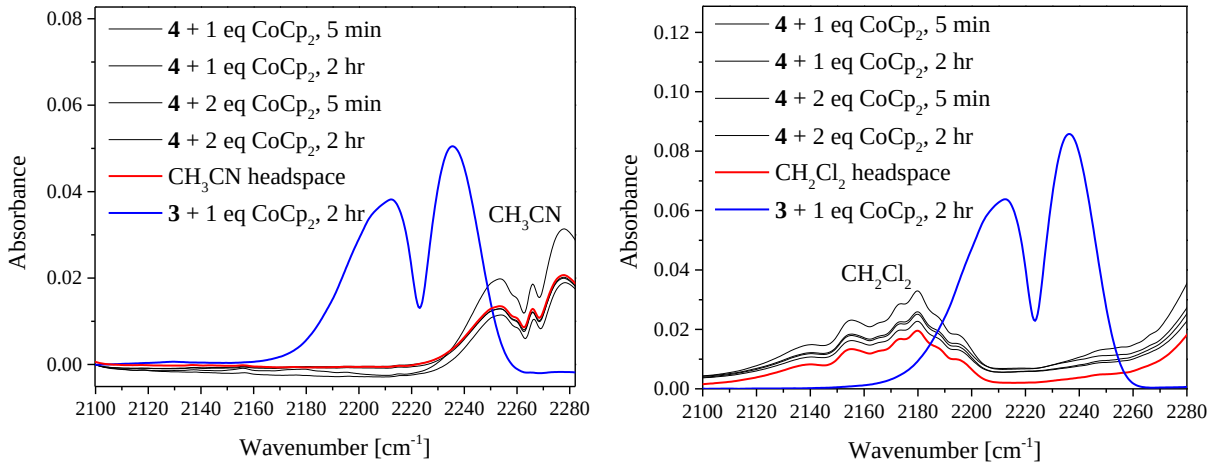

Figure 4.17 Left: Gas-headspace IR measurements for **4** (10 μmol) with 0.5 or 1 eq $CoCp_2$ in CH_3CN, taken after either 5 minutes or 2 hours. Right: Analogous gas-headspace IR measurements taken in CH_2Cl_2. In both plots, the solvent background (red) and N_2O yield from **3** (blue) are provided for reference.

stretching frequencies between **4** and **1-3** may be attributed to subtle electronic differences in the ligand sphere. Nonetheless, a major difference between **4** and **1-3** is that the DNIC species from **4** are stable over the course of 2 hours, whereas those of **1-3** are not. Accordingly, the chemical

reduction of **4** in CH_3CN or CH_2Cl_2 with 1 or 2 eq of $CoCp_2$ does not generate any N_2O (Figure 4.17). The mechanistic implications of this are discussed further below.

Mechanistic Implications for FNORs

As illustrated in Figure 4.7 above, the initial reduction of the hs-$[\{FeNO\}^7]_2$ complexes **1-3** contains two divergent reaction pathways, resulting in both the formation of hs-$Fe^{II}\{Fe(NO)_2\}^{9/10}$ DNIC products as well as some initial N_2O. We propose that the one electron reduced hs-$[\{FeNO\}^7\{FeNO\}^8]$ dimer contains two competing routes with rate constants k_1 and k_2, for the semi-reduction to generate N_2O or DNIC formation, respectively, that are influenced by the structural parameters of the Fe-NO core (Scheme 4.3). The t = 5 minute N_2O data presented in Table 4.3 and Figure 4.12 have direct ramifications for the FNOR N-N coupling mechanism. Within this set of data it is important to note (1) that the DNIC products are more stable in CH_3CN, and (2) that within the DNIC products, the hs-$Fe^{II}\{Fe(NO)_2\}^{10}$ is more stable than the hs-$Fe^{II}\{Fe(NO)_2\}^9$. As such, the data set that best isolates the N_2O yield arising solely from semireduction (k_1 pathway) is the data for 2 eq $CoCp_2$ in CH_3CN, at t = 5 min. Here, the N_2O generated within 5 minutes is significantly inhibited (maximum N_2O yield = 8.7 %) compared to $[Fe_2(BPMP)(OPr)(NO)_2](OTf)_2$ dicussed in Chapter 2 depending on the key structural parameters within the Fe-NO units of **1-3**. In complexes with greater N-N distances and N-Fe-Fe-N dihedral angles, a greater portion of hs-$Fe^{II}\{Fe(NO)_2\}^{9/10}$ DNIC intermediates accumulate. Accordingly, **2** contains the lowest ratio of N_2O generated within 5 minutes due to its extended ON-NO bond distance of 3.78 Å and N-Fe-Fe-N dihedral angle of 76.8° while **1** generates slightly more N_2O due to its 3.13 Å N-N distance and 51.2° dihedral angle. However, **3** sits as a clear outlier, generating the highest yields of N_2O despite containing the longest N-N distance at 3.96 Å and dihedral angle

Scheme 4.3 Schematic overview of the proposed reaction intermediates and pathways towards N_2O formation upon 1 or 2 electron reduction of the initial hs-[{FeNO}^{7}]$_2$.

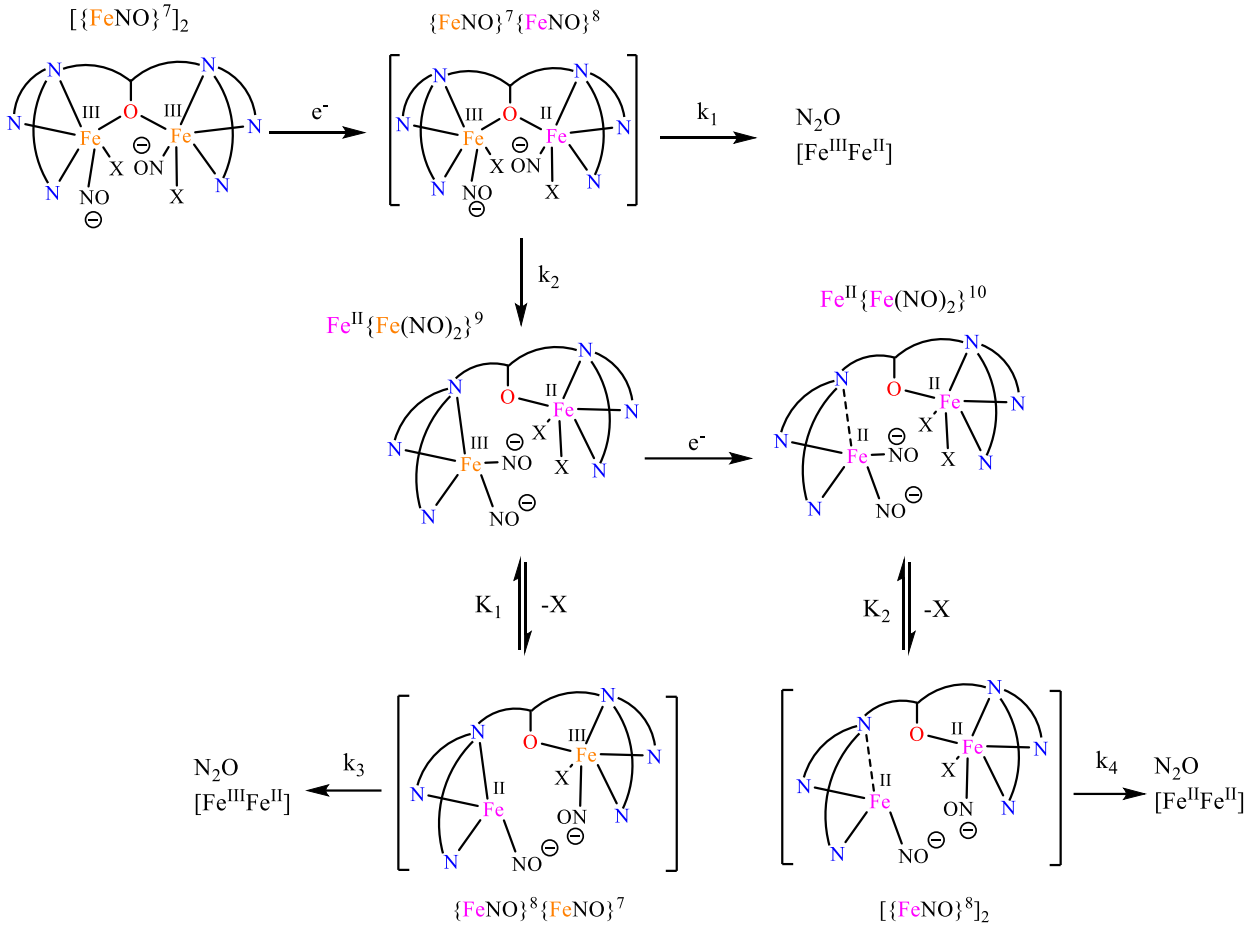

at 85.1°. However, the structural parameters from the crystal structure of **3** may contain an artificially expanded core structure to accommodate a H-bonding interaction between each MeOH and the adjacent NO. While this structure may still exist in CH_2Cl_2, in coordinating or protic solvents the MeOH can feasibly be displaced or contain other H-bonding interactions that may allow for a more contracted solution-state structure. Future work will involve additional DFT modelling of the CH_3CN bound structure to evaluate differences in the predicted core structure in the absence of protic ligands. Despite this outlier, the data presented in this chapter clearly support the idea that N-N coupling is perturbed by the substitution of a bridging carboxylate with two monodentate ligands. This data provides additional evidence for the necessity of the two NO units

to bind in close proximity and with a limited N-Fe-Fe-N dihedral angle to facilitate N-N coupling. Here, a distortion of the ON-NO angle by ~50% and the Fe-Fe distance of 0.33 Å leads to a drop of the N_2O yield from 90% to about 10%. This is certainly unexpected, and shows that in diiron enzymes, the core conformation has to be precisely controlled to allow for quantitative N-N coupling and N_2O formation. This requirement is less stringent for O_2 avtivation, and this could be a distinction between primarily O_2 versus primarily NO activating FDPs.

Mechanism of N_2O Formation from the DNIC Products

The comparison of the DNIC stabilities between **1-3** and **4** is mechanistically interesting. While the bulk material in both the dinculear and mononuclear systems contains an equivalent of DNIC and Fe^{II}, the key distinction is that the Fe^{II} in the dinuclear systems **1-3** is tethered in close proximity to the DNIC center. Since N-N coupling from two NO units within a DNIC is mechanistically unfeasible, we propose that the NO lost from the hs-$Fe^{II}\{Fe(NO)_2\}^9$ intermediate, or NO^- lost from the hs-$Fe^{II}\{Fe(NO)_2\}^{10}$ is trapped by the tethered Fe^{II} center (coupled with the displacement of X, as shown in Scheme 4.3) to generate a hs-$\{FeNO\}^7\{FeNO\}^8$ or hs-$[\{FeNO\}^8]_2$ intermediate in two equilibria with $K_1 > K_2$ due to the decreased solution stability of the hs-$Fe^{II}\{Fe(NO)_2\}^9$ compared to the hs-$Fe^{II}\{Fe(NO)_2\}^{10}$. A fraction of the hs-$\{FeNO\}^7\{FeNO\}^8$ or hs-$[\{FeNO\}^8]_2$ species will proceed to generate more N_2O via semi- or super-reduction with k_3 or k_4, respectively, where the efficacy of N_2O formation depends on the same structural prerequisites discussed above for semireduction (k_1). Based on previous DFT calculations on the semi/superreduction of $[Fe_2(BPMP)(OPr)(NO)_2]^{2+/1+/0}$,[23] the activation barriers for semi- and superreduction within BPMP are nearly identical, and suggests that $k_3 \sim k_4 \sim k_1$. The K_1/K_2 equilibria are therefore the primary factors that affects the yields of N_2O over 2 hours, with $K_1 >$

K_2, and accordingly N_2O from 1 eq $CoCp_2$ > 2 eq $CoCp_2$, due to the lower stability of the hs-$Fe^{II}\{Fe(NO)_2\}^9$ intermediate towards NO loss. Interestingly, the solution stabilities between the same DNIC oxidation states varies across **1-3** (see Figure 4.10). As highlighted in Scheme 4.3, in order for the tethered Fe^{II} to capture NO from the decomposition of hs-$Fe^{II}\{Fe(NO)_2\}^{9/10}$ intermediates, the monodentate ligand X must be displaced. We therefore propose that the lability of the ligand X also affects the efficacy of NO capture from the adjacent Fe^{II} center and accordingly the N_2O yields over this 2 hr period. Consequently **3** generates the largest N_2O yields due its weakly coordinating MeOH ligand followed next by **1** ($^-$OTf) and **2** (NMeIm). This argument can be further extended to rationalize the decreased N_2O yields across the board in CH_3CN compared to CH_2Cl_2: CH_3CN is a coordinating solvent and like the ligands X, will similarly compete with NO to bind the adjacent Fe^{II} center. Overall, these data contribute experimental evidence that shows that under the correct circumstances, DNICs can facilitate N_2O formation via NO loss and entrapment by an adjacent hs-Fe^{II} center, a new mechanism for NO reduction and N_2O formation from DNICs that has not been realized thusfar in the literature. First, the generation of DNICs upon perturbing the N-Fe-Fe-N potentially has important implications in distinguishing FDPs from other nonheme diiron enzymes like RNR. Whereas the *Tm.* FDP contains an active site pocket with two 5c-Fe^{II} centers containing adjacent (coplanar) vacant sites for NO binding, therefore enabling NOR activity, whereas RNR contains two weakly bond water molecules that sit nearly orthogonal to each-other, thus inhibiting NOR activity when NO binds.

4.3 Experimental Section

General Considerations

Air sensitive materials were prepared in either an MBraun glovebox, or using standard Schlenk techniques. Low temperature experiments were conducted in an Inert Technologies glovebox modified with a cold well. All solvents were dried using standard techniques, freeze-pump-thawed to remove dioxygen, and stored over molecular sieves. All reagents were purchased from commercial sources and were used as received, unless noted below. $[Fe(OTf)_2](CH_3CN)_2$, $CoCp_2$, and NO(g) were prepared, purified, and used as described in Chapter 2. The following characterization methods were used as described in Chapter 2: IR (ATR/Solution/SEC), EPR, cyclic voltammetry, and elemental analysis. Gas-IR and IR (KBr) were taken on a Thermo-Nicolet iS50 benchtop IR spectrometer.

X-Ray Crystallography

Brown plates of **3** were grown from a methanol/diethyl ether solution of the compound at 22 deg. C. A crystal of dimensions 0.06 x 0.03 x 0.03 mm was mounted on a Rigaku AFC10K Saturn 944+ CCD-based X-ray diffractometer equipped with a low temperature device and Micromax-007HF Cu-target micro-focus rotating anode (λ = 1.54187 A) operated at 1.2 kW power (40 kV, 30 mA). The X-ray intensities were measured at 85(1) K with the detector placed at a distance 42.00 mm from the crystal. A total of 2028 images were collected with an oscillation width of 1.0° in ω. The exposure times were 8 sec. for the low angle images, 45 sec. for high angle. Rigaku d*trek images were exported to CrysAlisPro for processing and corrected for absorption. The integration of the data yielded a total of 75322 reflections to a maximum 2θ value of 139.24° of which 4604 were independent and 4349 were greater than $2\sigma(I)$. The final cell constants (Table 1) were based on the xyz centroids of 20796 reflections above $10\sigma(I)$. Analysis of the data showed negligible decay during data collection. The structure was solved and refined with the Bruker SHELXTL (version 2018/3) software package, using the space group P-42d with

Z = 8 for the formula $C_{38}H_{41}N_8O_{14}F_9S_3Fe_2$. All non-hydrogen atoms were refined anisotropically with the hydrogen atoms placed in a combination of idealized and refined positions. The di-iron complex lies on a two-fold rotation axis of the crystal lattice as does one of the triflate anions. Full matrix least-squares refinement based on F^2 converged at R1 = 0.0635 and wR2 = 0.1645 [based on I > 2sigma(I)], R1 = 0.0671 and wR2 = 0.1682 for all data.

Green needles of **4** were grown from an acetonitrile/diethyl ether solution of the compound at -35 deg. C. A crystal of dimensions 0.04 x 0.02 x 0.01 mm was mounted on a Rigaku AFC10K Saturn 944+ CCD-based X-ray diffractometer equipped with a low temperature device and Micromax-007HF Cu-target micro-focus rotating anode (λ = 1.54187 A) operated at 1.2 kW power (40 kV, 30 mA). The X-ray intensities were measured at 85(1) K with the detector placed at a distance 42.00 mm from the crystal. A total of 2028 images were collected with an oscillation width of 1.0° in ω. The exposure times were 10 sec. for the low angle images, 75 sec. for high angle. Rigaku d*trek images were exported to CrysAlisPro for processing and corrected for absorption. The crystal was found to be a two component, non-merohedral twin. Details of the twin analysis are given in the CIF file. The integration of the data yielded a total of 31281 reflections to a maximum 2θ value of 1340.26° of which 3983 were independent and 2643 were greater than 2σ(I). The final cell constants (Table 1) were based on the xyz centroids of 3783 reflections above 10σ(I). Analysis of the data showed negligible decay during data collection. The structure was solved and refined with the Bruker SHELXTL (version 2018/3) software package, using the space group C2/c with Z = 4 for the formula $C_{14}H_{13}N_4O_7F_6S_2Fe$. All non-hydrogen atoms were refined anisotropically with the hydrogen atoms placed in idealized positions. Reflections from both twin components as well as overlaps were used as the basis of an HKLF5 format reflection file for refinement. Full matrix least-squares refinement based on F^2

converged at R1 = 0.0683 and wR2 = 0.1585 [based on I > 2sigma(I)], R1 = 0.0840 and wR2 = 0.1643 for all data.

N_2O Quantification

Two new standard curves for the quantification of NO were generated either via the base-catalyzed HNO donor Piloty's Acid or via the rapid and quantitative semireduction of a clean (by elemental analysis) batch of $[Fe_2(BPMP)(OAc)(NO)_2](OTf)_2$. The Piloty's acid standard curve was generated on five data points spanning 1 – 10 μmol of expected N_2O release exactly as described in our previous publication. [3, 24]. A similar approach was used for the chemical reduction of $[Fe_2(BPMP)(OAc)(NO)_2](OTf)_2$: five data points spanning 1-10 μmol of complex were repeated in triplicate. $[Fe_2(BPMP)(OAc)(NO)_2](OTf)_2$ (1-10 μmol) was dissolved in 1.5 mL CH_2Cl_2 and transferred to a septum sealed 25 mL RBF. 1.1 (10% excess) equivalents of $CoCp_2$ were dissolved in 1 mL CH_2Cl_2 and syringed into the 25 mL RBF. After exactly 15 minutes, the headspace of the reaction vessel was transferred for precisely 20 seconds into a 10 cm Pike HT gas cell that was pre-evacuated on the Schlenk line to 150 mbarr. Gas-IR measurements were then taken on the Thermo-Nicolet iS50 IR spectrometer. After converting the IR data into absorbance and subtracting the gas-headspace IR of a solvent blank, the N_2O stretch was integrated from 2150-2275 cm^{-1}, and the integrations were plotted against the expected μmol of N_2O.

Computational Methods

Optimization and frequency calculations on all complexes were performed with Gaussian 09 using the BP86[7] functional and the 6-311G(d)[8-10] and TZVP[11, 12] basis sets. All structures were organized into three fragments consisting of (1) the organic ligands, (2) the first Fe or $\{Fe(NO)_x\}^y$ unit, and (3) the second Fe or $\{Fe(NO)_x\}^y$ unit. An initial ferromagnetic optimization was first performed using BP86/6-311G(d) and, for **1**-**3**, that optimized structure was used as an initial guess

for the antiferromagnetic optimization. DNIC structures were treated as uncoupled and both iron centers therefore were given parallel spins. Fully optimized BP86/6-311G(d) structures were then used as a starting guess for the corresponding BP86/TZVP calculations.

Generation of ^{15}NO Complexes 2-^{15}NO and 4-^{15}NO

^{15}NO was generated following a modified literature precedent via the reduction of $Na^{15}NO_2$. 40 mg (571 μmol) $Na^{15}NO_2$ was suspended in 1.5 mL THF and transferred to a septum sealed 25 mL RBF. The RBF was partially evacuated using the glovebox vacuum pump before syringing in 106.4 mg (571 μmol) of ferrocene (Fc) dissolved in 1.5 mL THF. Separately, 206 μL (1142 μmol) trimethylsilyl trifluoromethanesulfonate (TMSOTf) was diluted in 1 mL THF in a vial, and both the vial and 25 mL RBF were placed in the glovebox freezer to cool them to -35 ºC. The TMSOTf solution was then slowly syringed into the RBF resulting in an immediate color change to dark blue with evident gas evolution. After stirring at RT for 1 hour, a gas-tight syringe was used to transfer the ^{15}NO into a separate pre-evacuated Schlenk flask containing either $[Fe_2(BPMP)(NMeIm)_2](OTf)_3$ or $[Fe(BMPA)(OTf)_2]$ dissolved in ~5 mL CH_3CN. The Schlenk flasks were stirred under ^{15}NO for 1 hour and a fraction of the solutions were used immediately for solution IR studies on **2-^{15}NO** and **4-^{15}NO**, while the remaining portion was precipitated for IR (KBr) characterization by syringing in ~36 mL diethyl ether.

Synthesis of Metallated Precursors

General Procedure. The metallation of BPMP follows a modified procedure from Chapter 2 that can be applied to the synthesis of all three complexes.[3] The following is a representative procedure and scale that can be applied for the syntheses of each complex. 200 mg (386 μmol) BPMP and 27.1 (386 μmol) KOMe are added to a 100 mL RBF in the glovebox and dissolved in 2 mL MeOH. 326 mg (772 μmol) of $[Fe(OTf)_2](CH_3CN)_2$ is dissolved in 1 mL MeOH and added to the RBF

resulting in a yellow to orange/yellow color change. For the synthesis of the X = NMeIm complex, 123 μL (1.54 mmol) of NMeIm was first syringed into the solution causing it to turn orange. The solution was then stirred for 1 hr and then precipitated with Et_2O. The X = OTf/MeOH solution was similarly stirred for 1 hr and precipitated with Et_2O. From here the precipitate was filtered off using a fritted funnel and the filtrate was discarded. The precipitate on the frit was then washed with CH_2Cl_2 to remove Na/KOTf byproducts and the filtrate for the X = NMeIm and OTf complexes was precipitated with hexanes, while the CH_2Cl_2 filtrate for the X = MeOH complex was concentrated under reduced pressure, and the resulting solid was re-dissolved in MeOH and precipitated in Et_2O. The final precipitates were filtered to afford the precursor complexes containing X_2 ligation. Specific characterization data is provided for each complex below.

[Fe_2(BPMP)$(OTf)_2$](OTf). Yield: 242 mg (62%). UV-Vis (λ_{max}) = 375 nm (CH_2Cl_2). Elemental anal. Calcd for Calcd for $C_{36}H_{33}F_9Fe_2N_6O_{10}S_3$: C, 39.72; H, 3.06; N, 7.72; found (%): C, 40.89; H, 3.32; N, 7.54.

[Fe_2(BPMP)$(NMeIm)_2$)$(OTf)_3$. Yield: 259 mg (58%). UV-Vis (λ_{max}) =380 nm (CH_2Cl_2). Elemental anal. Calcd for $C_{44}H_{45}F_9Fe_2N_{10}O_{10}S_3$•$CH_2Cl_2$: C, 40.93; H, 4.00; N, 10.56; found (%): C, 40.41; H, 3.54; N, 10.47.

[Fe_2(BPMP)$(MeOH)_2$)$(OTf)_3$. Yield: 383 mg (80%). UV-Vis (λ_{max}) = 408 nm (MeOH). Elemental anal. Calcd for $C_{38}H_{41}F_9Fe_2N_6O_{12}S_3$•$Et_2O$: C, 41.12; H, 4.19; N, 6.85; found (%): C, 41.80; H, 3.69; N, 7.55.

Synthesis of NO Complexes 1-4

[Fe_2(BPMP)$(OTf)_2$$(NO)_2$)(OTf) (1). 191 mg of [$Fe_2$(BPMP)$(OTf)_2$](OTf) was dissolved in ~4 mL CH_2Cl_2 in a 100 mL Schlenk flask. The flask was placed on the NO-Schlenk line, partially evacuated, and filled with NO(g) resulting in an immediate color change to brown. The flask was

brought back into the glovebox and precipitated with ~ 36 mL of hexanes and stored in the glovebox freezer overnight. The flask was then removed from the glovebox and the NO(g) was purged out of the headspace using high pressure N_2, and then was brought back into the box to filter off the product as a brown powder. Yield: 147 mg (73 %). Characterization: IR (KBr) ν(NO) 1800 cm^{-1}. UV-Vis (λ_{max}) = 370 nm shoulder (CH_2Cl_2).

[Fe_2(BPMP)(NMeIm)$_2$(NO)$_2$)(OTf)$_3$ (2). 311 mg of [Fe_2(BPMP)(NMeIm)$_2$](OTf)$_3$ was dissolved in ~4 mL CH_2Cl_2 in a 100 mL Schlenk flask. The flask was placed on the NO-Schlenk line, partially evacuated, and filled with NO(g) resulting in an immediate color change to brown-red. The flask was brought back into the glovebox and precipitated with ~ 36 mL of hexanes and stored in the glovebox freezer overnight. The flask was then removed from the glovebox and the NO(g) was purged out of the headspace using high pressure N_2, and then was brought back into the box to filter off the product as a black/brown oily solid. Yield: 246 mg (75.4 %). Characterization: Elemental anal. Calcd for $C_{44}H_{45}F_9Fe_2N_{12}O_{12}S_3$: C, 40.26; H, 3.46; N, 12.80; found (%): C, 41.30; H, 3.71; N, 11.82. IR (KBr) ν(NO) 1756 cm^{-1}. UV-Vis (λ_{max}) = 360 nm shoulder (CH_2Cl_2).

[Fe_2(BPMP)(MeOH)$_2$(NO)$_2$)(OTf)$_3$ (3). 259 mg of [Fe_2(BPMP)(MeOH)$_2$](OTf)$_3$ was dissolved in ~4 mL CH_2Cl_2 in a 100 mL Schlenk flask. The flask was placed on the NO-schlenk line, partially evacuated, and filled with NO(g) resulting in an immediate color change to brown. The flask was brought back into the glovebox and precipitated with ~ 36 mL of hexanes and stored in the glovebox freezer overnight. The flask was then removed from the glovebox and the NO(g) was purged out of the headspace using high pressure N_2, and then was brought back into the box to filter off the product as a brown powder. Yield: 172 mg (63 %). Characterization: Elemental

anal. Calcd for $C_{38}H_{41}F_9Fe_2N_8O_{14}S_3$: C, 37.64; H, 3.41; N, 9.24; found (%): C, 37.54; H, 3.60; N, 8.57. IR (KBr) ν(NO) 1800 cm^{-1}. UV-Vis (λ_{max}) = 425 nm (MeOH).

[Fe(BMPA)(OTf)$_2$(NO)] (4). BMPA (138 mg, 712 μmol) was dissolved in 2 mL CH_3CN and placed in a 100 mL Schlenk flask. Separately, $[Fe(OTf)_2](CH_3CN)_2$ (300 mg, 712 μmol) was dissolved in 2 mL CH_3CN and added slowly to the Schlenk flask leading to the immediate color change from light yellow to bright orange. This solution was immediately nitrosylated without isolating the metallated precursor complex, affording a green-brown solution with partial precipitation of the nitrosylated product. The solution was then further precipitated with ~ 24 mL of Et_2O and stored in the glovebox freezer overnight. The flask was then removed from the glovebox and the NO(g) was purged out of the headspace using high pressure N_2, and then was brought back into the box to filter off the microcrystalline green product. Yield: 196 mg (47.5 %). Characterization: Elemental anal. Calcd for $C_{14}H_{13}F_6FeN_4O_7S_2$: C, 28.83; H, 2.25; N, 9.61; found (%): C, 29.23; H, 2.33; N, 9.36. IR (KBr) ν(NO) 1848 cm^{-1}. UV-Vis (λ_{max}) = 350 nm (CH_3CN).

4.4 References

(1) Jana, M., Pal, N., White, C. J., Kupper, C., Meyer, F., Lehnert, N.;Majumdar, A. Functional Mononitrosyl Diiron(II) Complex Mediates the Reduction of NO to N_2O with Relevance for Flavodiiron NO Reductases. *J. Am. Chem. Soc.* **2017**, *140*, 14380-14383.

(2) Jana, M., White, C. J., Pal, N., Demeshko, S., Cordes, C., Meyer, F., Lehnert, N.;Majumdar, A. Functional Models for the Mono- and Dinitrosyl Intermediates of FNORs: Semireduction versus Superreduction of NO. *J. Am. Chem. Soc.* **2020**, *142*, 6600-6616.

(3) White, C. J., Speelman, A. L., Kupper, C., Demeshko, S., Meyer, F., Shanahan, J. P., Alp, E. E., Hu, M., Zhao, J.;Lehnert, N. The Semireduced Mechanism for Nitric Oxide Reduction by Non-Heme Diiron Complexes: Modeling Flavodiiron Nitric Oxide Reductases. *J. Am. Chem. Soc.* **2018**, *140*, 2562-2574.

(4) Kindermann, N., Schober, A., Demeshko, S., Lehnert, N.;Meyer, F. Reductive Transformations of a Pyrazolate-Based Bioinspired Diiron−Dinitrosyl Complex. *Inorg. Chem.* **2016**, *55*, 11538-11550.

(5) Speelman, A. L. "Investigation of the Electronic Structure and Reactivity of Non-Heme Iron Nitrosyl and Nitroxyl Complexes". Ph.D. Thesis, University of Michigan, Ann Arbor, MI, **2016**.

(6) Frisch, M. J., Trucks, G. W., Schlegel, H. B., Scuseria, G. E., Robb, M. A., Cheeseman, J. R., Scalmani, G., Barone, V., Mennucci, B., Petersson, G. A., Nakatsuji, H., Caricato, M., Li, X., Hratchian, H. P., Izmaylov, A. F., Bloino, J., Zheng, G., Sonnenberg, J. L., Hada, M., Ehara, M., Toyota, K., Fukuda, R., Hasegawa, J., Ishida, M., Nakajima, T., Honda, Y., Kitao, O., Nakai, H., Vreven, T., Montgomery, J. A., Jr., Peralta, J. E., Ogliaro, F., Bearpark, M., Heyd, J. J., Brothers, E., Kudin, K. N., Staroverov, V. N., Kobayashi, R., Normand, J., Raghavachari, K., Rendell, A., Burant, J. C., Iyengar, S. S., Tomasi, J., Cossi, M., Rega, N., Millam, J. M., Klene, M., Knox, J. E., Cross, J. B., Bakken, V., Adamo, C., Jaramillo, J., Gomperts, R., Stratmann, R. E., Yazyev, O., Austin, A. J., Cammi, R., Pomelli, C., Ochterski, J. W., Martin, R. L., Morokuma, K., Zakrzewski, V. G., Voth, G. A., Salvador, P., Dannenberg, J. J., Dapprich, S., Daniels, A. D., Farkas, O., Foresman, J. B., Ortiz, J. V., Cioslowski, J.;Fox, D. J.; Gaussian, Inc.: Wallingford, CT, 2009.

(7) Perdew, J. P. Density-functional approximation for the correlation energy of the inhomogeneous electron gas. *Phys. Rev. B* **1986**, *33*, 8822-8824.

(8) Perdew, J. P., Burke, K.;Wang, Y. Generalized gradient approximation for the exchange-correlation hole of a many-electron system. *Phys. Rev. B* **1996**, *54*, 16533-16539.

(9) Wachters, J. H. Gaussian basis set for molecular wavefunctions containing third-row atoms. *J. Chem. Phys.* **1970**, *52*, 1033.

(10) Hay, P. J. Gaussian basis sets for molecular calculations - representation of 3D orbitals in transition-metal atoms. *J. Chem. Phys.* **1977**, *66*, 4377-4384.

(11) Schaefer, A., Horn, H.;Ahlrichs, R. J. Fully optimized contracted Gaussian basis sets for atoms Li to Kr. *J. Chem. Phys.* **1992**, *97*, 2571-2577.

(12) Schaefer, A., Huber, C.;Ahlrichs, R. Fully optimized contracted Gaussian basis sets of triple zeta valence quality for atoms Li to Kr. *J. Chem. Phys.* **1994**, *100*, 5829-5835.

(13) Speelman, A. L., Zhang, B., Silakov, A., Skodje, K. M., Alp, E. E., Zhao, J., Hu, M. Y., Kim, E., Krebs, C.;Lehnert, N. Unusual Synthetic Pathway for an $\{Fe(NO)_2\}^9$ Dinitrosyl Iron Complex (DNIC) and Insight into DNIC Electronic Structure via Nuclear Resonance Vibrational Spectroscopy. *Inorg. Chem.* **2016**, *55*, 5485-5501.

(14) Tonzetich, Z. J., Héroguel, F., Do, L. H.;Lippard, S. J. Chemistry of Nitrosyliron Complexes Supported by a β-Diketiminate Ligand. *Inorg. Chem.* **2011**, *50*, 1570-1579.

(15) Tsai, M. L., Tsou, C. C.;Liaw, W. F. Dinitrosyl Iron Complexes (DNICs): From Biomimetic Synthesis and Spectroscopic Characterization towards Unveiling the Biological and Catalytic Roles of DNICs. *Acc. Chem. Res.* **2015**, *48*, 1184-1193.

(16) Shih, W.-C., Lu, T.-T., Yang, L.-B., Tsai, F.-T., Chiang, M.-H., Lee, J.-F., Chiang, Y.-W.;Liaw, W.-F. New members of a class of dinitrosyliron complexes (DNICs): The characteristic EPR signal of the six-coordinate and five-coordinate {Fe(NO)2}9 DNICs. *J. Inorg. Biochem.* **2012**, *113*, 83-93.

(17) Tsai, F.-T., Lee, Y.-C., Chiang, M.-H.;Liaw, W.-F. Nitrate-to-Nitrite-to-Nitric Oxide Conversion Modulated by Nitrate-Containing {Fe(NO)2}9 Dinitrosyl Iron Complex (DNIC). *Inorganic Chemistry* **2013**, *52*, 464-473.

(18) Chen, C.-H., Ho, Y.-C.;Lee, G.-H. Synthesis and reactivity of the five-coordinate {Fe(NO)2}9 [(TMEDA)Fe(NO)2I]. *J. Organomet. Chem.* **2009**, *694*, 3395-3400.

(19) Ye, S.;Neese, F. The Unusual Electronic Structure of Dinitrosyl Iron Complexes. *J. Am. Chem. Soc.* **2010**, *132*, 3646–3647.

(20) Speelman, A. L.;Lehnert, N. Characterization of a High-Spin Non-Heme $\{FeNO\}^8$ Complex: Implications for the Reactivity of Iron Nitroxyl Species in Biology. *Angew. Chem. Int. Ed.* **2013**, *52*, 12283-12287.

(21) Speelman, A. L., White, C. J., Zhang, B., Alp, E. E., Zhao, J., Hu, M., Krebs, C., Penner-Hahn, J.;Lehnert, N. Non-heme High-Spin {FeNO}$^{6-8}$ Complexes: One Ligand Platform Can Do It All. *J. Am. Chem. Soc.* **2018**, *140*, 11341-11359.

(22) Biswas, S., Kurtz, D. M., Montoya, S. R., Hendrich, M. P.;Bominaar, E. L. The Catalytic Role of a Conserved Tyrosine in Nitric Oxide-Reducing Non-heme Diiron Enzymes. *ACS Catal.* **2020**, 8177-8186.

(23) Van Stappen, C.;Lehnert, N. Mechanism of N-N Bond Formation by Transition Metal-Nitrosyl Complexes: Modeling Flavodiiron Nitric Oxide Reductases. *Inorg. Chem.* **2018**, *57*, 4252-4269.

(24) Zheng, S., Berto, T. C., Dahl, E. W., Hoffman, M. B., Speelman, A. L.;Lehnert, N. The Functional Model Complex $[Fe_2(BPMP)(OPr)(NO)_2](BPh_4)_2$ Provides Insight into the Mechanism of Flavodiiron NO Reductases. *J. Am. Chem. Soc.* **2013**, *135*, 4902−4905.

Chapter 5

Tuning Reduction Potential: Synthesis and Characterization of Primary Coordination Sphere Carboxylate Ligands For Diiron Complexes

The complexes discussed thus far in Chapters 2-4 form stable hs-{FeNO}^{7} complexes that undergo intra- and intermolecular semi- or superreduction in the presence of additional chemical or electrochemical reductive equivalents.[1-3] While these complexes demonstrate that reduction is a potent means of carrying out the facile reduction of NO to N_2O, studies on the *Tm* FDP enzyme illustrate that direct-coupling is a viable, albeit kinetically slower, possibility in enzyme systems.[4] This is likely achieved through both primary- and secondary-coordination sphere interactions within the active site pocket. Within the primary-coordination sphere, each Fe center contains N_2O_3 ligation, with one monodentate carboxylate, a bridging carboxylate, a bridging hydroxide, and two histidine ligands per iron center, whereas the model complexes discussed in chapters 2-4 provide either N_3O_2 or N_4O primary coordination spheres for iron. Consequently, the diiron cores of these complexes sit at too positive redox potentials and are unable to stabilize the diferric state, as illustrated by their more positive $Fe^{III}Fe^{II}/Fe^{II}Fe^{II}$ redox couples compared to those of functional FNORs, like the *E. coli* flavorubredoxin (FlRd, see Scheme 5.1)[5], as well as their irreversible oxidation to the Fe^{III}/Fe^{III} state in their corresponding cyclic voltammograms. As a result, direct-coupling is inhibited in these systems. Additionally, recent DFT studies[6, 7] on *Tm* FDP suggests that the FNOR active site may provide further assistance in direct-coupling via a secondary

Scheme 5.1 . $Fe^{III}Fe^{II}/Fe^{II}Fe^{II}$ reduction potentials of two FNOR model complexes and of *E. coli* Flavorubredoxin (FlRd). All potentials are listed with respect to the Fc^{+}/Fc couple.

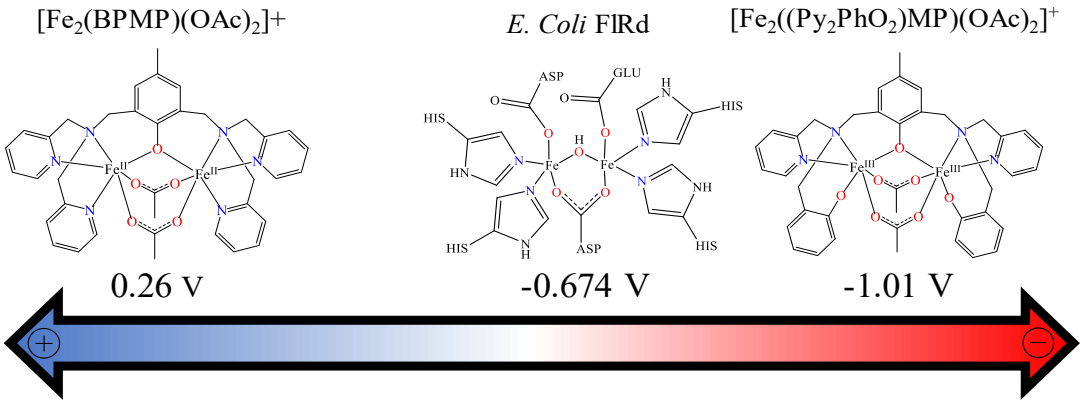

coordination sphere H-bonding interaction between Y197 and one of the bound NO ligands, resulting in decreased activation barriers for both N-N coupling and N-O bond cleavage en route to N_2O formation.

Inspired by the phosphatase community's numerous dinucleating ligand scaffolds with additional O-donor phenolate or carboxylate ligation[8], our laboratory recently published a BPMP derivative where two phenolates replace two of the pyridine donor groups.[9-11] This complex overshoots the FNOR $Fe^{III}Fe^{II}/Fe^{II}Fe^{II}$ redox couple in FlRd by -0.34 V, sitting at -1.01 V vs. Fc^{+}/Fc (Scheme 5.1). Interestingly, the corresponding diferrous complex does not generate a stable dinitrosyl complex, but instead, carries out quantitative and rapid direct-coupling. This chapter continues with phosphatase-inspired ligand derivatives focused on tuning the reduction potentials of our FNOR model complexes via primary coordination sphere modifications to be closer to those of FNORs by using O-donor ligands that contain intermediate-strength electron-donating properties: aliphatic and aromatic carboxylates.

5.1 Synthesis of Aliphatic Carboxylate and Benzoate Derivatives of BPMP[12]

Initial attempts to synthesize carboxylate derivatives of BPMP

Our initial approach to synthesize aliphatic carboxylate- and benzoate-containing BPMP derivatives mirrored the approach taken in the synthesis of the BPMP ligand: first, the desired carboxylate arm is prepared, and then appended to a symmetric central phenol building block, 2,6-bis(chloromethyl)-4-methylphenol, via a S_N2 coupling reaction. The syntheses of three target ligand arms (**1a-c**) that would allow for the preparation of both symmetric and asymmetric BPMP derivatives with mixed aliphatic carboxylate (**1b, 1c**)[13-15] and benzoate (**1a**)[16] arms are shown in Scheme 5.2. These syntheses were carried out following literature precedent via either reductive

Scheme 5.2 Synthetic scheme for the synthesis of ligand arms **1a-c**.

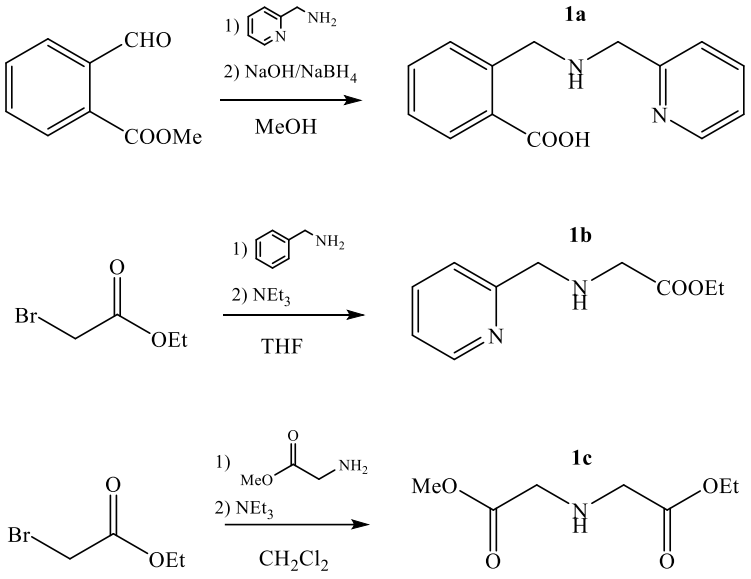

amination (**1a**) or S_N2 coupling (**1b, 1c**) of the corresponding starting materials. At this point, only the *ortho*-benzoate ligand derivative was targeted, although in principle, the synthesis of the *meta*-benzoate analog of **1a** could also be adapted from the S_N2 syntheses of **1b** and **1c**, whereby ethyl 3-(chloromethyl)benzoate and 2-picoylamine would be reacted in the presence of NEt_3. Ultimately, the synthesis of the *meta*-benzoate analog followed a different synthetic approach, which is described in the next section. In the next step, the ligand arms **1a-b** were reacted with 2,6-bis(chloromethyl)-4-methylphenol to generate the symmetric carboxylate derivatives of

BPMP (**2a** and **2c**, Scheme 5.3).[13, 17]. While this coupling successfully generates average yields of **2c**, the crude **2a** contains numerous impurities after workup and additional purification was not attempted. Due to the issues with impurities and low-to-average yields for **2a** and **2c**, an alternate, more convergent coupling route was developed for the synthesis of symmetric ligand analogs (including the *meta*-benzoate ligand), which is discussed below.

Scheme 5.3 Synthetic scheme for the synthesis **2a**, **2c** from **1a** and **1b**.

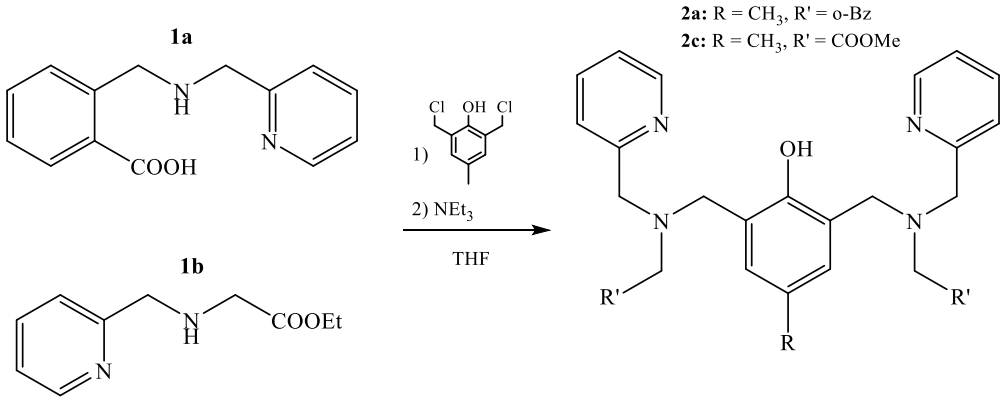

New approach for the synthesis of symmetric carboxylate derivatives of BPMP

Moving forward, attempts were made to synthesize a common synthetic branching point for the synthesis of all desired symmetric ligands. This was achieved by converting *p*-cresol or 4-(*tert*-butyl)phenol precursors into their 2,6-diformyl derivatives (**4a-b**, see Scheme 5.4) via a Duff reaction.[18] From here, since the synthesis of **2a** was unsuccessful via S_N2 coupling (a clean product could not be obtained, see above), the corresponding reductive amination reaction between **4a** and **1a** was attempted. However, this again resulted in poor yields of the desired ligand **2a** after aqueous workup. Alternatively, following literature precedent, a single pyridine arm can first be appended to **4a-b** cleanly and quantitatively in an initial reductive amination with 2-picolylamine to generate 4-methyl-2,6-bis[[(2-pyridinylmethyl)amino]methyl]-phenol (**5a**) and the corresponding *tert*-butyl derivative (**5b**).[19] In this way, ligands containing a 4-methyl or *tert*-butyl phenolic backbone can be synthesized from a single starting point via S_N2 coupling reactions with the desired ester-

protected halide-precursors, affording the four desired ester-protected symmetric aliphatic carboxylate and benzoate derivatives **2a-d**, which can be subsequently deprotected via hydrolysis to obtain **3a-d** (Scheme 5.4).[13]

Scheme 5.4 Synthetic scheme for the synthesis of the precursors **5a-b** and subsequent S_N2 couplings and hydrolyses to generate the symmetric carboxylate and benzoate ligands **3a-d**.

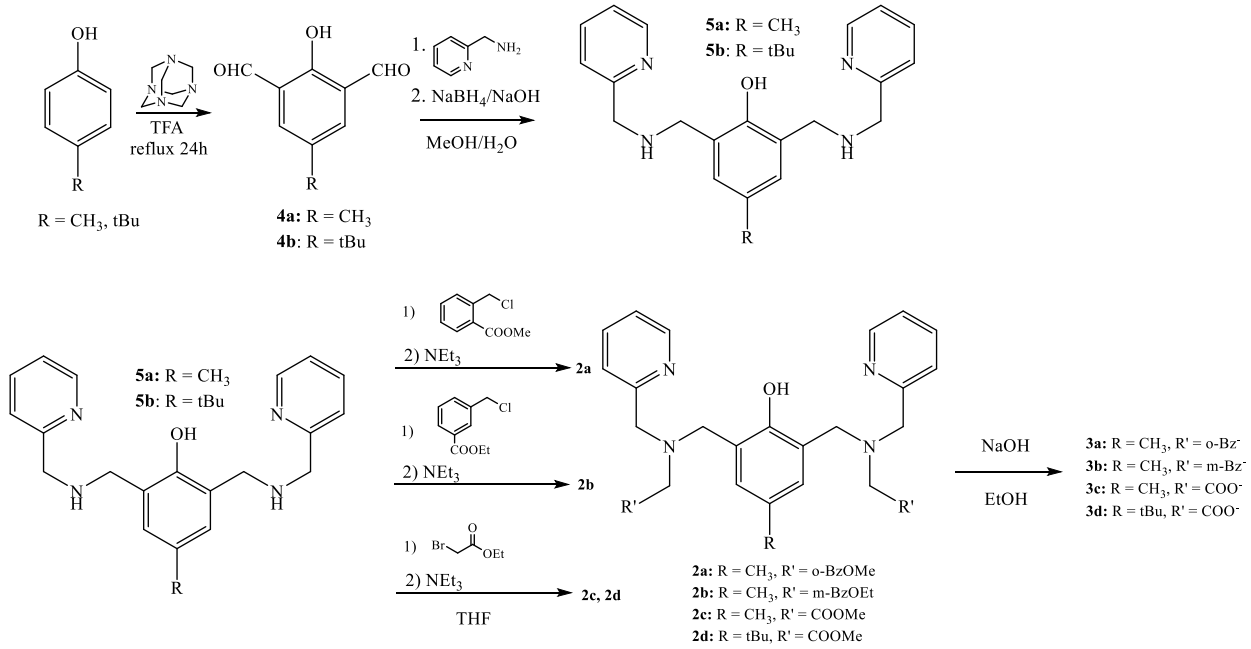

Synthesis of the Asymmetric Ligand 3e

Asymmetric ligand derivatives were synthesized starting from 2-hydroxy-5-methylbenzaldehyde (Scheme 5.5). Asymmetric functionalization was achieved via a literature precedent[20] whereby the chloromethylation of 2-hydroxy-5-methylbenzaldehyde is achieved by refluxing with p-formaldehyde and HCl, affording quantitative yields of 3-(chloromethyl)-2-hydroxy-5-methylbenzaldehyde (**6**). A subsequent S_N2 addition of di-2-picoylamine affords quantitative yields of 3-[[Bis(2-pyridinylmethyl)amino]methyl]-2-hydroxy-5-methylbenz-aldehyde (**7**) as the primary branching point for additional synthetic steps.[21, 22] Initial attempts at the reductive amination between **7** and either ligand arm **1b** or **1c** (see above) with $NaBH_4$ were

unsuccessful. As such, **7** was reduced to 2-[[Bis[(pyridin-2-yl)methyl]amino]methyl]-6-(hydroxymethyl)-4-methylphenol[23] (**8**) with $NaBH_4$ and subsequently halogenated with $SOCl_2$ to obtain 2-[[bis[(pyridin-2-yl)methyl]methyl]-6-(chloromethyl)-4-methylphenol (**9**).[23] From here, **1c** can be successfully appended via S_N2 coupling to make **2e**, followed by hydrolysis to **3e**.

Scheme 5.5 Synthetic scheme for the synthesis of the asymmetric ligand **3e**.

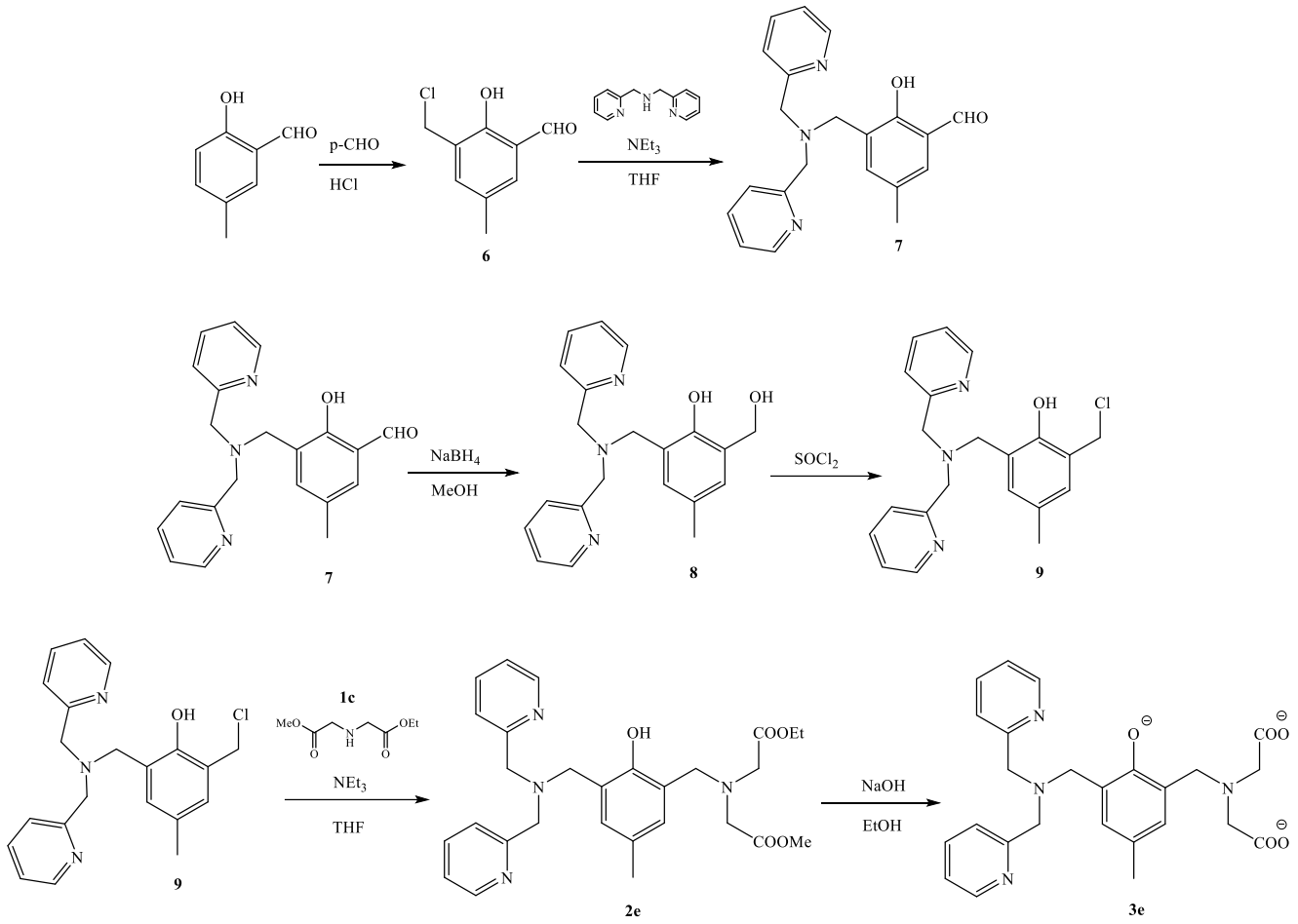

Future work will require additional refinement of the asymmetric synthesis. Starting from **7**, the reductive amination with **1b** or **1c** may proceed successfully with milder reductants like $NaBH(OAc)_3$. Alternatively, mirroring the synthesis of symmetric carboxylate ligands above, it may be feasible to first perform a reductive amination with **7** and either 2-picoylamine[22] or methyl

glycinate, followed by a subsequent S_N2 with ethyl 2-bromoacetate to generate asymmetric derivatives with either one or two aliphatic carboxylate-containing arms.

Metallation and Nitrosylation of 3a-c

3a-c can be metallated and nitrosylated via modified procedures initially developed for BPMP.[2] Here, the corresponding trisodium salts of the ligands **3a-c** are anaerobically metallated with two equivalents of $Fe(OTf)_2$ and one equivalent of NaOAc, affording a yellow-orange solution of metallated complexes **10a-12a**. Owing to the differences in solubility between the aliphatic carboxylate and benzoate derivatives of H[BPMP], the workup and washing conditions required to remove Na/KOTf salt byproducts that form during the metallation vary for each analog and are described in the Experimental Section below. The diferrous complexes **10a-12a** are then nitrosylated following general nitrosylation protocols described in Chapter 2 to afford their dinitrosyl analogs **10b-12b** (Scheme 5.6).

Scheme 5.6 Overview of proposed dinitrosyl complexes discussed in this chapter.

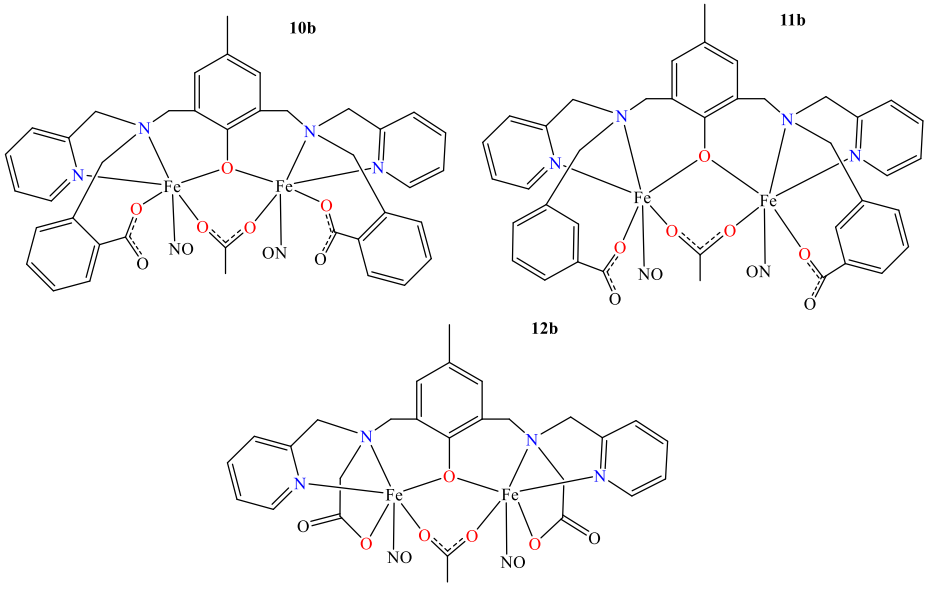

5.2 Characterization and Reactivity of Diiron Complexes with Aliphatic Carboxylate and Benzoate Ligand Derivatives of BPMP

Characterization of Benzoates 10a-b, 11a-b

Preliminary UV-Vis characterization of **10a-b** revealed typical broad, moderate-intensity features centered at 415 nm and 445 nm, assigned to iron(II)-to-pyridine MLCT[24] and NO^- to Fe(III) LMCT transitions[25-27], respectively (Figure 5.1). The IR spectrum of **10a** contains a broad band with peaks at 1607, 1594, and 1569 cm^{-1} corresponding to both benzoate and pyridine vibrational modes. Upon nitrosylation to **10b**, a new N-O stretching band appears at 1724 cm^{-1} in the IR spectrum – shifted 41 cm^{-1} to lower energy compared to the analogous BPMP complex discussed in Chapter 2. This shift is attributed to the increased electron donation from the benzoate ligands and corresponding, decreased π-donation from NO^- to Fe(III) (Figure 5.1). The cyclic

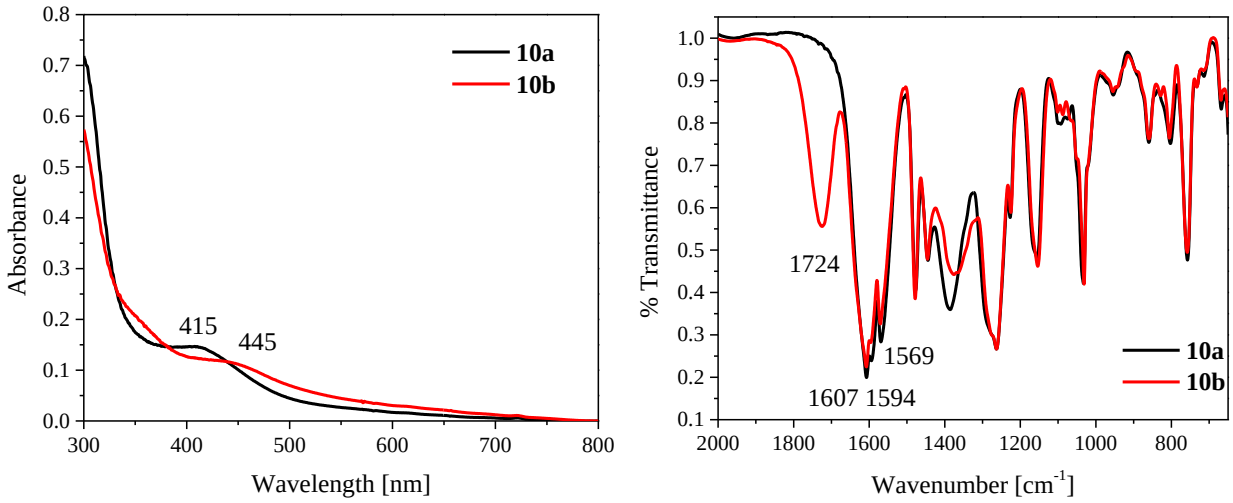

Figure 5.1 Left: Overlay of the UV-Vis spectra of **10a-b**, taken in acetone. Right: IR (KBr) overlay of **10a-b**, illustrating the appearance of a new N-O stretching band at 1724 cm^{-1}.

voltammogram of **10a** contains two irreversible oxidation events at -0.38 V and -0.11 V vs. Fc^+/Fc corresponding to the $Fe^{II}Fe^{II}/Fe^{II}Fe^{III}$ and $Fe^{II}Fe^{III}/Fe^{III}Fe^{III}$ couples, respectively, with a minor impurity giving rise to a third oxidation event at 0.10 V (Figure 5.2). On the reverse scan, re-reduction of the decomposition product(s) occurs at -0.30 V and –0.77 V. The impurity may

originate from a fraction of bis-OAc or no-OAc bridged complexes existing in equilibrium with the mono-OAc-bridged complex **10a**, or potentially due to an equilibrium between diiron and monoiron complexes (see DFT discussion below). Importantly, this places the redox couple of **10a** ~500 mV more negative than BPMP but still ~300 mV positive of the FlRd couple. This complex serves as a middle-ground between our initially reported BPMP complex[2] and the second generation (Py_2PhO_2)MP derivative[9]. In line with the increased electron donation to the diiron core, the irreversible reduction of **10b** occurs at -1.52 V vs Fc^+/Fc, a -0.51 V shift compared to BPMP (Figure 5.2), with several new oxidation and re-reduction events (originating from decomposition products) appearing on the reverse oxidative and re-reductive scans.

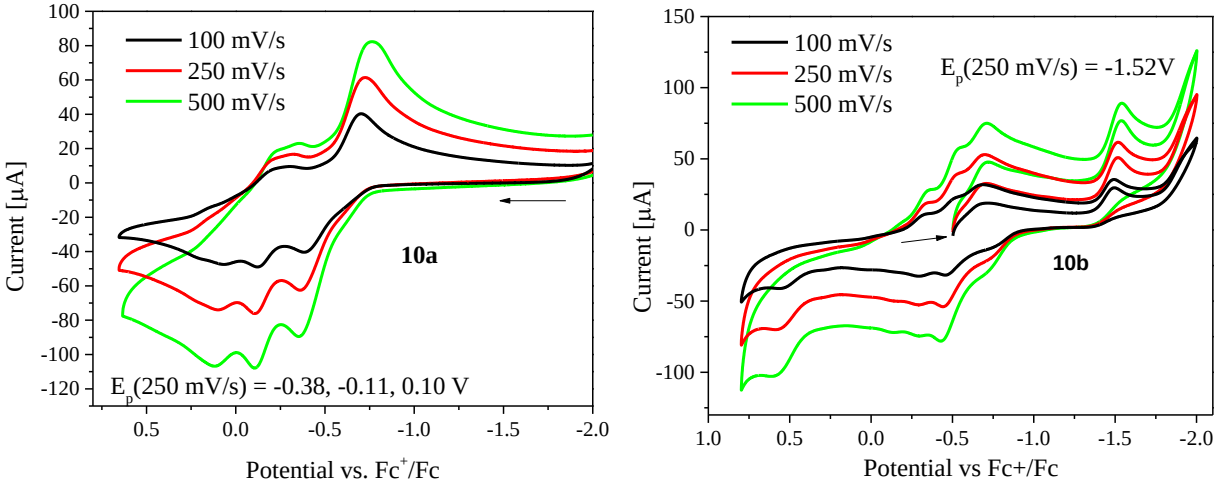

Figure 5.2 Left: The cyclic voltammogram of **10a** exhibits two main oxidation events at -0.38 and -0.11V vs. Fc^+/Fc corresponding to the $Fe^{II}Fe^{II}/Fe^{II}Fe^{III}$ and $Fe^{II}Fe^{III}/Fe^{III}Fe^{III}$ couples. Right: The cyclic voltammogram of **10b** shows an irreversible reduction of the iron-nitrosyl unit at -1.52 V. Conditions: ~5 mM **10a-b** with ~0.1M [TBA](OTf) as the supporting electrolyte in acetone solution.

Lastly, the complexes **10a-b** were characterized by Mössbauer and EPR spectroscopies. As expected, the metallated precursor **10a** is EPR silent arising from antiferromagnetic coupling between the two Fe(II) centers. Accordingly, this complex exhibits a typical Fe(II) isomer shift and quadrupole doublet of 1.21 mm/s and 3.15 mm/s, respectively, by Mössbauer spectroscopy (Figure 5.3). Interestingly, upon nitrosylation to **10b,** a strong g~2 signal appears by EPR

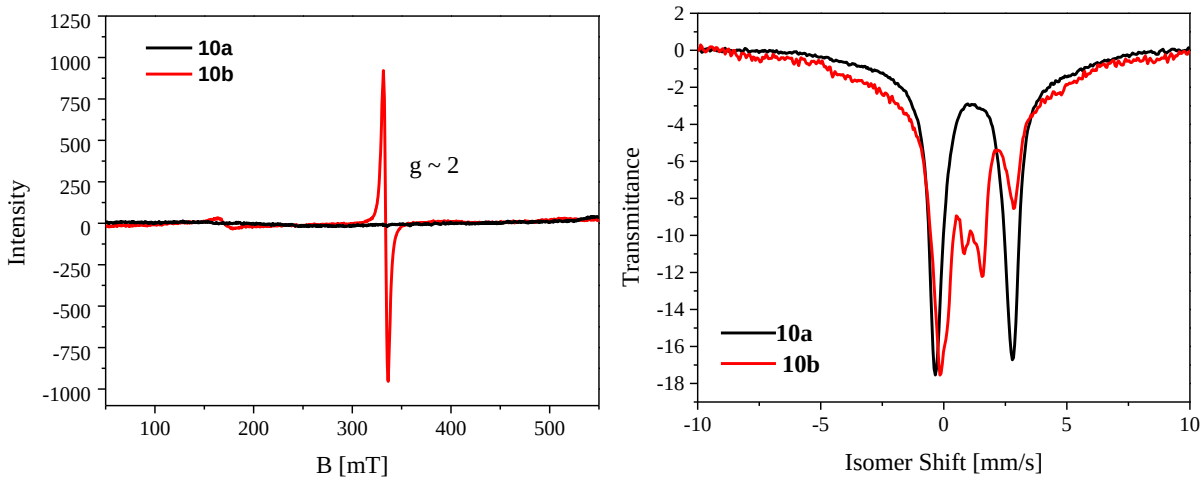

Figure 5.3 Left: Overlay of the EPR spectra of **10a** and **10b** in acetone. Conditions: **[10a]** = [**10b**] = ~2 mM in acetone. Data were collected at 4K with 2 mW microwave power and a 1G modulation amplitude. Right: Mössbauer spectra of **10a** and **10b**, illustrating a clean diferrous starting material that forms multiple new NO-containing species upon nitrosylation.

spectroscopy (Figure 5.3), likely indicating that the complex does not completely form a diiron dinitrosyl product, which would be EPR silent. This signal likely arises from the formation of a diiron mononitrosyl species where the hs-Fe(II) (S = 2) is antiferromagnetically coupled to a hs-$\{FeNO\}^7$ (S = 3/2), affording a ground state with S_t = 1/2 (see Chapter 2 for an analogous compound from the Majumdar laboratory). Alternatively, this could also arise from the formation of a mixed-valent complex either via adventitious oxidation or bimolecular N-N coupling. In line with this, the Mössbauer spectrum of **10b** consists of at least three quadrupole doublets, arising from a combination of hs-$\{FeNO\}^7$, Fe(II) and Fe(III) species. With the CV, Mössbauer and EPR data in hand, it is clear that the nitrosylated system contains an equilibrium of numerous species. There is clearly at least one $\{FeNO\}^7$ quadrupole doublet present, which could feasibly represent either mono- or dinitrosyl species since their coordination and electronic environments would be quite similar. The presence of an Fe(III) signal is unexpected – while adventitious oxidation is plausible and much more likely for more electron-rich ligand systems, a direct-coupling could also generate a ferric byproduct and cannot be excluded without additional N_2O yield tests. Finally,

based on the Mössbauer data, there is also a significant portion of un-nitrosylated Fe(II) precursor present, either due to poor nitrosylation or facile NO loss in solution.

While the *ortho*-benzoate **10a-b** remained soluble in polar aprotic solvents, allowing for its characterization as shown above, the meta-benzoate analog **11a-b** suffered from extremely low to no solubility in aqueous, polar, and nonpolar solvents, confounding thorough spectroscopic characterization. As such, DFT was utilized to further evaluate the structures of both **10a** and **11a**. DFT studies revealed that both complexes **10a** and **11a** are too sterically encumbered for the benzoate donor groups to feasibly bind to the diiron core, with **10a** containing a significantly twisted benzoate ligand, with the carboxylate group twisted by 37° out of the aromatic plane (Figure 5.4). Even worse, **11a** is unable to access a conformation where the benzoates groups can bind to the iron centers at all. Due to these steric restrictions, we suspect that these complexes

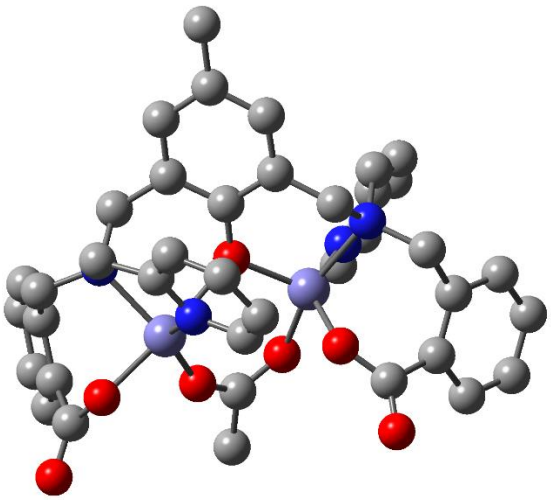

Figure 5.4 The UBP86/TZVP optimized structure of **10a**, where the benzoate ligation requires the carboxylates to twist 37° out of the aromatic plane.

either bind to a single iron center or form extended oligomer networks via bridging carboxylates. In particular, the lack of solubility of **11a** implies formation of an inorganic polymer (MOF). Future work on these complexes will first require DFT screening of the conformational flexibility of related complexes with extended methylene chains that link the benzoate arms to the tertiary

amine groups of the ligand, to identify a linker that allows for better coordination of the benzoate groups to the iron centers. As a further improvement, additional ligand backbone modifications like using a *tert*-butyl phenolic backbone should also be considered, to improve the solubility of the complexes in organic solvents.

Characterization and Reactivity of Aliphatic Carboxylates 12a-b

The initial UV-Vis spectroscopic characterization of **12a** and **12b** shows quite similar absorption features compared to the *ortho*-benzoate (**10a-b**) analogs, with a broad MLCT band at 415 nm in **12a** and a broader LMCT band at 440 nm upon nitrosylation to **12b** (Figure 5.5). The IR spectrum of **12a** contains a sharp pyridine stretching band at 1605 cm^{-1} with two broad shoulders on either side at 1572 cm^{-1} and 1637 cm^{-1}, attributed to carboxylate bands (Figure 5.5). Upon nitrosylation to yield **12b**, a new N-O stretching feature appears at 1750 cm^{-1}, which is 15 cm^{-1} lower in energy than the N-O stretch in the original BPMP complex and 26 cm^{-1} higher in

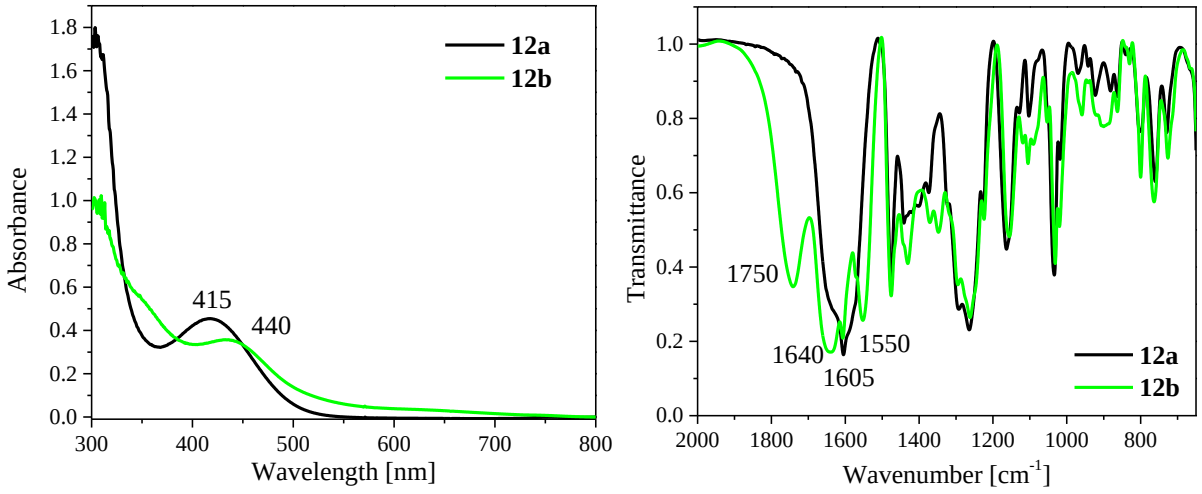

Figure 5.5 Left: UV-Vis spectra of **12a** and **12b** taken in methanol. Right: IR (KBr) of **12a** and **12b** illustrating the formation of a new NO band at 1750 cm^{-1} and a splitting of the carboxylate bands to give features at 1640 cm^{-1} and 1550 cm^{-1}.

energy than the corresponding feature in **10b**. This finding is in line with the idea that the aliphatic carboxylate groups have an intermittent electron donicity, between pyridines and benzoates. In

contrast to **10b**, the carboxylate bands of **12b** shift upon nitrosylation to 1640 cm^{-1} and 1550 cm^{-1}. This is not unexpected, as the Fe(II) centers in **12a** become partially oxidized upon nitrosylation to yield the [hs-{FeNO}^{7}]$_2$ complex **12b**, which has an Fe(III)-NO^- electronic structure. Upon nitrosylation, shorter Fe-carboxylate bond lengths should result, and the carboxylate ligands should be sensitive to the resulting change in donicity. Consequently, the anionic character of the monodentate carboxylate arms should become more localized at the binding O-atom, giving the adjacent C-O bond distinct double-bond character. This causes a shift of the corresponding C-O stretching mode to higher wavenumbers, whereas the bound C-O unit should move closer towards a bond order of ~1, shifting its stretching frequency towards lower wavenumbers.

Electrochemically, **12a-b** have relatively similar reduction potentials compared to the benzoate analogs **10a-b**. **12a** shows two irreversible oxidative events shifted slightly more positive than those of **10a**, at -290 mV and 30 mV vs Fc^+/Fc, corresponding to the $Fe^{II}Fe^{II}/Fe^{II}Fe^{III}$ and $Fe^{II}Fe^{III}/Fe^{III}Fe^{III}$ couples, respectively. Upon nitrosylation to **12b**, a new irreversible reductive event appears at -1.56 V on the initial reductive scan, with two oxidative events at -275 mV and 20 mV on the reverse (oxidative) scan (Figure 5.6), which I interpret as a reformation of **12**a after N_2O release. This stands in contrast to the iron-NO complexes with the H-BPMP[2] and N-Et-HPTB[1, 3] ligands discussed in Chapters 2 and 3, where the formation of a μ-oxo product upon electrochemical reduction results in new oxidative events on the reverse scan that do not simply correspond to the precursor complex. The recovery of the two oxidation events originating from **12a** after reduction of **12b** is likely due to the experimental conditions – the presence of the polar protic solvent MeOH allows the μ-oxo bridge of the initial product to be protonated, resulting in the release of H_2O and recovery of the metallated precursor **12a**. This indicates that **12a** might be

a potent catalyst for the electrocatalytic reduction of NO to N_2O, capable of mediating multiple turnovers in protic solvents.

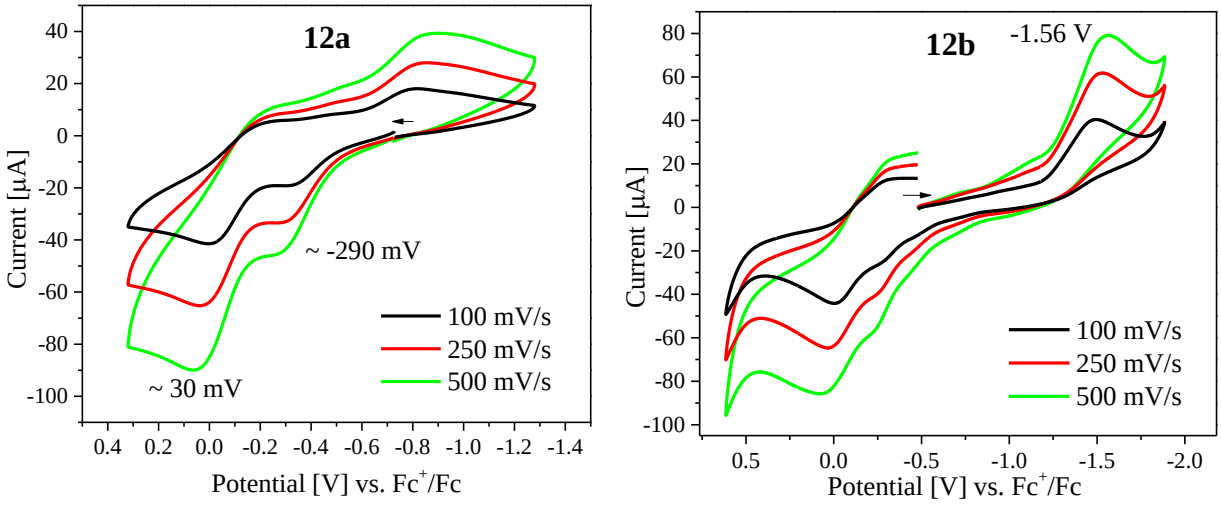

Figure 5.6 Left: The cyclic voltammogram of **12a** exhibits two oxidation events at -290 and 30 mV vs. Fc^+/Fc corresponding to $Fe^{II}Fe^{II}/Fe^{II}Fe^{III}$ and $Fe^{II}Fe^{III}/Fe^{III}Fe^{III}$ couples. Right: The cyclic voltammogram of **12b** illustrates irreversible reduction of the iron-nitrosyl unit at -1.56 V. Conditions: ~5 mM **12a-b** with ~0.1M [TBA](OTf) as the supporting electrolyte in methanol.

Both complexes **12a** and **12b** are only soluble in polar-protic or aqueous solvents, with a minimal (~0.5 mM) solubility in polar aprotic solvents like CH_3CN. These solubility properties confound detailed spectroscopic studies, as both MeOH and H_2O do not have solution IR windows in the 1700-1800 cm^{-1} range where we would be able to track the N-O stretching band in IR spectroelectrochemistry and related experiments. Solubility in polar aprotic solvents like CH_3CN and CH_2Cl_2 is desirable since both solvents have solution IR windows ranging from 1500 cm^{-1} to 2300 cm^{-1}. In order to mitigate these solubility issues, the synthesis of a *tert*-butyl phenolic analog of **3c** (**3d**) was undertaken, and a corresponding synthetic procedure was fully optimized (see Section 5.1). Future work on these complexes will involve the metallation of **3d**, nitrosylation, and characterization of the resulting complexes. Additional backbone derivatizations are also possible, starting either from alkylated pyridine or carboxylate starting materials should complexes with ligand **3d** share similar solubility issues as the complexes with ligand **3c**. For example,

Scheme 5.7 highlights numerous commercially available pyridine, quinoline, and carboxylate starting materials with either aldehyde, amine, or halide functionalities. The coupling of these starting materials to **4a-b**, **5a-b**, or **7** and **9** can be directly adapted from the S_N2 and reductive

Scheme 5.7 Overview of additional commercially available pyridine, quinoline, and ester-protected carboxylate derivatives that can be appended to several synthetic intermediates via modified S_N2 or reductive amination procedures.

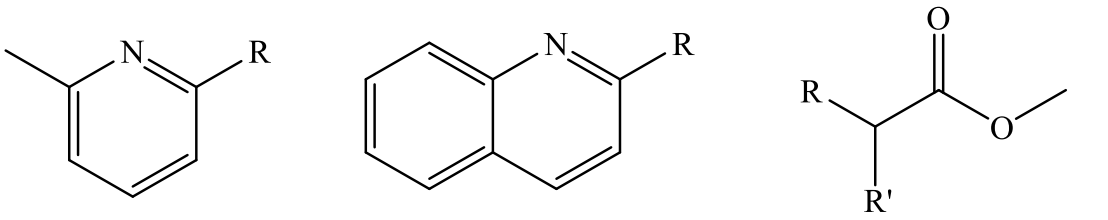

R = CHO
R = CH_2Br

R = CH_2NH_2
R = CHO
R = CH_2Cl

R = NH_2; R' = $CH((CH)_3)_2$
R = NH_2; R' = $C((CH)_3)_3$
R = Br; R' = $CH((CH)_3)_2$

amination protocols and workups discussed in this chapter and may provide an additional increase in solubility in aprotic solvents.

Nonetheless, the solution stability of **12b** was tested in a saturated CH_3CN solution via solution IR spectroscopy, illustrating a rapid decay of the N-O stretching band over the course of 1 hr (Figure 5.7). The solution decay of **12b** (by NO loss) was also monitored by UV-Dip probe experiments, using a 96 uM solution of **12b** in MeOH. The data show a decrease in the 440 nm band over the course of 2 hrs with two isosbestic points located at 438 and 468 nm (Figure 5.7). Importantly, as evaluated by IR gas-headspace analysis, the RT decomposition of **12b** in MeOH over 2 hrs in the absence of any external chemical reductant affords a substoichiometric 26% yield of N_2O (Figure 5.7), implying that this complex is capable of carrying out the direct-coupling of two NO to N_2O and H_2O in MeOH. Given that this complex has reduction potentials ~300 mV more positive than FlRd, the relatively slow kinetics of NO reduction are not unexpected. The slow N-N coupling combined with NO loss in solution (which could be counteracted by

conducting the reaction in the presence of excess NO gas) may in part rationalize the low N_2O yield. Importantly, additional isotopic labelling studies like those described in Chapter 2 are needed to determine whether this N-N coupling occurs intramolecularly, as a bimolecular coupling

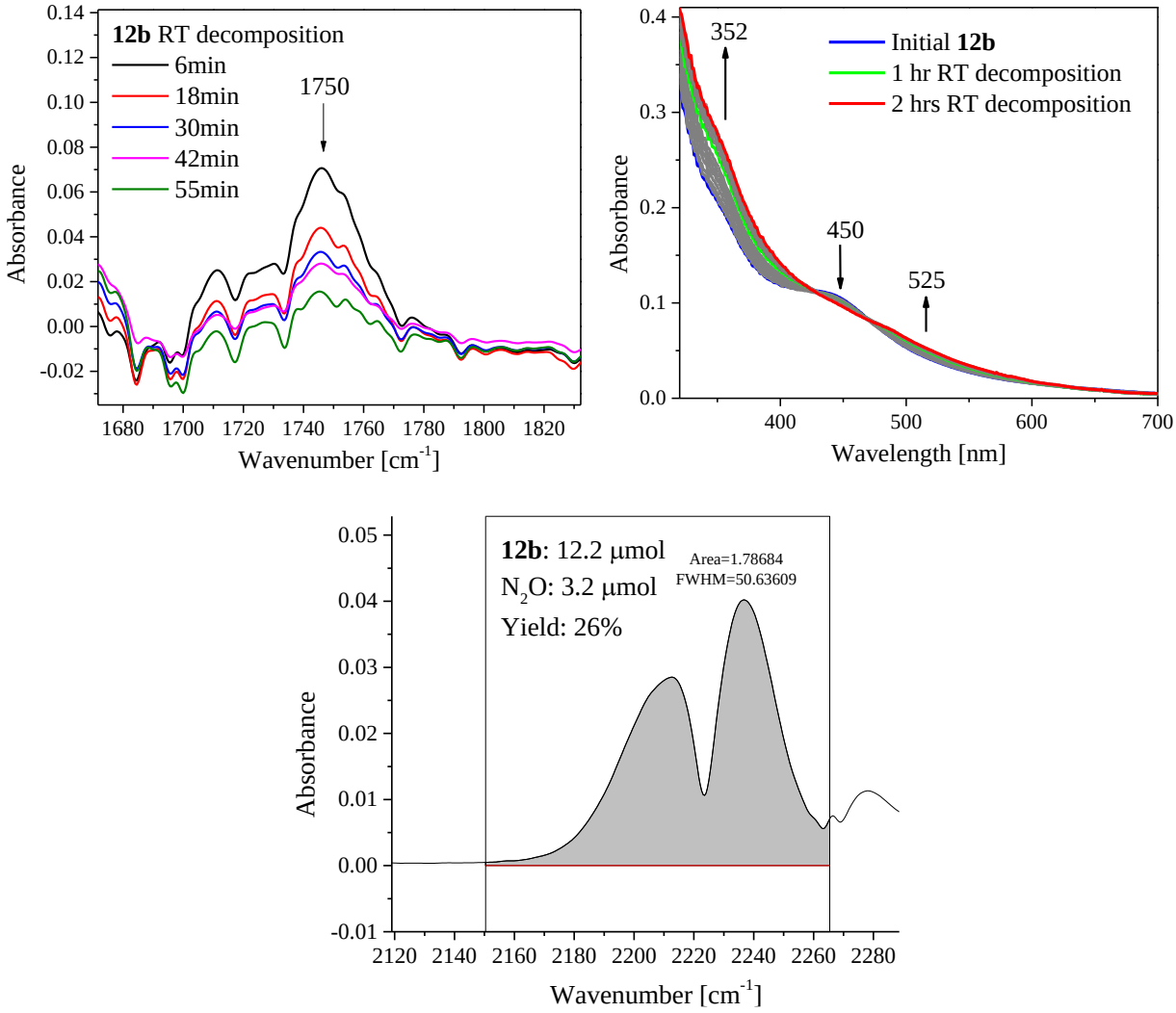

Figure 5.7 Top Left: Test of the solution stability of a saturated solution of **12b** in CH_3CN, showing a decay of the N-O band at 1750 cm^{-1} over the course of 1 hr. Top Right: UV-Vis dip probe experiment of a 96 µM solution of **12b** in MeOH, which shows a similar decay of the NO-related absorption band at 450 nm with isosbestic points at 438 and 468 nm. Bottom: IR gas-headspace analysis of a 12.2 µmol solution of **12b**, after stirring in MeOH at RT for 2hrs.

route can currently not be excluded with N_2O yields falling below 50%. Additionally, since the dinitrosyl complex is stable when stored as a solid powder and has a defined reductive event by CV at -1.56 V vs. Fc^+/Fc, a direct comparison of the rate of semi-reduction (using a suitable

reductant that is soluble in MeOH) and direct-coupling could in-principle be conducted with this complex. Alternatively, should **3d** or related derivatives have increased solubilities in CH_3CN or CH_2Cl_2, further studies comparing the rates of NO reduction in protic vs aprotic solvents could be carried out, and the μ-oxo product could be isolated and characterized.

5.3 Experimental Section

General Considerations

Air sensitive materials were prepared under a dinitrogen atmosphere in either an MBraun glovebox, or using standard Schlenk techniques. All solvents were dried using standard techniques, freeze-pump-thawed to remove dioxygen, and stored over molecular sieves. All reagents were purchased from commercial sources and were used as received, unless noted below. $Fe(OTf)_2$ was recrystallized from ~10 mL of acetonitrile with ~70 mL of diethyl ether and dried under high vacuum to give $[Fe(OTf)_2](CH_3CN)_2$. Decamethylcobaltocene ($CoCp_2^*$) was sublimed prior to each use under static vacuum and stored at -35° C in the glovebox freezer. Nitric oxide was passed over an Ascarite II column and subsequently through a -80° C cold trap to remove higher N_xO_y impurities. All spectroscopic techniques were carried out as described in Chapter 2 and all NMR data are included in Section 5.5 (NMR Appendix).

Synthesis of Ligand Arms (1 a-c)

2-(((Pyridin-2-ylmethyl)amino)methyl)benzoate (1a). The synthesis of this ligand follows a literature procedure modified from the synthesis of the corresponding unprotected carboxylate.[16] 0.651 g, 3.97 mmol methyl-2-formyl-benzoate was dissolved in 10 mL MeOH with 0.224 g, 4.15 mmol NaOMe in a 100 mL RBF equipped with a rubber septa. 2-picoylamine (0.426 g, 3.94 mmol) was slowly added to the RBF in the glovebox and the reaction was stirred for 2 hrs before

placing the flask under low pressure N_2 on the Schlenk line. Under a positive pressure of N_2, $NaBH_4$ (0.177 g, 4.69 mmol) was added to the 0° C chilled solution, which was then stirred at RT for 30 mins. The solution was neutralized with concentrated HCl to pH ~7 causing the formation of a white precipitate, which was filtered off and the filtrate was extracted with CH_2Cl_2 followed by concentration to a yellow oil. Attempts to recrystallize this from CH_2Cl_2 with hexanes resulted in the formation of a yellow oil. Yield: 44% Characterization: ^{1}H NMR (400 MHz, $CDCl_3$): 8.55 (m, 1H); 7.88 (d, 1H); 7.64 (d, 1H); 7.51 (dd, 1H); 7.46 (d, 1H); 7.40 (d, 1H); 7.31(d, 1H); 7.19 (m, 1H); 4.93 (s, 2H); 4.45 (s, 2H).

Ethyl 2-[[(pyridin-2-yl)methyl]amino]acetate (1b). This synthesis follows a literature procedure with scaling.[13, 14] 3.65 g (33.8 mmol) ethylbromoacetate was dissolved in 10 mL THF within a 50 mL RBF. Then, 2.81 g (16.8 mmol) 2-picolylamine[28] was dissolved in 10 mL THF in a dropping funnel and added dropwise to the RBF over 30 mins, resulting in the immediate formation of a white precipitate. After stirring for 3 hrs, the salt byproduct was filtered off and the resulting the yellow filtrate was concentrated to a yellow oil, placed in a 5 mL RBF and vacuum distilled with heating to ~150° C to collect the desired product as a clear oil, leaving a black sludge in the distillation flask. Yield: 63%. Characterization: ^{1}H NMR (400 MHz, $CDCl_3$): 8.55 (d, 1H); 7.64 (d, 1H); 7.32 (d, 1H); 7.16 (m, 1H); 4.19 (m, 3H); 3.94 (s, 2H); 3.47(s, 2H); 2.15 (br, 1H); 1.27 (t, 3H).

Methyl 2-[(2-ethoxy-2-oxoethyl)amino]acetate (1c). This procedure was adapted from a related protocol.[15] The methyl ester of glycine hydrochloride (1.51g, 12.0 mmol) was combined with one equivalent of NEt_3 (1.21 g, 12.0 mmol) and 20 mL CH_2Cl_2 in a 100 mL RBF. Ethylbromoacetate (2.0 g, 12.0 mmol) and the second equivalent of NEt_3 (1.21 g, 12.0 mmol) were combined in 20 mL CH_2Cl_2 and slowly added to the amine suspension. The reaction was stirred at RT for 3 days

followed by filtration of the salt byproduct and concentration of the filtrate to a pale oil. The oil was run on a 1.5 in column containing ~100 g silica using 10% MeOH/DCM. The desired product elutes first (R_f ~0.8, visualized with Iodine). Yield: 35%. Characterization: ^{1}H NMR (400 MHz, CD_2Cl_2): 4.17 (m, 2H); 3.71 (s, 3H); 3.45 (s, 2H); 3.42 (s, 2H); 1.97 (br, 1H); 1.27 (t, 3H)

Synthesis of Symmetric Ligands (2 a-d, 3 a-d, 4 a-b, 5 a-b)

Dimethyl-2,2'-((((2-hydroxy-5-methyl-1,3-phenylene)bis(methylene))bis((pyridin-2-ylmethyl)azanediyl))bis(methylene))dibenzoate (2a). Three routes for this synthesis were tested. Route 1: 0.980 g, 3.24 mmol of **1a** was combined with NEt_3 (900 µL, 6.5 mmol) and 10 mL DMSO in a 100 mL RBF under N_2 and equipped with a dropping funnel and condenser. 2,6-bis(chloromethyl)-4-methylphenol (0.333 g, 1.62 mmol) was dissolved in 20 mL DMSO and added slowly to the stirred solution. The solution was refluxed overnight affording an orange-red solution. The solution was filtered and concentrated to an orange oil, resulting in numerous impurities by ^{1}H NMR and TLC. Additional purification was not attempted. Route 2: 0.986 g, 3.25 mmol of **1a** was dissolved in 20 mL MeOH and **4a** (0.266 g, 1.62 mmol) was separately dissolved in 20 mL MeOH and then slowly added to **1a**, resulting in a dark yellow solution. After 2 hrs, excess $NaBH_4$ (0.306 g 8.09 mmol) was slowly added, affording a pale yellow solution. The solution was neutralized with 4M HCl, the insoluble material was filtered, and the filtrate was concentrated under reduced pressure. The resulting solid was dissolved in MeOH and precipitated with Et_2O, yielding a white powder. Route 3: **5a** (1.81 g, 5.2 mmol) and NEt_3 (1.077 g, 10.6 mmol) were combined in 10 mL CH_2Cl_2 under N_2. Separately, methyl 2-chloromethylbenzoate (1.92 g, 10.4 mmol) dissolved in 10 mL CH_2Cl_2 was added dropwise. The solution was stirred at RT for 48 hrs, then diluted to 40 mL DCM and washed with 2x40 mL saturated brine. The organic layer

was dried over Na_2SO_4, filtered, concentrated, and purified via column chromatography using 7% MeOH/CH_2Cl_2. The desired product elutes as the 3rd spot with R_f ~0.6. Upon combining and concentrating fractions containing the desired product, 0.998 g was isolated as a viscous orange oil. Yield: 26.3 % pure product; 53% total crude. Note that column purification is not necessary – the subsequent hydrolysis workup of crude material removes impurities from this step. Characterization: ^{1}H NMR (400 MHz, $CDCl_3$): 10.55 (br, 1H); 8.49 (d, 2H); 7.72 (m, 4H); 7.53 (t, 2H); 7.35 (m, 4H); 7.20 (t, 2H); 7.08 (t, 2H); 6.91 (s, 2H); 4.04 (s, 4H); 3.81 (s, 6H); 3.76 (s, 4H); 3.70 (s, 4H); 2.19 (s, 3H).

Diethyl-3,3'-((((2-hydroxy-5-methyl-1,3-phenylene)bis(methylene))bis((pyridin-2-ylmethyl)azanediyl))bis(methylene))dibenzoate (2b). This procedure was modified from the synthesis of **2a** Route 3, using methyl 3-(chloromethyl)benzoate. The crude material was taken directly to hydrolysis, as that workup removes impurities from this synthesis. Characterization: ^{1}H NMR (400 MHz, $CDCl_3$): 10.56 (br, 1H); 8.52 (d, 2H); 7.98 (s, 2H); 7.88 (d, 2H); 7.60 (m, 4H); 7.43 (d, 2H); 7.34 (t, 2H); 7.13 (t, 2H); 6.97 (s, 2H); 4.34 (q, 4H); 3.77 (s, 4H); 3.71 (s, 8H); 2.24 (s, 3H); 1.37 (t, 6H).

Glycine *N*,*N*'-[(2-hydroxy-5-methyl-1,3-phenylene)bis(methylene)]bis[*N*-(2-pyridinyl-methyl)-, 1,1'-diethyl ester (2c). This compound can be synthesized via two routes.[13] Route 1: This method was modified from Route 1 of the **2a** synthesis. Here, **1b** (1.602 g, 8.29 mmol) and NEt_3 (1.14 mL, 8.29 mmol) were combined in 24 mL MeOH in a 2-neck RBF equipped with a dropping funnel that contains 2,6-bis(chloromethyl)-4-methylphenol (0.842 g, 4.11 mmol) dissolved in 16 mL MeOH. This solution was added dropwise to the stirring amine solution resulting in immediate precipitation of the quaternary amine salt. After stirring at RT overnight, the solvent was removed under reduced pressure, the yellow oil was re-dissolved in 20 mL H_2O

and extracted with 2x40 mL $CHCl_3$. The organic layers were combined, dried, filtered, and the filtrate was concentrated to a yellow oil of clean product. Route 2: This route can be adapted from Route 3 of the **2a** synthesis, using THF in place of CH_2Cl_2 and ethyl bromoacetate in place of methyl 2-chloromethylbenzoate and a modified workup. Workup: The precipitate was filtered, and the solvent was removed under reduced pressure, then placed under high-vacuum on the Schlenk line overnight, resulting in a viscous oil. Yield: 100 %. Characterization: ^{1}H NMR (400 MHz, $CDCl_3$): 8.51 (d, 2H); 7.63 (t, 2H); 7.49 (d, 2H); 7.15 (t, 2H); 6.95 (s, 2H); 4.16 (q, 3H); 3.96 (s, 2H); 3.87 (s, 2H); 3.40 (s, 2H); 2.22 (s, 3H); 1.25 (t, 3H).

Glycine *N*,*N*'-[(2-hydroxy-5-(*tert*-butyl)-1,3-phenylene)bis(methylene)]bis[*N*-(2-pyridinyl-methyl)-, 1,1'-diethyl ester (2d). This synthesis was adapted from Route 3 of the **2a** synthesis using THF in place of CH_2Cl_2, **5b** in place of **5a**, and ethyl bromoacetate in place of methyl 2-chloromethylbenzoate with a modified workup. Workup: The precipitate was filtered, and the solvent was removed under reduced pressure, then placed under high-vacuum on the Schlenk line overnight, resulting in a viscous oil. Representative scale: **5b** (2.0 g, 5.1 mmol), NEt_3 (1.03 g, 10.2 mmol), ethyl bromoacetate (1.71 g, 10.2 mmol). Yield: 100%. Characterization: ^{1}H NMR (400 MHz, $CDCl_3$): 8.52 (s, 2H); 7.63 (t, 2H); 7.50 (d, 2H); 7.14 (m, 4H); 4.14 (m, 4H); 3.97 (s, 4H); 3.91 (s, 4H); 3.42 (s, 4H); 1.26 (m, 9H + 3H).

Sodium 2,2'-((((5-methyl-2-oxido-1,3-phenylene)bis(methylene))bis((pyridin-2-ylmethyl)-azanediyl))bis(methylene))dibenzoate (3a). The corresponding ester (**2a**, 0.474 g, 0.736 mmol) was dissolved in 5 mL MeOH and added slowly to a 7 mL solution of NaOH (0.218 g, 5.45 mmol), and stirred overnight resulting in a subtle color change from orange-yellow to yellow. The solvent was removed under reduced pressure and the product was resuspended in iPrOH, yielding a solution that slowly becomes cloudy with a fine white precipitate. The chilled solution was filtered

and rinsed with abundant chilled iPrOH and the precipitate was dried under high vacuum with heating overnight. Yield: 51%. Characterization: ^{1}H NMR (400 MHz, CD_3OD): 8.22 (d, 2H); 7.60 (t, 3H); 7.45 (m, 4H); 7.35 (d, 2H); 7.20 (m, 4H); 7.09 (t, 2H); 6.80 (s, 2H); 3.88 (s, 4H); 3.70 (s, 4H); 3.58 (s, 4H); 2.14 (s, 3H). Elemental anal. Calcd for $C_{37}H_{33}N_4Na_3O_5 \bullet 3H_2O$: C, 60.32; H, 5.35; N, 7.61; found: C, 60.73; H, 4.99; N, 7.63. Mass spectrum (+ESI): m/z (calcd): 617.27; (expt): 617.22

Sodium 3,3'-((((5-methyl-2-oxido-1,3-phenylene)bis(methylene))bis((pyridin-2-ylmethyl)-azanediyl))bis(methylene))dibenzoate (3b). This procedure follows that of **3a** with the following exceptions: (1) the corresponding ester **2b** was used, (2) the hydrolysis was carried out in EtOH, and (3) the tan powder was rinsed with chilled iPrOH and then chilled EtOH. Yield: 67.2% Characterization: ^{1}H NMR (400 MHz, CD_3OD): 8.43 (d, 2H); 7.95 (s, 2H); 7.83 (d, 2H); 7.75 (t, 2H); 7.56 (d, 2H); 7.45 (d, 2H); 7.31 (t, 2H); 7.25 (t, 2H); 6.95 (s, 2H); 3.75 (s, 4H); 3.68 (s, 8H); 2.23 (s, 3H).

Sodium *N*,*N*'-[(2-hydroxy-5-methyl-1,3-phenylene)bis(methylene)]bis[*N*-(2-pyridinyl-methyl)-, 1,1'-diacetate (3c). The procedure follows that of **3a** with the following modifications: (1) the corresponding ester **2c** was used[13], (2) the hydrolysis was carried out in EtOH, and (3) the fine white powder was rinsed with abundant chilled iPrOH and then EtOH. Average Yield: 43%. Characterization: ^{1}H NMR (400 MHz, CD_3OD): 8.45 (d, 2H); 7.64 (t, 2H); 7.27 (d, 2H); 7.19 (t, 2H); 6.78 (s, 2H); 3.64 (s, 4H); 3.56 (s, 4H); 3.07 (s, 4H); 2.15 (s, 3H). Elemental anal. Calcd for $C_{25}H_{25}N_4Na_3O_5 \bullet 2.5H_2O$: C, 52.19; H, 5.25; N, 9.59; found: C, 52.54; H, 5.19; N, 9.39.

Sodium *N*,*N*'-[(2-hydroxy-5-(*tert*-butyl)-1,3-phenylene)bis(methylene)]bis[*N*-(2-pyridinyl-methyl)-, 1,1'-diacetate (3d). The procedure follows that of **3a** with the following modifications: (1) the corresponding ester **2d** was used, (2) the hydrolysis was carried out in EtOH, and (3) the

off-white powder was rinsed with abundant chilled iPrOH and then EtOH. Characterization: ^{1}H NMR (400 MHz, CD_3OD): 8.46 (d, 2H); 7.61 (t, 2H); 7.23 (d, 2H); 7.16 (t, 2H); 6.96 (s, 2H); 3.66 (s, 4H); 3.60 (s, 4H); 3.11 (s, 4H); 1.25 (s, 9H). Elemental anal. Calcd for $C_{28}H_{31}N_4Na_3O_5 \bullet H_2O$: C, 56.95; H, 5.63; N, 9.49; found: C, 56.82; H, 5.28; N, 9.36.

2,6-Diformyl-4-cresol (4a). This compound was synthesized using a modified literature procedure.[18] 4.13 g (37.4 mmol) of p-cresol and 10.55 g (65.6 mmol) of hexamethylenetetramine were combined in a 100 mL RBF under N_2. 50 mL anhydrous TFA was slowly added and the solution was stirred under reflux for 24 hrs. Workup: the orange-red solution was poured into a beaker containing 150 mL of 4M HCl and stirred for 10 mins before proceeding with liquid-liquid extraction. The acidic solution was extracted twice with 200 mL CH_2Cl_2 and the combined CH_2Cl_2 layers were back-extracted sequentially with 200 mL HCl, 200 mL deionized water, and 200 mL brine solution. The organic layer was then dried over Na_2SO_4, filtered, and the solvent was removed under reduced pressure to afford a clumpy yellow precipitate. Purification: the crude product was loaded onto a 1.5 in diameter column loaded with ~200 g of silica and run with 100% CH_2Cl_2. The first spot that elutes contains the desired diformyl product (R_f ~0.6). Average yield: 46%. Characterization: ^{1}H NMR (400 MHz, $CDCl_3$): 11.45 (s, 1H); 10.20 (s, 2H); 7.76 (s, 2H); 2.38 (s, 3H).

2,6-Diformyl-4-tert-butylphenol (4b). This compound was synthesized following a modified literature procedure.[18] 5.14 g (34.2 mmol) of 4-tert-butylphenol was combined with 12.0 g (85.8 mmol, 2.5 eq) of hexamethylenetetramine in a 2-neck RBF equipped with a reflux condenser that was purged with N_2. Under a high flux of N_2, 60 mL of trifluoroacetic acid was added slowly with stirring. The vessel was then placed under low pressure N_2 and refluxed for 48 hrs. Workup: The workup follows **4a**. Purification: The crude product was loaded onto a 1.5 in diameter column with

~200 g of silica and run with 100% CH_2Cl_2. The mono-formyl complex elutes first (R_f ~0.75), and can be salvaged for a second Duff reaction (using 1 equivalent of hexamethylenetetramine), followed shortly by the desired product (R_f ~0.6). Yield: 86.3 %. Characterization: ^{1}H NMR (400 MHz, $CDCl_3$): 11.49 (s, 1H); 10.26 (s, 2H); 7.99 (s, 2H); 1.37 (s, 9H).

4-Methyl-2,6-bis[[(2-pyridinylmethyl)amino]methyl]-phenol (5a). This synthesis follows a modified literature procedure.[19] In the glovebox, **4a** (1.5 g, 9.1 mmol) was suspended in 20 mL MeOH in a 100 mL RBF with a septum. 2-picoylamine (1.94 g, 17.9 mmol) was similarly dissolved in 20 mL MeOH and transferred to the RBF, causing the aldehyde to slowly dissolve, resulting in a bright yellow solution. After stirring for 3 hrs at RT, the RBF was placed on the Schlenk line and a 10 mL solution of H_2O was used to sequentially dissolve NaOH (0.659 g, 16.5 mmol) and suspend $NaBH_4$ (1.59g, 42.0 mmol). This solution was then syringed into the RBF under low N_2 pressure, resulting in the formation of a pale solution that was stirred for 24 hr. Next, the methanol was removed under reduced pressure affording a ~20 mL aqueous solution. This solution was extracted with 2x40 mL $CHCl_3$, dried over $MgSO_4$, filtered, and concentrated again to a yellow oil. Yield: 100%. Characterization: ^{1}H NMR (400 MHz, $CDCl_3$): 8.56 (s, 2H); 7.64 (t, 2H); 7.29 (d, 2H + $CHCl_3$); 6.84 (s, 2H); 3.91 (2s, 8H); 2.23 (s, 3H).

4-(*Tert*-butyl)-2,6-bis[[(2-pyridinylmethyl)amino]methyl]-phenol (5b). The procedure for **5a** can be adapted for the synthesis of **5b**, using **4b** in place of **4a**. Yield: 97%. Characterization: ^{1}H NMR (400 MHz, $CDCl_3$): 8.53 (d, 2H); 7.60 (t, 2H); 7.26 (d, 2H + $CHCl_3$); 7.00 (s, 2H); 3.91 (2s, 8H); 1.24 (s, 9H).

Synthesis of Asymmetric Ligands (2 e-f, 3 e-f,6-9)

***N*-[[3-[[bis(2-pyridinylmethyl)amino]methyl]-2-hydroxy-5-methylphenyl]methyl]-*N*-(2-methoxy-2-oxoethyl)glycine ester (2e).** In a 100 mL RBF, **1c** (1.2 g, 6.85 mmol) and NEt_3 (0.69

g, 6.85 mmol) were dissolved in 15 mL CH_2Cl_2. Separately, **9** (2.52 g, 6.85 mmol) was suspended in 25 mL CH_2Cl_2 and slowly added to the stirring solution under a N_2 atmosphere, resulting in a yellow-green solution. After 24 hours, the solution was filtered, the filtrate was concentrated and the residue was washed with THF. The precipitate was then dissolved in CH_3CN and precipitated overnight with Et_2O, affording a yellow-green oil. Purification: The crude product was run on a 1.5 in column containing ~150 mL of silica using 10% MeOH/CH_2Cl_2. The dead volume was collected until the first yellow-colored band approached the lower sand layer, upon which 10 mL fractions were taken. The product elutes as the 4th spot in fractions 3-8 with a Rf ~0.4. The fractions were combined, concentrated, and spilled. Fractions after 8 had some residual product, which was concentrated and carried on to the subsequent hydrolysis step. Characterization: ^{1}H NMR (400 MHz, $CDCl_3$): 8.54 (d, 2H); 7.63 (t, 2H); 7.43 (d, 2H); 7.14 (t, 2H); 6.98 (s, 1H); 6.93 (s, 1H); 4.19 (m, 2H); 3.97 (s, 2H); 3.86 (s, 3H); 3.75 (2s, 4H); 3.71 (s, 2H); 3.59 (d, 3H); 3.47 (d, 1H); 2.23 (s, 3H); 1.27 (m, 3H). Note: this NMR has an extra CH_2 peak with CH_2 integrations close to 3H. The subsequent hydrolysis step takes care of this, but also leaves residual NaOH. This might require subsequent treatment with acid and extraction.

Sodium *N*-[[3-[[bis(2-pyridinylmethyl)amino]methyl]-2-hydroxy-5-methylphenyl]methyl]-*N*-(2-methoxy-2-oxoethyl)glycine (3e). The minimal **2e** salvaged from the column was dissolved in ~10 mL MeOH and excess NaOH (143 mg) was added. The solution was stirred overnight at RT, and the solvent was then removed under reduced pressure. The resulting white precipitate was dissolved in ~10 mL iPrOH (everything dissolves) and precipitated with Et_2O. The resulting powder contains the desired product with residual NaOH. Further purification via neutralization then extraction is necessary. Characterization: ^{1}H NMR (400 MHz, CD_3OD): 8.53 (d, 2H); 7.73

(t, 2H); 7.36 (d, 2H); 7.24 (t, 2H); 6.87 (s, 1H); 6.77 (s, 1H); 3.81 (s, 4H); 3.74 (s, 2H); 3.60 (s, 2H); 3.36 (s, 2H); 3.16 (s, 2H); 2.17 (s, 3H);

3-(Chloromethyl)-2-hydroxy-5-methylbenzaldehyde (6). This synthesis follows a literature procedure with scaling.[20] 2-hydroxy-5-methylbenzaldehyde (5.0 g, 32.0 mmol) was combined with paraformaldehyde (1.92 g, 64.0 mmol) in a 100 mL RBF with 50 mL of concentrated HCl. The solution was stirred under gentle heating at ~60^{o} C for 3 hrs before cooling and extracting the desired product with 3x50 mL CH_2Cl_2. The organic layers were combined, dried over Na_2SO_4, filtered, and concentrated to a yellow oil, which was re-dissolved in minimal CH_2Cl_2 and precipitated with hexanes, affording a pale yellow/tan product as needles. The product was dried under high vacuum overnight. Yield: 56%. Characterization: ^{1}H NMR (400 MHz, $CDCl_3$): 11.26 (s, 1H); 9.88 (s, 1H); 7.48 (s, 1H); 7.36 (s, 1H); 4.68 (s, 2H); 2.37 (s, 3H).

3-[[Bis(2-pyridinylmethyl)amino]methyl]-2-hydroxy-5-methylbenzaldehyde (7). This reaction follows a literature procedure with scaling.[21] Di-2-picoylamine (1.08 g, 5.4 mmol) and NEt_3 (0.55 g, 5.4 mmol) were combined in 12 mL THF and **6** (1.0 g, 5.4 mmol) was dissolved in separate 12 mL THF and placed in a dropping funnel to be slowly added to the stirring amine solution in a 50 mL RBF. Upon addition of **6**, the flask was placed under N_2 and stirred at RT for 2.5 hrs, resulting in a bright yellow solution with a white precipitate. The salt byproduct was filtered off, and the filtrate was concentrated to a yellow/orange oil that slowly solidifies as orange needles upon cooling. Yield: 91%. Characterization: ^{1}H NMR (400 MHz, $CDCl_3$): 10.44 (s, 1H); 8.58 (s, 2H); 7.66 (t, 2H); 7.45 (s, 1H); 7.40 (d, 2H); 7.22 (s, 1H); 7.18 (t, 2H); 3.90 (s, 4H); 3.81 (s, 2H); 2.28 (s, 3H).

2-[[Bis[(pyridin-2-yl)methyl]amino]methyl]-6-(hydroxymethyl)-4-methylphenol (8). This procedure follows a literature protocol.[23] **7** (3.16 g, 5.76 mmol) was suspended in ~50 mL MeOH

in a 100 mL RBF and $NaBH_4$ (~2 g, 17.3 mmol) was slowly added, affording vigorous H_2 production and partial bleaching of the solution from bright-yellow to pale yellow. The reaction was stirred for 1 hr and then acidified with concentrated HCl to a pH ~2, affording a white precipitate and yellow solution. The precipitate was filtered off and the filtrate was concentrated, resuspended in saturated bicarbonate solution, and extracted with 2x50 mL CH_2Cl_2. The organic layer was dried, filtered, and the filtrate was concentrated affording a viscous yellow oil. Yield: 77%. Characterization: ^{1}H NMR (400 MHz, $CDCl_3$): 11.31 (s, 1H); 8.58 (s, 2H); 7.64 (t, 2H); 7.33 (d, 2H); 7.18 (t, 2H); 6.95 (s, 1H); 6.83 (s, 1H); 4.74 (s, 2H); 3.88 (s, 4H); 3.77 (s, 2H); 2.24 (s, 3H).

2-[[Bis[(pyridin-2-yl)methyl]methyl]-6-(chloromethyl)-4-methylphenol (9). This procedure follows a literature protocol.[23] **8** was dissolved in minimal (~3 mL) CH_2Cl_2 and syringed into a 50 mL RBF under a N_2 atmosphere containing ~5 mL of freshly distilled $SOCl_2$. The solution was stirred at RT for 3 hrs before concentrating under reduced pressure. The oily residue was washed with hexanes and then dissolved in CH_2Cl_2 and precipitated with hexanes, affording a yellow oil. The solvent was decanted, and the oil was dried under high vacuum. The resulting oily solid is highly hydroscopic and becomes green if it is left open to the atmosphere. The product was stored in a vial within a P_2O_5 desiccator until further use. Yield: nearly quantitative. Characterization: ^{1}H NMR (400 MHz, $CDCl_3$): 8.72 (d, 2H); 8.27 (m, 4H); 7.72 (t, 2H); 6.89 (s, 2H); 4.69 (s, 4H); 4.61 (s, 2H); 4.08 (s, 2H); 2.14 (s, 3H).

Metallations and Nitrosylations

General Metallation Procedure. The metallation of **3a-c** follows a protocol adapted from the H[BPMP] metallation; a representative scale is used here.[2] In a 100 mL RBF in the glovebox, the desired ligand **3a-c** (~300 μmol) was dissolved in minimal MeOH (~2-3 mL) resulting in a pale-

yellow solution. Two equivalents of $Fe(OTf)_2x2CH_3CN$ (~600 μmol) dissolved in 1 mL MeOH were added, resulting in the formation of an orange solution. One equivalent of NaOAc (~300 umol) in 1 mL MeOH was then added resulting in a deep orange solution that was stirred for 1 hr before precipitating the metallated products **10a–12a** with Et_2O. Specific workup procedures are noted in individual sections.

General Nitrosylation Procedure. The metallated complexes **10a-12a** were individually dissolved in ~7 mL MeOH or CH_3CN in a 100 mL Schlenk flask and placed under an NO atmosphere, resulting in a color change from yellow/orange to brown. The flasks were brought back into the glovebox and the products were precipitated with 36-48 mL Et_2O. The NO(g) headspace was then flushed out via high-pressure N_2 on the Schlenk line, and the flasks were returned to the glovebox to filter off the nitrosylated products **10b-12b**. Note that the vacuum must be turned off just before the solvent reaches the powder on the frit, as all complexes reported here are sensitive to NO loss under vacuum. Yields: 42-70 %. Characterization is listed under each individual complex.

$[Fe_2(PhO(Py)_2(o\text{-}Bz)_2)(OAc)]$ (10a). Workup: The precipitate was filtered and washed with CH_2Cl_2. The CH_2Cl_2 filtrate was then precipitated with hexanes and filtered again to afford a pale-yellow product that turned orange/peach upon further drying. Characterization: UV-Vis: λ_{max} = 415 nm.

$[Fe_2(PhO(Py)_2(m\text{-}Bz)_2)(OAc)]$ (11a). Workup: Precipitation with Et_2O was unnecessary – addition of $Fe(OTf)_2$ $x2CH_3CN$ resulted in the immediate formation of a yellow precipitate. The solution was vacuum filtered and the precipitate was rinsed with THF. The resulting precipitate is insoluble in MeOH, acetone, CH_2Cl_2, Et_2O and very minimally soluble in CH_3CN, THF, and DMF. Yield: 68%.

[Fe_2(PhO(Py)$_2$($OAc)_2$)(OAc)] (12a). Workup: The precipitate was vacuum filtered in the glovebox and the pale-yellow powder was washed with abundant THF. Yield: 76%. Characterization: Elemental anal. Calcd for $C_{27}H_{28}Fe_2N_4O_7$: C, 51.29; H, 4.46; N, 8.86; found: C, 52.43; H, 4.81; N, 9.31. UV-Vis: λ_{max} = 415 nm

[Fe_2(PhO(Py)$_2$(o-Bz)$_2$)(OAc)$(NO)_2$] (10b). This procedure directly follows the general protocol described above using MeOH as the solvent. Yield: 64% Characterization: IR (KBr): ν_{NO} = 1724 cm^{-1}. UV-Vis: λ_{max} = 445 nm

[Fe_2(PhO(Py)$_2$(m-Bz)$_2$)(OAc)$(NO)_2$] (11b). A suspension of **11a (**190 mg, 224 μmol) in 5 mL CH_3CN was nitrosylated following the general protocol described above, resulting in a brown suspension of **11b**. Precipitation with Et_2O was unnecessary – NO was flushed from the headspace and the product was immediately filtered. The isolated complex is insoluble in CH_2Cl_2, Et_2O, hexane, MeOH, acetone, H_2O, DMF, pyridine, and DMSO with extremely low solubility in CH_3CN and THF. Yield: 89%. Characterization: IR (KBr): ν_{NO} = 1743 cm^{-1}

[Fe_2(PhO(Py)$_2$($OAc)_2$)(OAc)$(NO)_2$] (12b). This procedure directly follows the general protocol described above using MeOH as the solvent. Representative scale: **12a** (189 mg, 300 μmol). Yield: 67%. Characterization: Elemental anal. Calcd for $C_{37}H_{33}Fe_2N_4Na_3O_5$•NaOTf: C, 50.86; H, 3.71; N, 6.24; found: C, 51.51; H, 4.16; N, 6.05. IR (KBr): ν_{NO} = 1750 cm^{-1}. UV-Vis : λ_{max} = 440 nm.

5.4 References

(1) Jana, M., Pal, N., White, C. J., Kupper, C., Meyer, F., Lehnert, N.;Majumdar, A. Functional Mononitrosyl Diiron(II) Complex Mediates the Reduction of NO to N_2O with Relevance for Flavodiiron NO Reductases. *J. Am. Chem. Soc.* **2017**, *140*, 14380-14383.

(2) White, C. J., Speelman, A. L., Kupper, C., Demeshko, S., Meyer, F., Shanahan, J. P., Alp, E. E., Hu, M., Zhao, J.;Lehnert, N. The Semireduced Mechanism for Nitric Oxide Reduction by Non-Heme Diiron Complexes: Modeling Flavodiiron Nitric Oxide Reductases. *J. Am. Chem. Soc.* **2018**, *140*, 2562-2574.

(3) Jana, M., White, C. J., Pal, N., Demeshko, S., Cordes, C., Meyer, F., Lehnert, N.;Majumdar, A. Functional Models for the Mono- and Dinitrosyl Intermediates of FNORs: Semireduction versus Superreduction of NO. *J. Am. Chem. Soc.* **2020**, *142*, 6600-6616.

(4) Caranto, J. D., Weitz, A., Giri, N., Hendrich, M. P.;Kurtz, D. M. J. A Diferrous-Dinitrosyl Intermediate in the N_2O-Generating Pathway of a Deflavinated Flavo-Diiron Protein. *Biochemistry* **2014**, *53*, 5631–5637.

(5) Vicente, J. B.;Teixeira, M. Redox and Spectroscopic Properties of the *Escherichia coli* Nitric Oxide-detoxifying System Involving Flavorubredoxin and Its NADH-oxidizing Redox Partner. *J. Biol. Chem.* **2005**, *280*, 34599-34608.

(6) Lu, J., Bi, B., Lai, W.;Chen, H. Origin of Nitric Oxide Reduction Activity in Flavo-Diiron NO Reductase: Key Roles of the Second Coordination Sphere. *Angew. Chem. Int. Ed.* **2019**, *58*, 3795-3799.

(7) Biswas, S., Kurtz, D. M., Montoya, S. R., Hendrich, M. P.;Bominaar, E. L. The Catalytic Role of a Conserved Tyrosine in Nitric Oxide-Reducing Non-heme Diiron Enzymes. *ACS Catal.* **2020**, 8177-8186.

(8) Erxleben, A. Mechanistic Studies of Homo- and Heterodinuclear Zinc Phosphoesterase Mimics: What Has Been Learned? *Front. Chem.* **2019**, *7*.

(9) Dong, H. T., White, C. J., Zhang, B., Krebs, C.;Lehnert, N. Non-Heme Diiron Model Complexes Can Mediate Direct NO Reduction: Mechanistic Insight into Flavodiiron NO Reductases. *J. Am. Chem. Soc.* **2018**, *140*, 13429-13440.

(10) Neves, A., de Brito, M. A., Vencato, I., Drago, V., Griesar, K.;Haase, W. FeIIIFeIII and FeIIFeIII Complexes as Synthetic Analogues for the Oxidized and Reduced Forms of Purple Acid Phosphatases. *Inorg. Chem.* **1996**, *35*, 2360-2368.

(11) Krebs, B., Schepers, K., Bremer, B., Henkel, G., Althaus, E., Müller-Warmuth, W., Griesar, K.;Haase, W. Model Compounds for the Oxidized Uteroferrin-Phophate Complex with Novel Dinucleating Ligands Containing Phenolate and Pyridine Donors. *Inorg. Chem.* **1994**, *33*.

(12) Elemental analyses of the complexes described within this chapter show deviations that in some cases are outside the acceptable limit.. Analysis of the data is therefore limited due to unknownimpurities.

(13) Jarenmark, M., Kappen, S., Haukka, M.;Nordlander, E. Symmetrical and unsymmetrical dizinc complexes as models for the active sites of hydrolytic enzymes. *Dalton Trans.* **2008**, 993-996.

(14) Jarenmark, M., Csapó, E., Singh, J., Wöckel, S., Farkas, E., Meyer, F., Haukka, M.;Nordlander, E. Unsymmetrical dizinc complexes as models for the active sites of phosphohydrolases. *Dalton Trans.* **2010**, *39*, 8183-8194.

(15) Adamus, J., Paneth, P.;Reimschűssel, W. Synthesis of N,N-dimethyl[2-14C] morpholinium chloride. *J. Label. Compd. Radiopharm.* **1982**, *19*, 309-312.

(16) Li, X., Bera, M., Musie, G. T.;Powell, D. R. Copper(II) promoted imidazolidine ring formation and complexation: A unique reaction course. *Inorg. Chim. Acta* **2008**, *361*, 1965-1972.

(17) Carlsson, H., Haukka, M., Bousseksou, A., Latour, J.-M.;Nordlander, E. Nickel Complexes of Carboxylate-Containing Polydentate Ligands as Models for the Active Site of Urease. *Inorganic Chemistry* **2004**, *43*, 8252-8262.

(18) Lindoy, L. F., Meehan, G. V.;Svenstrup, N. Mono- and Diformylation of 4-Substituted Phenols: A New Application of the Duff Reaction. *Synthesis* **1998**, *1998*, 1029-1032.

(19) Chen, X., Wang, J., Sun, S., Fan, J., Wu, S., Liu, J., Ma, S., Zhang, L.;Peng, X. Efficient enhancement of DNA cleavage activity by introducing guanidinium groups into diiron(III) complex. *Bioorg. Med. Chem. Lett.* **2008**, *18*, 109-113.

(20) Wei, Z., Liu, Y.-q., Wang, S.-z., Yao, L., Nie, H.-f., Wang, Y.-a., Liu, X.-Y., Zheng, Z.-b.;Li, S. Conjugates of salicylaldoximes and peripheral site ligands: Novel efficient nonquaternary reactivators for nerve agent-inhibited acetylcholinesterase. *Bioorg. & Med. Chem.* **2017**, *25*, 4497-4505.

(21) Bosch, S., Comba, P., Gahan, L. R.;Schenk, G. Dinuclear Zinc(II) Complexes with Hydrogen Bond Donors as Structural and Functional Phosphatase Models. *Inorg. Chem.* **2014**, *53*, 9036-9051.

(22) Koval, Iryna A., Pursche, D., Stassen, Arno F., Gamez, P., Krebs, B.;Reedijk, J. The Dicopper(II) Complex of the Novel Asymmetric Dinucleating Ligand Hpy3asym as a Structural Model of Catechol Oxidase. *Eur. J. Inorg. Chem.* **2003**, *2003*, 1669-1674.

(23) Gouré, E., Carboni, M., Troussier, A., Dubourdeaux, P., Clémancey, M., Gon, N., Balasubramanian, R., Lebrun, C., Pécaut, J., Blondin, G.;Latour, J.-M. Deprotonation in Mixed-Valent Diiron(II,III) Complexes with Aniline or Benzimidazole Ligands. *Inorg. Chem.* **2015**, *54*, 6257-6266.

(24) Borovik, A. S., Hendrich, M. P., Holman, T. R., Munck, E., Papaefthymiou, V.;Que, L., Jr. Models for Diferrous Forms of Iron-Oxo Proteins. Structure and Properties of $[Fe_2BPMP(O_2CR)_2]BPh_4$ Complexes. *J. Am. Chem. Soc.* **1990**, *112*, 6031-6038.

(25) Berto, T. C., Speelman, A., Zheng, S.;Lehnert, N. Mono- and Dinuclear Non-Heme Iron-Nitrosyl Complexes: Models for Key Intermediates in Bacterial Nitric Oxide Reductases. *Coord. Chem. Rev.* **2013**, *257*, 244-259.

(26) Jackson, T. A., Yikilmaz, E., Miller, A.-F.;C., B. T. Spectroscopic and Computational Study of a Non-Heme Iron $\{Fe{-}NO\}^7$ System: Exploring the Geometric and Electronic Structures of the Nitrosyl Adduct of Iron Superoxide Dismutase. *J. Am. Chem. Soc.* **2003**, *125*, 8348-8363.

(27) Feig, A. L., Bautista, M. T.;Lippard, S. J. A Carboxylate-Bridged Non-heme Diiron Dinitrosyl Complex. *Inorg. Chem.* **1996**, *35*, 6892-6898.

(28) This reaction can also be carried out more cost-efficiently using NEt3 as a sacrificial base instead of using 2 equivalents of 2-picoylamine.

3.5 NMR Appendix

2-(((Pyridin-2-ylmethyl)amino)methyl)benzoate (1a).

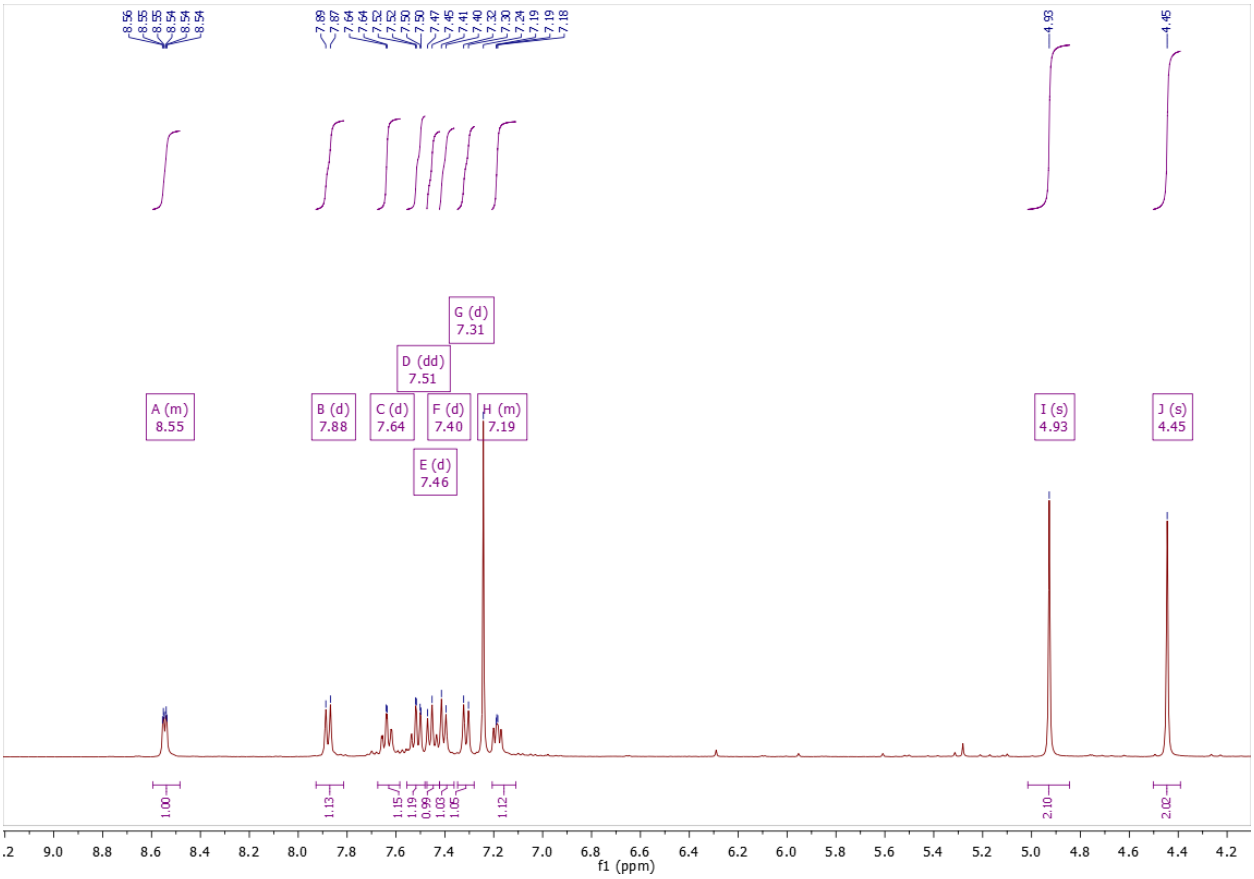

Ethyl 2-[[(pyridin-2-yl)methyl]amino]acetate (1b).

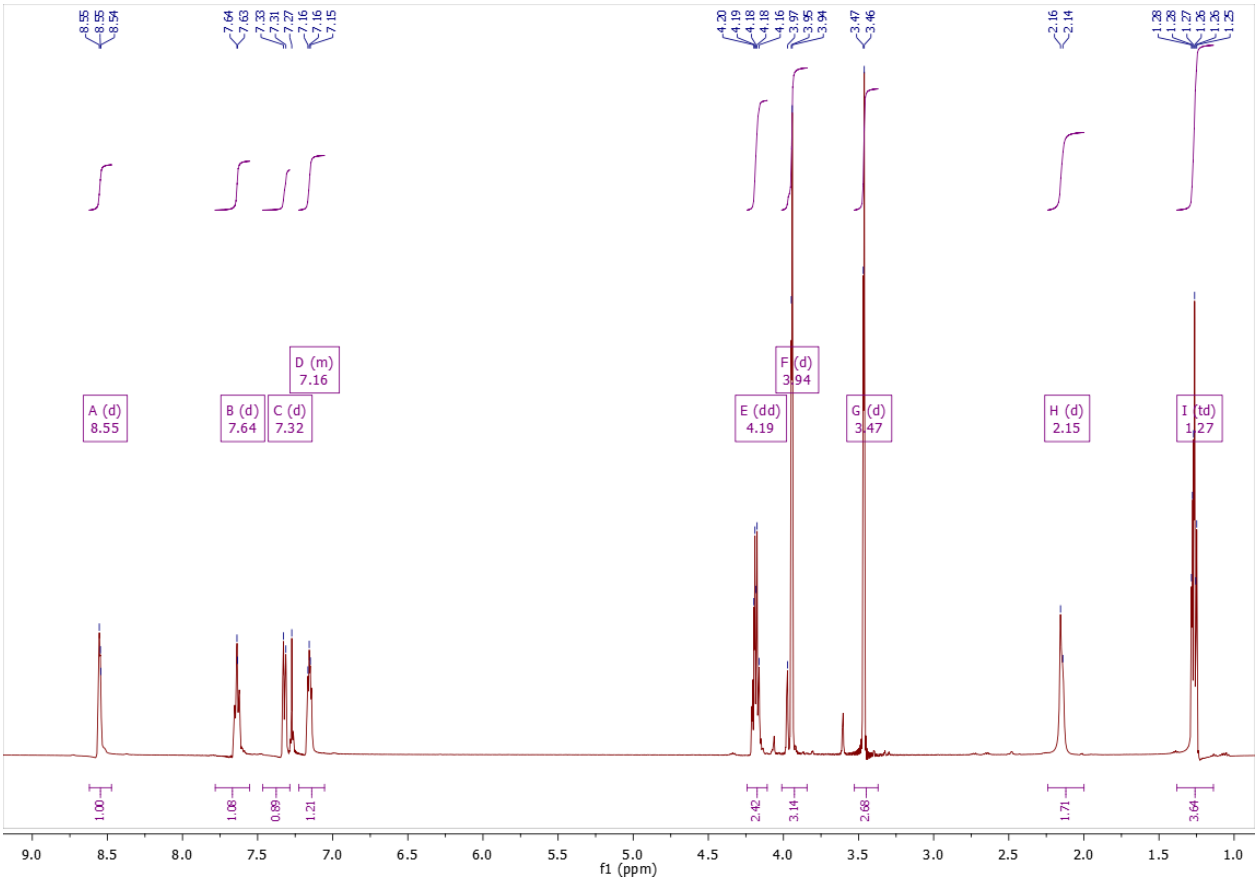

Methyl 2-[(2-ethoxy-2-oxoethyl)amino]acetate (1c).

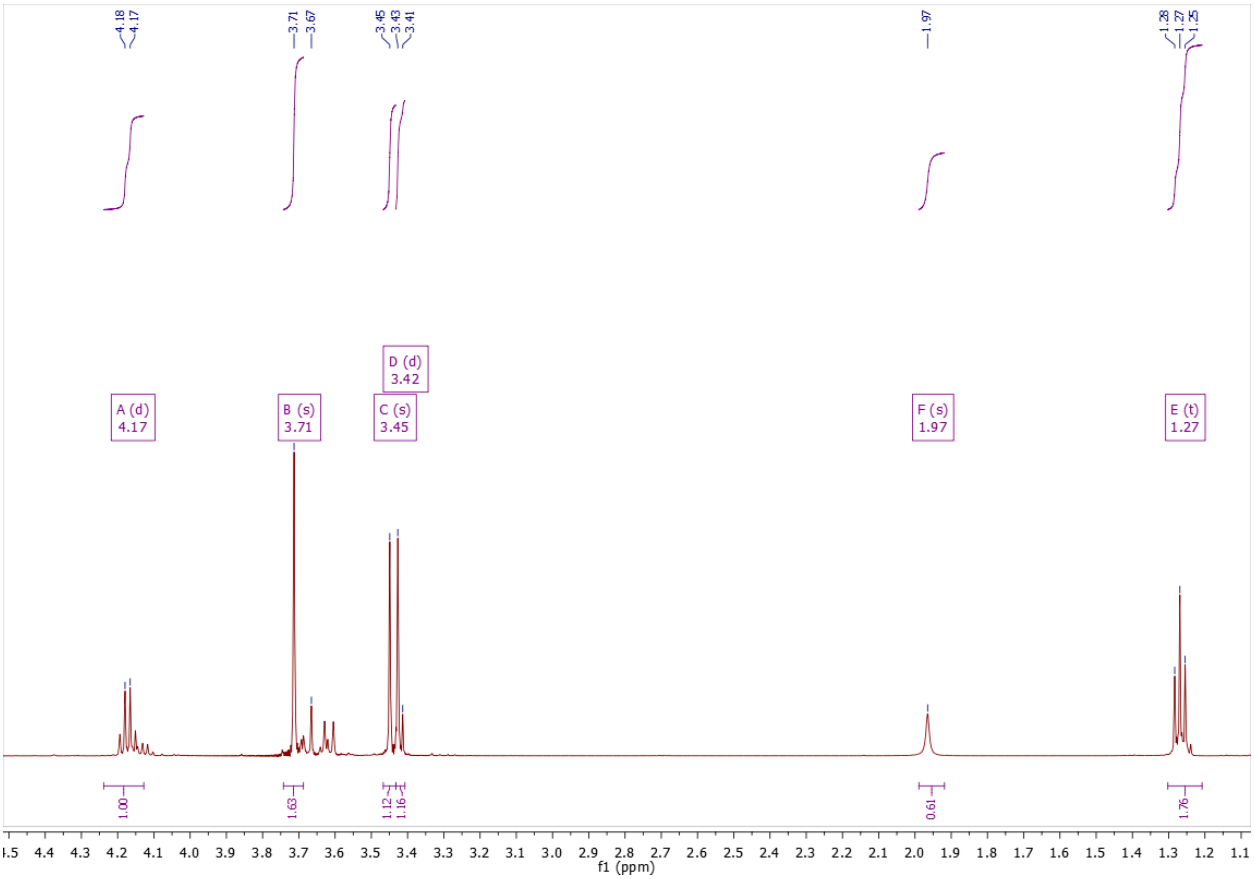

Dimethyl-2,2'-((((2-hydroxy-5-methyl-1,3-phenylene)bis(methylene))bis((pyridin-2-ylmethyl)azanediyl))bis(methylene))dibenzoate (2a).

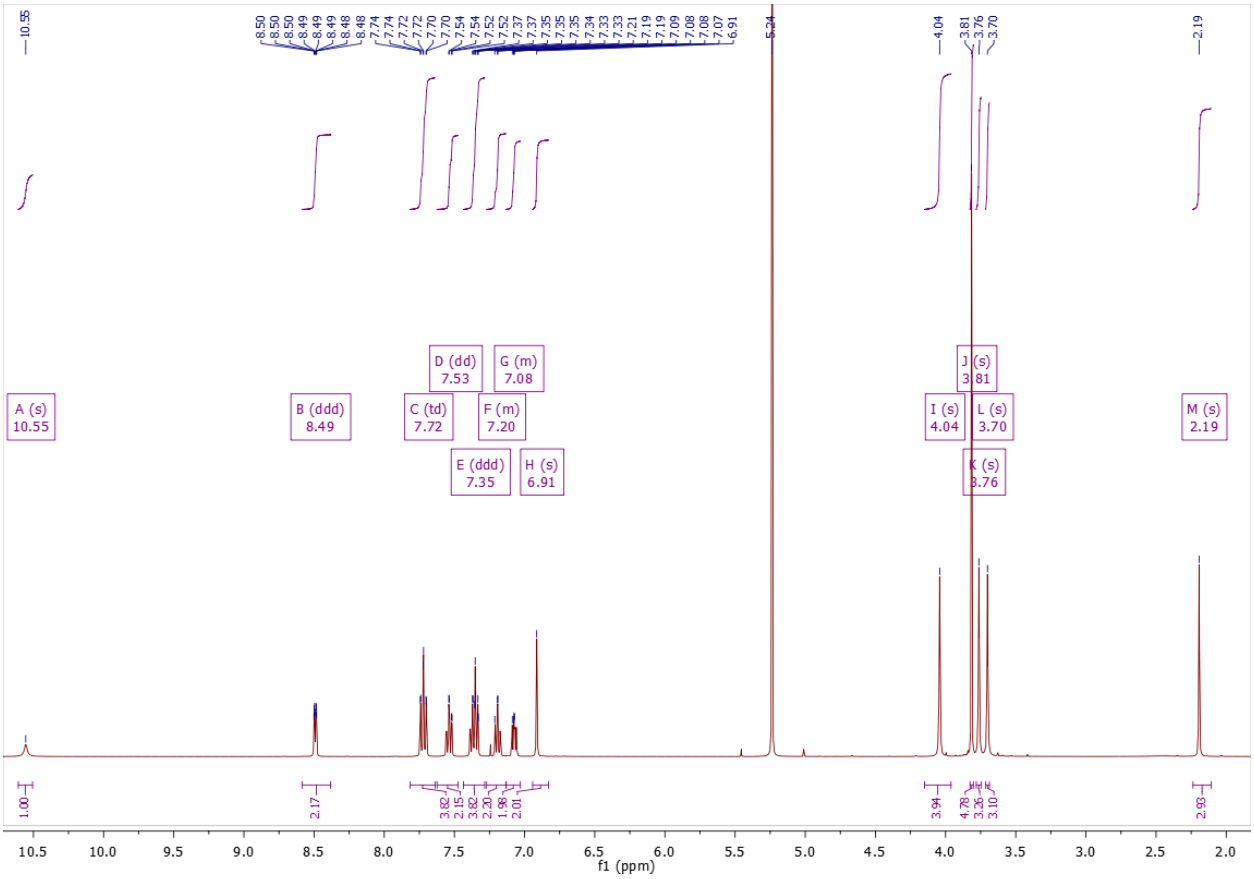

Diethyl-3,3'-((((2-hydroxy-5-methyl-1,3-phenylene)bis(methylene))bis((pyridin-2-ylmethyl)azanediyl))bis(methylene))dibenzoate (2b).

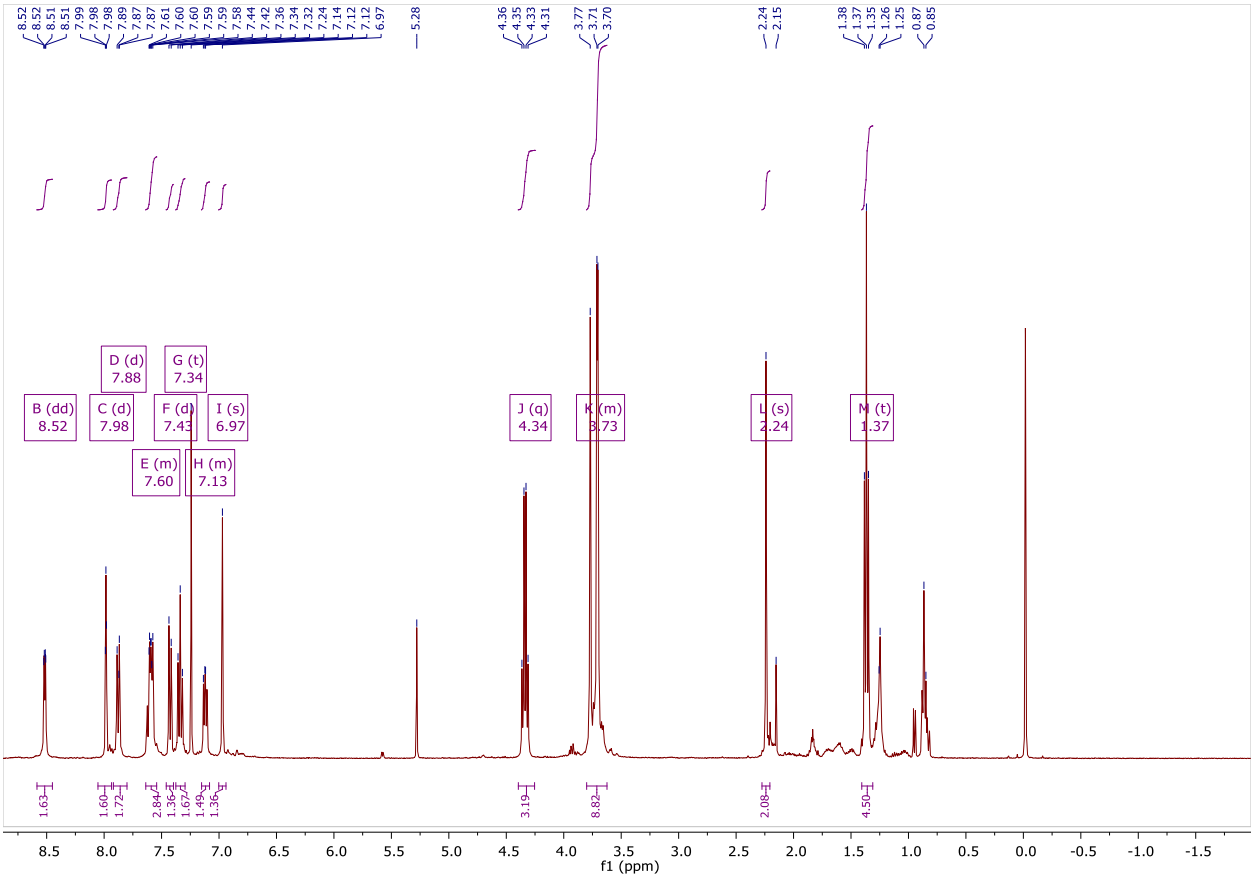

Glycine *N*,*N*'-[(2-hydroxy-5-methyl-1,3-phenylene)bis(methylene)]bis[*N*-(2-pyridinylmethyl)-, 1,1'-diethyl ester (2c).

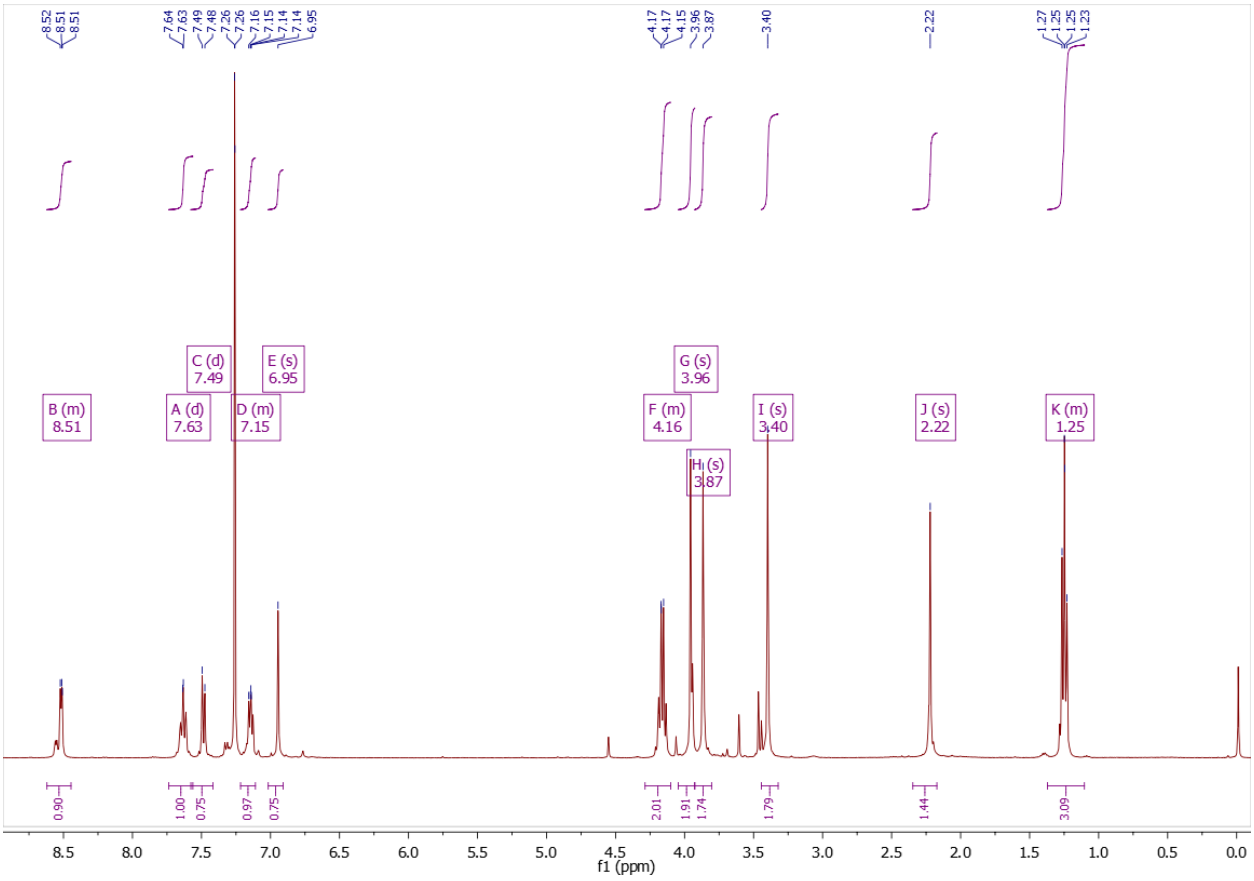

Glycine *N*,*N*'-[(2-hydroxy-5-(*tert*-butyl)-1,3-phenylene)bis(methylene)]bis[*N*-(2-pyridinylmethyl)-, 1,1'-diethyl ester (2d).

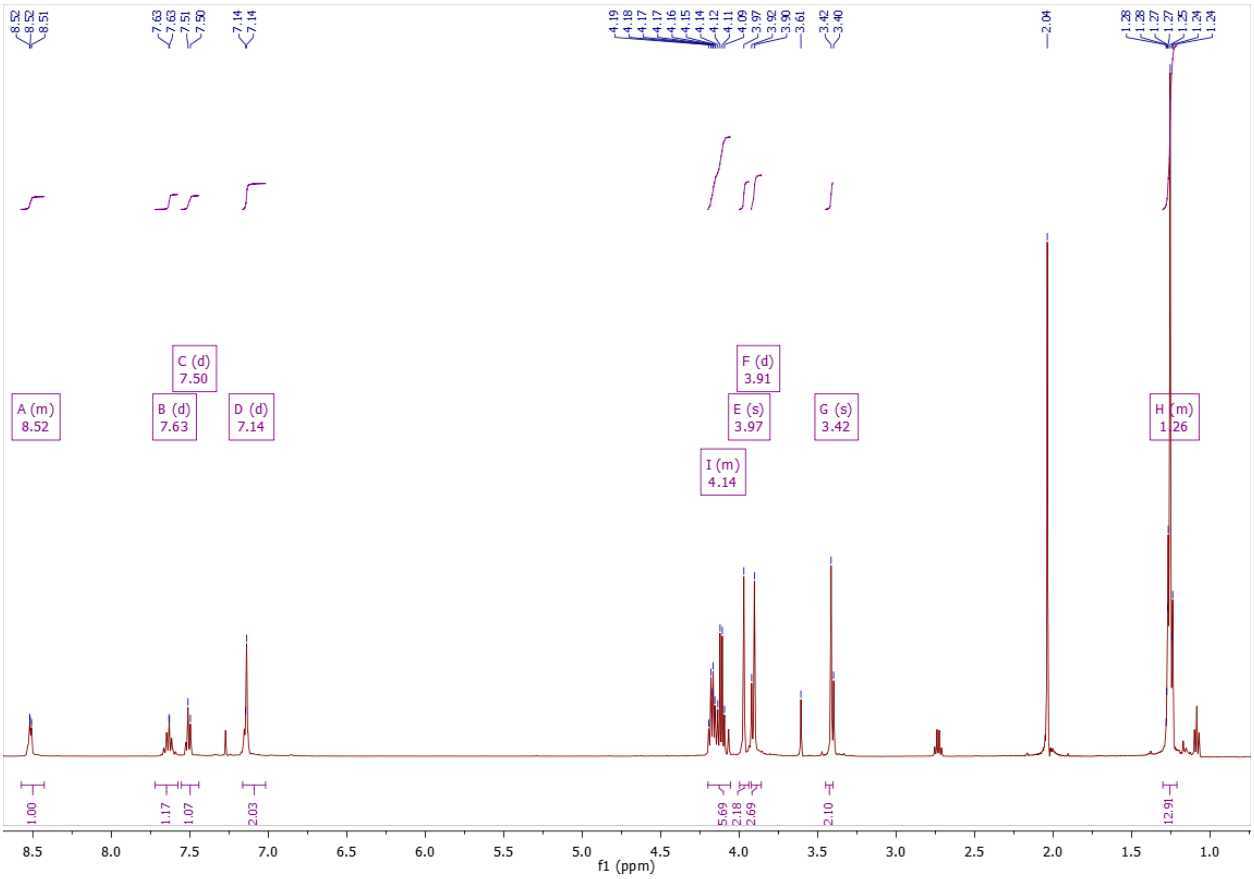

Sodium 2,2'-((((5-methyl-2-oxido-1,3-phenylene)bis(methylene))bis((pyridin-2-ylmethyl)-azanediyl))bis(methylene))dibenzoate (3a).

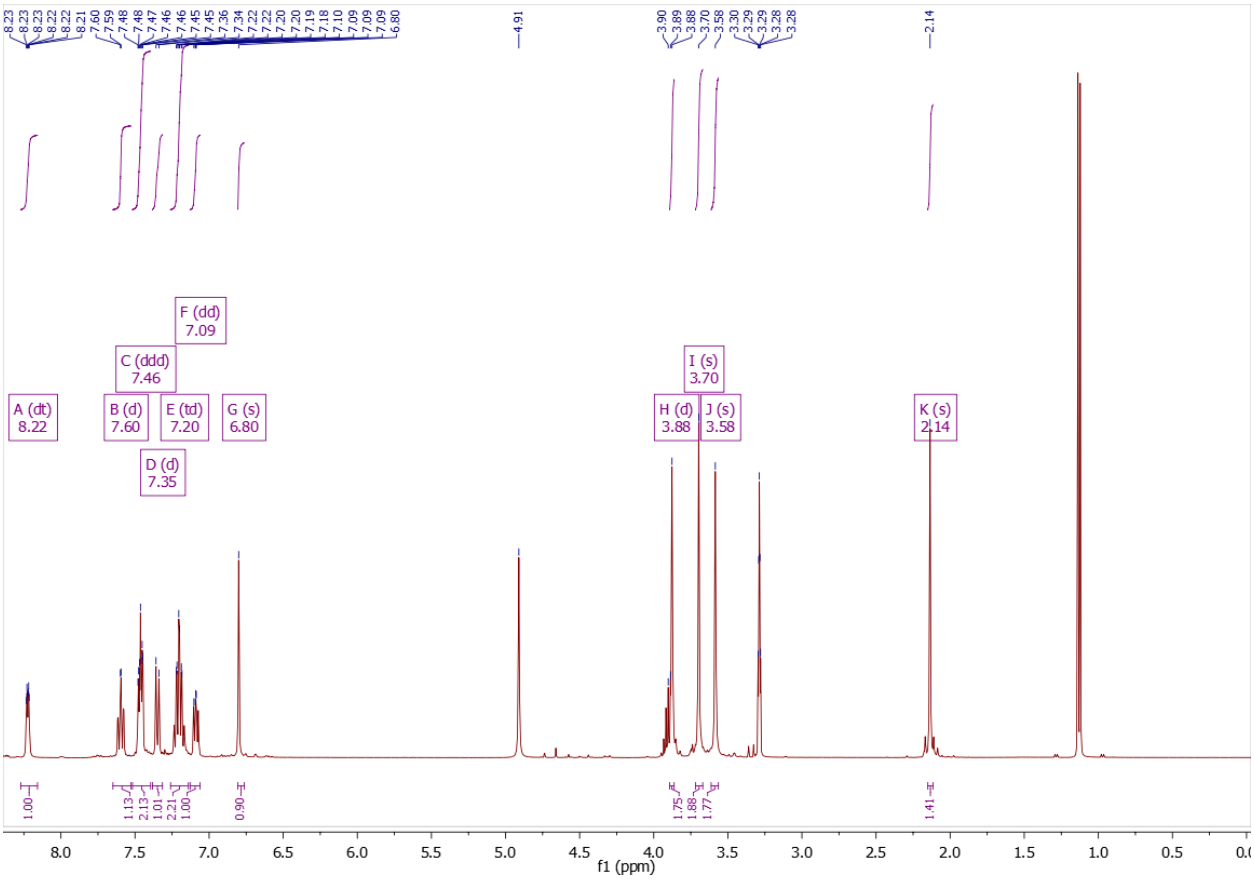

Sodium 3,3'-((((5-methyl-2-oxido-1,3-phenylene)bis(methylene))bis((pyridin-2-ylmethyl)azanediyl))bis(methylene))dibenzoate (3b).

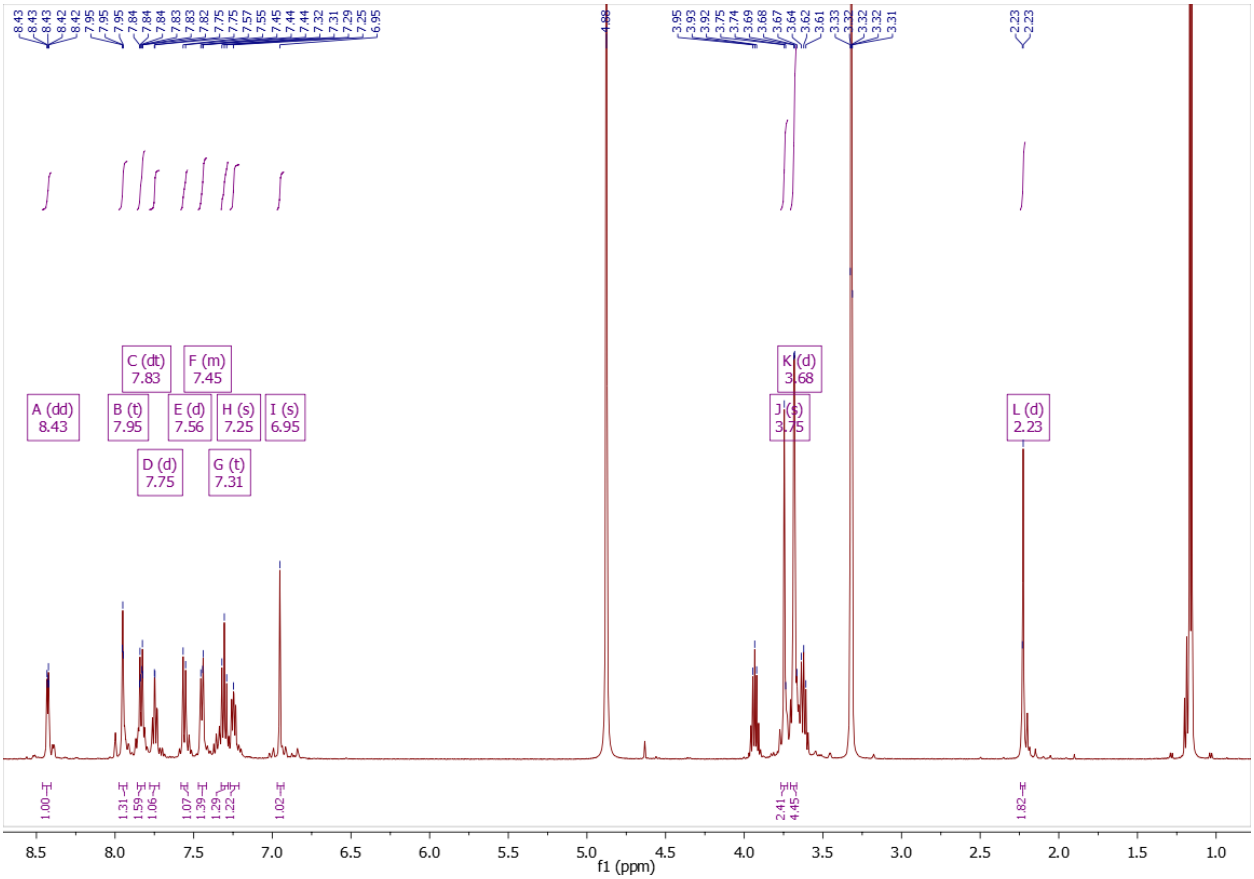

Sodium *N*,*N*'-[(2-hydroxy-5-methyl-1,3-phenylene)bis(methylene)]bis[*N*-(2-pyridinylmethyl)-, 1,1'-diacetate (3c).

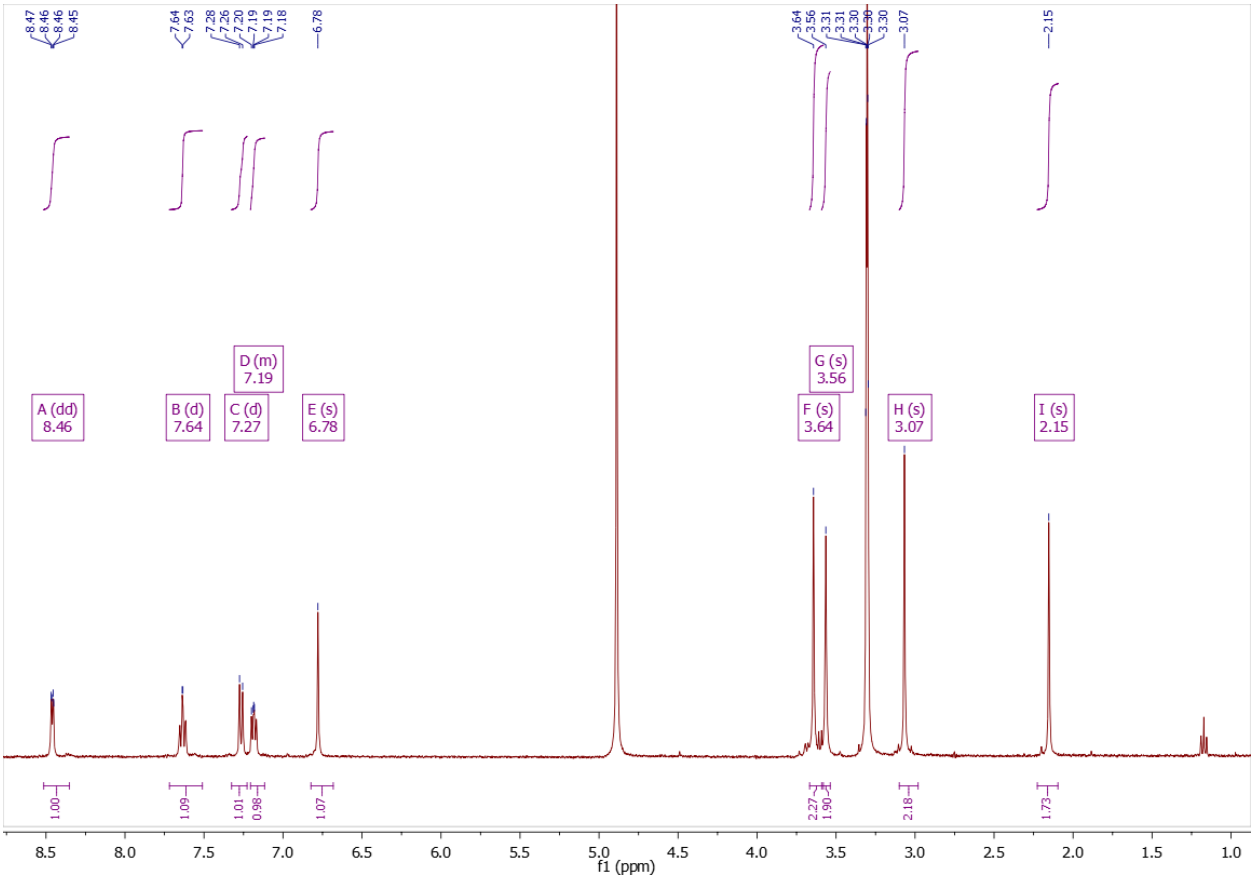

Sodium *N*,*N*'-[(2-hydroxy-5-(*tert*-butyl)-1,3-phenylene)bis(methylene)]bis[*N*-(2-pyridinylmethyl)-, 1,1'-diacetate (3d).

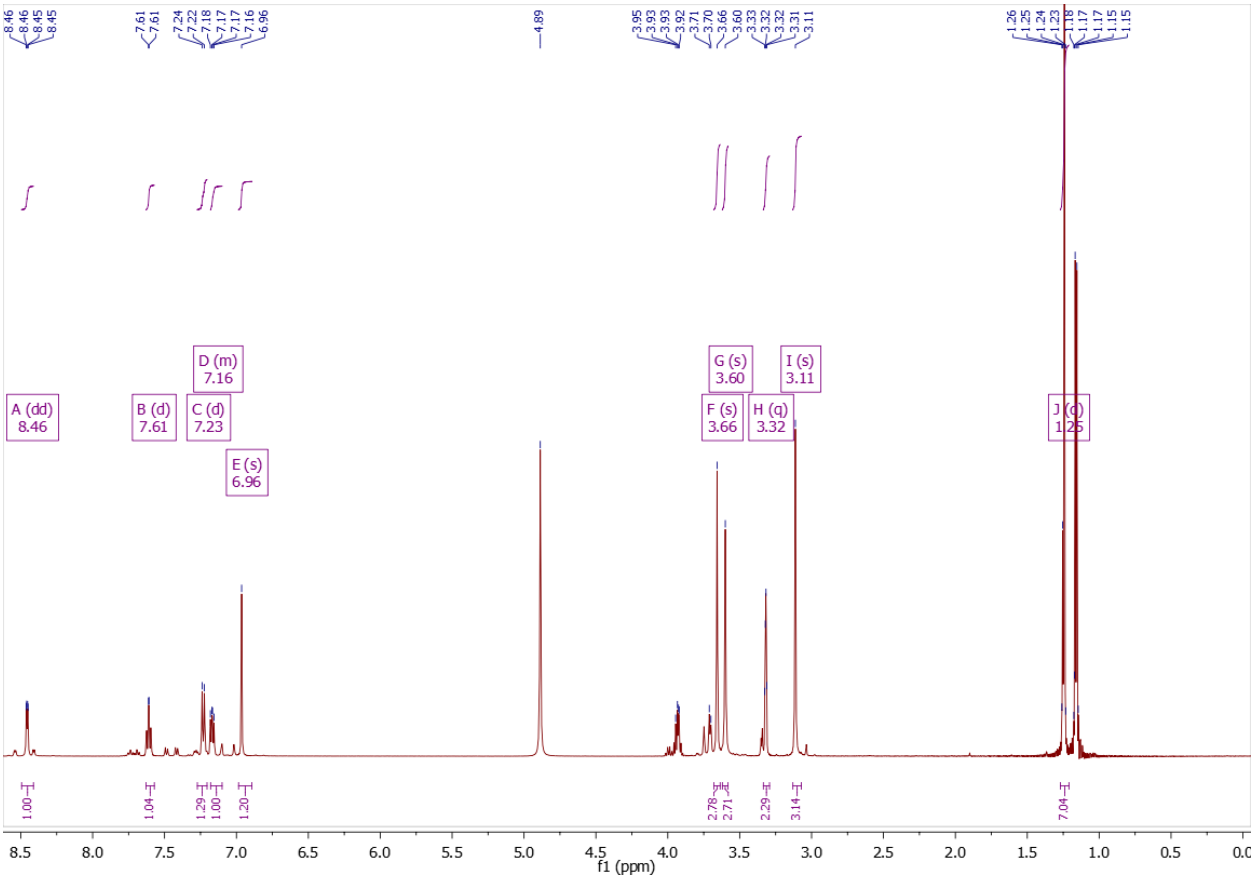

2,6-Diformyl-4-cresol (4a).

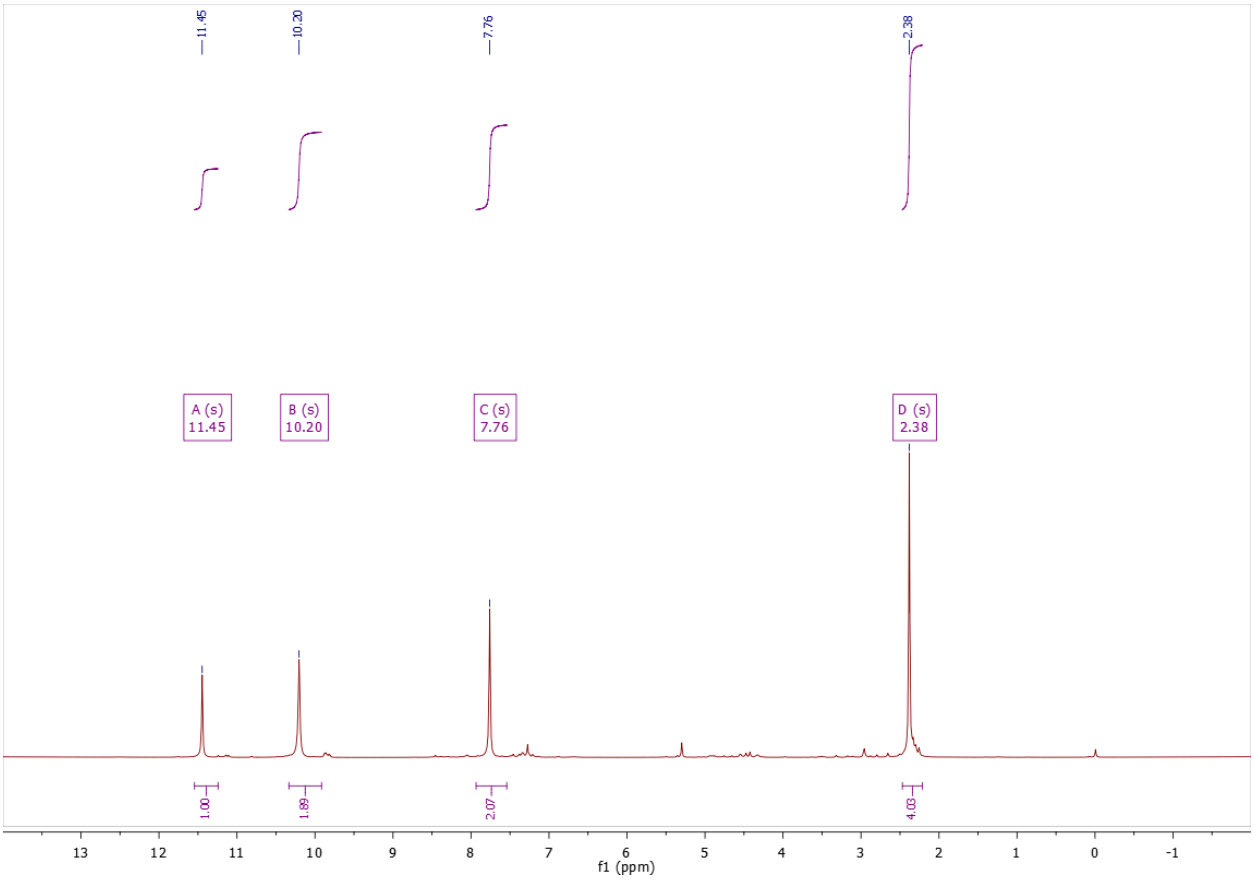

2,6-Diformyl-4-tert-butylphenol (4b).

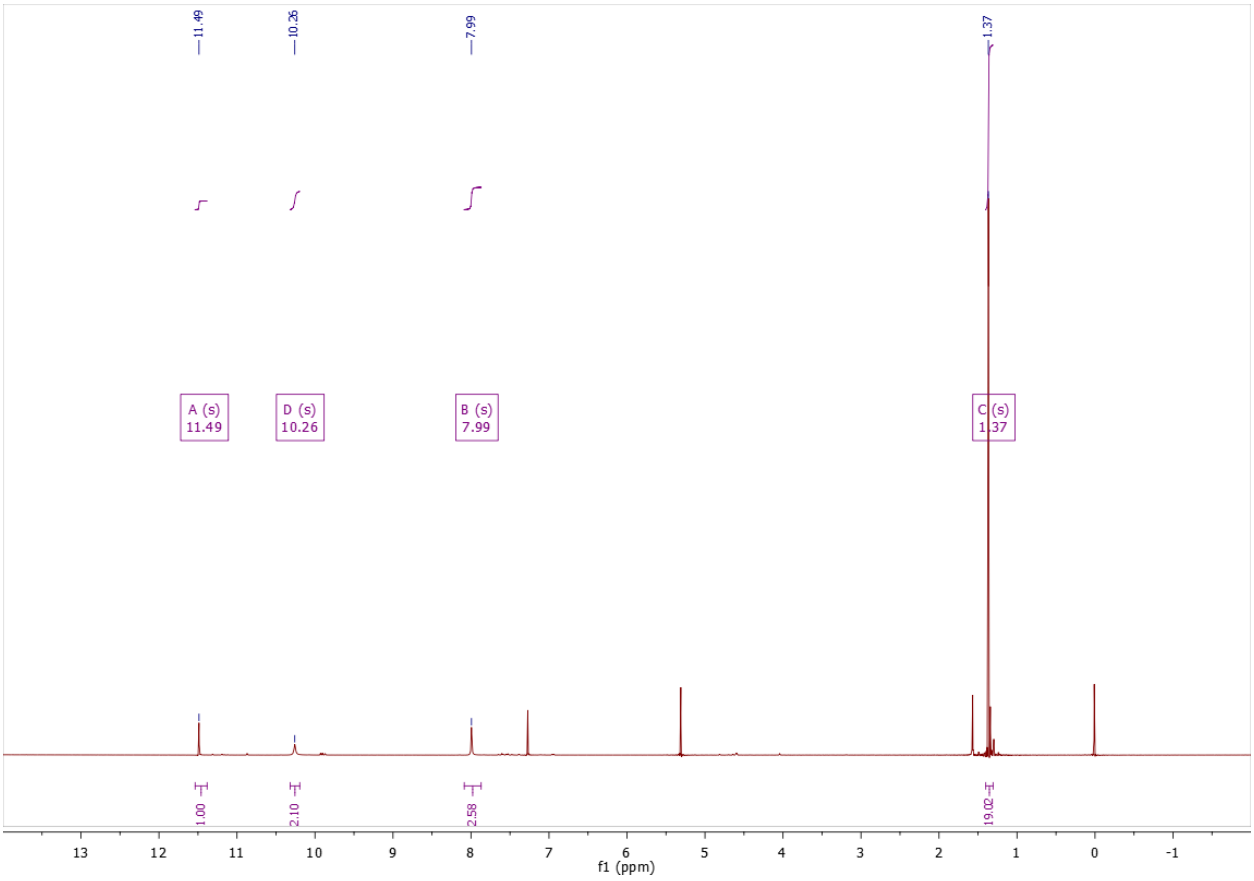

4-Methyl-2,6-bis[[(2-pyridinylmethyl)amino]methyl]-phenol (5a).

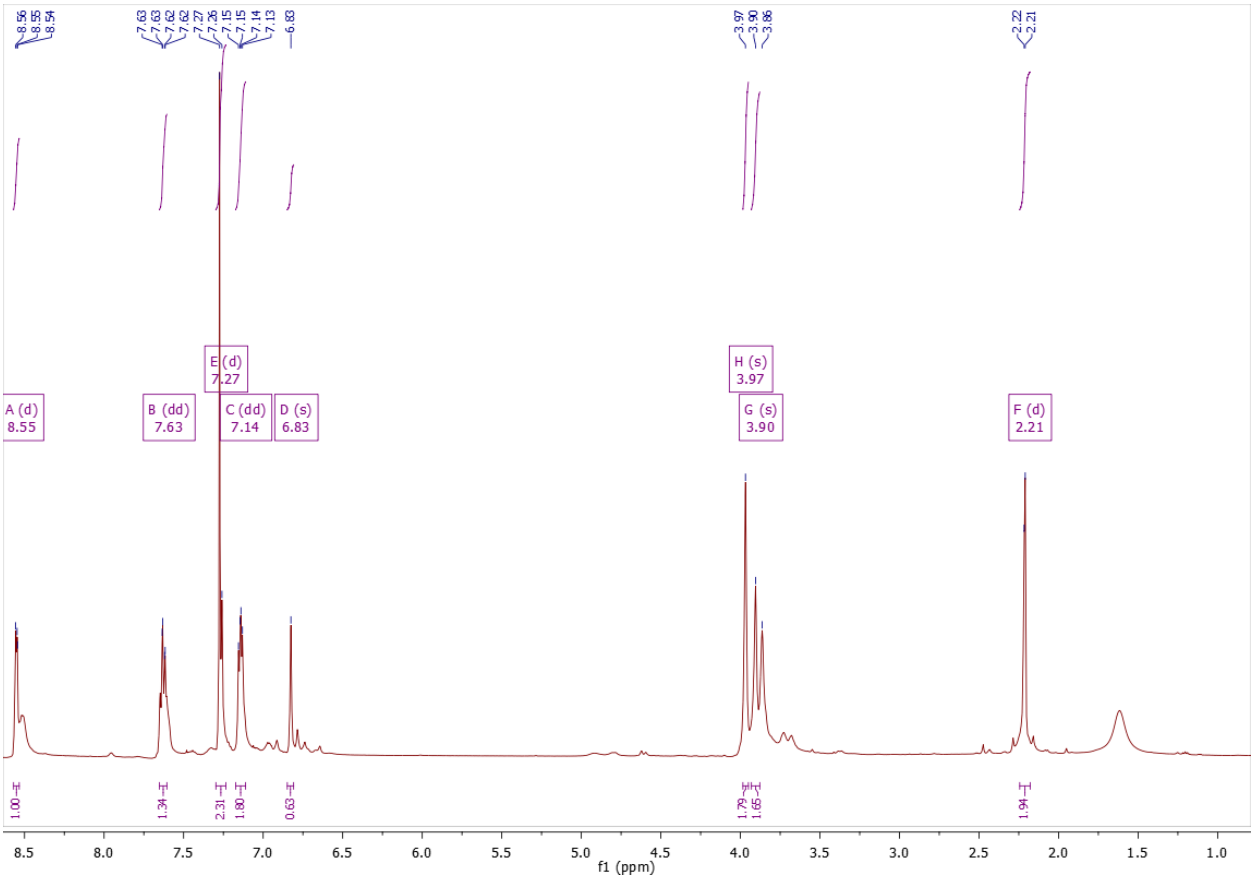

4-(*Tert*-butyl)-2,6-bis[[(2-pyridinylmethyl)amino]methyl]-phenol (5b).

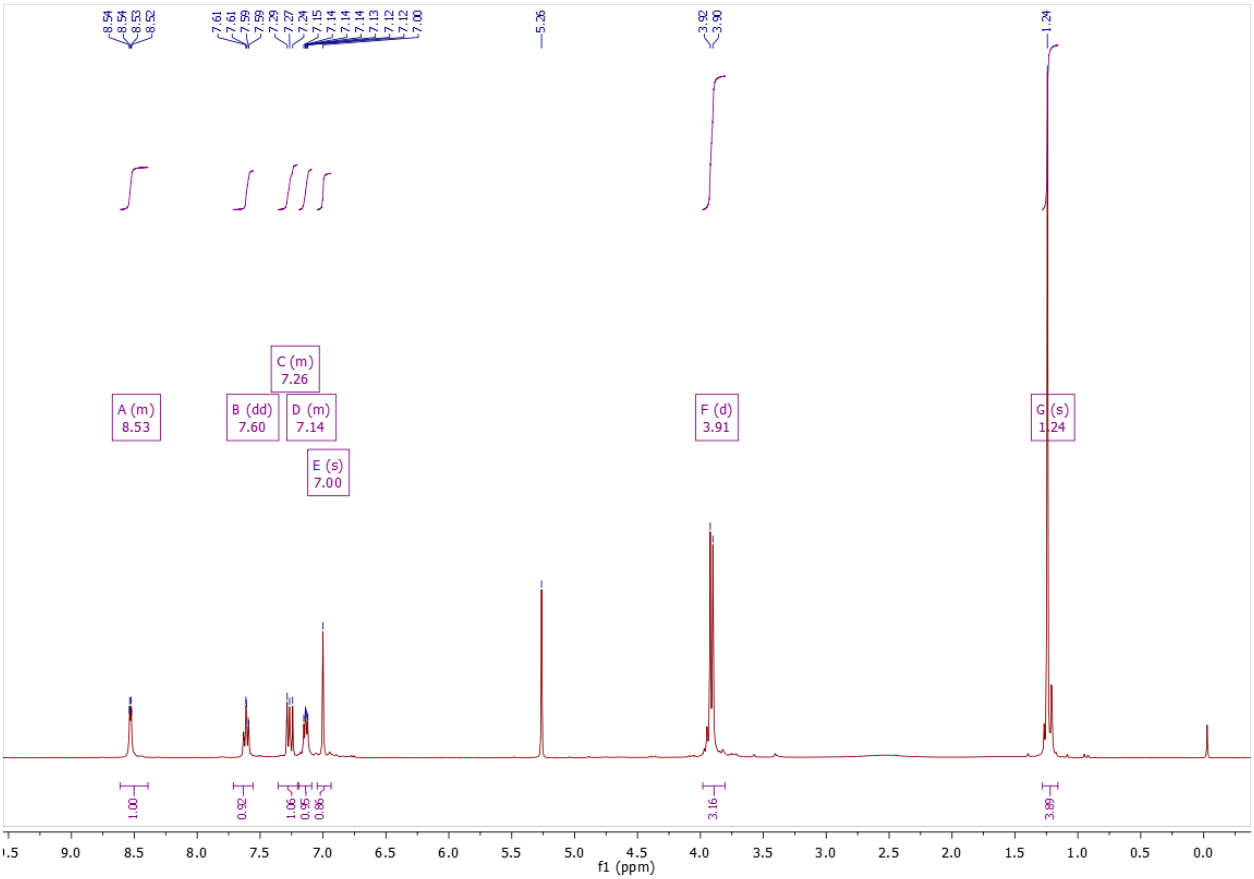

***N*-[[3-[[bis(2-pyridinylmethyl)amino]methyl]-2-hydroxy-5-methylphenyl]methyl]-*N*-(2-methoxy-2-oxoethyl)glycine ester (2e).**

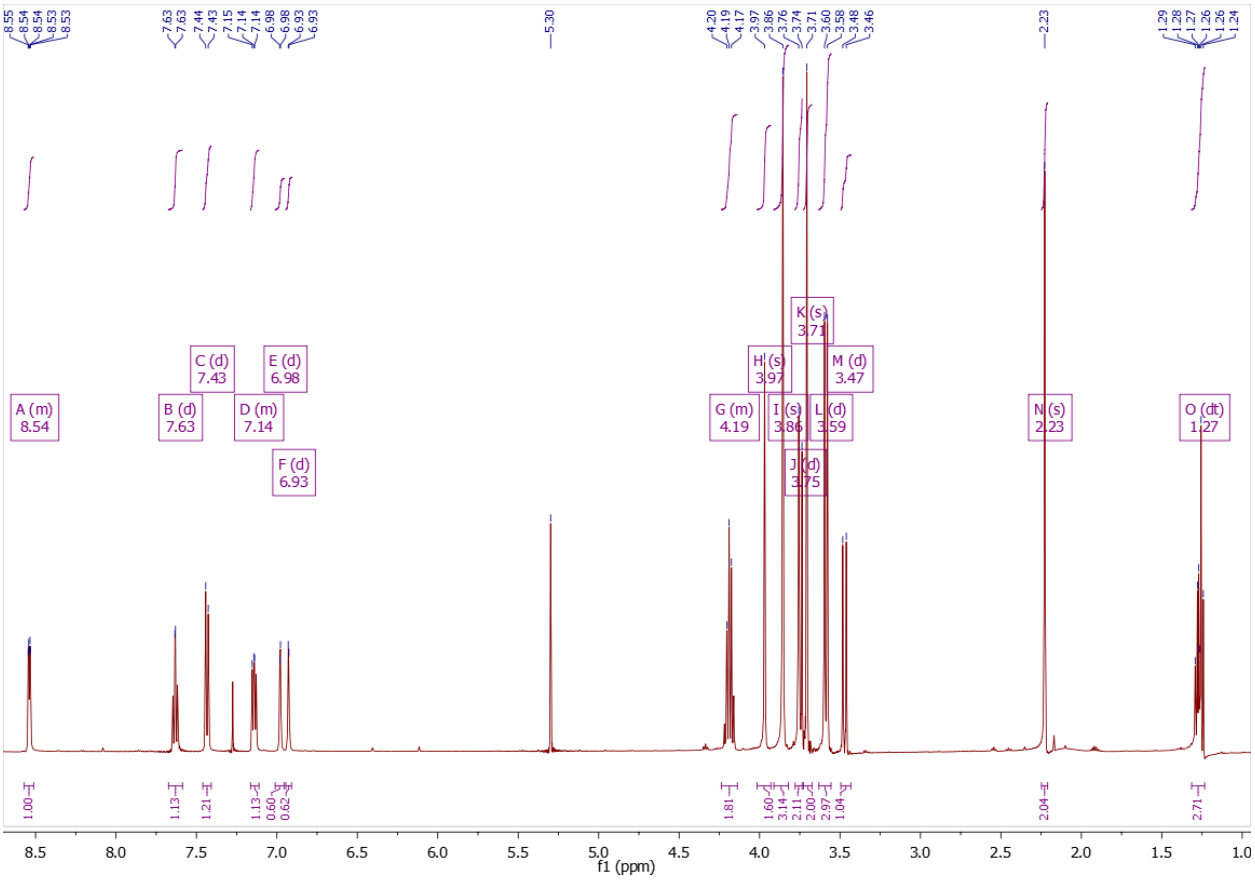

Sodium *N*-[[3-[[bis(2-pyridinylmethyl)amino]methyl]-2-hydroxy-5-methylphenyl]methyl]-*N*-(2-methoxy-2-oxoethyl)glycine (3e).

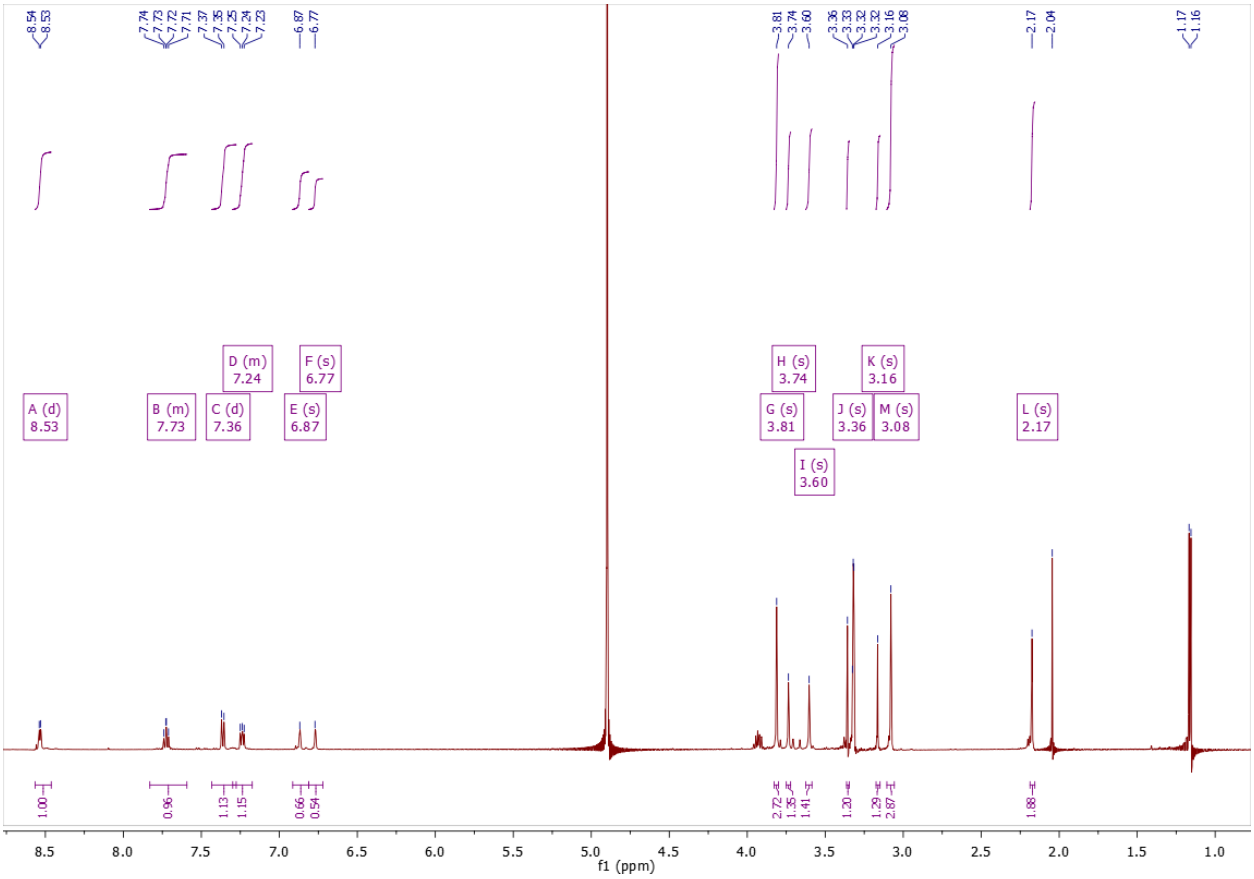

3-(Chloromethyl)-2-hydroxy-5-methylbenzaldehyde (6).

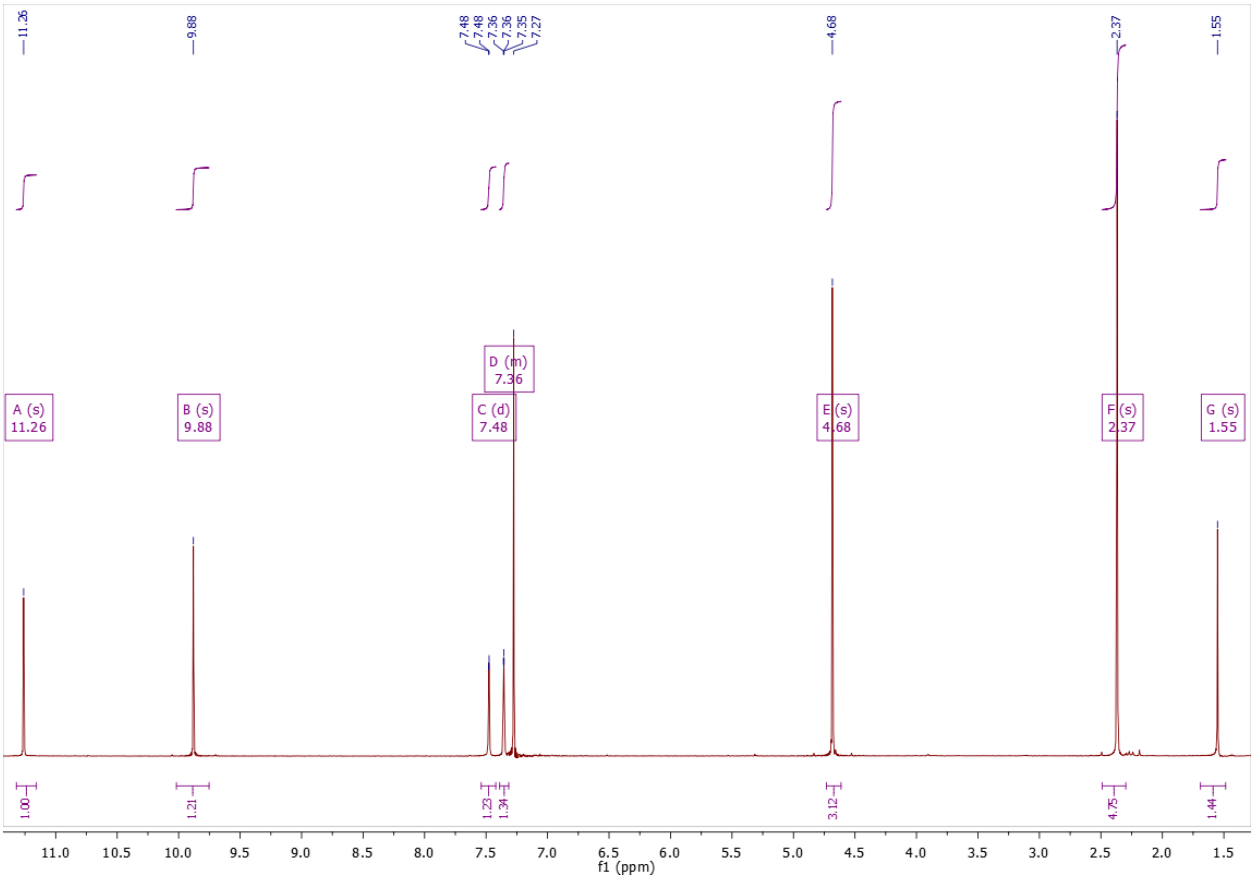

3-[[Bis(2-pyridinylmethyl)amino]methyl]-2-hydroxy-5-methylbenzaldehyde (7).

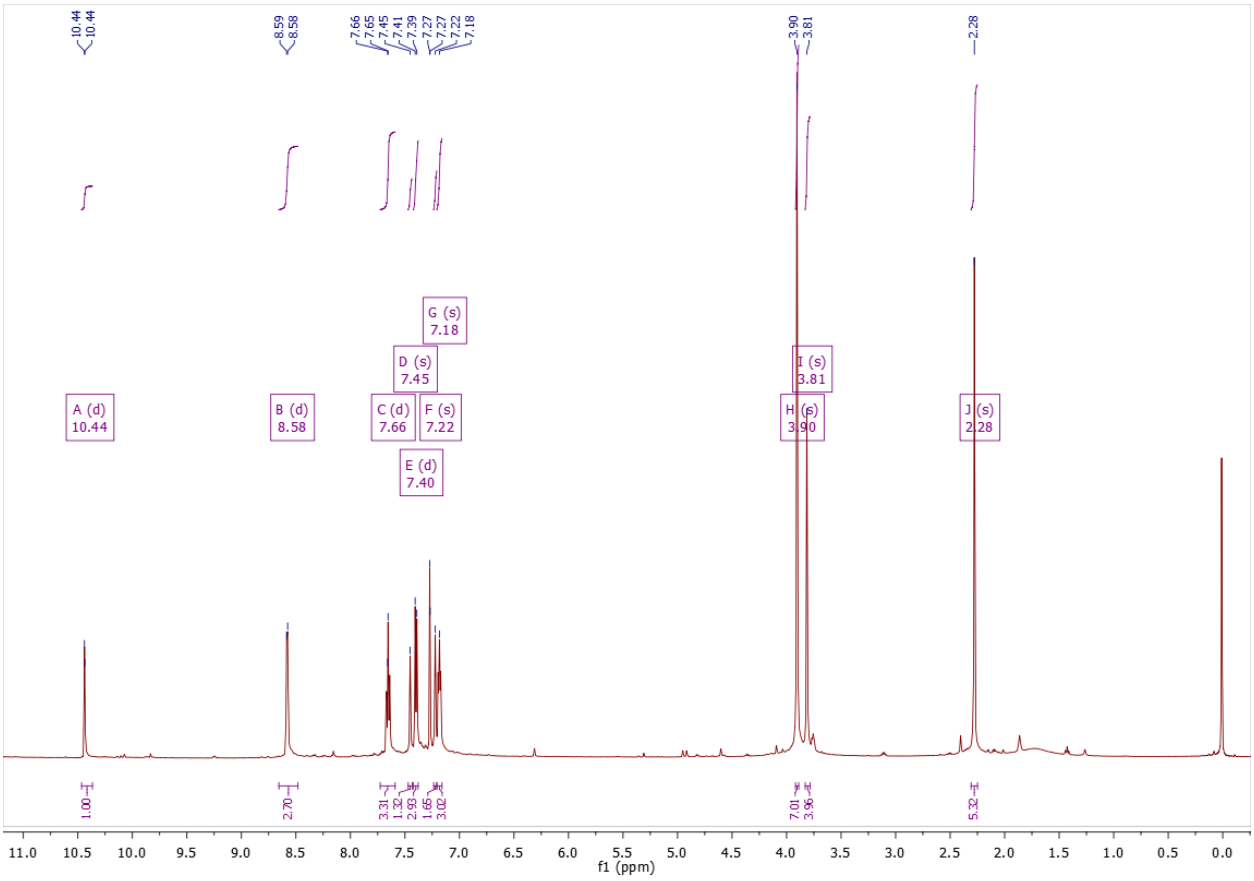

2-[[Bis[(pyridin-2-yl)methyl]amino]methyl]-6-(hydroxymethyl)-4-methylphenol (8).

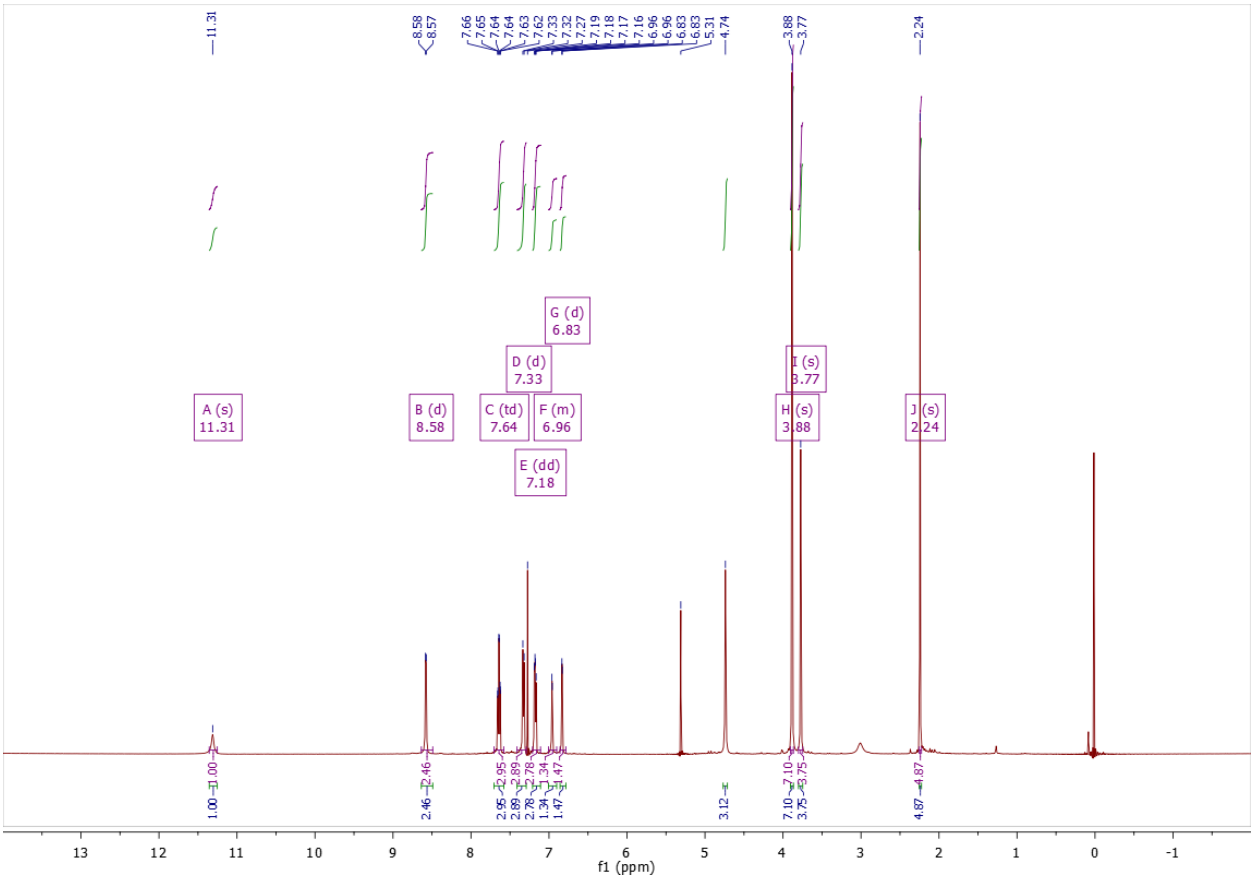

2-[[Bis[(pyridin-2-yl)methyl]methyl]-6-(chloromethyl)-4-methylphenol (9).

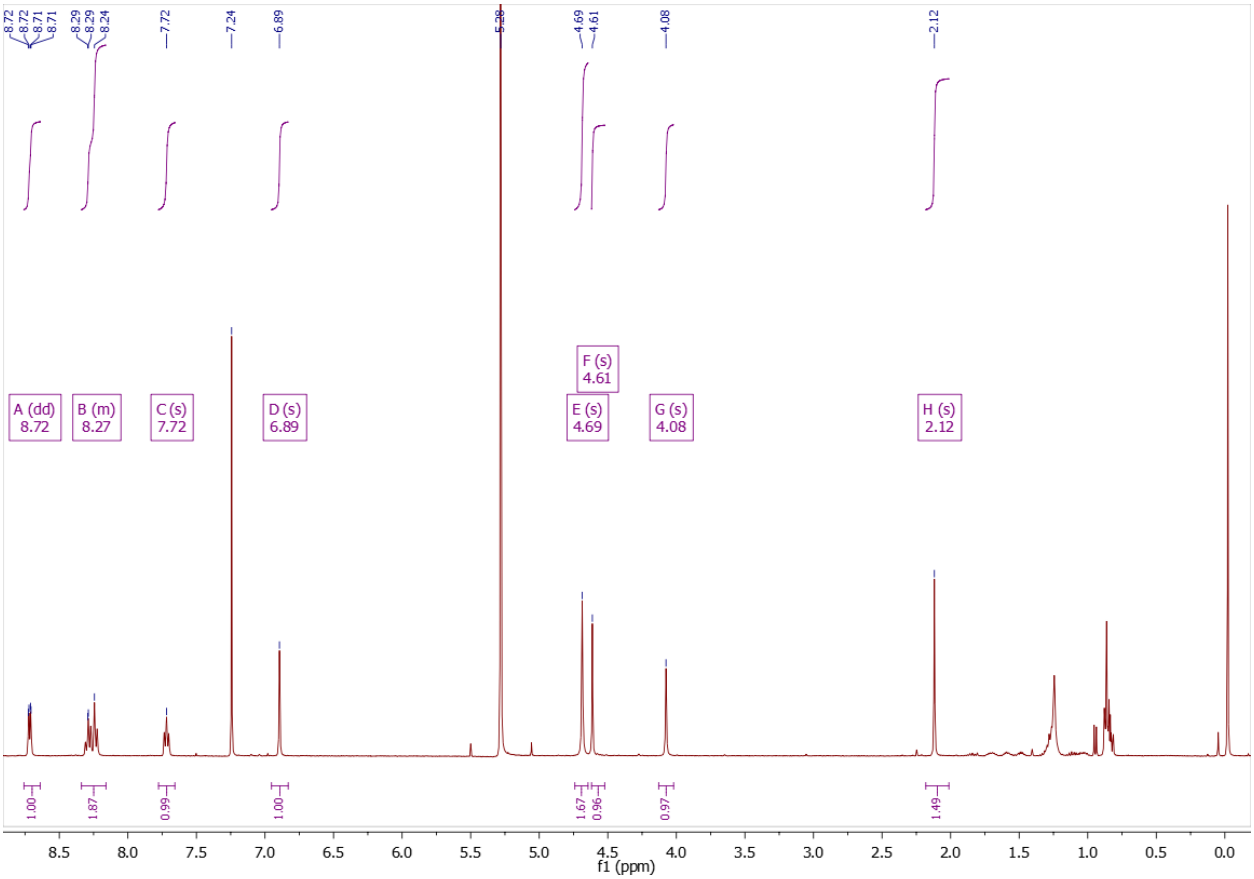

Chapter 6

Conclusions

While thorough studies on the *Thermatoga maritima* FDP[1-4] underscored the importance of hs-Fe^{II}{FeNO}^{7} and hs-[{FeNO}^{7}]$_2$ species as crucial intermediates in the catalytic reduction of two 2NO to N_2O within FDPs, several questions remained in understanding how FNORs carry out efficient NO reduction. Importantly, the *Tm* FDP could carry out NO reduction both with and without the participation of its FMN redox cofactor, though at a reduced rate when the FMN was removed.[2] This implies that the hs-[{FeNO}^{7}]$_2$ intermediate is in fact catalytically competent for catalysis and does not require additional activation by reduction to either the hs-{FeNO}^{7}{FeNO}^{8} or the hs-[{FeNO}^{8}]$_2$ state prior to N-N coupling, although it is important to note that single turnover is slow, taking ~120 seconds to generate N_2O. At the time, this stood in stark contrast to the reactivity of hs-{FeNO}^{7} model complexes, which are generally stable towards N-N coupling due to the covalent nature of the Fe-NO bond.[5, 6] Additionally, the *Tm* FDP acts primarily as an O_2 reductase *in vivo* and it was unclear if the same reactivity could be ascribed to native FNORs.[1] Until the work described in this thesis, a comprehensive study of both structural and electronic effects and how they could affect the mechanism by which high-spin iron-nitrosyls carry out N-N coupling between two NO units had not been carried out. The synthesis, characterization, and reactivity of several hs-Fe^{II}{FeNO}^{7} and hs-[{Fe(NO)}^{7}]$_2$ model complexes with coligands of

varying electron donicity or steric bulk are described in this thesis, and their differences in N-N coupling reactivity are discussed within the context of these perturbations.

6.1 Summary of Thesis

In Chapter 2, the synthesis of the stable hs-$[\{FeNO\}^7]_2$ complex, $[Fe_2(BPMP)(OPr)(NO)_2](OTf)_2$, is reported and its chemical reduction is analyzed.[8] X-Ray crystallographic data shows that the bridging OPr binds to one face of the complex, enforcing a near coplanar binding geometry between the two NO units (N-Fe-Fe-N dihedral angle: 4.90°). While this complex is stable in solution, the addition of one equivalent of reductant leads to rapid (< 156 ms at RT; k_{obs} > 100 s^{-1}) and quantitative intramolecular N-N coupling. This result constitutes the first example of facile semireduction from a diiron dinitrosyl complex:

$$[\{FeNO\}^7]_2 + e^- \rightarrow Fe^{II}\text{-}O\text{-}Fe^{III} + N_2O$$

Based on low-temperature UV-Vis, solution IR, and EPR spectroscopies, this reduction proceeds even at -80 °C, resulting in a transient mixed-valent S = ½ product (and N_2O) that is stable at -80 °C but decays upon warming to RT to afford an EPR-silent species, **[X]**. Based on data collected in Chapter 3, we propose that **[X]** is an antiferromagnetically coupled dimer of two mixed-valent complexes, linked via bridging oxo or hydroxo units.[9] Over time, **[X]** decays further to a diferrous bis-OPr bridged complex, $[Fe_2(BPMP)(OPr)_2](OTf)$, and an unidentified ferric byproduct as determined by X-Ray crystallography, cyclic voltammetry, and Mössbauer spectroscopy. The results from this chapter suggest that chemical reduction serves as a potent means of chemically achieving facile N-N coupling, with single turnover kinetics distinctively faster than those of the *T. maritima* enzyme. Based on the results from a related hs-$[\{FeNO\}^7]_2$ system from Meyer and coworkers[10] with trans-NO units that was unable to facilitate N-N coupling, we further

hypothesized that our facile N-N coupling was aided by the near coplanar ON-NO binding geometry. This point is further elaborated in detail in Chapter 4.

Chapter 3 expands on the work discussed in Chapter 2 by contrasting the reactivities of a hs-$Fe^{II}\{FeNO\}^7$ and hs-$[\{FeNO\}^7]_2$ complex, $[Fe_2(N\text{-}Et\text{-}HPTB)(NO)(DMF)_3](BF_4)_3$ and $[Fe_2(N\text{-}Et\text{-}HPTB)(NO)_2(DMF)_2](BF_4)_3$, of the exact same ligand scaffold, and by structurally characterizing the immediate mixed-valent product after chemical reduction and N_2O release.[9, 11] Here, the hs-$[\{FeNO\}^7]_2$ complex is the second reported model system that undergoes facile unimolecular semireduction as determined by gas-headspace N_2O analysis. In contrast, the hs-$Fe^{II}\{FeNO\}^7$ complex is the first example of a diiron system that undergoes rapid superreduction. Since this reaction must occur intermolecularly, additional activation compared to the hs-$[\{FeNO\}^7]_2$ complex is required. Furthermore, the immediate mixed-valent product of N-N coupling from the hs-$[\{FeNO\}^7]_2$ complex was isolated and structurally characterized by X-Ray crystallograpy, revealing a tetrairon core composed of two mixed-valent dimers that are linked via three oxo/hydroxo bridges, where the third oxygen atom is proposed to originate from trace moisture in the solvent. This is the first time that the oligomerized tetrameric products from these reactions were unambiguously characterized. Based on this finding, an analogous structure was proposed for **[X]** in Chapter 2, suggesting that this may be a general reaction product for the reduction of hs-$[\{FeNO\}^7]_2$ complexes.

Since the same coligand is used in these mono- and di-nitrosyl diiron complexes, these compounds allow for a direct comparison of their levels of activation for N-N coupling. As might be expected, these data directly support the necessity of the two NO units to be held in proximity to decrease the barrier for N-N coupling, allowing for facile semireduction with the hs-$[\{FeNO\}^7]_2$ complex, but requiring additional super-reduction with the hs-$Fe^{II}\{FeNO\}^7$ complex. Interestingly,

DFT calculations on the reduced $Fe^{II}\{FeNO\}^8$ and $\{FeNO\}^7\{FeNO\}^8$ species show that the additional electron in the $\{FeNO\}^7\{FeNO\}^8$ complex populates the nonbonding d_{xy} orbital, whereas the electron in the $Fe^{II}\{FeNO\}^8$ complex occupies the antibonding d_{xz}/π^*_x orbital. Despite the increased activation of the mononitrosyl Fe-NO unit, owing to the population of an Fe-NO antibonding π^*-orbital, the N-N coupling still experimentally proceeds only via a superreduced pathway (reaction of two hs-$\{FeNO\}^8$ species), highlighting the necessity of having two NO units bound in close proximity to facilitate N-N coupling in these systems.

In Chapter 4 a series of $[Fe_2(BPMP)(X)_2(NO)_2]^{3+/1+}$ analogs (X = NMeIm, MeOH, $^-$OTf) containing two monodentate ligands in place of a bridging propionate are presented, and their reduction reactions were investigated. Importantly, the absence of a bridging carboxylate enables a conformational flexibility of the binding geometries of both the monodentate ligands as well as the NO units, allowing for a series of N-Fe-Fe-N dihedral angles and (O)N-N(O) distances to be screened and reactivities compared. As characterized either by X-Ray crystallography or DFT optimized structures, N-N distances range from 3.13 to 3.78 Å and N-Fe-Fe-N dihedral angles range between 56.2 to 85.1°. Interestingly, all the above derivatives have perturbed reactivity and decomposition pathways compared to complexes discussed in Chapters 2, 3, and 5. At low temperatures and rapid timescales (~5 min), the one electron chemical reduction of $[Fe_2(BPMP)(X)_2(NO)_2]^{3+/1+}$ leads to two main decomposition routes that occur in parallel: (1) the rapid formation of substoichiometric N_2O, and (2) the formation of a hs-$Fe^{II}\{Fe(NO)_2\}^9$ DNIC. Similarly, the same two parallel reactions occur upon the addition of two equivalents of reductant, except with the formation of a hs-$Fe^{II}\{Fe(NO)_2\}^{10}$ DNIC. The t = 5 minute N_2O yields have direct mechanistic implications for FNORs, with significantly inhibited N_2O yields from semi-reduction not exceeding 8.7% within this timeframe. This data supports the necessity of having two NO

ligands in close proximity and in a coplanar geometry. Interestingly, the DNICs that form undergo a highly atypical decomposition in solution, ultimately decaying with the accumulation of additional N_2O over 2 hrs. Consistent with the electronic structure descriptions of hs-$\{Fe(NO)_2\}^{9/10}$ DNICs discussed in Chapter 1,[12-15] the hs-$Fe^{II}\{Fe(NO)_2\}^9$ DNIC affords greater N_2O yields across all three monodentate ligand variants, presumably due to weaker Fe-NO bonds in this state. Additionally, all three X = OTf, NMeIm, and MeOH analogs form *identical* DNIC N-O stretching bands in CH_2Cl_2 solution, at 1788 and 1715 cm^{-1} for the hs-$Fe^{II}\{Fe(NO)_2\}^9$ state, and at 1689 and 1632 cm^{-1} for the hs-$Fe^{II}\{Fe(NO)_2\}^{10}$ state. This finding suggests that the primary coordination sphere about the DNIC-containing Fe center does not contain the monodentate ligand X, which was proposed to migrate to the Fe^{II} component to allow for DNIC formation. Furthermore, EPR spectroscopy of the EPR-active hs-$Fe^{II}\{Fe(NO)_2\}^9$ intermediate contains a S = ½ signal, pointing towards additional primary coordination sphere perturbations. Here, a S = ½ signal can only occur from a spin uncoupled system where the EPR-silent hs-Fe^{II} (S = 2) component is not coupled with the hs-$\{Fe(NO)_2\}^9$ (S = ½) center, suggesting that the central phenolate no longer bridges the diiron core. Based on a large body of previously reported 4-coordinate and 5-coordinate DNIC complexes, the DNIC coordination number has been found to directly affect the splitting of the symmetric/antisymmetric DNIC stretches, with a typical band splitting ($\Delta\nu_{NO}$) of 73 cm^{-1} for 5-coordinate cationic DNICs, and $\Delta\nu_{NO}$ of 45-60 cm^{-1} for 4-coordinate neutral DNICs.[16] This would imply that the hs-$Fe^{II}\{Fe(NO)_2\}^9$ DNIC is likely 5-coordinate, while the hs-$Fe^{II}\{Fe(NO)_2\}^{10}$ becomes 4-coordinate. The DFT optimized hs-$Fe^{II}\{Fe(NO)_2\}^{9/10}$ structures supports this assignment, with a 5-coordinate DNIC consisting of BPMP coordination via its tertiary amine and two pyridine arms. Upon reduction to the hs-$Fe^{II}\{Fe(NO)_2\}^{10}$ state, the Fe-N (tertiary amine) bond elongates resulting in a pseudo-tetrahedral

4-coordinate structure. Lastly, the dinuclear DNIC products were chemically modelled with mononuclear system with BMPA ligation. The reduction of [Fe(BMPA)$(OTf)_2$(NO)] with 0.5 or 1 eq of $CoCp_2$ generated remarkably similar hs-$\{Fe(NO)_2\}^{9/10}$ DNIC products compared to the dinuclear analogs, and more importantly, these mononuclear DNICs are stable in solution towards N-N coupling. This finding suggests that the presence of a tethered Fe^{II} in the dinuclear hs-$Fe^{II}\{Fe(NO)_2\}^{9/10}$ intermediates is capable of facilitating N-N coupling by trapping the NO or NO^- released from the hs- $Fe^{II}\{Fe(NO)_2\}^{9/10}$ as it decays in solution. These findings are overall quite surprising given the general stability of DNICs towards N-N coupling, and represent and unprecedented route towards N-N coupling in DNIC chemistry, where the DNICs transfer a NO or NO^- to a nearby Fe^{II} to generate hs-$\{FeNO\}^7\{FeNO\}^8$ or hs-$[\{FeNO\}^8]_2$ intermediates that then proceed to generate N_2O..

Finally, in Chapter 5 the primary-coordination sphere donicity of the BPMP ligand was perturbed to reach redox potentials of the corresponding diiron complexes that are closer to those of native FNORs. Whereas the Chapter 2 BPMP complex[8] sits ~900 mV more positive than the $Fe^{III}Fe^{II}/Fe^{II}Fe^{II}$ reduction potential in native FNORs, our diiron complex with the second generation Py_2PhO_2MP ligand,[17] containing two symmetric phenolates in place of two pyridines, sits ~350 mV more negative than this potential. Accordingly, this complex does not stabilize a hs-$[\{FeNO\}^7]_2$ unit, but instead, proceeds with rapid direct-coupling of NO to N_2O affording a diferric product. Carboxylate-containing BPMP derivatives were therefore chosen as a middle ground in terms of ligand donicity, and the corresponding syntheses of symmetric benzoate and aliphatic carboxylate derivatives of BPMP were optimized here. Both [Fe_2(PhO$(Py)_2(OAc)_2$)$(OAc)(NO)_2$] and [Fe_2(PhO$(Py)_2$(o/m-Bz)$_2$)$(OAc)(NO)_2$] contain redox potentials that are ~500 mV more negative than the BPMP analog discussed in Chapter 2, though they still sit ~300 mV more positive

than the $Fe^{III}Fe^{II}/Fe^{II}Fe^{II}$ couple in the FlRd FNOR.[18] While DFT optimizations of these structures revealed that the benzoate derivatives were too sterically bulky to feasible bind a diiron core, the aliphatic carboxylate derivative can feasibly form a diiron complex and a corresponding dinitrosyl adduct, and its ability to facilitate N-N coupling was investigated. The hs-$[\{FeNO\}^7]_2$ complex is stable in the solid state. However, when stirred in a methanolic solution over 2 hrs, N_2O was slowly and substoichiometrically released in the absence of any chemical reductant following a slow and inefficient direct-coupling mechanism, affording 26% N_2O. This was not completely unexpected, given that the redox potential still sits more positive than that of native FNORs. Unfortunately, detailed solution IR studies on the decomposition of the NO complex were precluded due to its poor solubility in both CH_2Cl_2 and CH_3CN. Moving forward, the synthesis of a tBu-$PhO(Py)_2(OAc)_2$ ligand derivative with a *tert*-butyl phenolic backbone was optimized, and alternate commercially available precursors are proposed for the synthesis of additional derivatives in future studies that have improved solubility.

The combined results from these chapters paint a more complete picture of the structural and electronic prerequisites that are necessary to achieve the facile reduction of NO to N_2O by non-heme diiron cores, with direct relevance to FNORs. First, N-N coupling requires the participation of *two* hs-$\{FeNO\}^7$ centers, and furthermore has a lower activation barrier for unimolecular coupling between the two NO in a hs-$[\{FeNO\}^7]_2$ core compared to bimolecular coupling from two hs-$\{FeNO\}^7$ centers. Second, while direct-coupling between two hs-$\{FeNO\}^7$ is possible with more negative redox potentials, activation of one hs-$\{FeNO\}^7$ to make a hs-$\{FeNO\}^7/\{FeNO\}^8$ intermediate via a one-electron reduction significantly enhances N-N coupling rates by ~10^3 compared to the rate in the *Tm.* FDP. Lastly, the N-Fe-Fe-N dihedral angle and (O)N-N(O) distance must be tightly regulated, keeping the two NO ligands in a *cis* conformation. When

dihedral angles reach ~50º and (O)N-N(O) distances reach 3.1 Å then N_2O yields drop below 10%, and DNICs become the major product.

6.2 Future Directions

While the work discussed in this thesis broadly details the primary-coordination sphere structural and electronic prerequisites for N-N coupling, Nature typically engineers beautifully crafted enzyme active site pockets, utilizing primary-quaternary structure to carry out efficient catalysis. In recent years, several DFT[19, 20] and experimental[2] studies have emphasized this point within the context of FNORs, highlighting a key conserved secondary coordination sphere (SCS) Y197 that is within hydrogen-bonding distance to one bound NO. A detailed QM/MM study[3] revealed that the participation of H-bonding from this Y197 decreases the activation barriers for both N-N coupling and N-O bond cleavage, supporting one elegant way that the enzyme may carry out an efficient direct-coupling at potentials that are more positive than those of our (Py_2PhO_2)MP model complex. This was recently supported by a mutagenesis study[2] in which the Y197F variant is shown to no longer be catalytically competent for N-N coupling. These results highlight the significance in SCS H-bonding interactions in decreasing the activation barrier for N-N coupling. The synthesis and characterization of BPMP complexes that incorporate SCS interactions are therefore warranted. As an alternate route towards activating stabile hs-[{FeNO}^{7}]$_2$ model complexes for N-N coupling would be to polarize the Fe-NO bond via an alternate source, such as via addition of exogenous Lewis-acids like BR_3 or Lanthanide triflates.

Additionally, there are several possible extensions to the research discussed within each chapter. The stable hs-{FeNO}^{7} complexes reported in Chapters 2, 3, and 5 all share a common

proposed, though never spectroscopically captured or isolated, hs-{FeNO}^{8} intermediate that forms immediately upon chemical reduction. In fact, non-heme hs-{FeNO}^{8} species have been notoriously challenging to capture and stabilize and have required either creative steric protection[21] or electron poor ligands[22] to stabilize such species. Within the context of FNOR model complexes that carry out semi/superreduction, Goldberg's mononitrosyl hs-{FeNO}^{8} that slowly decays to generate substoichiometric N_2O is the sole example of a spectroscopically captured hs-{FeNO}^{8} intermediate.[23] Interestingly, in Chapter 3, the CV of $[Fe_2$(N-Et-HPTB)(NO)(DMF)$_3](BF_4)_3$ shows a quasi-reversible hs-Fe^{II}{FeNO}$^{7/8}$ couple, with increased reversibility at higher scan rates, suggesting that the hs-Fe^{II}{FeNO}^{8} may be possible to capture either at low temperatures or at stopped-flow time scales.[9, 11]

In Chapter 4, the N_2O yields for the series of $[Fe_2(BPMP)(X)_2(NO)_2]^{3+/1+}$ and $[Fe(BMPA)(OTf)_2(NO)_2]$ were reported, and the mechanisms by which these complexes generate N_2O and DNIC products was investigated. While the N_2O yield trends at the t = 5 minute data point could be rationalized based on the corresponding complexes N-Fe-Fe-N dihedral angle and ON-NO distance for the X = OTf and NMeIm complex, the X = MeOH complex stood as a clear outlier. We suspect that the H-bonding interaction between the MeOH and adjacent NO in the crystal structure of the X = MeOH complex may artificially lead to an expanded core structure with the largest (O)N-N(O) distance and N-Fe-Fe-N dihedral angle to accommodate the H-bond. Alternatively, the presence of weakly acidic MeOH protons may assist in the N-N coupling pathway. DFT optimizations on the non-hydrogen bonding CH_3CN-bound analog would provide a useful comparison of the core-structure metrics in the absence of H-bonding interactions. As another useful control, the synthesis and reactivity studies on the X = MeO^- complex is warranted. Additionally, the hs-{Fe(NO)$_2$}$^{9/10}$ DNIC products of the reduction of $[Fe(BMPA)(OTf)_2(NO)]$

were within ~4 cm^{-1} of the corresponding hs-$Fe^{II}\{Fe(NO)_2\}^{9/10}$ DNICs of the dinuclear complexes, presumably due to slightly different donicity between the R_2NH ligation of BMPA and R_3N ligation of BPMP. Additional derivatization of BMPA via alkylation with CH_3I or a related alkylating agent may provide a closer electronic model of the proposed BPMP DNIC products. Lastly, while obtaining crystal structures of the dinuclear DNICs is unlikely due to their instability, the X-Ray crystallographic structural characterization of the BMPA DNICs would compliment the mechanistic proposals for the dinuclear DNICs, and particularly lend further support to our coordination number proposals.

In Chapter 5, the preliminary synthesis and characterization of a first-generation symmetric carboxylate complex is reported. While this complex could generate substoichiometric N_2O via direct-coupling upon its slow decomposition in MeOH solution, additional spectroscopic studies were precluded due to the complexes insolubility in other polar aprotic organic solvents. Nonetheless, these preliminary data are encouraging because they illustrate that a pseudo-stable hs-$[\{FeNO\}^7]_2$ could be synthesized and stored, allowing us to characterize its decomposition via solution IR. The preliminary synthesis of a more soluble derivative containing a tBuPhO backbone was optimized, but future work is needed to metallate/nitrosylate and characterize this complex. Additional potential building blocks for further derivatization are proposed but their syntheses have not been optimized.

Another experimental subtlety from this chapter originates from CV measurements of $[Fe_2(PhO(Py)_2(OAc)_2)(OAc)(NO)_2]$ in methanolic solution. For this complex, the hs-$\{FeNO\}^{7/8}$ reduction is irreversible, however, on the reverse (re-oxidative) scan, new oxidative events appear, corresponding to the re-generation of the metallated precursor complex $[Fe_2(PhO(Py)_2(OAc)_2)(OAc)]$. This stands in contrast to the complexes discussed in Chapters 2

and 3, where the CVs taken in aprotic solvents result in the formation of new redox events, attributed to the oxidation/reduction of the μ-oxo bridged products. Multiple turnover studies would be of general interest in gauging the effectiveness of the model complexes discussed in this thesis as catalysts for the reduction of NO. Specifically, these data suggest that MeOH may act as a suitable proton donor under multiple turnover conditions that can protonate the basic μ-oxo product that forms upon N-N coupling and N_2O release from $[Fe_2(PhO(Py)_2(OAc)_2)(OAc)(NO)_2]$, thereby recreating the diferrous starting complex after further reduction. This complex therefore seems particularly suitable for multiple turnover studies.

6.3 References

(1) Hayashi, T., Caranto, J. D., Wampler, D. A., Kurtz, D. M., Jr.;Moënne-Loccoz, P. Insights into the Nitric Oxide Reductase Mechanism of Flavodiiron Proteins from a Flavin-Free Enzyme. *Biochemistry* **2010**, *49*, 7040−7049.

(2) Caranto, J. D., Weitz, A., Giri, N., Hendrich, M. P.;Kurtz, D. M. J. A Diferrous-Dinitrosyl Intermediate in the N_2O-Generating Pathway of a Deflavinated Flavo-Diiron Protein. *Biochemistry* **2014**, *53*, 5631–5637.

(3) Caranto, J. D., Weitz, A., Hendrich, M. P.;Kurtz, D. M., Jr. The Nitric Oxide Reductase Mechanism of a Flavo-Diiron Protein: Identification of Active-Site Intermediates and Products. *J. Am. Chem. Soc.* **2014**, *136*, 7981–7992.

(4) Weitz, A. C., Giri, N., Caranto, J. D., Kurtz, D. M., Bominaar, E. L.;Hendrich, M. P. Spectroscopy and DFT Calculations of a Flavo-diiron Enzyme Implicate New Diiron Site Structures. *J. Am. Chem. Soc.* **2017**, *139*, 12009-12019.

(5) Zhang, Y., Pavlosky, M. A., Brown, C. A., Westre, T. E., Hedman, B., Hodgson, K. O.;Solomon, E. I. Spectroscopic and Theoretical Description of the Electronic Structure of the S = 3/2 Nitrosyl Complex of Non-heme Iron Enzymes. *J. Am. Chem. Soc.* **1992**, *114*, 9189-9191.

(6) Brown, C. A., Pavlosky, M. A., Westre, T. E., Zhang, Y., Hedman, B., Hodgson, K. O.;Solomon, E. I. Spectroscopic and theoretical description of the electronic structure of S= 3/2 iron-nitrosyl complexes and their relation to O2 activation by non-heme iron enzyme active sites. *J. Am. Chem. Soc.* **1995**, *117*, 715-732.

(7) Frederick, R. E., Caranto, J. D., Masitas, C. A., Gebhardt, L. L., MacGowan, C. E., Limberger, R. J.;Kurtz, D. M., Jr. Dioxygen and Nitric Oxide Scavenging by *Treponema denticola* Flavodiiron Protein: A Mechanistic Paradigm for Catalysis. *J. Biol. Inorg. Chem.* **2015**, *20*, 603-613.

(8) White, C. J., Speelman, A. L., Kupper, C., Demeshko, S., Meyer, F., Shanahan, J. P., Alp, E. E., Hu, M., Zhao, J.;Lehnert, N. The Semireduced Mechanism for Nitric Oxide Reduction by Non-Heme Diiron Complexes: Modeling Flavodiiron Nitric Oxide Reductases. *J. Am. Chem. Soc.* **2018**, *140*, 2562-2574.

(9) Jana, M., White, C. J., Pal, N., Demeshko, S., Cordes, C., Meyer, F., Lehnert, N.;Majumdar, A. Functional Models for the Mono- and Dinitrosyl Intermediates of FNORs: Semireduction versus Superreduction of NO. *J. Am. Chem. Soc.* **2020**, *142*, 6600-6616.

(10) Kindermann, N., Schober, A., Demeshko, S., Lehnert, N.;Meyer, F. Reductive Transformations of a Pyrazolate-Based Bioinspired Diiron−Dinitrosyl Complex. *Inorg. Chem.* **2016**, *55*, 11538-11550.

(11) Jana, M., Pal, N., White, C. J., Kupper, C., Meyer, F., Lehnert, N.;Majumdar, A. Functional Mononitrosyl Diiron(II) Complex Mediates the Reduction of NO to N_2O with Relevance for Flavodiiron NO Reductases. *J. Am. Chem. Soc.* **2017**, *140*, 14380-14383.

(12) Speelman, A. L., Zhang, B., Silakov, A., Skodje, K. M., Alp, E. E., Zhao, J., Hu, M. Y., Kim, E., Krebs, C.;Lehnert, N. Unusual Synthetic Pathway for an $\{Fe(NO)_2\}^9$ Dinitrosyl Iron Complex (DNIC) and Insight into DNIC Electronic Structure via Nuclear Resonance Vibrational Spectroscopy. *Inorg. Chem.* **2016**, *55*, 5485-5501.

(13) Tonzetich, Z. J., Do, L. H.;Lippard, S. J. Dinitrosyl Iron Complexes Relevant to Rieske Cluster Nitrosylation. *J. Am. Chem. Soc.* **2009**, *131*, 7964-7965.

(14) Ye, S.;Neese, F. The Unusual Electronic Structure of Dinitrosyl Iron Complexes. *J. Am. Chem. Soc.* **2010**, *132*, 3646–3647.

(15) Tran, C. T., Skodje, K. M.;Kim, E. Monomeric Dinitrosyl Iron Complexes: Synthesis and Reactivity; Karlin, K. D., Ed.; John Wiley & Sons, Inc. : Hoboken, NJ, 2014, p 339.

(16) Tsai, M. L., Tsou, C. C.;Liaw, W. F. Dinitrosyl Iron Complexes (DNICs): From Biomimetic Synthesis and Spectroscopic Characterization towards Unveiling the Biological and Catalytic Roles of DNICs. *Acc. Chem. Res.* **2015**, *48*, 1184-1193.

(17) Dong, H. T., White, C. J., Zhang, B., Krebs, C.;Lehnert, N. Non-Heme Diiron Model Complexes Can Mediate Direct NO Reduction: Mechanistic Insight into Flavodiiron NO Reductases. *J. Am. Chem. Soc.* **2018**, *140*, 13429-13440.

(18) Vicente, J. B.;Teixeira, M. Redox and Spectroscopic Properties of the *Escherichia coli* Nitric Oxide-detoxifying System Involving Flavorubredoxin and Its NADH-oxidizing Redox Partner. *J. Biol. Chem.* **2005**, *280*, 34599-34608.

(19) Lu, J., Bi, B., Lai, W.;Chen, H. Origin of Nitric Oxide Reduction Activity in Flavo-Diiron NO Reductase: Key Roles of the Second Coordination Sphere. *Angew. Chem. Int. Ed.* **2019**, *58*, 3795-3799.

(20) Biswas, S., Kurtz, D. M., Montoya, S. R., Hendrich, M. P.;Bominaar, E. L. The Catalytic Role of a Conserved Tyrosine in Nitric Oxide-Reducing Non-heme Diiron Enzymes. *ACS Catal.* **2020**, 8177-8186.

(21) Speelman, A. L., White, C. J., Zhang, B., Alp, E. E., Zhao, J., Hu, M., Krebs, C., Penner-Hahn, J.;Lehnert, N. Non-heme High-Spin $\{FeNO\}^{6-8}$ Complexes: One Ligand Platform Can Do It All. *J. Am. Chem. Soc.* **2018**, *140*, 11341-11359.

(22) Chalkley, M. J.;Peters, J. C. A Triad of Highly Reduced, Linear Iron Nitrosyl Complexes: $\{FeNO\}^{8-10}$. *Angew. Chem. Int. Ed.* **2016**, *55*, 11995-11998.

(23) Confer, A. M., McQuilken, A. C., Matsumura, H., Moënne-Loccoz, P.;Goldberg, D. P. A Nonheme, High-Spin $\{FeNO\}^8$ Complex that Spontaneously Generates N_2O. *J. Am. Chem. Soc.* **2017**, *139*, 10621-10624.